

***PHOTON FACTORY
ACTIVITY REPORT***

1994

#12



NATIONAL LABORATORY FOR HIGH ENERGY PHYSICS; KEK

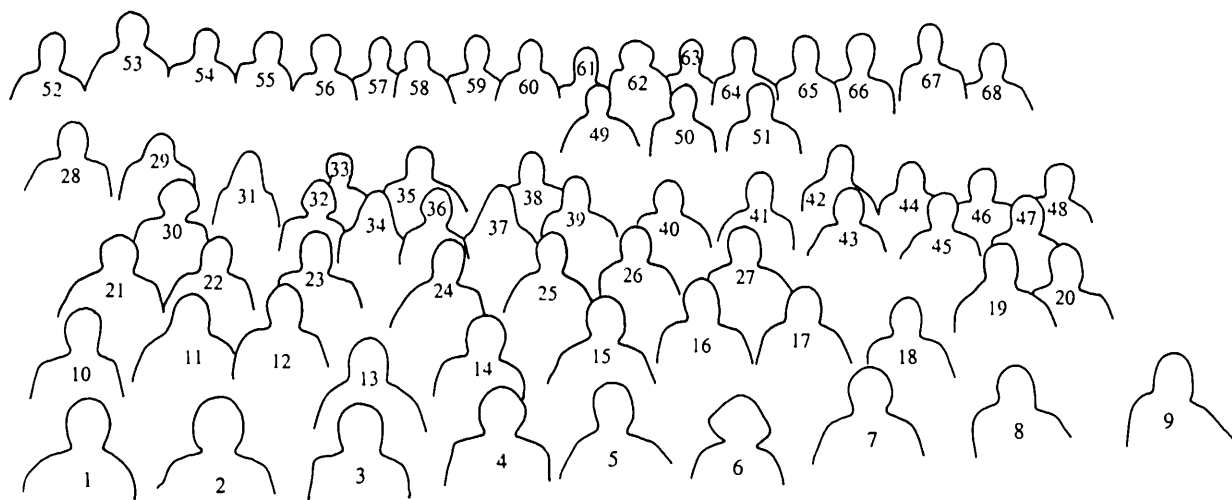
Photon Factory

Activity Report

1994



Staff members and visitors of the Photon Factory gathered in front of the PF office building.



- | | | |
|-------------------|-------------------|------------------|
| 1. T. Honda | 24. Y. Otake | 47. Y. Takiyama |
| 2. Yo. Saito | 25. N. Watanabe | 48. S. Yamaguchi |
| 3. I. Sato | 26. H. Hanaki | 49. A. Koyama |
| 4. M. Kihara | 27. T. Matsushita | 50. A. Iida |
| 5. S. Fukuda | 28. H. Kawata | 51. K. Haga |
| 6. N. Usami | 29. T. Suwada | 52. A. Higuchi |
| 7. T. Kosuge | 30. M. Noji | 53. K. Tsuchiya |
| 8. Y. Uchida | 31. M. Kimura | 54. A. Yagishita |
| 9. Yu. Saito | 32. F. Mori | 55. S. Kamada |
| 10. S. Asaoka | 33. D. Cookson | 56. T. Kasuga |
| 11. M. Nomura | 34. K. Ouchi | 57. S. K. Wu |
| 12. M. Kobayashi | 35. F. Johnson | 58. H. Sugiyama |
| 13. Y. Amemiya | 36. S. Takano | 59. Y. L. Yan |
| 14. H. Kobayakawa | 37. A. Kikuchi | 60. A. Mishina |
| 15. T. Kamitani | 38. G. Foran | 61. K. Iwano |
| 16. I. Abe | 39. K. Ohsumi | 62. T. Mori |
| 17. S. Anami | 40. K. Tanaka | 63. T. Nakajima |
| 18. K. Ito | 41. K. Kobayashi | 64. T. Shidara |
| 19. T. Azuma | 42. A. Ueda | 65. S. Yamamoto |
| 20. Y. Hori | 43. N. Nakamura | 66. T. Hatano |
| 21. T. Nogami | 44. A. Toyoshima | 67. Y. Kitajima |
| 22. S. Tokumoto | 45. C. O. Pak | 68. R. Colella |
| 23. A. Hosoya | 46. T. Sekitani | |

PREFACE

Photon Factory Activity Report #12 deals with our activities in the period from October 1993 through September 1994.

We operate two light sources at the Photon Factory; the 2.5-GeV Photon Factory storage ring, which is a dedicated light source, and the 6.5-GeV TRISTAN Accumulation Ring, which is parasitically used as a light source. We keep more than seventy experimental stations at two facilities, and accept experiments primarily according to approval by the Program Advisory Committee. The number of proposals to the Photon Factory has been still growing. Three-hundred eighty two proposals were approved by the PAC in FY1994, which is an increase by thirteen percent compared to the previous year. Remarkable was growth in biology proposals, particularly proposals in protein crystallography. In FY1994, we accepted approximately 20,000 man-days as general users, and almost ten percent of them were from abroad. We always open the facility to users, not only domestic but also international.

Recently we have been concentrating our effort to upgrading of the light sources and reconstruction of the experimental stations to keep the Photon Factory an attractive research facility in the forthcoming years.

We have already started a program of reducing the emittance of the 2.5-GeV storage ring, which now operates with an emittance of 110 nm-rad, to 27 nm-rad by modifying the lattice, with the goal of operation at the reduced emittance in the fall of 1997.

We also have conceived of a conversion of the TRISTAN Accumulation Ring to a dedicated light source of high energies. The on-going TRISTAN project will terminate by the end of 1995, and the TRISTAN Main Ring will be converted to a new B-Factory. At this moment, the TRISTAN Accumulation Ring will be disused as the injector to the Main Ring, and conversion of the AR to a dedicated light source becomes possible.

Reconstruction of the experimental stations is also of primary importance. Scrap-and-build of old beamlines has been continually pursued, as we will describe in the text. A plan has been seriously considered to implement third protein crystallography station in collaboration with Tsukuba Advanced Research Alliance (TARA) of Tsukuba University. So far, since the beginning of the Photon Factory history, we have collaborated with other institutions; universities, national institutes and private companies, in order to facilitate implementation of experimental stations. We are confident much more of the importance of collaboration with other institutions to form strong research groups for advanced study.

The former Director of the Photon Factory, Professor Hiroshi Iwasaki ended his term of office on March 31, 1994. Professor Iwasaki joined the Photon Factory in 1986 and, after five-year service as Head of Instrumentation Division, became the Director of the Photon Factory in April, 1991. We all thank him for his leadership and enthusiasm for science during his office.



Motohiro Kihara

Director, Photon Factory

Editorial Board

HYODO, Kazuyuki
KASUGA, Toshio
NAKAMURA, Norio
NASU, Keiichiro*
SAITO, Yoshio
SHIMOMURA, Osamu
YAMAMOTO, Shigeru
(*Chief editor)

Acknowledgments

The editors would like to thank Ms. Miyako Kimura and Sumie Imai for their help in editing this issue.

KEK Progress Report 95-1 A/M

© National Laboratory for High Energy Physics, 1995

KEK Reports are available from:

Technical Information & Library
National Laboratory for High Energy Physics
1-1 Oho, Tsukuba-shi
Ibaraki-ken, 305
JAPAN

Phone: +81-298-64-1171
Fax: +81-298-64-4604
e-mail: LIBRARY@KEKVAX.KEK.JP
Telex: 3652-534 (Domestic)
(0)3562-534 (International)
Cable: KEKOH

You can jump to the article by clicking its title.

CONTENTS

	Page
PREFACE	
CONTENTS	G – 1
OUTLINE OF THE PHOTON FACTORY	G – 2
INTRODUCTION	I – 1
SCIENTIFIC DISCIPLINES	
A. Introduction	S – 1
B. Theoretical Researches	S – 1
C. Atomic and Molecular Science	S – 6
D. VUV and Soft X-ray Spectroscopy of Solids	S – 11
E. X-ray Scattering Spectroscopy of Magnetic Materials	S – 17
F. Structural Properties of Condensed Matters	S – 20
G. Properties of Solid Surfaces and Adsorbates	S – 26
H. Structures and Functions of Proteins	S – 29
I. Radiobiology Using Synchrotron Radiation	S – 33
J. X-ray Microbeams and X-ray Microscopy	S – 38
EXPERIMENTAL FACILITIES	
A. Beamlines	E – 1
B. New Instrumentation	E – 6
ACCELERATOR OPERATIONS, RESEARCHES AND DEVELOPMENTS	
A. Injector Linac	A – 1
B. PF Storage Ring	A – 2
C. Tristan Accumulation Ring	A – 17
PROJECTS	
A. The Tristan Super Light Facility	P – 1
B. VUV-FEL	P – 20
C. KEKB	P – 23
D. Slow-Positron Source	P – 30
COLLABORATIONS	
A. Introduction	C – 1
B. Research Center for Spectrochemistry, Univ. of Tokyo	C – 1
C. Synchrotron Radiation Laboratory, Institute for Solid State Physics, Univ. of Tokyo	C – 3
D. Other Ministries	C – 6
E. Industry Beamlines	C – 9
F. The Australian National Beamline Facility	C – 11
USERS' SHORT REPORTS	
Contents	i
Users' Short Reports	1
Author Index	400
LIST OF PUBLISHED PAPERS 1993/94	

OUTLINE OF THE PHOTON FACTORY

INTRODUCTION

The Photon Factory (PF) is a national synchrotron radiation research facility affiliated with the National Laboratory for High Energy Physics (KEK) supervised by the Ministry of Education, Science and Culture. It is located at the northern end of Tsukuba Science City, which is about 60 km north-east of Tokyo. The PF consists of a 2.5-GeV electron/positron linear accelerator, a 2.5-GeV electron/positron storage ring as a dedicated light source, TRISTAN accumulation ring as a parasitic light source and beamlines and experimental stations for exploiting synchrotron radiation in studies involving such research fields as physics, chemistry, biology, medical sciences, pharmacology, earth sciences and lithography. All of the facilities for synchrotron radiation research are open to scientists of universities and research institutes belonging to the government, public organizations, private enterprises and those of foreign countries. The members of institutions affiliated with the Ministry of Education, Science and Culture are given the highest priority among all users. Applications from other organizations are also admitted.

OVERVIEW OF THE FACILITY

The plan view of the facility is shown in Fig. 1. The 2.5-GeV linac housed in a 450 m long enclosure is used as an injector for both the PF storage ring and the accumulation ring (AR) of TRISTAN main ring. The PF storage ring was already equipped with the flexibility of storing positrons in place of electrons. A part of the AR has been used as a high energy synchrotron radiation source producing radiation from its bending magnet and two insertion devices. One of the insertion devices produces elliptically polarized radiation, and the other highly brilliant radiation in the X-ray region. The AR has been operated for synchrotron radiation users with an energy range from 5.8 to 6.5 GeV.

ORGANIZATION AND STAFF

The organization of KEK is shown in Fig. 2. The PF is composed of three divisions: Injector Linac, Light Source and Instrumentation. A working group has been organized for the design study of the use of the TRISTAN Main Ring for synchrotron radiation science. The organization of the PF including its personnel is shown in Fig. 3. The Advisory Council for the PF was established to discuss scientific programs and management of the PF. The council consists of twenty one senior scientists including ten non-KEK members (Table 1a and 1b). The term of membership is two years. The Program Advisory Committee (PAC) consisting of the members listed in Table 2a and 2b receives proposals of users and decides priorities for the experiments.

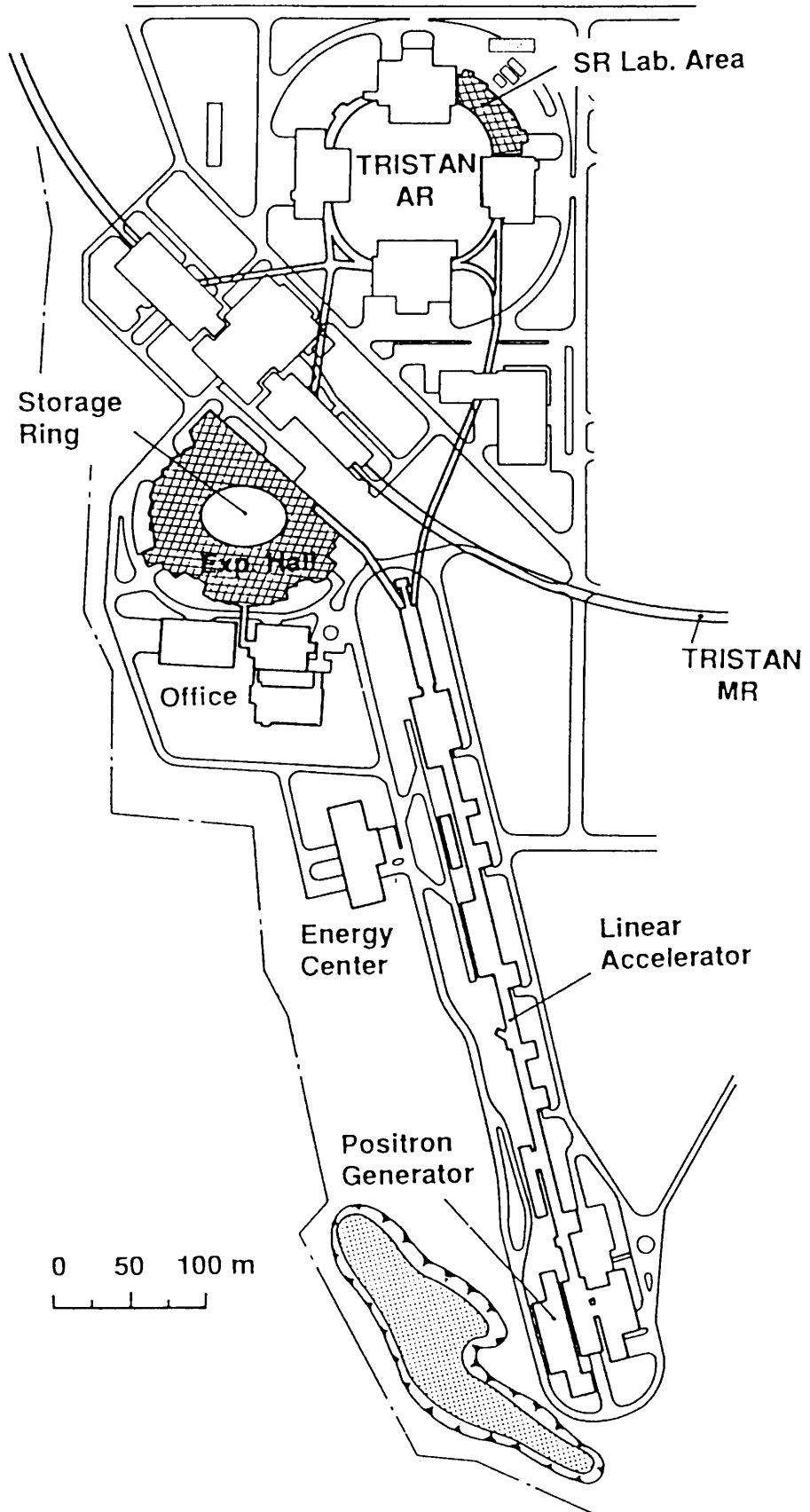
In Table 3 the names of the staff members are listed in alphabetical order to help make direct contact. Also, the numbers of staff members and visiting scientists are summarized in Table 4.

BUDGET AND OPERATION TIME

The budget of the PF is supplied by the Ministry of Education, Science and Culture. The annual budget after commissioning of the facilities is shown in Table 5. The numbers of beam channels in each year are shown in Table 6.

The machine operation time is divided into three terms per year. Summary and timetable of the machine operation in FY 1994 are shown in Tables 7 and 8, respectively.

In Table 9, we have shown the total number of proposals approved by the aforementioned PAC.



Plan view of the Photon Factory

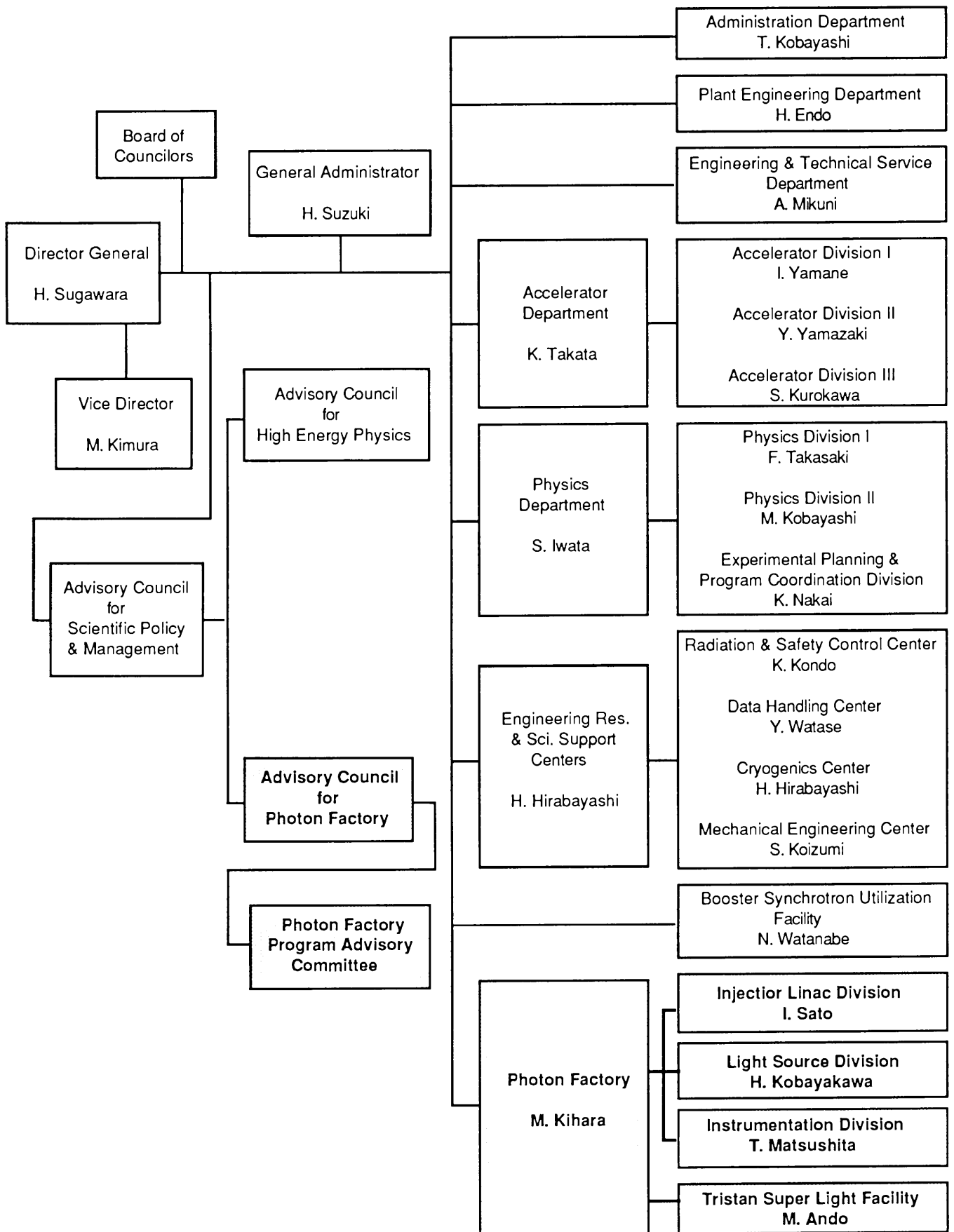


Fig. 2 Organization of KEK

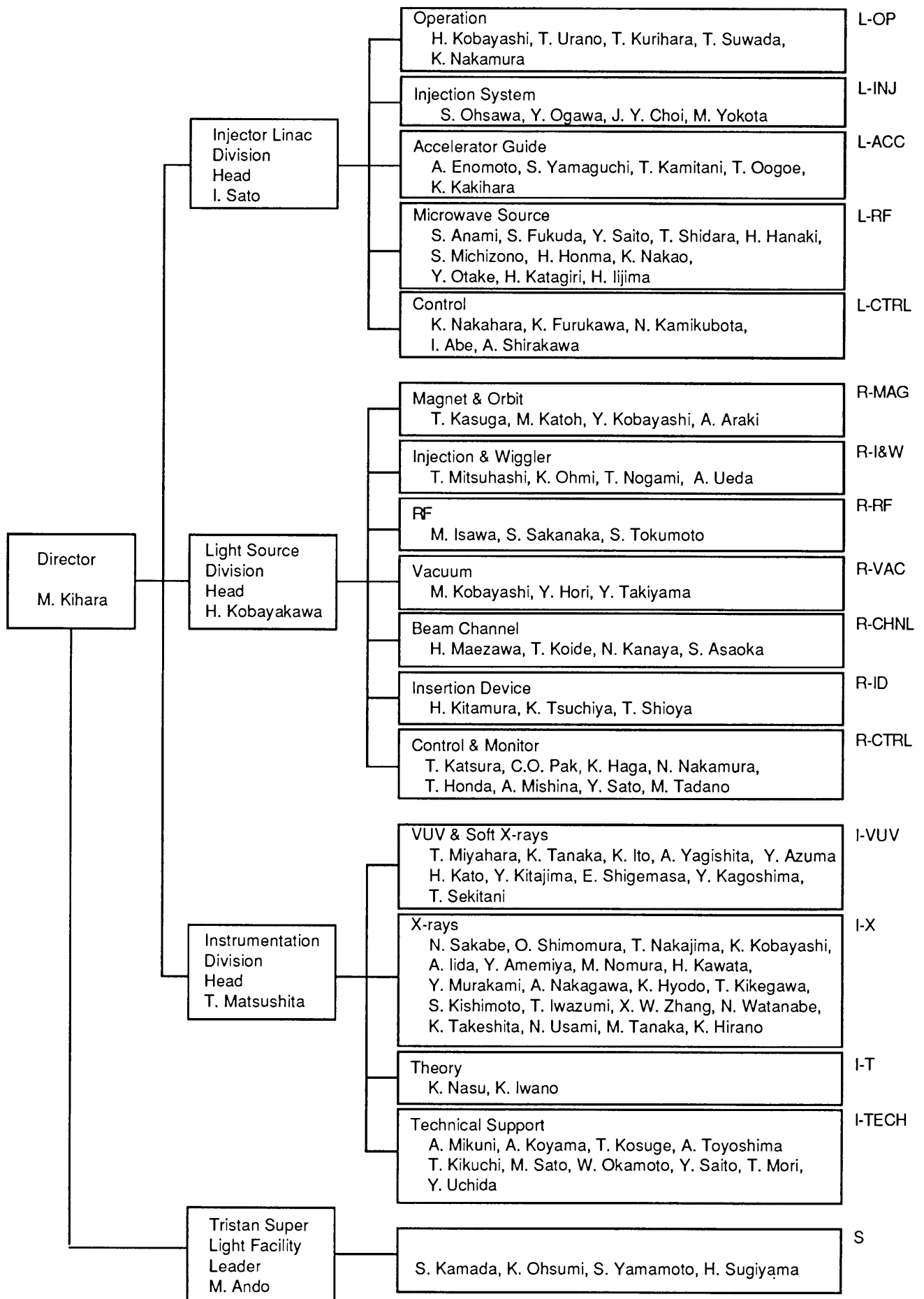


Fig. 3 Organization of the Photon Factory

Table 1a Members of Advisory Council; April '91 ~ March '93

** Chairman * Vice-Chairman

ANAMI, Shozo	Injector Linac Division, PF, KEK
ANDO, Masami	Tristan Super Light Facility, PF, KEK
FUJII, Yasuhiko	Institute for Solid State Physics, University of Tokyo
HARADA, Jinpei	Faculty of Engineering, Nagoya University
HIEDA, Kotaro	Faculty of Science, Rikkyo University
ISHII, Takehiko*	Institute for Solid State Physics, University of Tokyo
ITO, Kenji	Instrumentation Division, PF, KEK
KATSUBE, Yukiteru	Institute for Protein Research, Osaka University
KIKUTA, Seishi	Faculty of Engineering, University of Tokyo
KOBAYAKAWA, Hisashi	Light Source Division, PF, KEK
KOBAYASHI, Hitoshi	Injector Linac Division, PF, KEK
KOBAYASHI, Masanori	Light Source Division, PF, KEK
MAEZAWA, Hideki	Light Source Division, PF, KEK
MATSUSHITA, Tadashi	Instrumentation Division, PF, KEK
NAKAJIMA, Tetsuo	Instrumentation Division, PF, KEK
NITTONO, Osamu	Faculty of Engineering, Tokyo Institute of Technology
OHTA, Toshiaki	Faculty of Science, Hiroshima University
SAKABE, Noriyoshi	Instrumentation Division, PF, KEK
SATO, Isamu**	Injector Linac Division, PF, KEK
SUZUKI, Kenji	Institute for Materials Research, Tohoku University
TOKONAMI, Masayasu	Faculty of Science, University of Tokyo

Table 1b Members of Advisory Council; April '94 ~ March '96

** Chairman * Vice-Chairman

ANAMI, Shozo	Injector Linac Division, PF, KEK
ANDO, Masami	Tristan Super Light Facility, PF, KEK
FUJII, Yasuhiko	Institute for Solid State Physics, University of Tokyo
HIEDA, Kotaro	Faculty of Science, Rikkyo University
ISHII, Takehiko*	Institute for Solid State Physics, University of Tokyo
ITO, Kenji	Instrumentation Division, PF, KEK
KIKUTA, Seishi	Faculty of Engineering, University of Tokyo
KOBAYAKAWA, Hisashi	Light Source Division, PF, KEK
KOBAYASHI, Masanori	Light Source Division, PF, KEK
MAEZAWA, Hideki	Light Source Division, PF, KEK
MATSUSHITA, Tadashi	Instrumentation Division, PF, KEK
MITSUI, Yukio	Department of Bio Engineering, Nagaoka University of Technology
NAKAHARA, Kazuo	Injector Linac Division, PF, KEK
NAKAJIMA, Tetsuo	Instrumentation Division, PF, KEK
NITTONO, Osamu	Faculty of Engineering, Tokyo Institute of Technology
OHTA, Toshiaki	Faculty of Science, Hiroshima University
SATO, Isamu**	Injector Linac Division, PF, KEK
SHIMOMURA, Osamu	Instrumentation Division, PF, KEK
SHIOTANI, Nobuhiro	Tokyo University of Fisheries
SUGA, Yoshimasa	Faculty of Engineering Science, Osaka University

Table 2a Members of Program Advisory Committee; Fiscal Year '93

* Chairman

KOBAYAKAWA, Hisashi	Light Source Division, PF, KEK
KOSUGI, Nobuhiro	Institute for Molecular Science, Okazaki National Research Institute
MATSUSHITA, Tadashi*	Instrumentation Division, PF, KEK
MURATA, Takatoshi	Department of Physics, Kyoto University of Education
NASU, Keiichiro	Instrumentation Division, PF, KEK
OHTA, Toshiaki	Faculty of Science, Hiroshima University
SAKATA, Makoto	School of Engineering, Nagoya University
SATO, Isamu	Injector Linac Division, PF, KEK
SHIMOMURA, Osamu	Instrumentation Division, PF, KEK
SUEMATSU, Hiroyoshi	Faculty of Science, University of Tokyo
TANAKA, Nobuo	Faculty of Bioscience and Biotechnology, Tokyo Institute of Technology
TANIGUCHI, Masaki	Faculty of Science, Hiroshima University
TOKUNAGA, Fumio	Faculty of Science, Osaka University
YAGISHITA, Akira	Instrumentation Division, PF, KEK
YOSHIDA, Satohiro	Faculty of Engineering, Kyoto University
UEKI, Tatsuo	Institute of Physical and Chemical Research

Table 2b Members of Program Advisory Committee; Fiscal Year '94

* Chairman

ASHIDA, Tamaichi	School of Engineering, Nagoya University
KOBAYAKAWA, Hisashi	Light Source Division, PF, KEK
KOSUGI, Nobuhiro	Institute for Molecular Science, Okazaki National Research Institute
MATSUSHITA, Tadashi*	Instrumentation Division, PF, KEK
NASU, Keiichiro	Instrumentation Division, PF, KEK
OYANAGI, Hiroyuki	Electrotechnical Laboratory
SAKAI, Nobuhiko	Faculty of Science, Himeji Institute of Technology
SAKATA, Makoto	School of Engineering, Nagoya University
SATO, Isamu	Injector Linac Division, PF, KEK
SATO, Yukinori	Research Institute for Scientific Measurements, Tohoku University
TANAKA, Nobuo	Faculty of Bioscience and Biotechnology, Tokyo Institute of Technology
TANIGUCHI, Masaki	Faculty of Science, Hiroshima University
TSUJI, Kazuhiko	Faculty of Science and Technology, Keio University
UEKI, Tatsuo	Institute of Physical and Chemical Research
WAKABAYASHI, Katsuzo	Faculty of Engineering Science, Osaka University

Table 3 Staff members of the Photon Factory

Name		Responsibility*	e-mail address
Research Staff			
KIHARA, Motohiro	Apr. 1, 94 J	Director	KIHARAM@KEKVAX.KEK.JP
IWASAKI, Hiroshi	Mar. 31, 94 R	Director	
ANAMI, Shozo		L-RF	ANAMI@KEKVAX.KEK.JP
CHOI, Jae-Young	Sept. 1, 94 J	L-INJ	CHOU@KEKVAX.KEK.JP
ENOMOTO, Atsushi		L-ACC	ENOMOTOA@KEKVAX.KEK.JP
FUKUDA, Shigeki		L-RF	SFUKUDA@KEKVAX.KEK.JP
FURUKAWA, Kazuro		L-CTRL	FURUKAWA@KEKVAX.KEK.JP
HANAKI, Hirofumi		L-RF	HANAKI@KEKVAX.KEK.JP
KAMIKUBOTA, Norihiko		L-CTRL	KAMI@KEKVAX.KEK.JP
KAMITANI, Takuya		L-ACC	KAMITANI@KEKVAX.KEK.JP
KOBAYASHI, Hitoshi		L-OP	HITOSHIK@KEKVAX.KEK.JP
KURIHARA, Toshikazu		L-OP	TKURIHAR@KEKVAX.KEK.JP
MICHIZONO, Shin'ichiro		L-RF	MICHIZON@KEKVAX.KEK.JP
NAKAHARA, Kazuo		L-CTRL	NAKAHAR@KEKVAX.KEK.JP
OGAWA, Yujiro		L-INJ	OGAWAYJ@KEKVAX.KEK.JP
OHSAWA, Satoshi		L-INJ	OHSAWA@KEKVAX.KEK.JP
SAITO, Yoshio		L-RF	
SATO, Isamu		L-Head	
SHIDARA, Tetsuo		L-RF	SHIDARA@KEKVAX.KEK.JP
SUWADA, Tsuyoshi		L-OP	SUWADA@KEKVAX.KEK.JP
URANO, Takao		L-OP	URANO@KEKVAX.KEK.JP
YAMAGUCHI, Seiya		L-RF	SYAMA@KEKVAX.KEK.JP
HAGA, Kaichi		R-CTRL	HAGA@KEKVAX.KEK.JP
HONDA, Tohru		R-CTRL	HONDAT@KEKVAX.KEK.JP
HORI, Yoichiro		R-VAC	HORI@KEKVAX.KEK.JP
ISAWA, Masaaki		R-RF	ISAWA@KEKVAX.KEK.JP
KANAYA, Noriichi		R-CHNL	KANAYA@KEKVAX.KEK.JP
KASUGA, Toshio	Apr. 1, 93 J	R-MAG	KASUGAT@KEKVAX.KEK.JP
KATOH, Masahiro		R-MAG	KATOHM@KEKVAX.KEK.JP
KATSURA, Tomotaro		R-CTRL	KATSURA@KEKVAX.KEK.JP
KITAMURA, Hideo		R-ID	KITAMURA@KEKVAX.KEK.JP
KOBAYAKAWA, Hisashi		R-Head	KOBAYAKA@KEKVAX.KEK.JP
KOBAYASHI, Masanori		R-VAC	KOBYASIMR@KEKVAX.KEK.JP
KOBAYASHI, Yukinori		R-MAG	YUKINORI@KEKVAX.KEK.JP
KOIDE, Tsuneharu		R-CHNL	
MAEZAWA, Hideki		R-CHNL	MAEZAWAH@KEKVAX.KEK.JP
MITSUHASHI, Toshiyuki		R-I&W	MITSUHAS@KEKVAX.KEK.JP
NAKAMURA, Norio		R-CTRL	NORIO@KEKVAX.KEK.JP
OHMI, Kazuhito		R-I&W	OHMI@KEKVAX.KEK.JP
PAK, Cheol On		R-CTRL	PAK@KEKVAX.KEK.JP
SAKANAKA, Shyogo		R-RF	SAKANAKA@KEKVAX.KEK.JP
TSUCHIYA, Kimichika		R-ID	TSUCHIYA@KEKVAX.KEK.JP
AMEMIYA, Yoshiyuki		I-X	AMEMIYA@KEKVAX.KEK.JP
AZUMA, Yoshiro	Jan. 1, 94 J	I-VUV	AZUMA@KEKVAX.KEK.JP
HIRANO, Keiichi	Apr. 1, 92 J	I-X	HIRANO@KEKVAX.KEK.JP
HYODO, Kazuyuki		I-X	HYODO@KEKVAX.KEK.JP
IIDA, Atsuo		I-X	AIIDA@KEKVAX.KEK.JP
ITO, Kenji		I-VUV	ITO@KEKVAX.KEK.JP
IWANO, Kaoru	Jul. 1, 93 J	I-T	IWANO@KEKVAX.KEK.JP
IWAZUMI, Toshiaki		I-X	IWAZUMI@KEKVAX.KEK.JP
KAGOSHIMA, Yasushi		I-VUV	KAGOSIMA@KEKVAX.KEK.JP
KATO, Hiroo		I-VUV	HIROO@KEKVAX.KEK.JP
KAWATA, Hiroshi		I-X	KAWATA@KEKVAX.KEK.JP
KIKEGAWA, Takumi		I-X	KIKEGAWA@KEKVAX.KEK.JP
KISHIMOTO, Syunji		I-X	KISIMOTO@KEKVAX.KEK.JP
KITAJIMA, Yoshinori		I-VUV	KITAJIMA@KEKVAX.KEK.JP

(to be continued)

Name		Responsibility*	e-mail address
KOBAYASHI, Katsumi		I-X	KOBAYASK@KEKVAX.KEK.JP
MATSUSHITA, Tadashi		I-Head	MATSUS@KEKVAX.KEK.JP
MIYAHARA, Tsuneaki		I-VUV	MIYAHARA@KEKVAX.KEK.JP
MURAKAMI, Youichi	Oct. 1, 94 J	I-X	MYOUICHI@KEKVAX.KEK.JP
NAKAGAWA, Atsushi		I-X	NAKAGAWA@KEKVAX.KEK.JP
NAKAJIMA, Tetsuo		I-X	TETSUO@KEKVAX.KEK.JP
NASU, Keiichiro	Nov. 16, 92 J	I-T	KNASU@NASUWS1.KEK.JP
NOMURA, Masaharu		I-X	NOMURAM@KEKVAX.KEK.JP
SAKABE, Noriyoshi	Mar. 31, 94 R	I-X	SAKABE@KEKVAX.KEK.JP
SEKITANI, Tetsuji	Apr. 1, 92 J	I-VUV	SEKITANI@KEKVAX.KEK.JP
SHIGEMASA, Eiji		I-VUV	SIGEMASA@KEKVAX.KEK.JP
SHIMOMURA, Osamu	Oct. 1, 92 J	I-X	SHIMOMURA@KEKVAX.KEK.JP
TAKESHITA, Kunikazu		I-X	TAKESHIT@KEKVAX.KEK.JP
TANAKA, Ken'ichiro		I-VUV	TANAKAK@KEKVAX.KEK.JP
TANAKA, Masahiko		I-X	MASAHIKO@KEKVAX.KEK.JP
USAMI, Noriko		I-X	USAMI@KEKVAX.KEK.JP
WATANABE, Nobuhisa		I-X	NOBUHISA@KEKVAX.KEK.JP
YAGISHITA, Akira		I-VUV	YAGISITA@KEKVAX.KEK.JP
ZHANG, Xiaowei		I-X	XIAOWEI@KEKVAX.KEK.JP
ANDO, Masami		S-Leader	ANDO@KEKVAX.KEK.JP
KAMADA, Susumu		S	KAMADA@KEKVAX.KEK.JP
OHSUMI, Kazumasa		S	OHSUMIK@KEKVAX.KEK.JP
SUGIYAMA, Hiroshi		S	HIROSHIS@KEKVAX.KEK.JP
YAMAMOTO, Shigeru		S	SHIGERU@KEKVAX.KEK.JP
Supporting Staff			
ABE, Isamu		L-CTRL	ABEI@KEKVAX.KEK.JP
HONMA, Hiroyuki		L-RF	
IJIMA, Hitoshi		L-RF	
KAKIHARA, Kazuhisa		L-ACC	KAKIHARA@KEKVAX.KEK.JP
KATAGIRI, Hiroaki		L-RF	KATAGIRI@KEKVAX.KEK.JP
NAKAMURA, Kie		L-OP	KIE@KEKVAX.KEK.JP
NAKAO, Katsumi		L-RF	NAKAOK@KEKVAX.KEK.JP
OOGOE, Takao		L-ACC	OOGOE@KEKVAX.KEK.JP
OTAKE, Yuji		L-OP	OTAKE@KEKVAX.KEK.JP
SHIRAKAWA, Akihiro		L-CTRL	SIRAKAWA@KEKVAX.KEK.JP
YOKOTA, Mitsuhiro		L-INJ	YOKOTA@KEKVAX.KEK.JP
ARAKI, Akira	Jun. 30, 94 L	R-MAG	
ASAOKA, Seiji		R-CHNL	
MISHINA, Atsushi		R-CTRL	MISHINA@KEKVAX.KEK.JP
NAKAMURA, Hajime	Jun. 1, 93 L	R-CTRL	
NOGAMI, Takashi		R-I&W	NOGAMI@KEKVAX.KEK.JP
SATO, Yoshihiro		R-CTRL	YOSHIHIR@KEKVAX.KEK.JP
SHIOYA, Tatsuro		R-ID	SHIOYA@KEKVAX.KEK.JP
TADANO, Mikito	Jun. 1, 93 J	R-CTRL	TADANO@KEKVAX.KEK.JP
TAKIYAMA, Youichi		R-VAC	TAKIYAMA@KEKVAX.KEK.JP
TOKUMOTO, Shuichi		R-RF	TOKUMOTO@KEKVAX.KEK.JP
UEDA, Akira		R-I&W	UEDA@KEKVAX.KEK.JP
KIKUCHI, Takashi		I-TECH	KIKUCHI@KEKVAX.KEK.JP
KOSUGE, Takashi		I-TECH	KOSUGE@KEKVAX.KEK.JP
KOYAMA, Atsushi		I-TECH	KOYAMA@KEKVAX.KEK.JP
MIKUNI, Akira		I-TECH	MIKUNI@KEKVAX.KEK.JP
MORI, Takeharu		I-TECH	MORIT@KEKVAX.KEK.JP
OKAMOTO, Wataru		I-TECH	OKAMOTOW@KEKVAX.KEK.JP
SAITO, Yuuki		I-TECH	YSAITO@KEKVAX.KEK.JP
SATO, Masato		I-TECH	SATOM@KEKVAX.KEK.JP
TOYOSHIMA, Akio		I-TECH	TOYOSIMA@KEKVAX.KEK.JP
UCHIDA, Yoshinori		I-TECH	UCHIDA@KEKVAX.KEK.JP

*: Refer to Fig. 3 for abbreviations.

J: Date when he/she joined the PF.

Name		Responsibility*	e-mail address
KOBAYASHI, Katsumi		I-X	KOBAYASK@KEKVAX.KEK.JP
MATSUSHITA, Tadashi		I-Head	MATSUS@KEKVAX.KEK.JP
MIYAHARA, Tsuncaki		I-VUV	MIYAHARA@KEKVAX.KEK.JP
MURAKAMI, Youichi	Oct. 1, 94 J	I-X	MYOUICHI@KEKVAX.KEK.JP
NAKAGAWA, Atsushi		I-X	NAKAGAWA@KEKVAX.KEK.JP
NAKAJIMA, Tetsuo		I-X	TETSUO@KEKVAX.KEK.JP
NASU, Keiichiro	Nov. 16, 92 J	I-T	KNASU@NASUWSI.KEK.JP
NOMURA, Masaharu		I-X	NOMURAM@KEKVAX.KEK.JP
SAKABE, Noriyoshi	Mar. 31, 94 R	I-X	SAKABE@KEKVAX.KEK.JP
SEKITANI, Tetsuji	Apr. 1, 92 J	I-VUV	SEKITANI@KEKVAX.KEK.JP
SHIGEMASA, Eiji		I-VUV	SIGEMASA@KEKVAX.KEK.JP
SHIMOMURA, Osamu	Oct. 1, 92 J	I-X	SHIMOMURA@KEKVAX.KEK.JP
TAKESHITA, Kunikazu		I-X	TAKESHIT@KEKVAX.KEK.JP
TANAKA, Ken'ichiro		I-VUV	TANAKAK@KEKVAX.KEK.JP
TANAKA, Masahiko		I-X	MASAHIKO@KEKVAX.KEK.JP
USAMI, Noriko		I-X	USAMI@KEKVAX.KEK.JP
WATANABE, Nobuhisa		I-X	NOBUHISA@KEKVAX.KEK.JP
YAGISHITA, Akira		I-VUV	YAGISITA@KEKVAX.KEK.JP
ZHANG, Xiaowei		I-X	XIAOWEI@KEKVAX.KEK.JP
ANDO, Masami		S-Leader	ANDO@KEKVAX.KEK.JP
KAMADA, Susumu		S	KAMADA@KEKVAX.KEK.JP
OHSUMI, Kazumasa		S	OHSUMIK@KEKVAX.KEK.JP
SUGIYAMA, Hiroshi		S	HIROSHIS@KEKVAX.KEK.JP
YAMAMOTO, Shigeru		S	SHIGERU@KEKVAX.KEK.JP
Supporting Staff			
ABE, Isamu		L-CTRL	ABEI@KEKVAX.KEK.JP
HONMA, Hiroyuki		L-RF	
IJIMA, Hitoshi		L-RF	
KAKIHARA, Kazuhisa		L-ACC	KAKIHARA@KEKVAX.KEK.JP
KATAGIRI, Hiroaki		L-RF	KATAGIRI@KEKVAX.KEK.JP
NAKAMURA, Kie		L-OP	KIE@KEKVAX.KEK.JP
NAKAO, Katsumi		L-RF	NAKAOK@KEKVAX.KEK.JP
OOGOE, Takao		L-ACC	OOGOE@KEKVAX.KEK.JP
OTAKE, Yuji		L-OP	OTAKE@KEKVAX.KEK.JP
SHIRAKAWA, Akihiro		L-CTRL	SIRAKAWA@KEKVAX.KEK.JP
YOKOTA, Mitsuhiro		L-INJ	YOKOTA@KEKVAX.KEK.JP
ARAKI, Akira	Jun. 30, 94 L	R-MAG	
ASAOKA, Seiji		R-CHNL	
MISHINA, Atsushi		R-CTRL	MISHINA@KEKVAX.KEK.JP
NAKAMURA, Hajime	Jun. 1, 93 L	R-CTRL	
NOGAMI, Takashi		R-I&W	NOGAMI@KEKVAX.KEK.JP
SATO, Yoshihiro		R-CTRL	YOSHIHIR@KEKVAX.KEK.JP
SHIOYA, Tatsuro		R-ID	SHIOYA@KEKVAX.KEK.JP
TADANO, Mikito	Jun. 1, 93 J	R-CTRL	TADANO@KEKVAX.KEK.JP
TAKIYAMA, Youichi		R-VAC	TAKIYAMA@KEKVAX.KEK.JP
TOKUMOTO, Shuichi		R-RF	TOKUMOTO@KEKVAX.KEK.JP
UEDA, Akira		R-I&W	UEDA@KEKVAX.KEK.JP
KIKUCHI, Takashi		I-TECH	KIKUCHI@KEKVAX.KEK.JP
KOSUGE, Takashi		I-TECH	KOSUGE@KEKVAX.KEK.JP
KOYAMA, Atsushi		I-TECH	KOYAMA@KEKVAX.KEK.JP
MIKUNI, Akira		I-TECH	MIKUNI@KEKVAX.KEK.JP
MORI, Takcharu		I-TECH	MORIT@KEKVAX.KEK.JP
OKAMOTO, Wataru		I-TECH	OKAMOTOW@KEKVAX.KEK.JP
SAITO, Yuuki		I-TECH	YSAITO@KEKVAX.KEK.JP
SATO, Masato		I-TECH	SATOM@KEKVAX.KEK.JP
TOYOSHIMA, Akio		I-TECH	TOYOSIMA@KEKVAX.KEK.JP
UCHIDA, Yoshinori		I-TECH	UCHIDA@KEKVAX.KEK.JP

*: Refer to Fig. 3 for abbreviations.

J: Date when he/she joined the PF.

L: Date when he/she left the PF.

R: Date when he/she retired from the PF.

Table 4 Annual numbers of staff & visiting scientists

Position	Department	1984	1985	1986	1987	1988	1989	1990	1991	1992	1993	1994
Chief Director		1	1	1	1	1	1	1	1	1	1	1
Professor	Injector Linac	3	3	4	4	4	3	3	4	3	3	3
	Light Source	4	3	4	4	4	4	5	5	4	5	5
	Instrumentation	1	2	3	4	5	5	5	6	8	9	8
Associate Professor	Injector Linac	2	2	1	2	3	5	7	6	7	7	7
	Light Source	5	5	3	3	3	5	4	3	3	3	3
	Instrumentation	5	8	7	9	7	10	9	8	10	10	11
Research Associate	Injector Linac	9	10	11	10	10	9	8	9	9	9	10
	Light Source	6	8	9	12	12	9	11	11	12	12	12
	Instrumentation	10	10	13	13	14	11	15	15	15	18	18
Technical Staff	Injector Linac	6	6	7	8	9	10	11	11	11	11	11
	Light Source	6	6	7	7	8	10	10	10	10	10	9
	Instrumentation	4	4	8	9	11	10	9	10	10	10	10
Visiting Scientist	Injector Linac	2	2	2	2	2	2	2	2	2	1	0
	Light Source	4	4	4	4	4	4	4	4	4	3	3
	Instrumentation	6	6	6	6	6	6	6	7	6	6	3
Total		74	80	90	98	103	104	110	112	115	118	114

Table 5 Budget in each fiscal year

(in million yen)

Item	1984	1985	1986	1987	1988	1989	1990	1991	1992	1993	1994
Salary	484	510	561	561	642	757	764	859	898	939	1,029
PF Storage Ring (channel, insertion device, etc.)	0	153	131	647	0	0	196	103	0	0	0
PF Experiments	134	184	190	196	237	341	367	399	375	366	366
PF Operation & Maintenance	552	653	820	907	962	1,078	1,107	1,107	1,042	1,015	1,096
Computer Rentals	135	135	136	136	141	145	145	145	145	145	140
Positron Source & Electric Plant Operation	0	41	138	208	258	300	308	300	253	224	175
Cooling System & Electric Operation	124	180	211	214	217	231	235	240	218	212	218
Electricity	257	338	381	331	355	425	423	423	423	418	431
PF-Industrial Cooperative Experiments	84	95	185	166	302	219	171	174	154	132	86
AR Construction and Experiments				398	267	387	250	260	148	145	145
B Factory (Linac Upgrade)											400
Miscellaneous	115	127	162	120	301	243	287	388	564	877	567
Total	1,885	2,416	2,915	3,884	3,682	4,126	4,253	4,398	4,220	4,473	4,653

Table 6 Yearly account of beam channels

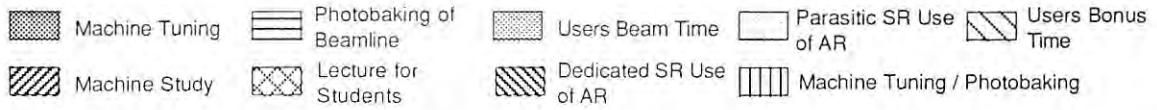
Belonging	1984	1985	1986	1987	1988	1989	1990	1991	1992	1993	1994
PF	8	10	12	13	13	15	15	17	20	21	21
Institutes	1	1	1	3	4	4	4	4	3	2	2
Industry	2	4	4	4	4	4	4	4	4	4	4
Total	11	15	17	20	21	23	23	25	27	27	27

Table 7 Summary of operation in FY 1994 (April 1994 - March 1995) (hours)

Cycle	Linac	PF Ring	Users' time	AR	Dedicated to SR at AR
1	2152	1876	1525	2196	1943
2	2047	1896	1555	2019	1520
3	767	719	499	714	587
Total	4966	4491	3579	4929	4050

Table 8 Timetable of the Machine Operation in FY 1994.

PF : PF ring AR : TRISTAN accumulation ring



Cycle	Time	MON	TUE	WED	THU	FRI	SAT	SUN	MON	TUE	WED	THU	FRI	SAT	SUN	MON	TUE	WED	THU	FRI	SAT	SUN
		9 17	9 17	9 17	9 17	9 17	9 17	9 17	9 17	9 17	9 17	9 17	9 17	9 17	9 17	9 17	9 17	9 17	9 17	9 17	9 17	9 17
1-1	Date	3/28	29	30	31	4/1	2	3	4	5	6	7	8	9	10	11	12	13	14	15	16	17
	Linac																					
	PF AR																					
1-1 / 1-2	Date	18	19	20	21	22	23	24	25	26	27	28	29	30	5/1	2	3	4	5	6	7	8
	Linac																					
	PF AR																					
1-2	Date	9	10	11	12	13	14	15	16	17	18	19	20	21	22	23	24	25	26	27	28	29
	Linac																					
	PF AR																					
1-3	Date	30	31	6/1	2	3	4	5	6	7	8	9	10	11	12	13	14	15	16	17	18	19
	Linac																					
	PF AR																					
1-4	Date	20	21	22	23	24	25	26	27	28	29	30	7/1	2	3	4	5	6	7	8	9	10
	Linac																					
	PF AR																					
2-1	Date	9/26	27	28	29	30	10/1	2	3	4	5	6	7	8	9	10	11	12	13	14	15	16
	Linac																					
	PF AR																					
2-1 / 2-2	Date	17	18	19	20	21	22	23	24	25	26	27	28	29	30	31	11/1	2	3	4	5	6
	Linac																					
	PF AR																					
2-2 / 2-3	Date	7	8	9	10	11	12	13	14	15	16	17	18	19	20	21	22	23	24	25	26	27
	Linac																					
	PF AR																					
2-3	Date	28	29	30	12/1	2	3	4	5	6	7	8	9	10	11	12	13	14	15	16	17	18
	Linac																					
	PF AR																					
2-3	Date	19	20	21	22	23	24	25	26	27	28	29	30	31	1/1	2	3	4	5	6	7	8
	Linac																					
	PF AR																					
3-1	Date	2/6	7	8	9	10	11	12	13	14	15	16	17	18	19	20	21	22	23	24	25	26
	Linac																					
	PF AR																					
3-1 / 3-2	Date	27	28	3/1	2	3	4	5	6	7	8	9	10	11	12	13	14	15	16	17	18	19
	Linac																					
	PF AR																					
3-2	Date	20	21	22	23	24	25	26	27	28	29	30	31	4/1	2	3	4	5	6	7	8	9
	Linac																					
	PF AR																					

SEMINARS, MEETINGS AND WORK SHOPS

Twelve seminars were given by an in-house staff and visiting scientists who visited the PF in 1994. Ten users' meetings or work shops were held in FY 1994, including the annual PF symposium.

PF Seminars

Perkins, S. (Royal Free Hospital School of Medicine, University of London) Recent Developments in Neutron and X-ray Scattering Applied to the Solution Structures of the Complement Proteins of Immune Defence and to Time-Course Studies of the Oxidative Modification of Low Density Lipoproteins	October 5, 1993
Haensel, R. (ESRF) Synchrotron Radiation Experiment with 3rd Generation Source: New Possibilities, New Challenges	November 16, 1993
Pianetta, P. (SSRL) X-ray Fluorescence Analysis of Trace Contaminants on Si Wafers	November 17, 1993
Lindau, I. (University of Lund) High-Resolution Core Level Spectroscopy Using Synchrotron Radiation	November 17, 1993
Nielsen, J. A.- (ESRF) Experiments with Hard X-ray Undulator Radiation at the ESRF	March 22, 1994
Koike, M. (LBL, University of California) High Resolution VUV/EUV Monochromator Beamlines for Low Emittance Synchrotron Radiation	March 29, 1994
Sato, Y. (Faculty of Pharmaceutical Science, University of Tokyo) Crystal Structure Analysis of Proteins Such as Antibody and Hydrolytic Enzyme by Synchrotron Orbital Radiation X-ray	June 24, 1994
Hall, R. (CNRS) One Photon Double Ionization of Atoms and Molecules	June 24, 1994
Larkins, F. (University of Melbourne) Calculation of Normal and Resonant X-ray and Auger Spectra of Molecules	July 13, 1994
Miyahara, T. (Photon Factory, KEK) From Atomic Assembly to Solid	July 29, 1994
Abbate, M. (LNLS, Campinas, Brazil) The O 1s and V 2p X-ray Absorption Spectra of Vanadium Oxides	September 30, 1994
Maruyama, H. (Faculty of Science, Okayama University) Research for Magnetism by Magnetic X-ray Circular Dichroism	September 30, 1994

Users' Meetings

Workshop of BL 4C	December 17-18, 1993
PF Slow-Positron Source Workshop	December 21-22, 1993
The 11th Photon Factory Symposium (Annual Users' Meeting)	January 10-11, 1994
Workshop on the Reconstruction of BL-11 at the Photon Factory	March 14, 1994
Workshop on the Study of Protein Structure by Time-Resolved X-ray Solution Scattering: Present and Perspective	March 23-24, 1994
Workshop on Injector Linac Energy-Upgrade	March 24-25, 1994
User's Meeting of Powder Diffraction Group	July 6, 1994
17th International Linac Conference	August, 21-26, 1994
Workshop of BL NE3	September 17, 1994
Future of Prospect of VIV-SX Region Research	September 27-28, 1994

Publications

PHOTON FACTORY NEWS ISSN 0916-0604

Vol.12, No.1-4

GRADUATE UNIVERSITY FOR ADVANCED STUDIES

The National Graduate University was established in 1988. It has the following three schools:

School of Cultural Studies

School of Mathematical and Physical Sciences

School of Life Sciences.

KEK has participated in the University to form the Department of Synchrotron Radiation Science and the Department of Accelerator Science, both of which belong to the School of Mathematical and Physical Sciences.

Students in the Department of Synchrotron Radiation Science are expected to study the basic theory of emission of synchrotron radiation, its characteristics, and interaction of radiation with matter, and then engage in research by using various facilities at the PF. The research field includes the development of radiation sources, optical elements, and instruments for diffraction, scattering, spectroscopy, and irradiation experiments as well as exploration of new areas of applying synchrotron radiation to science and technology.

PROPOSAL GUIDELINES FOR EXPERIMENTERS AT PHOTON FACTORY

1. HOW TO SUBMIT A PROPOSAL

Photon Factory is open to everybody in scientific research. A proposal should be filed on an application form which is available on request from the Research Cooperation Section of the Administration Department of KEK. An applicant should carefully read the guide before filing an application. A spokesperson should get the agreement of the members to join the team.

An overseas applicant is requested to find an appropriate "contact person in Japan (CPJ)", who will mediate between the applicant and KEK*. Please contact the person in charge of the experimental station you want to use, if you do not know any appropriate CPJ. He/she will select the person appropriate for the applicant's research plan. A list of the people in charge of the experimental stations can be found in this report.

All experimental proposals are subject to approval of the Photon Factory Program Advisory Committee (PF-PAC). In Table 9, we have shown the total number of proposals approved by this PAC. The CPJ will be informed about the decision.

* The contact person in Japan will help you translate Japanese and English, assist with visa applications and your experiments. In order to assure his/her agreement the signature or seal imprint of the CPJ is required.

2. CATEGORY OF PROPOSALS

2.1 for university researchers etc.

There are four categories of application; G(eneral), S(pecial), P(reliminary) and U(rgent). The character, process of approval and terms of validity are different among those categories. Photon Factory is planning to improve the proposal evaluation system, thus the second deadline for categories G and P is not fixed and the limitations for category P is subject to change. Please contact Research Cooperation Section before submission.

G is the category for general experiments using synchrotron radiation. Deadlines of application and valid terms are as follows:

Deadlines: July 14, 1995 (a) and November 2, 1995 (b)

Valid terms:

from October, 1995 to September, 1997 for (a)
from April, 1996 to March, 1998 for (b)

P is the category for preliminary experiments in order to determine the feasibility of proposals for categories G or S. There are some limitations as listed below.

- 1) The maximum beamtime for one project is less than about 120 hours.
- 2) One spokesperson can have only one project at a time.
- 3) More than three proposals of this category cannot be approved for an experimental station at a PF-PAC.

Deadlines: July 14, 1995 (a) and November 2, 1995 (b)

Valid terms:

from October, 1995 to September, 1996 for (a)
from April, 1996 to March, 1997 for (b)

S is the special category for those experiments that may be difficult to do but may have extremely high scientific value. Among those could be experiments for the development of a difficult technique or those requiring special operation of the storage ring. Photon Factory supports the projects of this category financially within certain limits; the funds cannot be used for travel expenses or salary. At least one Japanese scientist should be included in a team. The process of judgement is different from other categories. An applicant has to express his/her plan orally before the PF-PAC. Deadline and valid term are as follows:

Deadline: September 14, 1995 (a) and March 15, 1996 (b)

Valid term:

from April, 1996 to March, 1999 for (a)

from October, 1996 to September, 1999 for (b)

The progress report should be presented at the "Photon Factory Symposium" which takes place every year.

U is the category for urgent proposals which cannot be postponed until the next deadline, and which are of extremely high scientific value. Once approved, these projects may exclude already assigned beamtime for other projects. Applicants can apply at any time but the valid terms are limited as follows:

a project approved between October and March:
until end of March

a project approved between April and September:
until end of September.

Results of a project should be reported at the "Photon Factory Symposium."

2.2 for researchers in private companies etc.

Photon Factory is also open for scientists working in private corporations within certain limits. However, a fee is charged for beamtime.

3. ACCOMMODATION

KEK provides guest houses at low cost for visiting scientists. In the case of domestic experimenters, please contact the person in charge of your experimental station. Overseas experimenters should ask the CPJ to book rooms. KEK supports travel and living expenses for domestic experimenters within certain limits but does not do so for overseas experimenters.

4. OTHERS

- (1) Experimenters must obey the safety rules at KEK and PF.
- (2) Further procedure may be requested in order to carry out an experiment.
- (3) If there are question regarding procedures please contact
Research Cooperation Section, Administration
Department, National Laboratory for High Energy
Physics,
Oho, Tsukuba 305, Japan
FAX: +81-298-64-4602

Table 9 Number of proposals approved by the PAC.

Research Field	1983	1984	1985	1986	1987	1988	1989	1990	1991	1992	1993	1994
(A) EXAFS	42	26	35	40	61	66	57	71	69	67	81	75
(B) Biology	18	18	28	28	32	38	57	61	75	89	92	121
(C) X-Ray	24	29	75	54	73	65	61	80	92	109	111	134
(D) VUV & Soft X-Ray	19	12	27	26	28	28	36	27	45	44	55	52
Total	103	85	165	148	194	197	211	239	281	309	339	382

List of proposals accepted in FY 1994

Proposal Number	Spokesperson	Title
94-G001	J. Akimitsu College of Science and Engineering, Aoyama Gakuin Univ.	Local structure of Cu ion in copper oxide Cu Ge O ₃
94-G002	T. Tanaka Faculty of Engineering, Kyoto Univ.	Structural analysis of molybdenum bronzes by XAFS
94-G003	S. Funahashi School of Science, Nagoya Univ.	Structural studies on the redox reactions of Pd(II, III), Ag(I, II, III), and Sn(II, IV) complexes
94-G004	A. Nishijima National Institute of Materials and Chemical Research	XAFS study on the effect of complexane type ligands on the structure of Mo and W compounds in aqueous solutions
94-G005	N. Mōri Institute for Solid State Physics, Univ. of Tokyo	L _{III} -edge spectroscopy in CeX(X=P, As, Sb, Bi) and Yb ₄ As ₃ under pressure
94-G006	H. Kanai Faculty of Living Science, Kyoto Prefectural Univ.	Microstructural analysis of the effects of alumina supports on the states of molybdenum species
94-G007	M. Matsuura Miyagi National College of Technology	Fluorescence XAFS studies on the structure of Fe clusters in La rich La-Fe alloys
94-G008	Y. Nishiyama Institute for Chemical Reaction Science, Tohoku Univ.	The structure analyses of metal ion in pyrolyzed brown coal
94-G009	H. Sakane Faculty of Engineering, Yamanashi Univ.	XAFS studies on the local structure of the interlayer ion in synthetic fluorine mica ion-exchangers
94-G010	K. Sakaue School of Science, Kwansei Gakuin Univ.	EXAFS study on local structure of K _{1-x} (NH ₄) _x I
94-G011	M. Ichikawa Catalysis Research Center, Hokkaido Univ.	Synthesis and EXAFS studies of monolayer dispersed metal carbonyls in zeolite cages
94-G012	Y. Kubozono Faculty of Science, Okayama Univ.	Structural change of myoglobin Fe site induced by addition of surface active agents
94-G013	S. Emura Institute of Scientific and Industrial, Osaka Univ.	Temperature dependence of Debye-Waller factor of d ¹⁰ type impurities in NaCl structure and GaAs
94-G014	S. Kawasaki Faculty of Science, Hokkaido Univ.	Structural analysis of pressure-induced amorphous GeO ₂

Proposal Number	Spokesperson	Title
94-G015	T. Yamaguchi Faculty of Science, Fukuoka Univ.	In situ XAFS of intermediates in electron transfer reactions of Ru cluster complexes
94-G016	T. Yamaguchi Faculty of Science, Hokkaido Univ.	XAFS studies of Fe(III) and Cr(III) saccharide complexes
94-G017	M. Sakurai Institute for Materials Research, Tohoku Univ.	Role of the small amount of additives on the crystallization of Fe-B-Si amorphous material
94-G019	J. M. Webb School of Mathematical & Physical Sciences, Murdoch Univ.	XAFS measurements on iron-containing organic-inorganic nanocomposite structures
94-G020	C. H. Yo. Department of Chemistry, Yonsei Univ.	Studies of the structural and the electronic configuration of the transition metals existed in perovskite compounds
94-G021	S. K. Park Department of Chem. Engineering, POSTECH	Structural study of copper thin films by EXAFS
94-G022	H. Schneider Institute for Materials Research, DLR	EXAFS measurements on Cr-doped mullite precursors
94G023	Y. Nishihata Faculty of Science, Okayama Univ.	EXAFS study on the Debye-Waller factor in KTaO_3 and SrTiO_3
94-G024	H. Ishida College of Liberal Arts and Science, Okayama Univ.	EXAFS studies on the structural phase transitions in $\text{CH}_3\text{NH}_3\text{MX}_3$ (M=Pb, Sn; X=Cl, Br, I)
94-G025	H. Sato Faculty of Science, Hiroshima Univ.	EXAFS study on diluted magnetic semiconductors $\text{Cd}_{1-x}\text{Mn}_x\text{Te}$
94-G026	H. Nasu Faculty of Engineering, Mie Univ.	Study of the structure of the glasses with large optical nonlinearity
94-G027	S. Yanagida Faculty of Engineering, Osaka Univ.	In-situ investigation on surface structure of quantum-confined cadmium sulfide clusters under photo-induced electron transfer reaction conditions
94-G028	Y. Iwasawa Graduate School of Science, Univ. of Tokyo	In-situ EXAFS studies of the bimetallic ensemble structures and reaction intermediates on Rh-Sn/SiO ₂ and Pt-Sn/SiO ₂
94-G029	Y. Iwasawa Graduate School of Science, Univ. of Tokyo	Polarized total reflection EXAFS analyses for the anisotropic structures of MoO ₃ /TiO ₂ (110) catalysts

Proposal Number	Spokesperson	Title
94-G030	T. Yokoyama Graduate School of Science, Univ. of Tokyo	S K-edge XAFS studies on sulfur dioxide adsorbed on Ni and Cu single crystal surfaces
94-G031	B. Mikami Research Institute for Food Science, Kyoto Univ.	X-ray structural analysis of soybean storage protein
94-G032	A. Suzuki School of Engineering, Nagoya Univ.	Crystal structure analysis of wheat germ protease inhibitor
94-G033	H. Kumagai Faculty of Agriculture Kyoto Univ.	X-ray structure analysis of monoamine oxidase from escherichia coli
94-G034	M. Konno Faculty of Science, Ochanomizu Univ.	Identification of active sites by comparison of crystal structures between cyclophilines present in membrane and cytoplasm
94-G035	S. Iwata Max-Plank Institute für Biophysik	X-ray analysis of the photosynthetic reaction center of rhodospseudomonas viridis
94-G036	Y. Morimoto Faculty of Engineering, Tokushima Univ.	Estimation of processing method for diffraction data from super-macromolecular crystals
94-G037	H. Mizuno National Institute of Agrobiological Resources	X-ray structural analysis of functionally mutated α -amylase
94-G038	K. Miki Faculty of Science, Kyoto Univ.	X-ray crystallographic studies of photolyase (DNA photoreactivating enzyme)
94-G039	K. Miki Faculty of Science, Kyoto Univ.	X-ray crystallographic studies of chaperonin
94-G040	T. Fujii Institute for Chemical Research, Kyoto Univ.	Structural studies on archaeobacterial ferredoxin
94-G041	S. Yoshikawa Faculty of Science, Himeji Institute of Technology	X-ray diffraction experiments for bovine heart cytochrome c oxidase crystals
94-G042	K. Fukuyama Faculty of Science, Osaka Univ.	X-ray crystallographic analysis of α -amylase inhibitor
94-G043	Y. Shirakihara Hygo Univ. of Education	X-ray crystal analysis of $\alpha 3\beta 3$ complex of F1-ATPase from a thermophilic bacterium
94-G044	N. Kato School of Medicine, Nagoya Univ.	Structural analysis of crystals of bacterial lipopolysaccharides (LPS)

Proposal Number	Spokesperson	Title
94-G045	K. Watanabe Kyoto Prefectural Univ.	Structure analysis of proline residues responsible for enhancing protein thermostability
94-G046	Y. Mitsui Faculty of Engineering, Nagaoka Univ. of Technology	X-ray crystallographic analysis of BphC derived from pseudomonas sp. KKS102
94-G047	K. Hamada Faculty of Science, Shimane Univ.	Structural studies of serratiaprotease by an anomalous scattering of Ca
94-G048	R. W. Pickersgill Reading Laboratory Institute of Food Research	Elucidation of the structure of plant cell wall degrading enzymes
94-G049	J. Hajdu Laboratory of Molecular Biophysics, Oxford Univ.	Development of fast monochromatic data collection techniques and studies on high oxidation state metal centers and free radical enzymes
94-G050	I. Andersson Uppsala Biomedical Center, Swedish Univ. of Agric. Sci.	Understanding catalysis in ribulose-1, 5-bisphosphate carboxylase/oxygenase: high resolution diffraction studies on the enzymes from spinach and synechococcus
94-G051	M. W. Parker St Vincent's Institute of Medical Research	Structural studies of glutathione s-transferases
94-G052	B. W. Matthews Institute of Molecular Biology, Univ. of Oregon	Weissenberg data collection of beta-galactosidase from E. coli
94-G053	F. Frolow Faculty of Chemistry, Waizmann Institute of Science	High resolution (1.5Å) study of the structure of bacterioferritin of E. Coli
94-G054	M. Cygler Biotechnology Research Institute, NRCC	High resolution study of lipases and esterases and their complexes with inhibitors
94-G055	G. Lu Department of Biology, Peking Univ.	The collection of diffraction data of bar-headed goose hemoglobin and antibacterial polypeptide LC1
94-G056	D. C. Rees Division of Chemistry, California Institute of Technology	X-ray diffraction studies of succinate quinone oxidoreductase: complex II
94-G057	Z. J. Lin Institute of Biophysics, Academia Sinica	The crystallographic structure of GAPDH complexed with the coenzyme and its analogous
94-G058	D. C. Wang Institute of Biophysics, Academia Sinica	X-ray crystal structure analysis of neurotoxins from Chinese scorpion venome
94-G059	Z. X. Xia Shanghai Institute of Organic Chemistry	X-ray data collection of methanol dehydrogenase at high resolution
94-G060	S. Hasnain Daresbury Laboratory	Weissenberg data collection of azurin and nitrite reductase

Proposal Number	Spokesperson	Title
94-G061	T. Sato Faculty of Engineering, Tokushima Univ.	X-ray structure analysis of prorylendopeptidase
94-G062	H. Shinagawa Research Institute for Microbial Diseases, Osaka Univ.	Structure-function relationships of protein complexes as studied by X-ray crystallography
94-G063	O. Matsumoto Faculty of Bioscience and Biotechnology, Tokyo Institute of Technology	Stereo structural motifs on functional nucleic acid fragments
94-G064	A. Takenaka Faculty of Bioscience and Biotechnology, Tokyo Institute of Technology	Structural analysis on pyrvate dehydrogenase complex
94-G065	A. Takenaka Faculty of Bioscience and Biotechnology, Tokyo Institute of Technology	X-ray analysis of a modelate thermostable enzyme, 3-isopropylmalate dehydrogenase
94-G066	O. Matsumoto Faculty of Bioscience and Biotechnology, Tokyo Institute of Technology	Dynamic reaction mechanisms on nuclease
94-G067	T. Nonaka Faculty of Engineering, Nagaoka Univ. of Technology	Dynamic structure analysis of ribonuclease A and ribonuclease S by time-resolved laue method
94-G068	M. Tanokura Graduate School of Science, Univ. of Tokyo	Study of catalytic mechanism of acid proteinases by time-resolved laue method
94-G069	N. Watanabe Photon Factory, KEK	High resolution crystal structure analysis of ω -amino acid transaminase
94-G070	Y. Hata Institute for Chemical Research, Kyoto Univ.	Structural study on reaction mechanism of dehalogenase by X-ray method
94-G071	M. Hirai Faculty of Engineering, Gunma Univ.	Structure formation and phase transition of polymer systems under electromagnetic field
94-G072	M. Kataoka Faculty of Science, Osaka Univ.	Effects of calcium-binding on solution structures of EF-hand calcium regulatory proteins
94-G073	M. Kataoka Faculty of Science, Osaka Univ.	Solution structures of molten globule and denatured states of globular proteins
94-G074	K. Hara Faculty of Engineering, Kyushu Univ.	Time resolved observation of polymer gel during dehydrating process
94-G075	Y. Muroga School of Engineering, Nagoya Univ.	Investigation of the conformational change of α -tropomyosin by SOR-SAXS

Proposal Number	Spokesperson	Title
94-G076	T. Yamaguchi Faculty of Science, Fukuoka Univ.	Small-angle X-ray scattering from solution of bile salt
94-G077	F. Tokunaga Faculty of Science, Osaka Univ.	Light-induced structural change of aminoacide-substituted bacteriorhodopsin
94-G078	H. Kihara Kansai Medical Univ.	Detection and analysis of protein folding intermediates monitored by stopped-flow X-ray scattering method
94-G079	H. Iwamoto School of Medicine, Teikyo Univ.	Effect of shortening on X-ray equatorial reflections from submaximally activated skeletal muscle fibers
94-G080	Y. Tajima Faculty of Science, Tokyo Metropolitan Univ.	Changes in the X-ray diffraction pattern due to actin-myosin interaction in isometrically contracting muscle
94-G081	S. Matsuoka Sapporo Medical College	Phase sequence during the main transition of phospholipid multilamellar vesicles
94-G082	P. J. Quinn Department of Biochemistry, King's College London	Dynamic phase behaviour of mixed aqueous dispersions of phospholipids and diacylglycerols
94-G083	S. Ueno Faculty of Applied Biological Science, Hiroshima Univ.	Dynamics of polymorphic phenomena in triacylglycerols
94-G084	H. Kihara Kansai Medical Univ.	Analysis of the folding intermediate of cytochrom c using pH jump method
94-G085	Y. Sugishita Institute of Clinical Medicine, Univ. of Tsukuba	Quantitative evaluation of transvenous coronary arteriography using synchrotron radiation: its ability for measuring coronary blood flow
94-G086	K. Kobayashi Photon Factory, KEK	Measurement of absorption spectra of biological molecules in aqueous solution
94-G087	T. Megumi Research Inst. for Advanced Sci. and Tech., Univ. of Osaka Prefecture	Phosphorylation of adenosine with monochromatic X-ray of K-shell absorption edge of phosphorus
94-G088	K. Hieda College of Science, Rikkyo Univ.	Effects of water on the induction of DNA strand breaks by the K-shell ionization of phosphorus
94-G089	N. Usami Photon Factory, KEK	Cell cycle dependence for biological effects by irradiation with monochromatic X-rays on <i>S. cerevisiae</i>
94-G090	N. Usami Photon Factory, KEK	Determination of Cleavage site produced by inner-shell photoabsorption of bromine in bromine-labelled oligonucleotide

Proposal Number	Spokesperson	Title
94-G091	K. Kobayashi Photon Factory, KEK	Measurement of mass attenuation coefficient of air in soft X-ray region
94-G092	S. Iida Faculty of Science, Toyama Univ.	Observation of X-ray speckle
94-G093	M. Yashima Research Laboratory of Engineering, Tokyo Institute of Technology	Lattice parameter and oxygen displacement of tetragonal zirconia solid solutions
94-G094	T. Otake Ocean Research Institute, Univ. of Tokyo	Distribution of trace elements in tissues of anguillid leptocephali
94-G095	S. Honma National Institute for Environmental Studies	Nondestructive SR-XRF imaging of trace elements in tissue or cell of biological samples
94-G096	Y. Ikeda Tokyo Univ. of Fisheries	The effect of environmental chemical pollutants on fish scales
94-G097	M. Okuno Faculty of Science, Kanazawa Univ.	Structural study of high-magnesium carbonate crystals in echinoid teeth
94-G098	H. Toraya Ceramics Research Laboratory Nagoya Institute of Technology	Test of long horizontal parallel slits for synchrotron powder diffraction and its application to structure analysis
94-G099	K. Ishida Faculty of Science and Technology, Science Univ. of Tokyo	Study of electronic state of copper in high-Tc compounds by X-ray powder diffraction near the Cu-K-edge
94-G100	T. Yamanaka College of General Education, Osaka Univ.	Cation distribution and phase transition in the solid solution γ -Fe ₂ SiO ₄ -Fe ₃ O ₄
94-G101	M. Miyamoto Graduate School of Science, Univ. of Tokyo	Determination of crystallographic orientation of small Ca-exsolved phase of olivine in an angrite meteorite
94-G102	M. Ohmase Faculty of Science, Himeji Institute of Technology	Studies on micro-structures in plagioclase crystals
94-G104	Y. Takanishi Faculty of Engineering, Tokyo Institute of Technology	Precise analysis of layer structure in ferroelectric and antiferroelectric smectic liquid crystals
93-G105	T. Shimura Faculty of Engineering, Osaka Univ.	X-ray diffraction study of microcrystallinity in SiO ₂ thin films on the Si surface
94-G106	I. Takahashi School of Engineering, Nagoya Univ.	Study of structure and interface morphology of ferroelectric thin-films by X-ray CTR scattering

Proposal Number	Spokesperson	Title
94-G107	Y. Kondo Faculty of Engineering, Tohoku Univ.	Defect production by Rb-1s and I-1s core excitation in RbCl and KI
94-G108	H. Suematsu Graduate School of Science, Univ. of Tokyo	Phase transitions and structural study of monolayer systems
94-G109	E. Matsubara Faculty of Engineering, Kyoto Univ.	Anomalous X-ray scattering study of plating bath for induced codeposition of Mo-Ni and Co-W amorphous alloys
94-G110	T. Yagi Institute for Solid State Physics, Univ. of Tokyo	In situ X-ray observation of the iron hydride under high temperature and high pressure
94-G111	I. Shirotani Muroran Institute of Technology	Phase transition of NaCl type metal phosphides at high pressures
94-G112	H. Yamaguchi Electrotechnical Laboratory	X-ray diffraction study of CuGeO ₃ under high pressure
94-G113	H. Kawamura Faculty of Science, Himeji Institute of Technology	Pressure-induced structural phase transition in oxygen up to megabar pressure
94-G114	A. Onodera Faculty of Engineering Science, Osaka Univ.	Search for pressure-induced structural phase transitions in aluminum pnictides
94-G115	T. Nakajima Photon Factory, KEK	Study of structural phase transformation by SR X-ray diffraction at milli-kelvin region
94-G116	Y. Ishikawa Faculty of Science, Toyama Univ.	Study of search for the structural change and the stability of CeNiSn as the anisotropic semiconducting dense Kondo lattice
94-G117	K. Tsuji Faculty of Science and Technology, Keio Univ.	Amorphization from the quenched high pressure phase in tetrahedrally-bonded materials
94-G118	M. Sakata School of Engineering, Nagoya Univ.	Successive structural transitions of La _{2-x-y} Nd _y M _x CuO ₄ (M=Ba, Sr)
94-G119	M. Mori Department of Natural Science Informatics, Nagoya Univ.	Icosahedral-icosahedral phase transition of Al-Pd-Mn quasicrystals
94-G120	Y. Kudo Faculty of Science, Tohoku Univ.	Effect of pressure on the crystal structure of phase F
94-G121	M. Shiono Faculty of Science, Kyushu Univ.	Absolute structure determination of CsCuCl ₃ and origin of double helical magnetic structure

Proposal Number	Spokesperson	Title
94-G122	M. Sawada Institute of Scientific and Industrial Research, Osaka Univ.	Crystal structures of permethylated cyclofructanes with metallic cations
94-G123	Y. Soejima Faculty of Science, Kyushu Univ.	Structure determination by differential pattern using anomalous dispersions
94-G124	S. Morimoto Faculty of Engineering Science, Osaka Univ.	Precise structure analysis of perovskite oxide: CaFeO_3 containing Fe^{4+}
94-G125	S. Kutsumizu Faculty of Engineering, Gifu Univ.	Temperature influences on the ionic aggregation in ethylene ionomers
94-G126	T. Hirai Faculty of Textile Science and Technology, Shinshu Univ.	Processes of fixing-and-releasing of strain in shape-memorizing polymer hydrogels
94-G127	E. Matsubara Faculty of Engineering, Kyoto Univ.	Study on the precipitation behavior of nanometer-sized fcc particles in Al-Ni-Re amorphous alloys by anomalous small-angle X-ray scattering
94-G128	A. Kawaguchi Institute for Chemical Research, Kyoto Univ.	Conformational change of ultra-drawn ultra-high molecular weight polyethylene in the process of melting
94-G129	T. Yamaguchi Faculty of Science, Fukuoka Univ.	Small-angle X-ray scattering from aqueous solutions of long chain polyoxyethylene surfactants
94-G130	K. Tashiro Faculty of Science, Osaka Univ.	Synchrotron X-ray study on crystallization kinetics of polyethylene blends
94-G131	Y. Masumoto Institute of Physics, Univ. of Tsukuba	Small angle X-ray scattering of CuBr clusters and microcrystals
94-G132	Y. Amemiya Photon Factory, KEK	Development of X-ray TV detectors for diffraction studies and its application
94-G134	S. Kishimoto Photon Factory, KEK	Time spectroscopy of nuclear excitation with an avalanche photodiode detector
94-G135	M. Suzuki Institute of Physical and Chemical Research	Development of a proportional scintillation X-ray imaging chamber
94-G136	J. G. Thompson Research School of Chemistry, Australian National Univ.	Metal atom ordering in fluorite-related composite modulated $\text{Nb}_2\text{Zr}_{x-2}\text{O}_{2x+1}$ ($x=7.1-10.3$) solid-solution
93-G137	E. N. Maslen Department of Physics, Univ. of Western Australia	Accurate synchrotron radiation $\Delta\rho$ imaging of materials for archetypal significance to chemical behaviour and the physical properties of materials

Proposal Number	Spokesperson	Title
94-G138	K. Ishida Faculty of Science and Technology, Science Univ. of Tokyo	Measurement of dynamical rocking curves of a Ge (GaAs) single crystal near the absorption edge
94-G139	O. Sakata Research Lab. of Engineering Materials, Tokyo Institute of Technology	In-plane structure analysis of As/Si (100) and other surfaces using the grazing-angle X-ray standing wave method
94-G140	H. Hashizume Research Lab. of Engineering Materials, Tokyo Institute of Technology	X-ray structures of dimers and atomic steps on silicon and gallium arsenide (100) surfaces
94-G141	S. Urakawa Faculty of Science, Okayama Univ.	Experimental study on the structure change of molten KCl and KBr under high pressure
94-G142	K. Mizuno Faculty of Science, Shimane Univ.	First stage of formation process of dislocation loops as a vacancy source and sink
94-G143	H. Nakajima Interdisciplinary Graduate School of Engineering Science, Kyushu Univ.	In-situ observation of grain boundary migration in Fe-3%Si alloys
94-G144	K. Hirano Photon Factory, KEK	Development of X-ray polarizing microscopy
94-G145	J. Yoshimura Faculty of Engineering, Yamanashi Univ.	Study of the nonprojectiveness of X-ray Moiré-Fringe patterns
94-G146	A. Iida Photon Factory, KEK	Material characterization using X-ray micro-probe
94-G147	S. Nanao Institute of Industrial Science, Univ. of Tokyo	Study of magnetic structure of rare earth alloys by magnetic bragg scattering
94-G148	H. Fujihisa Institute for Solid State Physics, Univ. of Tokyo	Pressure dependence of electron density distribution on iodine by powder X-ray diffraction
94-G149	T. Yagi Institute for Solid State Physics, Univ. of Tokyo	Study of the equation of state for lower mantle minerals and the effect of non-hydrostaticity
94-G150	M. Imai National Research Institute for Metals	Pressure-induced phase transitions of the alkaline earth-metal disilicides
94-G151	Y. Fukai Chuo Univ.	A novel mechanism of metal-hydride formation
94-G152	K. Kusaba Institute for Materials Research, Tohoku Univ.	Pressure-induced phase transitions of AgCl

Proposal Number	Spokesperson	Title
94-G153	K. Tsuji Faculty of Science and Technology, Keio Univ.	Density of liquid selenium and tellurium under pressure
94-G154	K. Tsuji Faculty of Science and Technology, Keio Univ.	Structure of liquid alkali metals under pressure
94-G155	T. Makita Japan Atomic Energy Research Institute	Stress-induced martensitic transformation in gold and silver based β -phase alloys
94-G156	I. Shirovani Muroran Institute of Technology	Phase transition of ZrRuP and HfRuP at high temperatures and pressures
94-G157	T. Yamasaki Faculty of Engineering, Himeji Institute of Technology	Structural study of decomposition of metal-hydrides during heating at high pressures
94-G158	T. Iwazumi Photon Factory, KEK	Polarization analysis of fluorescent X-rays
94-G159	H. Maruyama Faculty of Science, Okayama Univ.	2p-MCXD studies on Pd in itinerant-ferromagnetic Pd-M alloys (M=Fe, Co and Ni)
94-G160	S. Nanao Institute of Industrial Science, Univ. of Tokyo	Magnetic circular dichroism in RE-TM amorphous thin films
94-G161	J. Chaboy Facultad de Ciencias, CSIC	Magnetic X-ray dichroism study on the rare earth <i>L</i> -edges and Iron <i>K</i> -edge in the case of permanent magnets RE ₂ Fe ₁₄ BH _x
94-G162	G. Oomi Faculty of General Education, Kumamoto Univ.	Development of Compton scattering technique at high pressure
94-G163	C. Uyama National Cardiovascular Center	Development of fluorescent X-ray CT
94-G164	I. Sato Photon Factory, KEK	Vibration and alignment issues on linac beam characteristics
94-G165	H. Kobayashi Photon Factory, KEK	Generation of synchrotron radiation and slow positrons using 2.5 GeV linac
94-G166	Y. Ito Research Center for Nuclear Sci. and Tech., Univ. of Tokyo	Storage of pulsed slow positrons
94-G167	S. H. Be Institute of Physical and Chemical Research	Study of photodesorption using high energy photon beam
94-G168	K. Ueda Research Inst. for Scientific Measurements, Tohoku Univ.	Electronic decay and ionic fragmentation following core excitation of CH _x F _{4-x}

Proposal Number	Spokesperson	Title
94-G169	Y. Tezuka Institute for Solid State Physics, Univ. of Tokyo	Resonant soft X-ray emission and resonant photoemission study on light transition metal compounds
94-G170	M. Yanagihara Research Inst. for Scientific Measurements, Tohoku Univ.	Study of the relaxation of the core-hole excited states by measuring soft-X-ray emission spectra and the polarization
94-G171	T. Nagata Faculty of Science and Technology, Meisei Univ.	Measurement of absolute photoionization cross sections of rare-earth atoms
94-G172	Y. Azuma Photon Factory, KEK	Time-of-flight measurements of lithium multiple photoionization
94-G173	K. Ueda Research Inst. for Scientific Measurements, Tohoku Univ.	Relaxation dynamics of core-excited molecules probed by angle-resolved photoion spectroscopy: BF_3
94-G174	S. Suga Faculty of Engineering Science, Osaka Univ.	High resolution photoemission spectroscopy of TM and L-pnictides
94-G175	K. Tanaka Photon Factory, KEK	Mass spectrometric study on reaction mechanism of photochemical etching
94-G176	H. Namba Faculty of Science, Univ. of Tokyo	Electronic states of single crystal stepped surfaces studied by ARUPS
94-G177	S. Aoki Institute of Applied Physics, Univ. of Tsukuba	3-dimensional imaging by soft X-ray holography
94-G178	Y. Kitajima Photon Factory, KEK	Surface reconstruction of metal single crystals induced by atomic adsorption
94-G179	J. Kawai Faculty of Engineering, Kyoto Univ.	Chemical state analysis of sulfur in coal fly ash
94-G180	A. Misu Faculty of Science, Science Univ. of Tokyo	Magneto-optical study of magnetic interaction in rare earth iron oxides
94-G181	Y. Sakisaka Faculty of Science, Hirosaki Univ.	Nature and adsorbate-induced modification of surface states on Cr(100) and (110)
94-G182	K. Edamoto Faculty of Science, Tokyo Institute of Technology	Angle-resolved photoemission study of the SiC layers formed on a Si surface

Proposal Number	Spokesperson	Title
94-G183	H. Kobayashi Research Center for Photoenergetics of Organic Materials, Osaka Univ.	Observation of surface states in the semiconductor band-gap by means of UPS
94-G184	A. Nishijima National Institute of Materials and Chemical Research	Study on surface structure of silica-alumina catalyst by XPS with variable incident energy
94-G185	K. Furuya Faculty of Science, Science Univ. of Tokyo	Electronic structure analysis of metal nitrides measured by N K-edge spectra
94-G186	K. Edamoto Faculty of Science, Tokyo Institute of Technology	Photoemission spectroscopy study of the Na, K, Cs adsorbed NbC(111) surface
94-G187	Y. Saito Seikei Univ.	Vacuum-ultraviolet-light assisted reaction at surface and interface of silicon-related materials
94-G188	A. Kakizaki Institute for Solid State Physics, Univ. of Tokyo	Electronic states of Ce/Ni and Ce/Pd
94-G189	S. Kono Research Inst. for Scientific Measurements, Tohoku Univ.	ARPES study of the electronic structures of single-domain Si(001) surfaces with adsorbates of Al, Ga and In
94-G191	S. Suga Faculty of Engineering Science, Osaka Univ.	ARUPS study of transition metal atom adsorbed TiS ₂ and M _x TiS ₂
94-G192	H. Daimon Faculty of Engineering Science Osaka Univ.	Angle-resolved photoelectron spectroscopy of the Si(111) 3×1-(Alkali or Ag)
94-G193	S. Imada Faculty of Engineering Science, Osaka Univ.	Spin-resolved photoemission of transition-metal and rare-earth compounds
94-G194	C. Egawa Faculty of General Education, Utsunomiya Univ.	Study of the electronic states of fcc iron films on a Rh(001) surface
94-G195	Y. Hatano Faculty of Science, Tokyo Institute of Technology	Dissociation of superexcited hydrogen molecules studied using pulsed synchrotron radiation under the single bunch operation of PF (II)
94-G196	Y. Hatano Faculty of Science, Tokyo Institute of Technology	Two dimensional measurements of fluorescence from neutral fragments produced by photo-dissociation of superexcited molecules
94-G197	S. Suga Faculty of Engineering Science, Osaka Univ.	Magnetic circular dichroism in soft and hard XAS of ferromagnets
94-G198	H. Daimon Faculty of Engineering Science, Osaka Univ.	Photoelectron holography

Proposal Number	Spokesperson	Title
94-G199	S. Nakai Faculty of Engineering, Utsunomiya Univ.	Soft X-ray resonant Raman scattering and resonant Auger electron spectra
94-G200	A. Yonath Max Planck Research Unit, DESY	Crystallography of ribosomes
94-G201	R. R. Chistyakov Zelenograd Research Institute of Physical Problems	X-ray investigation of magnetic phase diagram of Tb
94-G202	Y. Iwasawa Graduate School of Science, Univ. of Tokyo	Development of embedded catalysts and their reaction mechanisms studied by EXAFS
94-G203	Y. Iwasawa Graduate School of Science, Univ. of Tokyo	Dynamic study of surface structure of ultra-thin catalyst support under reaction conditions
94-G204	Y. Nishiyama Institute for Chemical Research Science, Tohoku Univ.	The structure of metal particles in hectrile which has size-controlled pore
94-G205	Y. Okamoto Faculty of Engineering Science, Osaka Univ.	Structural transformation and deactivation mechanism of catalytically active copper species on supported copper catalysts
94-G206	M. Ichikawa Catalysis Research Center, Hokkaido Univ.	Temperature dependence of EXAFS spectra of the entrapped metal clustes in zeolite supercages
94-G207	M. Nagao Faculty of Science, Okayama Univ.	Specific feature of copper-ion-exchanged zeolites for dinitrogen adsorption
94-G208	T. Miyanaga Faculty of Science, Hirosaki Univ.	Local structure of isolated mixed chalcogen chains confined in the channels of zeolite
94-G209	Y. Kou Lanzhou Institute of Chemical Physics, Chinese Academy of Sciences	XAFS studies on the surface coordinate geometry of fischer tropsch catalysts
94-G210	J. S. Lee Department of Chemical Engineering, POSTECH	XAFS study of organo-Cr or Sn modification of supported Ni catalyst
94-G211	J. C. Park Department of Chemistry, Pusan Women's Univ.	XAFS studies on the intracrystalline structure of metal complexes stabilized in an interlayer space of 2-dimensional host compounds
94-G213	L. Bonneviot Department of Chemistry, Laval Univ.	Coordination of titanium and vanadium in bimetallic vanadium titanium silicalites
94-G214	Y. Abe Faculty of Science and Technology, Science Univ. of Tokyo	Investigation on the structure of polyzirconoxanes in a liquid and a solid state

Proposal Number	Spokesperson	Title
94-G215	M. Kojima Faculty of Science, Okayama Univ.	EXAFS studies on the configurational changes of oxovanadium(IV) complexes
94-G216	M. Sato Faculty of Engineering, Kogakuin Univ.	Structure and formation mechanism of multinuclear Fe(III) complexes
94-G217	K. Ozutsumi Department of Chemistry, Univ. of Tsukuba	Coordination structure around lanthanide(III) ions in nonaqueous solvent mixtures
94-G218	S. Ikeda Ryukoku Univ.	Structural studies on macrocyclic metal complexes in solid state and nonaqueous solvents
94-G219	Y. Yukawa Faculty of Science, Niigata Univ.	XAFS of lanthanoid hexacyanocobaltate(III) hydrates
94-G220	I. Watanabe Faculty of Science, Osaka Univ.	Structure analysis of solution surface by total-reflection total-electron-yield XAFS
94-G221	S. Kashino Faculty of Science, Osakayama Univ.	Temperature dependence of local structure around Rb ⁺ and/or Cs ⁺ ions in Rb ₂ CsC ₆₀
94-G222	H. Maeda Faculty of Science, Okayama Univ.	XAFS study on the Debye-Waller factor in superconductors
94-G223	Y. Kubozono Faculty of Science, Okayama Univ.	EXAFS study on local structure of various Rb doped fullerene superconductors
94-G224	K. Kajiwara Faculty of Engineering and Design, Kyoto Institute of Technology	Local structural change in the vicinity of metal cations on Sol-Gel transition of polysaccharide solutions
94-G225	A. Ishida Institute of Scientific and Industrial Osaka Univ.	EXAFS study on the coordination change of Eu ³⁺ induced by photochemical reduction
94-G226	T. Yokoyama Graduate School of Science, Univ. of Tokyo	Anharmonic interatomic potentials of simple metal complexes determined by EXAFS
94-G227	J. Yamakawa Faculty of Science, Okayama Univ.	Temperature dependence of Debye-Waller factor in Bi ₂ CuO ₄ by EXAFS
94-G228	T. Mukoyama Institute for Chemical Research, Kyoto Univ.	X-ray absorption spectroscopy on the fluorination of benzyl halide by the combination of lead fluoride and sodium salt
94-G229	T. Moriga Faculty of Engineering, Tokushima Univ.	XAFS study on crystallization of calcium carbonate family

Proposal Number	Spokesperson	Title
94-G231	Y. Kawamoto Faculty of Science, Kobe Univ.	Local structures and optical properties of transition metals (Ni ²⁺ , Eu ³⁺ and Er ³⁺) in heavy metal fluoride glasses
94-G232	S. Sugiyama Faculty of Science, Tokushima Univ.	The relationship between the structure of hydroxyapatites and the catalytic activity for methane oxidation
94-G233	D. W. Moon Korea Research Institute of Standards and Science	XAFS analysis of Cu/SiO ₂ and Fe/SiO ₂ thin films by ion implantation method
94-G234	D. W. Moon Korea Research Institute of Standards and Science	Fluorescence XAFS analysis of Ta ₂ O ₅ /Si thin film by beam assisted deposition
94-G235	J. H. Choy Department of Chemistry, Seoul National Univ.	XAFS study on the third-row transition metal ions stabilized in an octahedral crystal-field with various oxidation state
94-G236	J. H. Choy Department of Chemistry, Seoul National Univ.	Application of X-ray absorption spectroscopy to the evolution of geometric and electronic structure of superconductor upon intercalation and electrochemistry
94-G237	S. Shin Institute for Solid State Physics, Univ. of Tokyo	The study of the local structures in the perovskite-type protonic conductors
94-G238	T. Mukoyama Institute for Chemical Research, Kyoto Univ.	Study of [LM] double electron excitation processes in Xe
94-G239	S. Tohno Institute of Atomic Energy, Kyoto Univ.	EXAFS analysis on the local structure of metal-semiconductor nano-composite particles (CdS-Ag, CdTe-Ag)
94-G240	Y. Takeda School of Engineering, Nagoya Univ.	Fluorescence EXAFS study on ordering structure of heteroepitaxially grown InGaAs
94-G241	Y. Takeda School of Engineering, Nagoya Univ.	Fluorescence EXAFS study on local structure of Fe/Cu multiple layer
94-G242	Y. Inoue Institute of Physical and Chemical Research	Fluorescence XAFS study on structure and function of the Mn-duster in intermediate state of photosynthetic oxygen evolution
94-G243	T. Ono Institute of Physical and Chemical Research	Fluorescence XAFS study on structure and function of Ca atom in photosynthetic oxygen evolving system; Sr substitution study
94-G244	Y. Shiro Institute of Physical and Chemical Research	Fluorescence XAFS study on iron environmental structure of novel hemoproteins
94-G245	Y. Nishiyama Institute for Chemical Reaction Science, Tohoku Univ.	The organic sulfur forms in coal and its desulphurization

Proposal Number	Spokesperson	Title
94-G246	S. Hayakawa Faculty of Engineering, Univ. of Tokyo	Surface sensitive XAFS with X-ray excited sample current detection
94-G247	H. Yamazaki Faculty of Science, Okayama Univ.	Magnetic XAFS study of magnetic structures and electronic states on Mn-Gd alloys
94-G248	Y. Kitagawa Institute for Protein Research, Osaka Univ.	Crystallographic study of the enzymatic reaction of <i>achrombactor</i> protease I
94-G249	S. Aibara Research Institute for Food Science, Kyoto Univ.	Evaluation and structure analysis of the protein crystals prepared in space microgravity
94-G250	K. Miki Faculty of Science, Kyoto Univ.	X-ray crystallographic studies of a dioxygenase, metapyrocatechase
94-G251	K. Miki Faculty of Science, Kyoto Univ.	X-ray crystallographic studies of farnesyl diphosphate synthase
94-G252	O. Nureki Institute of Physical and Chemical Research	X-ray crystallography of aminoacyl-tRNA synthetases
94-G253	S. Adachi Institute of Physical and Chemical Research	X-ray diffraction studies of Nitric oxide reductase cytochrome P450nor
94-G254	Y. Sugawara Kitasato Univ.	Crystal structure analysis of aleuria aurantia lectin
94-G255	M. Yamamoto Institute of Physical and Chemical Research	Crystal structure analysis of metalloproteinase, HR-2a and H2-proteinase
94-G256	Y. Shirakihara Hyogo Univ. of Education	X-ray crystal analysis of arginine deiminase
94-G257	N. Tanaka Faculty of Bioscience and Biotechnology, Tokyo Institute of Technology	Structural studies of isopropylmalate dehydrogenase with substrate
94-G258	N. Tanaka Faculty of Bioscience and Biotechnology, Tokyo Institute of Technology	Structural studies of isocitrate dehydrogenase
94-G259	S. W. Suh College of Natural Science, Seoul National Univ.	Structural investigations on the active sites of DNA-polymerase, α -amylase, and RNA N-glycosidase
94-G260	R. J. Read Department of Medical Microbiology and Infections Diseases, Univ. of Alberta	X-ray data collection on pertussis toxin
94-G261	S. J. Lippard Department of Chemistry, Massachusetts Institute of Technology	X-ray crystallographic studies of methane monooxygenase

Proposal Number	Spokesperson	Title
94-G262	A. Mondragon Department of Biochemistry, Northwestern Univ.	Structural studies of type I DNA topoisomerases
94-G263	J. N. Varghese Biomolecular Research Institute	Influenza neuraminidase antibody complexes and inhibitor complexes
94-G264	J. N. Varghese Biomolecular Research Institute	Structural studies of glucanases from barley seeds
94-G265	P. Curmi School of physics, UNSW	Crystal structure of the chaperonins: GroEL & GroES - proteins that fold proteins
94-G266	P. Curmi School of physics, UNSW	Crystal structure of myosin light chains and rubisco
94-G267	J. Martin Center for Drug Design Develop., Univ. of Queensland	X-ray crystallographic studies on complexes formed between HIV-1 protease and non-peptidic inhibitors
94-G268	J. Martin Center for Drug Design Develop., Univ. of Queensland	X-ray crystallographic studies on protein folding factors
94-G269	K. Z. Pan Fujian Inst. of Res. on the Str. of Matter, Chines Academy of Sciences	X-ray crystallography of ribosome inactivating proteins
94-G270	D. Stuart Laboratory of Molecular Biophysics, Univ. of Oxford	Structural studies on proteins of medical importance
94-G271	H. Michel Max-Planck-Institute für Biophysik	X-ray crystallographic analysis of the B800-850 light-harvesting complex from rhodospirillum molischianum
94-G272	L. T. J. Delbaere Department of Biochemistry, Univ. of Saskatchewan	Structure determination of phosphoenolpyruvate carboxykinase from escherichia coli K12
94-G273	M. Guss Department of Biochemistry, Univ. of Sydney	Protein crystallography: the structures of metalloproteins
94-G274	M. Guss Department of Biochemistry, Univ. of Sydney	Protein crystallography: ATPase components and glycosaminoglycan degrading enzymes
94-G275	M. C. Lawrence Biomolecular Research Institute	The structure and enzymatic mechanisms of sialic acid binding proteins: sialic acid aldolase and haemagglutinin neuraminidase
94-G276	K. Nagai Structural Studies Division, MRC Laboratory of Molecular Biology	Crystallographic studies of RNA-protein complexes within pre-mRNA splicing machinery
94-G277	S. Ikemizu Institute of Applied Biochemistry Univ. of Tsukuba	Crystallographic studies on substrate complexes of ω -amino acid: pyruvate aminotransferase

Proposal Number	Spokesperson	Title
94-G278	S. Harada Faculty of Pharmaceutical Sciences, Univ. of Tokyo	Dynamical crystal structure analysis of neutral protease, SCNP
94-G279	S. Adachi Institute of Physical and Chemical Research	Time-resolved Laue crystallographic study of ligand binding dynamics of myoglobin
94-G282	S. Harada Faculty of Pharmaceutical Sciences, Univ. of Tokyo	X-ray structure analysis of taste-modifying protein, curculin
94-G283	T. Kato Faculty of Science, Tokyo Metropolitan Univ.	Structure of giant micelles in aqueous solutions of surfactants
94-G284	S. Sakurai Dept. of Polymer Science and Engineering, Kyoto Institute of Technology	Ordering process of microseparated structures in block copolymers
94-G285	M. Imai Institute for Solid State Physics, Univ. of Tokyo	Ordering process during induction period of crystallization of polymers
94-G286	R. Niki Hokkaido Univ.	Characterization of β -casein micelle in the presence of calcium ion
94-G287	Y. Sano National Food Research Institute	Internal structure of southern Bean mosaic virus
94-G288	K. Fujimoto Faculty of Science and Technology, Keio Univ.	Observation of the initial process of the precipitation polymerization
94-G289	S. Aibara Research Institute for Food Science, Kyoto Univ.	Analysis of molecular mechanisms of wheat protein viscoelasticity
94-G290	Y. Hiragi Institute for Chemical Research, Kyoto Univ.	Structural kinetics of formation and deformation process of chaperonin from a thermophilic bacterium
94-G291	K. Kajiwara Faculty of Engineering and Technology, Kyoto Institute of Technology	Conformation and gelation of alginic acid in aqueous solutions
94-G292	M. Takahashi Faculty of Textile Science and Design, Shinshu Univ.	Polysaccharide-polysaccharide interaction mediated by water in polysaccharide/water system
94-G293	H. Urakawa Faculty of Engineering and Design, Kyoto Institute of Technology	Conformation of highly regularly branched polymer in solutions
94-G294	H. Urakawa Faculty of Engineering and Design, Kyoto Institute of Technology	Architecture dependence of polylactide crystallisation

Proposal Number	Spokesperson	Title
94-G295	M. Tanokura Biotechnology Research Center, Univ. of Tokyo	Analysis of the folding intermediate of aspergillus niger acid proteinase A using pH jump method
94-G296	I. Hatta School of Engineering, Nagoya Univ.	Electron density of phospholipid bilayers studied by a maximum entropy method
94-G297	H. Tsuruta SSRL, Stanford Univ.	Heterotropic allosteric transition of aspartate transcarbamylase studied with time-resolved solution X-ray scattering
94-G298	K. Takakura College of Liberal Arts, International Christian Univ.	Strand breaks in DNA induced by inner shell ionization of metals
94-G299	A. Yokoya Japan Atomic Energy Research Institute	Photoabsorption spectroscopy of biological molecules in the energy region of ultrasoft X-rays
94-G300	H. Maezawa School of Medicine, Tokai Univ.	Transformation of human cells induced by the K-shell photoionization of phosphorus atoms
94-G301	H. Maezawa School of Medicine, Tokai Univ.	Induction of strand breaks on pBR322 DNA following Gd inner-shell photoionization
94-G302	K. Hieda College of Science, Rikkyo Univ.	DNA strand breaks by X-ray absorptions at iodine L-shell in iododeoxyuracil substituted plasmid DNA
94-G303	Y. Itai Institute of Clinical Medicine, Univ. of Tsukuba	Angiography with synchrotron radiation
94-G304	Y. Itai Institute of Clinical Medicine, Univ. of Tsukuba	Monochromatic X-ray computed tomography for biomedical research
94-G305	T. Saito Jichi Medical School	X-ray contact microscopy of enzyme cytochemistry by X-ray zooming tube
94-G306	N. Nishizawa Univ. of Tokyo	Analysis of the microelemental states in plants
94-G307	M. Wakatsuki Institute of Materials Science, Univ. of Tsukuba	X-ray fluorescence analysis of the growth medium originated impurities in diamond single crystals
94-G308	A. Iida Photon Factory, KEK	Characterization of local layer structure of liquid crystals using X-ray microprobe
94-G309	M. Tanaka Photon Factory, KEK	Powder X-ray diffraction studies on structure and phase transition of perovskite type $REAlO_3$
94-G310	H. Maeda Japan Atomic Energy Research Institute	Diffuse scattering studies on secondary defects of quenched fcc metals

Proposal Number	Spokesperson	Title
94-G312	M. Takata School of Engineering, Nagoya Univ.	Studies on structure and quantum size effects of nanocrystals in glass
94-G313	Y. Ono Graduate School of Science, Univ. of Tokyo	Intersite ion distribution of synthetic zirconolite
94-G314	T. Yamanaka Faculty of Science, Osaka Univ.	Mechanism of pressure-induced amorphization of $\text{Ca}(\text{OH})_2$ and $\text{Mg}(\text{OH})_2$
94-G315	H. Horiuchi Faculty of Science, Univ. of Tokyo	Studies on the structure and phase transition of REAlO_3 (RE: rare-earth elements)
94-G317	M. Saito Institute for Advanced Materials Processing, Tohoku Univ.	Anomalous X-ray scattering study of cuprous halide-based superionic conducting glasses
94-G318	E. Matsubara Kyoto Univ.	Structural analyses of nanometer-sized precipitates in Al-based amorphous alloys by the DAFS method
94-G319	H. Yamaoka Faculty of Engineering, Kyoto Univ.	Characterization of thin polymer films by X-ray reflectometry
94-G320	H. Hashizume Research Lab. of Engineering Materials, Tokyo Institute of Technology	Microstructures of polished silicon surfaces by measurements of non-specular grazing-angle X-ray reflections
94-G321	E. Matsubara Kyoto Univ.	Structural analyses of amorphous oxide films by the grazing incident X-ray scattering (GIXS) method
94-G322	K. Uosaki Faculty of Science, Hokkaido Univ.	Structural study of semiconductor single crystal electrode/electrolyte solution interfaces by surface X-ray scattering at atomic level
94-G323	M. K. Sanyal Saha Institute of Nuclear Physics	Grazing incidence synchrotron X-ray scattering study of multilayer interfaces
94-G324	A. Koma Graduate School of Science, Univ. of Tokyo	Analysis of structure and growth mechanism of van der waals epitaxial films
94-G325	M. Harju Photon Factory, KEK	Time resolved microcrystal laue investigation of the unknown structure of ammonium nitrate phase II*
94-G326	A. Yoshiasa Faculty of Science, Osaka Univ.	Crystal structure refinement of $\text{Sr}_4\text{Fe}_6\text{O}_{13}$
94-G327	N. Sasaki Faculty of Education, Kagawa Univ.	Crystal structure analysis of aluminum borate whisker

Proposal Number	Spokesperson	Title
94-G328	K. Tanaka Nagoya Institute of Technology	X-ray structure analysis of room temperature fluorescent-phosphorescent organic crystals with very small sizes
94-G330	Y. Takeda School of Engineering, Nagoya Univ.	Atomic level structure determination of InP/InGaAsP/InP double heterostructures by X-ray CTR scattering
94-G331	Y. Takeda School of Engineering, Nagoya Univ.	Atomic level structure determination of AlGaP/InAs heterostructures by X-ray CTR scattering
94-G332	T. Takahashi Institute for Solid State Physics, Univ. of Tokyo	Structure analysis of interfaces of epitaxially grown Si/Ge system by X-ray scattering
94-G333	H. Ohno Japan Atomic Energy Research Institute	EXAFS of amorphous uranium compounds
94-G334	K. Nagata Faculty of Science, Fukuoka Univ.	Pressure dependences of inter- and intramolecular bond distances in selenium
94-G335	T. Nanba Faculty of Science, Kobe Univ.	Pressure induced structural phase transition in CdS and CuCl microcrystals
94-G336	N. Hamaya Faculty of Science, Ochanomizu Univ.	Precise determination of crystal structure of rare earth metals under pressure
94-G337	K. Kawamura Faculty of Science, Tokyo Institute of Technology	X-ray structure analysis for Na ₂ O-SiO ₂ -H ₂ O melts under high temperature and pressure
94-G338	E. Otani Faculty of Science, Tohoku Univ.	Determination of the phase boundaries and equation of state of the mantle minerals by the multianvil apparatus
94-G339	T. Irifune Faculty of Science, Ehime Univ.	Experimental study on the high pressure phase transformations in serpentine
94-G340	K. Kawamoto Faculty of Science, Tokyo Institute of Technology	Excess volume of mineral solid solutions under pressure and temperature
94-G341	T. Kato Faculty of Science, Tohoku Univ.	High pressure phase transition mechanism and its reaction kinetics
94-G342	K. Kusaba Institute for Materials Research, Tohoku Univ.	High pressure phase transitions of V ₂ O ₅
94-G343	A. P. Jones Department of Geological Sciences, Univ. College London	Density measurement of high pressure carbonate melts

Proposal Number	Spokesperson	Title
94-G344	H. Hirayama Radiation & Safety Control Center, KEK	Development of dosimetry technics for angiography
94-G345	M. Kitamura Faculty of Science, Kyoto Univ.	Analysis of the crystal with optical anomaly by X-ray topography using synchrotron radiation
94-G346	G. T. Barnes Department of Chemistry, Univ. of Queensland	Molecular organization and structural defects in condensed langmuir layers
94-G347	H. Hashizume Research Lab. of Engineering Materials, Tokyo Institute of Technology	High resolution mapping of strain distribution in multilayer structures
94-G348	T. Suzuki Institute of Industrial Science, Univ. of Tokyo	Study on structural defects in solid helium using SR-X ray topography
94-G349	M. Ando Photon Factory, KEK	Characterization of a hematite single crystal using its charge and magnetic bragg scattering
94-G350	M. Ando Photon Factory, KEK	Measurement of angular divergence of synchrotron radiation
94-G351	N. Shiotani Tokyo Univ. of Fisheries	Compton scattering studies of complex and disordered systems
94-G352	F. Itoh Faculty of Engineering, Gunma Univ.	Magnetic dichroism and magnetic compton profile of actinide compounds
94-G353	F. Itoh Faculty of Engineering, Gunma Univ.	Measurements of 3d-electron momentum densities by X-eX coincidence method
94-G354	H. Sakurai Faculty of Engineering, Gunma Univ.	Magnetic properties of multilayers
94-G355	H. Maruyama Faculty of Science, Okayama Univ.	X-ray magnetic scattering in antiferromagnetic Mn-fluorides
94-G356	Y. Tanaka Institute of Physical and Chemical Research	Magnetic compton scattering experiments using high energy X-rays (>130 keV)
94-G357	N. Kosugi Institute for Molecular Science	Angular distribution of the fragments ions after the inner-shell excitation of sulfur containing molecules
94-G358	S. Nakai Faculty of Engineering, Utsunomiya Univ.	Resonant auger spectra of Y-compounds in Y-L _{III} absorption edge

Proposal Number	Spokesperson	Title
94-G359	A. Yagishita Photon Factory, KEK	2p resonance auger electron spectroscopy of 3d transition metal atoms
94-G360	T. Sekiguchi Japan Atomic Energy Research Institute	Study of ion-desorption from formamide adsorption system by resonant core excitation
94-G361	A. Fujimori Graduate School of Science, Univ. of Tokyo	XAS and resonant XPS of perovskite-type transition-metal oxides
94-G362	T. Koizumi College of Science, Rikkyo Univ.	Photoionization of singly- and doubly-charged rare gas ions
94-G363	T. Yokoyama Graduate School of Science, Univ. of Tokyo	O K-edge NEXAFS and UPS on SO ₂ adsorbed on single crystal Ni surfaces
94-G364	K. Nakagawa Faculty of Education, Kobe Univ.	Fundamental processes of radiation damage in aromatic molecular crystals
94-G365	J. Kawai Faculty of Engineering, Kyoto Univ.	Escape depth of photoelectrons
94-G366	N. Miyamoto Research Inst. of Electrical Communication, Tohoku Univ.	Growth and reaction mechanisms of photo-assisted CVD investigated with SR photoelectron spectroscopy
94-G367	K. Yoshino Harvard Smithsonian Center for Astrophysics	Determination of spectroscopic properties of atmospheric molecules using the combination of VUV fourier transform spectrometer and synchrotron radiation
94-G368	Y. Nihei Institute of Industrial Science, Univ. of Tokyo	Chemical state resolved structural analysis by energy scanned X-ray photoelectron diffraction
94-G370	M. Niwano Research Inst. of Electrical Communication, Tohoku Univ.	Initial stages of oxidation of hydrogen-terminated Si surfaces
94-G371	S. Shin Institute for Solid State Physics, Univ. of Tokyo	High-resolution photoemission study of metal-insulator transition of V ₂ O ₃
94-G372	C. Y. Park Department of Physics, Sung-Kyun-Kwan Univ.	Angle resolved photo electron spectroscopy for Li-adsorbed Si(111) surface
94-G373	S. J. Oh Department of Physics, Seoul National Univ.	Study of magnetism of Fe and Mn overlayers on the Ag(001) surface by spin-resolved photoemission spectroscopy
94-G374	Y. Morioka Institute of Physics, Univ. of Tsukuba	Threshold electron spectroscopy of rare gas clusters

Proposal Number	Spokesperson	Title
94-G375	N. Kouchi Faculty of Science, Tokyo Institute of Technology	Absolute photoabsorption, photoionization, neutral-dissociation cross sections of some cyclic hydrocarbons and halocarbons in the VUV range
94-G376	T. Miyahara Photon Factory, KEK	Comparison between MCD signals due to different core excitations and critical examination of the sum rule
94-G380	T. Sano Faculty of Science, Hiroshima Univ.	Kinetic studies on the molecular recognition of calmodulin by the stopped-flow X-ray scattering method
94-G381	H. Tagawa Nihon Univ.	Dynamical SR-SAXS investigations on micro-phase segregated structures of multiblock polymers
94-G382	N. Sakai Faculty of Science, Himeji Institute of Technology	Measurements of magnetic compton profiles using a rapid superconducting magnet
94-G384	A. Koizumi Faculty of Science, Himeji Institute of Technology	X-ray magnetic scattering and absorption measurements under pulsed high magnetic field
94-G385	Y. Suda Faculty of Technology, Tokyo Univ. of Agriculture and Technology	High-resolution photoemission study of porous Si
94-P001	J. Deng Department of Chemistry, Fudan Univ.	Research on structures of Ni-P amorphous catalysts
94-P005	Y. Ono Graduate School of Science, Univ. of Tokyo	Differential patterson synthesis by imaging plate method
94-P006	H. Okabayashi Nagoya Institute of Technology	Structural study of aggregates formed by the insect laccifer lacca products
94-P008	H. Tsubakino Himeji Institute of Technology	Effects of addition of third elements on precipitation of δ' phase in Al-Li ternary alloys
94-P009	K. Ishibashi Faculty of Engineering, Kyushu Univ.	Test of superconducting tunnel junctions for X-ray detection
94-P010	K. Nagata Faculty of Science, Fukuoka Univ.	Pressure dependences of inter- and intramolecular bond distances in selenium
94-P011	M. Hasegawa Institute for Materials Research, Tohoku Univ.	Slow positron-beam study of irradiation-induced defects
94-P012	Y. Murata Institute for Solid State Physics, Univ. of Tokyo	Positron stimulated desorption from hydrogen adsorbed surface

Proposal Number	Spokesperson	Title
93-P013	Y. Kitajima Photon Factory, KEK	Monochromatization test of soft X-rays (800-1400 eV) by beryl crystal
94-P014	S. Hosokawa Faculty of Science, Hiroshima Univ.	Structural studies of amorphous GeSe and GeTe by anomalous X-ray scattering
93-P015	K. Isobe Institute for Molecular Science	Structural study of mixed metal sulfide clusters
94-P016	T. Hamanaka Faculty of Engineering Science, Osaka Univ.	Structural study of biological substances by circularly polarized X-ray scattering
94-P017	M. Ohkawa Faculty of Science, Hiroshima Univ.	Crystal structures of Fe-rich pumpellyites in low grade metamorphic rocks
94-P019	O. Haruyama Faculty of Science and Technology, Science Univ. of Tokyo	Study on the thermal-induced short range order in amorphous Pd-Ni-Si alloys by anomalous X-ray scattering
94-P020	N. Sakai Faculty of Science, Himeji Institute of Technology	Does crystalline alignment affect the compton scattering intensity?
94-Y001	M. Miyao Central Research Laboratory, Hitachi Ltd.	BL-8A; Soft X-ray diffractometry, X-ray absorption spectroscopy, soft X-ray microprobe. B; EXAFS experiments, total reflection measurement. C; Lithography, microprobe experiments, micro X-ray diffractometry
94-Y002	M. Ohtsuki Fujitsu Laboratories Ltd.	Exposure tests by synchrotron radiation in BL-17A, BL-17B, and BL-17C
94-Y003	K. Iinuma NEC Corp.	Soft X-ray lithography, photo-chemical reaction experiments and X-ray optics
94-Y004	S. Sasaki Japan Tabako Inc.	X-ray crystallographic studies on leukotriene producing enzymes
94-Y005	K. Kubodera Interdisciplinary Research Laboratory NTT	Materials analysis using synchrotron radiation
94-Y006	T. Hata Analytical and Metabolic Research Lab., Sankyo Corp.	Crystallographic studies of cytochrome P-450 _{sca} from streptomyces carbophilus
94-Y007	H. Ikenaga Central Laboratory for Key Technology, Kirin Brewery Co., Ltd.	Data collection from crystals of glycosylation-inhibiting factor at high resolution
94-Y008	K. Tanaka Central Research Institute, Mitsui Toatsu Chemicals, Inc.	Characterization of Cu-Al catalysts' precursor by XAFS
94-Y009	T. Onoda Mitsubishi Kasei Corp.	The structural analysis of Co, Ni, Ge catalysts by XAFS

Proposal Number	Spokesperson	Title
94-Y010	K. Suzuki Central Research Laboratory, Hitachi Ltd.	BL-8A; Soft X-ray diffractometry, X-ray absorption spectroscopy, soft X-ray microprobe. B; EXAFS experiments, total reflection measurement. C; Lithography, microprobe experiments, micro X-ray diffractometry
94-Y011	K. Iinuma NEC Corp.	Soft X-ray lithography, photo-chemical reaction experiments and X-ray optics
94-Y012	S. Sato Fujitsu Laboratories Ltd.	Exposure tests by synchrotron radiation in BL-17A, BL-17B, and BL-17C
94-Y013	K. Tanaka Central Research Institute, Mitsui Toatsu Chemicals, Inc.	XAFS analysis of Su catalysts for polyester synthesis
94-C001	Y. Ohishi Tsukuba Research Laboratory, Sumitomo Chemical Co., Ltd.	Small angle X-ray scattering study for dynamical structural change of polymers
94-C002	H. Akimoto Fundamental Research Lab., NEC Corp.	Characterization of semiconductor materials by high precision X-ray goniometer system
94-C003	T. Ishiguro New Nippon Steel Corp.	Dynamical observation of material processing using synchrotron radiation
94-C004	H. Yoshida Nikon Corp.	Measurements of X-ray multi-layer mirror by synchrotron radiation
94-C006	S. Kojima Research Center, Sony Corp.	Characterization of crystal defects and surface states of semiconductor crystals
94-C007	Y. Oku Kawasaki Heavy Industries, Ltd.	Development of synchrotron radiation beamline for medical applications
94-C008	S. Abeya ULSI Research Center, Toshiba Corp.	Micro structure analysis by synchrotron radiation
94-C009	M. Matsui Power Reactor and Nuclear, Fuel Development Corp.	Research and development of an intense CW electron linear accelerator system
94-C010	M. Hara Toray Research Center	Developments of electron yield detection in XAFS measurement
94-C013	K. Kondo Petroleum Energy Center	EXAFS study for petroleum purification and hydrodesulfurization catalysts
94-C016	H. Onda Mechanical Research Lab., Hitachi Ltd.	Research for shielding materials against high intensity radiations and high electric fields
94-C017	H. Ayato Fuji Photo Film Co., Ltd.	Local structure analysis of photographic silver halides
94-C022	A. Yamagisawa New Technology Corp.	Soft X-ray absorption cross-section of atoms and molecules under ultra-violet light irradiation

Proposal Number	Spokesperson	Title
94-C026	J. Suzaki Denki Kagaku Kogyo Co., Ltd.	Phase transition of highly oriented BN under high temperature and high pressure
94-C031	S. Terakado Tsukuba Research Center, Sanyo Electric Cop., Ltd.	Superfine design technology by synchrotron radiation
94-C032	T. Kiyokura Interdisciplinary Research Laboratory, NTT Corp. Ltd.	Research for nano-region electronic properties by synchrotron radiation
94-C033	E. Hamada Nippon Steel Corp.	Development of physical analysis technology using synchrotron radiation

G : General

P : Preliminary

Y : Approved for charged beam time.

C : Collaborations between the Photon Factory and institutes of private companies.

Introduction

INTRODUCTION

The Photon Factory has been running quite smoothly during the period covered by this Activity Report (October 1993 - September 1994). The Photon Factory operates two light sources; the 2.5-GeV Photon Factory storage ring and the 6.5-GeV TRISTAN Accumulation Ring. Both rings are supplied positrons or electrons by the 2.5-GeV linear accelerator.

The 2.5-GeV Photon Factory storage ring is our major facility, and more than 60 experimental stations are working routinely for synchrotron radiation research. It is proud of high stored current and long lifetime. In the routine operation, the start current is 370 mA, and after twenty-four hours the stored current is maintained at 300 mA. Scientists therefore can use the photon beam almost the whole day with no interruption. Also, beam availability has been very satisfactory; the failure rate was in the range of 1 to 1.5 percent during these three years.

The TRISTAN Accumulation Ring is fundamentally the injector of the TRISTAN high-energy electron-positron collider, and has been parasitically used as a light source. Although the current is below 40 mA and the lifetime is as short as three hours, the Accumulation Ring is characteristic of high energy and single bunch. With two insertion devices it has become a unique light source for synchrotron radiation research in this country.

The total operation time of the 2.5-GeV Photon Factory storage ring was 4908 hours in the FY1993. Among them the scheduled user time was 3747 hours. The single-bunch mode operation was performed for 312 hours, and a very limited time was devoted to the 3-GeV operation.

For the past few years we have actively pursued the upgrading of performance of the light sources as well as the beamlines and experimental stations.

Light Source Department has proposed the emittance-upgrade program at the 2.5-GeV Photon Factory storage ring, and has continued an R&D on hardware for a few years. The program includes modification of the lattice of the storage ring in order to reduce the ring emittance by a factor of 5 and to achieve 27 nm-rad. This improvement should keep the Photon Factory competitive to world-wide major light sources in the forthcoming years. The construction of magnets and power supplies required for this improvement started in FY1994. The conversion of the ring to the

new lattice will be scheduled during a long shutdown expected from January to September of 1997.

More than twelve years have already passed since the first photon beam was seen at the Photon Factory in 1982. Continuous upgrading of the beamlines and experimental stations are always necessary in order to perform top-grade, challenging research. Instrumentation Division thus has conceived of reconstruction or scrap-and-build of old beamlines and experimental stations in order to meet new scientific requirements for these years.

The experimental station that reached the final installation and commissioning phase during the period covered by this Activity Report is BL-12C, which is a new XAFS station. This station is designed to cover an energy range of 7 to 23 keV, and accept and focus photons radiated within a horizontal angular spread of 2 mrad.

The station BL-4C is planned to be reconstructed as a station for X-ray magnetic Bragg scattering. On this occasion the station BL-4B, which has been used alternately for powder diffraction and for X-ray camera for micro-sized crystals, will be separated into two hutches, so that each experimental apparatus does not need to move any more.

A new station for powder diffraction at non-ambient conditions such as high pressure and/or low temperature will be implemented at BL-18C, since BL-4C which was previously used for this purpose will be reconstructed to different purpose. Design study on BL-18C is in progress.

The construction of BL-16 has also been progressing. BL-16 is a beamline that follows a 53-pole multi-pole wiggler. It is divided in two branch lines; BL-16A is a general purpose line that provides with both white and monochromatic X-rays with energies of 5-25 keV, and BL-16U is a high-resolution, high-throughput soft X-ray line. BL-16U is completely redesigned. It has adopted a 24-m spherical grating monochromator, and it is expected to cover the photon energy range of 40 to 600 eV, and to get an photon flux of more than 10^{10} photons/sec with a resolution of 10,000.

Along with the above-mentioned activities directly concerned with synchrotron radiation activities at the existing light sources, four different projects are running at the Photon Factory.

TRISTAN Super Light Facility Project The Photon Factory has pursued for a long time a possibility of using the TRISTAN Main Ring as a brilliant light source. Calculations have shown that an emittance as low as 5 nm-rad can be obtained at the TRISTAN Main Ring, when it operates at an energy as low as 10 GeV. In cooperation with a long undulator, one can expect to realize an unprecedentedly-bright coherent x-ray source at the TRISTAN Main Ring. Two years ago, however, was authorized a plan to build in the Main Ring tunnel, a new B-factory, an asymmetric high-energy positron-electron collider. In consequence, the original idea of the TRISTAN Super Light Facility at the Main Ring has been canceled.

However, a bright x-ray beam from the low-emittance beam of the TRISTAN Main Ring is quite attractive for some sort of synchrotron radiation experiments. Hence, a decision was made to operate the TRISTAN Main Ring dedicatedly for synchrotron radiation experiments for three months in the fall of 1995. Design of the beam optics of the Main Ring for a reduced-energy operation was completed, and required modifications on ring components when operating as a light source have been carefully checked. Since a 5.4-m long undulator will be installed in a straight section, the lattice will be modified slightly. Damping wigglers will be installed in order to enhance emittance reduction as well as to stabilize coherent instabilities of the stored electron beam. The undulator has a unique feature in construction method. Since a very long undulator was supposed to be used in the original TSLF plan, our group scientists have conceived of building it with a number of smaller units. The construction and assembly of undulator units have progressed in success.

VUV-FEL Project Development of a short-wavelength free electron laser in a vacuum ultra-violet region has continued since 1992 at the 2.5-GeV Photon Factory storage ring. It aims at demonstrating oscillation at a wavelength of 177 nm. The ring is operated at an energy of 750 MeV in the FEL experiment. Spontaneous radiation from a transverse optical klystron located at the straight section BL-2 has been already observed in 1992.

Adjustment of a laser system and a beamline for transporting the laser beam are now in progress.

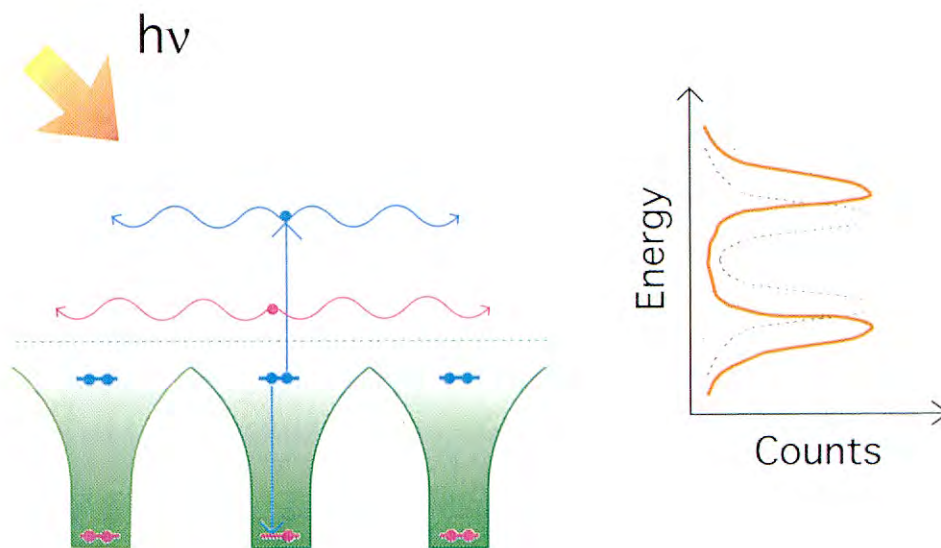
Linac Upgrade for the KEKB Project The recent biggest project for which the Photon Factory is responsible is the project of upgrading the energy of the Injector Linac for the B-factory. The B-factory, which is the KEK's biggest future project, is a new high-energy electron-positron collider of asymmetric energies of 3.5 GeV and 8 GeV. Hence, the Injector

Linac (presently 2.5 GeV) will be upgraded in order to supply the beams at the required energies. The energy of the linear accelerator is reinforced by increasing the output power of microwave klystrons and also doubling the peak microwave power with a pulse compression system as well as by increasing the number of accelerator guides. Research and development on a 50-MW klystron and the pulse compression system have been in progress quite satisfactorily.

Slow-positron source The high-power electron beam of the linear accelerator is attractive to produce very slow positrons. They are useful for materials research. A group in Injector Linac Division has developed a slow-positron source for a few years. Slow positrons generated at a target bombarded by the 2.5-GeV electron beam is transported through a 30-m transport line to an experimental area in the klystron gallery. In a preliminary test operation done in 1994 a positron beam intensity of 3×10^6 positrons/s was obtained with a 2.2-GeV electron beam of 1.25-kW average power.

Collaborative research in the field of synchrotron radiation has continued as the previous year between the Photon Factory and other institutions. As for the academic sector, Research Center for Spectrochemistry of University of Tokyo has operated their own experimental stations BL-7A and BL-7B for many years, and has conducted primarily surface science. Synchrotron Radiation Laboratory of Institute for Solid State Physics of University of Tokyo has also operated three experimental stations, BL-18A, BL-19A and BL-19B, and opened them to general users. Research on the advanced material characterization has been conducted at BL-13 as collaborative projects between the Photon Factory and national institutes in Tsukuba. Four industrial companies, NTT, Hitachi, NEC and Fujitsu have been operating their own beamlines. The Australian National Beamline Project entered the final year of its three-year construction phase, and work continued in the areas of beamline component installation and testing, experimental instrumentation commissioning and the development of software for data collection, reduction and analysis, with the goal of opening the beamline to the general user community by 1995.

Scientific Disciplines



Uneven energy sharing between a photo-electron and an Auger-electron

You can jump to the article by clicking its title.

CONTENTS

	Page
A. INTRODUCTION	S - 1
B. THEORETICAL RESEARCHES	S - 1
1. THEORY FOR ENERGY REDISTRIBUTION BETWEEN A PHOTOELECTRON AND AN AUGER ELECTRON	S - 1
2. THEORY FOR EXCITON EFFECTS ON LIGHT ABSORPTION SPECTRA OF F.C.C. TYPE C_{60} CRYSTAL	S - 3
3. T_{1u} HUBBARD MODEL FOR FERROMAGNETIC AND OPTICAL PROPERTIES OF POTASSIUM DOPED ZEOLITE	S - 5
C. ATOMIC AND MOLECULAR SCIENCE	S - 6
1. ATOMIC SPECTROSCOPY	S - 6
2. MOLECULAR SPECTROSCOPY	S - 7
2.1 Valence Electronic Excitation	S - 7
2.2 Core Electronic Excitation	S - 8
D. VUV AND SOFT X-RAY SPECTROSCOPY OF SOLIDS	S - 11
1. BASIC TECHNIQUE OF THE RESEARCHES	S - 11
2. SPECIAL FEATURES OF SYNCHROTRON RADIATION	S - 11
2.1 Utilization of polarized synchrotron radiation	S - 11
2.2 Utilization of the pulsed structure of synchrotron radiation	S - 12
3. PHYSICS OF SOLID STATE SPECTROSCOPY	S - 12
3.1 Single electron states in solids: Band structure	S - 12
3.2 Local electronic states without translational symmetry	S - 13
3.3 Electron correlation	S - 14
4. EXAMPLE OF THE STUDY IN FY 1994	S - 14
4.1 Photoemission spectroscopy	S - 14
4.2 Absorption spectroscopy and magnetic circular dichroism	S - 15
4.3 Soft x-ray emission and Auger electron spectroscopy	S - 16

E. X-RAY SCATTERING SPECTROSCOPY OF MAGNETIC MATERIALS	S - 17
1. X-RAY MAGNETIC SCATTERING STUDIES ON UTe	S - 17
2. MAGNETIC CIRCULAR X-RAY DICHOISM MEASUREMENT AT Pd L _{3,2} -EDGES IN Fe-Pd ALLOYS	S - 19
F. STRUCTURAL PROPERTIES OF CONDENSED MATTERS	S - 20
1. X-RAY MAGNETIC BRAGG SCATTERING TOPOGRAPHY FROM Fe ₃ O ₄	S - 20
2. MICRO-AREA DIFFRACTION SYSTEM USING POLYCHROMATIC SR	S - 21
3. Fe ²⁺ AND Fe ³⁺ IONS DISTRIBUTION IN MAGNETITE, DISTINGUISHABLE BY X-RAY ANOMALOUS SCATTERING	S - 22
4. CRYSTAL STRUCTURE OF ENDOHEDRAL METALLO-FULLERENE LA@C ₈₂	S - 23
5. SOLUTION X-RAY SCATTERING STUDY FOR THE STRUCTURE AND FUNCTION OF CALMODULIN-PEPTIDE COMPLEXES	S - 23
6. POST FCC STRUCTURE OF SOME LANTANIDES UNDER PRESSURE	S - 24
G. PROPERTIES OF SOLID SURFACES AND ADSORBATES	S - 26
1. XAFS STUDIES FOR ADSORBATE STRUCTURES AND BONDINGS	S - 26
2. ABSOLUTE X-RAY REFLECTIVITY MEASUREMENT FROM THE Si(111) $\sqrt{3}\times\sqrt{3}$ -Bi SURFACES	S - 27
3. SITE SPECIFIC FRAGMENTATION OF POLYMER THIN FILMS	S - 28
H. STRUCTURES AND FUNCTIONS OF PROTEINS	S - 29
1. FUNGAL PEROXIDASE	S - 29
2. HYDOXYLASE	S - 29
3. L-LACTATE DEHYDROGENASE	S - 29
4. INTERFERON- β (IFN- β)	S - 30
5. LYASE AND HYDROLASES	S - 30
6. β -GALACTOSIDASE	S - 31
7. PERTUSSIS TOXIN-SUGAR COMPLEX	S - 31
8. A VIRAL PROTEASE	S - 32
9. STRUCTURE ANALYSES OF CRYSTALS WITH VERY LARGE ASYMMETRIC UNIT	S - 32

I. RADIOBIOLOGY USING SYNCHROTRON RADIATION	S - 33
1. INTRODUCTION	S - 33
1.1 Radiobiological processes	S - 33
1.2 Usefulness of synchrotron radiation in radiobiology research, especially in the study of the initial processes	S - 33
1.3 Inner-shell photoabsorption and the Auger effect	S - 34
2. SOME OF THE RESULTS OBTAINED RECENTLY	S - 34
2.1 Amount of energy to produce double strand breaks in DNA	S - 34
2.2 Photon energy dependence of radical yield in water	S - 35
J. X-RAY MICROBEAMS AND X-RAY MICROSCOPY	S - 38
1. HARD X-RAY MICROBEAMS	S - 38
1.1 Brief summary	S - 38
1.2 Characterization of liquid crystals by X-ray μ -diffraction	S - 39
1.3 X-ray fluorescence analysis using X-ray microbeam	S - 40
2. SOFT X-RAY MICROSCOPY	S - 41
2.1 A scanning soft X-ray photoelectron microscope using circularly polarized radiation	S - 41
2.2 Zone plate soft X-ray microscope	S - 43

A. INTRODUCTION

In this section, we review scientific activities of the Photon Factory, over nine fields including theoretical studies.

B. THEORETICAL RESEARCHES

The theoretical group of Photon Factory is new. In fact, it has started in November, 1993. Now it consists of one professor, one research associate and two graduate students. In the following, we present a brief introduction to our researches which were performed in its first year.

1. THEORY FOR ENERGY REDISTRIBUTION BETWEEN A PHOTOELECTRON AND AN AUGER ELECTRON

As the first topic, we discuss the dynamics of two electrons propagating in a solid with energies above the vacuum level.¹⁾ There are two ways to prepare such a situation: electron impact and photoexcitation. In the following, we treat the latter case because the light source of this facility has enabled and will continue to enable such experiments of high resolution.

When the solid is shined with the light of high energy that exceeds the binding energy of an inner-shell electron, the electron is excited to the continuum above the vacuum level. In most cases, a core hole thus created is unstable, and its two dominant decay processes are photoemission and Auger transition. Here we do not take the former case into account because we are now interested in the dynamics of two electrons as mentioned at the beginning. The Auger transition, on the other hand, annihilates the hole created by the first process, but, instead, yields two holes with one more electron in the continuum. The first electron can have a variable energy depending on the energy of the photon, while the second electron has an almost definite energy representing the electronic level scheme. We here emphasize that the energy of the second electron is not completely definite, which phenomenon is nothing but our subject as is explained later in detail. Anyway, we have now two electrons with energies higher

than the vacuum level. Hereafter we call the first electron photoelectron and the second one Auger electron. Strictly speaking, both electrons might be called photoelectrons because it is impossible to distinguish two electrons in principle, but our naming is just for simplicity.

Let us now proceed to the most important part, that is, the mechanism of energy redistribution between the two electrons. If the consecutive two processes, namely, photoexcitation and Auger transition are separable, the Auger electron should have a definite energy. Such situation is realized in a case where the photoelectron has very little density around the atom that emitted it when the Auger transition occurs. In reality, however, the photoelectron is still existing with finite density around the atom, and so it feels the increase of the Coulomb potential due to the Auger transition. This is the origin of energy redistribution between the two electrons, which is sometimes called post collision interaction (PCI). In this report we particularly emphasize that this energy redistribution is essentially local in the sense that the phenomenon occurs when the two electrons are still existing around the initial atom. That gives the possibility that the way of energy redistribution will be strongly related to the local electronic structure around the atom. In the following, we give two theoretical results that demonstrate this conjecture. In the first example, we assume that the axial momentum is a good quantum number even in the solid, and so only treats a partial wave. In the second example, on the other hand, we assume that the spherical symmetry around the initial atom is very bad and make use of a cubic model. In obtaining both results, we calculate energy spectra of the electrons in the final state, using the T -matrix that describes the whole process. Here the electron-photon interaction is assumed to be weak and treated by the first-order perturbation theory. While, the Auger transition is also treated as a perturbation, but the self-energy is renormalized with an infinite number of repetitions of transitions and inverse transitions. The enhancement of the Coulomb field around the atom following the increase of its valency is expected to be rather strong and then treated exactly.

Let us show the first result, in which we have assumed that both the photoelectron and the Auger electron have the symmetry of s . The Coulomb

potential from the ion is assumed to be of a Yukawa-type, i.e., a screened Coulomb potential due to the screening in the solid. In Fig.1, we show an energy distribution spectrum in which only the contribution from the photoelectron is included. The energy is in the atomic unit(au), referenced from the vacuum level. Here the nominal energy of the photoelectron and the magnitude of the imaginary part of the self energy are set at 2.0 au and 0.2 au, respectively. As is easily seen, the peak in the positive energy region is shifted to the left. This is due to the energy redistribution between the photoelectron and the Auger electron. In the negative energy region, we notice several isolated peaks. They correspond to the contributions from the electrons that are returned to bound states after being excited to the extended states. It should be remarked that such bound states are those of the potential around the atom with two valence or shallow core holes. Such bound electrons, of course, can not escape from the atom and hence are not observed. The Auger electrons, however, can receive energy gains due to the energy losses of those photoelectrons and are expected to be observed.

Next, we show a result obtained using the cubic model. At present, for the light transition, we do not take account of the selection rule related to the angular momentum. Thus this model is applicable

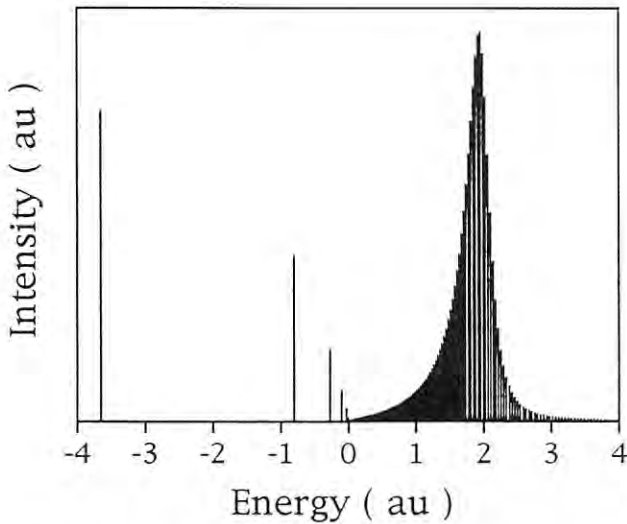


Fig. 1 The energy distribution spectrum of photoelectrons calculated for a s-wave model. The nominal energy of the photoelectron and the imaginary part of the self energy are 2.0 au and 0.2 au, respectively.

best to the system where the spherical symmetry for the continuum states is very bad around each constituent atom. The selection rule for the parity, on the other hand, is assumed to be satisfied. In Fig.2, we show a spectrum of energy distribution in which the contribution only from the photoelectron is included. The energy is in the atomic unit and referenced from the vacuum level. In this case, the nominal energy of the photoelectron and the magnitude of the imaginary part of the self energy are 2.0 au and 0.5 au, respectively. The potential is short-ranged with the screening length of 5.0 au. Again, we can see the peak shift to the lower energy from the nominal energy. In addition to this, we notice small enhancement around 0.8 au. Detailed study of the electronic structure clarifies that there is a resonance at the same position. We can therefore say that this enhancement comes from the electron that is deexcited to the resonance after being excited to the states around the nominal energy. It is worth while mentioning that this resonance is due to the potential around the atom with the two holes. Thus it can not be observed by the measurement of the ordinary absorption. Since the resonance is nothing but a local maximum around the atom that is focused on, this enhancement in the emission spectrum represents a local electronic structure in the same spatial region.

In summary, we have clarified that the local electronic structure affects the energy redistribution between the photoelectron and the Auger electron. This is because the phenomenon is essentially local

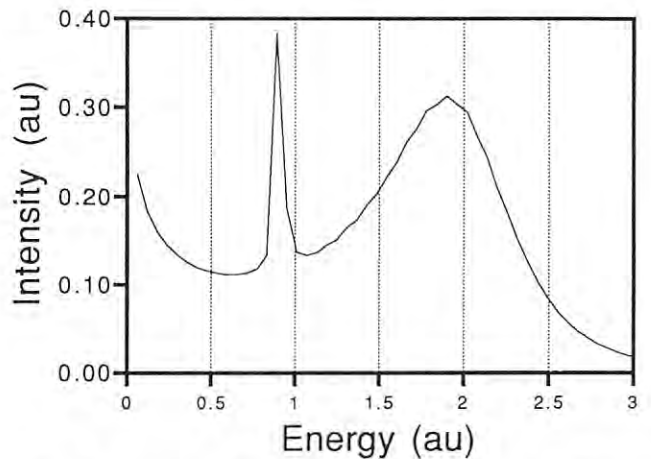


Fig. 2 Same as Fig.1, but for a cubic model. The nominal energy of the photoelectron and the imaginary part of the self energy are 2.0 au and 0.5 au, respectively.

in the sense that both the electrons must be within the potential range of the initial atom. In this report, we have not included the scattering of propagating electrons by the neighboring atoms. This effect is now under the investigation.

2. THEORY FOR EXCITON EFFECTS ON LIGHT ABSORPTION SPECTRA OF F.C.C. TYPE C_{60} CRYSTAL

The studies for fullerenes have made a dramatic progress in recent years. In particular, C_{60} has attracted much attention since its discovery in 1985, and, recently, it was found that the doped C_{60} crystal becomes superconducting with T_c of 18 to 33K, depending on the kind of dopant. Inspired by these new progresses in the experimental field, we have started our theoretical study for this very intriguing material and, as the first work, we focused on the optical properties to understand the electronic structures.^{2,3)}

Various experiments have been carried out to clarify their optical properties; photoemissions, inverse photoemissions, electron energy loss spectroscopies and so on. In the optical absorption spectra, these experiments have indicated that there are three main peaks, roughly speaking. They are all located in the higher energy region than 3eV, and are almost common to both the molecule and the crystal. This fact means that the neutral C_{60} solid is a molecular crystal. On the other hand, in the lower energy region than 3eV, a new peak appears in the case of the crystal, being absent in the case of the molecule. This difference seems to be very important to clarify the nature of excited states of the C_{60} system. However, up to the present, there has been no systematic study for this problem.

We have therefore calculated the absorption spectra of an isolated molecule and crystals in order to find the origin of this difference. We make use of a C_{60} -version of an extended Hubbard model, in which the crystal structure is assumed to be of two types: a simple cubic²⁾ and an f.c.c..³⁾ The electronic ground state is determined by the Hartree-Fock approximation (HFA). While, the excited states are obtained by the first-order perturbation theory with respect to electron-hole attractions, in addition to the HFA.

In other π -electron systems than the C_{60} , it is already well known that the Coulomb repulsion plays very important roles as well as the transfer. In connection with this problem, Lof *et al.* have shown from the Auger spectroscopy that the repulsion is very important in the C_{60} . Thus, the second purpose is to clarify effects of this repulsion on optical absorptions.

The model Hamiltonian is expressed as follows:

$$H = H_{intra} + H_{inter}, \quad (1)$$

$$H_{intra} = - \sum_{\langle i,j \rangle, \sigma} T_{i,j} C_{i\sigma}^\dagger C_{j\sigma} + U \sum_i n_{i\alpha} n_{i\beta} + \frac{V_0}{2} \sum_{\langle i,j \rangle, \sigma, \sigma'} n_{i\sigma} n_{j\sigma'}, \quad (2)$$

$$H_{inter} = -T_2 \sum_{\langle i,j \rangle, \sigma} C_{j\sigma}^\dagger C_{i\sigma} + \frac{V_1}{2} \sum_{\langle i,j \rangle, \sigma, \sigma'} n_{i\sigma} n_{j\sigma'}, \quad (3)$$

where $C_{i\sigma}^\dagger$ and $C_{i\sigma}$ are creation and annihilation operators of an electron at the i -th π -orbital of a C_{60} molecule, respectively. The transfer energies $T_{i,j}$ are expressed as $T_0(T_1)$, if the nearest-neighbor pair $\langle i,j \rangle$ corresponds to a long (short) bond, respectively. For other pairs, the values are set at zero. The transfer T_2 , on the other hand, means that for the closest pair of orbitals on neighboring molecules. The Coulombic energies are expressed as U , V_1 and V_2 , which are on-site, and nearest-neighbor ones inside a molecule, and between adjacent molecules, respectively.

In the following, we introduce our results only for the f.c.c. crystal because it is more realistic than the simple cubic.

In order to show the importance of exciton effects, we have drawn a spectrum without such effects ($T_1/T_0 = 1.1$, $T_2/T_0 = 0.2$, $V_0 = V_1 = 0$) in Fig.3. In this figure, there are four main peaks (A, B, C and D), and also many other small peaks. This spectral shape is very similar to the case of an isolated molecule, and hence it is clear that the main peaks come from intra-molecular transitions. While, the other small ones come from inter-molecular transitions or subsidiary intra-molecular transitions. These subsidiary intra-molecular transitions are such ones that are changed from forbidden to allowed because of a crystalline effect. Figure 4, on the other hand, shows a spectral shape with exciton effects ($T_1/T_0 = 1.1$, $T_2/T_0 = 0.2$, $V_0/T_0 = 0.4$, $V_1/T_0 = 0.17$). Comparing Fig.3

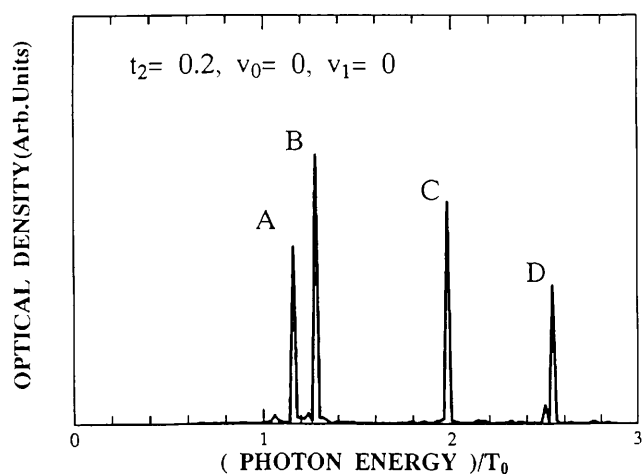


Fig. 3 The absorption spectrum calculated for an f.c.c. crystal of C_{60} . The parameters are $T_1/T_0 = 1.1$, $T_2/T_0 = 0.2$, and $V_0 = V_1 = 0$.

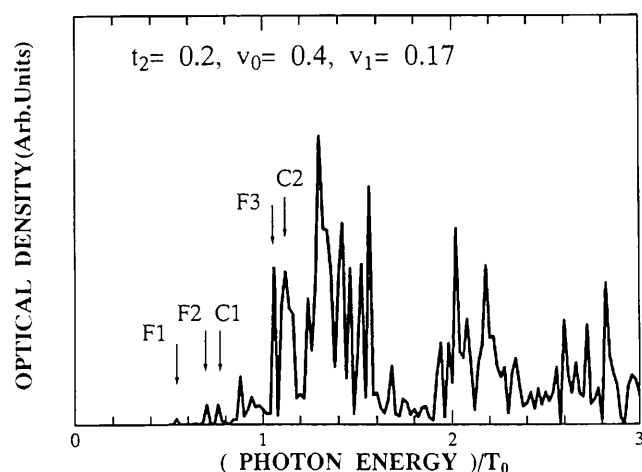


Fig. 4 Same as Fig.3, but with $T_1/T_0 = 1.1$, $T_2/T_0 = 0.2$, $V_0/T_0 = 0.4$, $V_1/T_0 = 0.17$.

with Fig.4, we can find that a strong peak newly appears at the energy region marked by C2. Even in Fig.3, we can see a small peak in the same energy region. However, in the case of Fig.4, it is strongly enhanced by the exciton effects. As is well known, there are two types of excitons; the intra-molecular exciton and the inter-molecular one. In order to clarify the significance of the inter-molecular exciton effect, we have also calculated the case where only the value of V_1 is changed to zero from that for Fig.4, and have found that the aforementioned strong peak is absent. It clearly shows that the inter-molecular exciton effect plays a more important role than the intra-molecular one to make a new strong peak appear in Fig.4. Further, we have also analyzed the excited state eigenfunctions of F1, F2, F3, C1 and C2 marked in Fig.4, so as to clarify the density distribution of the excited electron seen from the hole. The calculated probabilities that the electron and the hole are in the same molecule are 88.0%, 17.7% and 52.8% in the case of F1, F2 and F3, respectively, while C1 and C2 are 5.5% and 3.3%, re-

spectively. Therefore we can say that F1, F2 and F3 are Frenkel type excitons, while those for C1 and C2, being composed of an electron and a hole separated from each other at the neighboring two molecules, are the inter-molecular charge-transfer(CT) excitons. Thus, we can conclude that the experimentally observed peak around 2.5~2.8eV is mainly due to the CT exciton(C2). If we see Fig.4 in detail, we can also find another peak F3 near the peak C2, but its intensity is only about 20% of C2. The other peaks of the calculated spectrum are also in fair agreement with the experimental ones, qualitatively. Incidentally, we have also estimated the width of the HOMO and the LUMO bands using the model Hamiltonian shown in eq.(1). The result well reproduces the results of first-principle calculation.

In summary, we have studied the exciton effects on the spectral shape of optical absorption in the fcc type C_{60} crystal. We have clarified the origin of the new peak which is observed around 2.5~2.8eV. It is due to the inter-molecular CT exciton.

3. T_{1u} HUBBARD MODEL FOR FERROMAGNETIC AND OPTICAL PROPERTIES OF POTASSIUM DOPED ZEOLITE

Let us proceed to the last topic, which is the ferromagnetic and the optical properties of potassium doped zeolite.⁴⁾ Zeolite is a general name for a group of materials with porous characteristics. It has a periodic but complicated crystalline structure, wherein constituent atoms of this material make cages with a vacant space in them. This cage structure of atoms is quite rigid and connected with each other through a channel called a window.

When the zeolite is doped by alkali metal atoms, such as Na or K, these atoms become cations and attach to the inside wall of the cage. Electrons donated from K atoms mainly reside in the vacant space of the cage, because of the electrostatic attractions given from doped K ions as well as from host atoms. Since the cage is almost like a sphere, net attractions become almost spherically symmetric, resulting in localized levels such as a s-, p- and d-orbitals and so on. In our work, we only treat a case where cages make a simple cubic lattice. In this case, those levels have the symmetries of A_{1g} , T_{1u} , E_g , T_{2g} and so on. Doped electrons occupy these levels from lower one to upper ones, depending on K-loading density. The binding energies of these A_{1g} and T_{1u} levels relative to the outside of the cage are about 1.0 eV and 2.2 eV, respectively. These values can be estimated from the optical experiments. Since zeolite is a crystal, these levels of adjacent cages can overlap with each other through the aforementioned windows, as schematically shown in Fig. 5, and resulting in the itinerancy of these electrons. Nozue *et al.* have recently studied one type of zeolite, that is, K-LTA zeolite and found that it becomes ferromagnetic (FM), depending on electron concentration per a certain cage, i.e., α -cage. The magnetization at low temperatures takes its maximum value at 5 electrons per α -cage. The maximum transition temperature is about 10K, and the maximum magnetic moment per α -cage is $0.24 \mu_B$. This small moment favors an itinerant-electron picture as the origin of this magnetism, rather than the localized one. When 5 electrons are doped in an α -cage, the A_{1g} level is completely filled up by 2 electrons, and other 3 electrons occupy T_{1u} levels. If we see this situation from the itinerant-

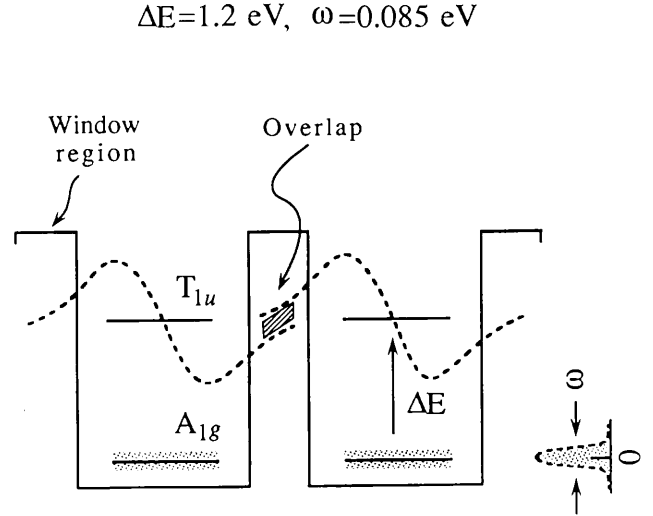


Fig. 5 The schematic picture of K-LTA. Each potential-well denotes the α -cage. The plateau between the wells corresponds the window. The Gaussian indicates the energy distribution of A_{1g} level. ΔE denotes the energy difference between A_{1g} and T_{1u} .

electron picture, it corresponds to the half-filled case of T_{1u} band. Thus, we can say that the K-LTA gives the most strong FM properties in the case of half-filled. For this reason, we will propose here one possible model, which is T_{1u} Hubbard model. This model is different from usual Hubbard models in the sense that each site contains three T_{1u} orbitals instead of one. Its Hamiltonian is given as

$$H = - \sum_{l,l'} \sum_{\sigma} \bar{A}_{l\sigma}^{\dagger} T(l-l') \bar{A}_{l'\sigma} + U \sum_l \bar{n}_{l\alpha} \bar{n}_{l\beta} - J \sum_l \sum_{\lambda, \lambda' (\neq \lambda)} S_{l\lambda} S_{l\lambda'}, \quad (4)$$

$$\bar{A}_{l\sigma}^{\dagger} = (\alpha_{l\sigma x}^{\dagger}, \alpha_{l\sigma y}^{\dagger}, \alpha_{l\sigma z}^{\dagger}),$$

$$\bar{n}_{l\sigma} = (n_{l\sigma x}, n_{l\sigma y}, n_{l\sigma z}).$$

The first term denotes the kinetic energy of electron. $a_{l\sigma}^{\dagger}$ denotes the creation operator of an electron at site l with spin σ ($= \alpha, \beta$) and orbital λ ($= x, y, z$). $T(l-l')$ denotes the transfer energy of an electron between two lattice sites l and l' , and is a (3×3) matrix spanned by x, y and z .

Since there are three orbitals in a site, we take the following four types of transfer energies. The first two are those between nearest-neighboring orbitals, namely, σ -type and π -type. The remaining two are those between next-nearest-neighboring

orbitals on the same plane. We express them as $T_{\sigma\sigma}$ and $T_{\pi\pi}$. If the plane is (x-y) plane, for example, $T_{\sigma\sigma}$ corresponds to perpendicular transfer such as x to y, while $T_{\pi\pi}$ to parallel transfer such as x to x.

The quantity U in eq. (1) denotes the intra-orbital repulsive energy, while $J (> 0)$ is the inter-orbital exchange energy within a single site.

The numerical results are summarized briefly in the remaining part of this section. Generally speaking, with a non-zero value of $T_{\sigma\sigma}$, the nesting of the Fermi surface is broken and so the antiferromagnetic (AF) state becomes unstable. Furthermore, the electronic density of states is enhanced at the Fermi energy. For these reasons, the FM state becomes stable compared with the metallic state or the AF state within a certain region of the phase diagram. In Fig.6, we show the magnetic phase diagram for the case with the parameter $T_{\pi\pi}/T_{\sigma} = 0.3$. As easily seen, the FM state appears in the region of $3.0 < (U+J)/T_{\sigma} < 8.0$, while in the region of $(U+J)/T_{\sigma} > 8.0$, only the AF state appears.

Let us turn to the other aspect of this material, i.e., the optical absorption spectrum. In the low doping regime, doped electrons occupy only the lowest level, namely, A_{1g} level and so we can observe the optical transitions from A_{1g} to T_{1u} . Since the doping is not spatially uniform, the concentration of K^+ is expected to fluctuate from cage to cage. This leads to the fluctuation of the energy of A_{1g} and gives the

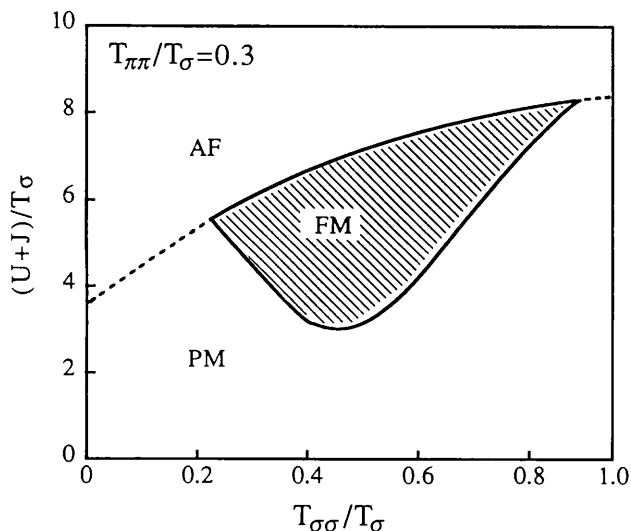


Fig. 6 The zero temperature phase diagram as functions of $(U+J)/T_{\sigma}$ and $T_{\sigma\sigma}/T_{\sigma}$.

broadening to the spectrum. Taking into consideration this effect and also other origins of the broadening such as thermal and zero-point vibrations of the lattice, we assume a Gaussian distribution of A_{1g} level and calculate the spectrum. The obtained spectrum is in good agreement with the experimental one. (see Ref.4)

Therefore we can say that we have succeeded in clarifying the zero-temperature magnetic phase diagram and the optical absorption in terms of the same model from a unified point of view.

References

- 1) K. Iwano and K. Nasu: preprint.
- 2) T. Tsubo and K. Nasu: J. Phys. Soc. Jpn., **63**, (1994) 2403.
- 3) T. Tsubo and K. Nasu: Solid State Comm., **91**, (1994) 907.
- 4) A.Z. Chowdhury and K. Nasu: J. Phys. Chem. Solids. **56** (1995) 1193.

C. ATOMIC AND MOLECULAR SCIENCE

Thanks to the improvement of beamlines and experimental apparatuses, the opportunities to study the spectroscopic details of free atoms and molecules are opened. From these sophisticated works, one can obtain the important information of electron correlation in free atoms and molecules. The precise description of the electron correlation is the big change of the modern atomic and molecular physics.

1. ATOMIC SPECTROSCOPY

The 4d photoabsorption of Ba^+ ions was revisited by a merging beam technique on BL-3B. The 4d spectrum of Ba^+ is shown in Figure 1. In contrast to the spectrum of Ba, the 4d absorption oscillator strength is distributed in several strong discrete transitions and in the continuum. The spectrum shown in Figure 1 is surprisingly different from the one measured by Lucatorto et al.. They used a dual laser technique to obtain their spectrum. The contamination of Ba atoms in Ba^+ ions may cause this serious difference. The 4d spectrum of Ba^+ by Lucatorto et al. is similar to their 4d spectrum of Ba. On the

other hand, the present spectrum of Ba^+ is similar to the one of Ba^{2+} by Lucatorto et al.. The present spectrum free from the contamination of Ba reveals that the redistribution of the 4d oscillator strength in photoabsorption of the Ba, Ba^+ , and Ba^{2+} sequence starts from the Ba^+ . Assignments of the discrete lines in Figure 1 are being undertaken by MCDF cal-

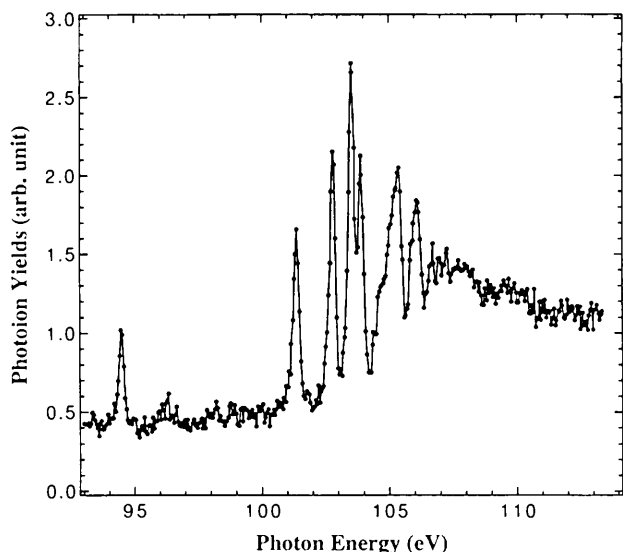


Fig. 1. Photoabsorption spectrum of Ba^+ . Photoion products (Ba^{2+} and Ba^{3+}) were counted by the merging beam technique. In contrast to the 4d spectrum of Ba, several strong discrete lines of $4d \rightarrow nf$ resonances are observed below the 4d ionization continuum. T. Koizumi, Y. Itoh, M. Sano, M. Kimura, T. M. Kojima, S. Kravis, A. Matsumoto, M. Oura, T. Sekoka and Y. Awaya.

culations.

On BL-3B, the double-core excitation of Li atoms is also successfully measured in the spectral region of 140-165 eV. In the spectrum shown on Figure 2, a particularly conspicuous feature is the "F" resonance at 152.32 eV whose strength is comparable to that of the $2s^22p$ "A" resonance. Several weaker peaks are clustered in the vicinity of the peak F. At higher energies, a few small peaks are found around the "M" resonance at 161.59 eV. Regularities of Rydberg series structures found in He double photoexcitation are missing in the spectrum. MCDF calculations have been performed to give assignments to the numerous resonance features. Comparison of measurements and calculations are presented on Table 1 and Figure 2. The MCDF calculations reproduce most features of the experimental spectrum. As the result of success of this theoretical work, one can understand that the double-core excited states are induced through initial-state configuration interaction.

2. MOLECULAR SPECTROSCOPY

2.1 Valence Electronic Excitation

The high photon flux and high energy resolution at BL-20B make it possible to study state-to-state neutral dissociation from superexcited states and to perform high resolution threshold photoelectron spectroscopy.

The fluorescence radiation spectra from excited

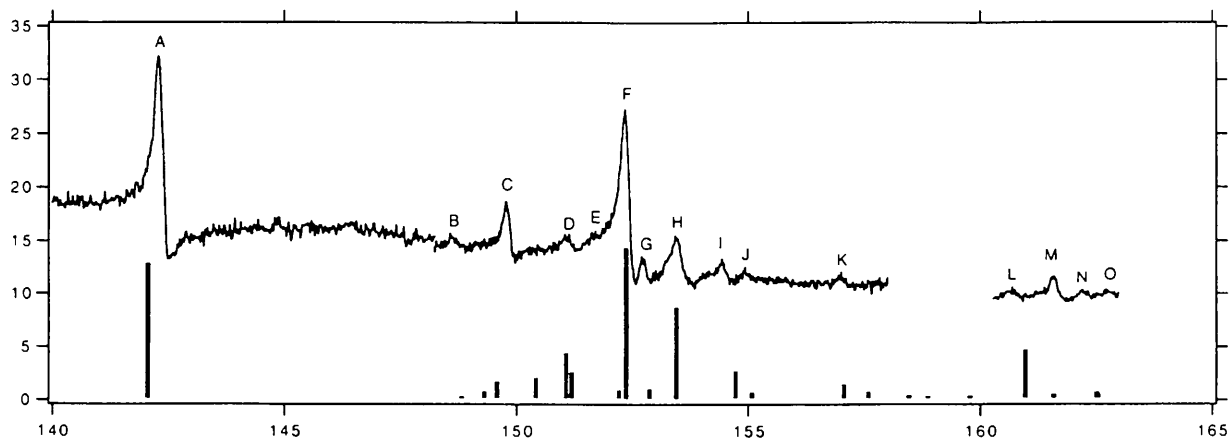
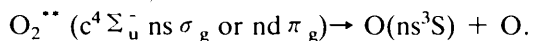


Fig. 2. Double-core excitation spectrum of Li atoms. Rydberg series are missing in the spectrum. The bar diagram overlaid indicates energy positions and relative intensities obtained by MCDF calculations. Y. Azuma, S. Hasegawa, F. Koike, G. Kutuluk, T. Nagata, E. Shigemasa, A. Yagisita and I. A. Sellin.

Table 1 Measured resonances compared with MCDF calculations. The E_0 value for "A" resonance was obtained by a Fano profile fit, while peak maximum positions are presented for other resonances. The experimental hv scale has absolute and relative accuracies of ± 0.1 and ± 0.03 eV, respectively.

Res.	E_0 [eV] Expt.	E_0 [eV] MCDF	Osc. Strength MCDF	Dominant Configuration Admixtures (in%) in the Excited States			
A	142.34	142.057	1.29346	74 $2s^2 2p$,	12 $2p^3$	8 $2s 2p 3s$	
B	148.7	148.839	0.0322998	30 $2p^3$,	15 $2p^2 3p$,	14 $2p^2 3p$,	14 $2s 2p 3s$
		149.32	0.0850236	40 $2s^2 4p$,	13 $2p^2 3p$,	12 $2p^2 4p$	
		149.587	0.178457	36 $2s 2p 4s$,	20 $2s^2 4p$,	10 $2s^2 5p$	
C	149.79	150.408	0.213238	65 $2s 2p 5s$,	20 $2s 2p 4s$		
D1	151.10	151.065	0.441158	36 $2s 2p 3d$,	20 $2s 2p 5s$,	12 $2s 2p 3s$	
D2		151.189	0.264139	50 $2s 2p 3d$,	16 $2p^2 3p$		
E	151.7	152.205	0.101476	56 $2p^2 4p$,	28 $2p^2 3p$,	9 $2s 2p 3s$	
F	152.32	152.355	1.44477	40 $2s 2p 3s$,	29 $2p^2 4p$,	25 $2p^2 4p$	
G	152.72	152.87	0.111862	83 $2p^2 5p$,	9 $2p^2 4p$		
H	153.43	153.442	0.874026	37 $2p^2 3p$,	29 $2s 2p 3s$,	13 $2p^2 4p$,	11 $2p^2 5p$
I	154.43	154.72	0.275326	40 $2s 2p 3d$,	26 $2s 2p 4s$,	12 $2s 2p 5s$	
J	155.0	155.068	0.0742149	85 $2s 2p 5s$			
K	157.0	157.044	0.15073	35 $2p^2 3p$,	21 $2p^3$,	12 $2s 2p 3s$	
		157.576	0.0836255	44 $2p^2 3p$,	16 $2p^2 4p$,	13 $2s^2 3s$	
L	160.6	159.767	0.0414757	40 $2s 3s 3p$,	31 $2p 3s^2$,	19 $2p 3p$	
M	161.59	160.976	0.477756	35 $2p 3p^2$,	33 $2p 3s^2$,	23 $2s 3s 3p$	
N	162.2	161.571	0.0563835	44 $2p 3p^2$,	22 $2p 3s 3p$,	12 $3s 3p$,	12 $2s 3p 3d$
O1	162.7	162.51	0.073798	25 $2s 3p 4s$,	23 $2p 3s 4s$,	16 $2p 3s 3d$,	13 $2p 3p^2$
O2		162.632	0.0536372	25 $2p 3s 4s$,	22 $2s 3p 4s$,	17 $2p 3d^2$,	13 $2p 3p^2$

O^+ atoms produced in the neutral photodissociation of O_2 molecules are measured as a function of excitation photon wavelength. Two-dimensional representation of the fluorescence spectra is shown in Figure 3. The two-dimensional location map reveals the striking behavior of neutral dissociation far beyond the IP, i. e., state-state dissociation of the $(C^4 \Sigma_u^-)ns \sigma_g$ and $nd \pi_g$, $v'=1$ Rydberg states. For $v'=1$ vibrational level of each Rydberg state, having the principal quantum number of n , converging to the $O^+ c^4 \Sigma_u^-$ state, the production of $O(ns^3S)$ atoms is strongly emphasized, where the n quantum number is conserved;



A threshold photoelectron spectrometer using the penetrating field technique has been constructed. Vibrational structures of Xenon dimer have been successfully studied by the spectrometer combined with a photoion time-of-flight analyzer. Especially the vibrational progression associated with the $C^2 \pi_{1/2} u$ state of Xe^{2+} has been observed for the first time, which is shown in Figure 4. The intensity distributions of the low vibrational levels show a Frank-Condon like profile. Note that the intensity of the

peak at 928.38 Å is strongly enhanced. This peak is attributed to the $D^2 \Sigma_{1/2}^+$ state. The population of high v' levels outside the Frank-Condon region of $C^2 \pi_{1/2} u$ state must occur via an indirect process.

2.2 Core Electronic Excitation

The high photon flux, high resolution, and high degree of linear polarization at the soft x-ray undulator beamline BL-2B provide us opportunities to develop new soft x-ray spectroscopy: high-resolution symmetry-resolved photoabsorption spectroscopy and photoelectron angular distributions from oriented free molecules.

High-resolution symmetry-resolved O K-edge spectra of O_2 molecules have been measured by detecting fragment photoions emitted parallel ($\Delta \Lambda = 0$) and perpendicular ($\Delta \Lambda = +1$) to the electric vector of the synchrotron radiation, which are shown in Figure 5. In the $\Delta \Lambda = 0$ spectrum, some unassigned peaks are found in the $1s \rightarrow 3p$ Rydberg state, converging to the $^4 \Sigma^-$ ionized state, on the broad resonance feature around 541eV. Comparison with *ab initio* potential energy curves indicates that the $1s \rightarrow 3p(^4 \Sigma^-)$

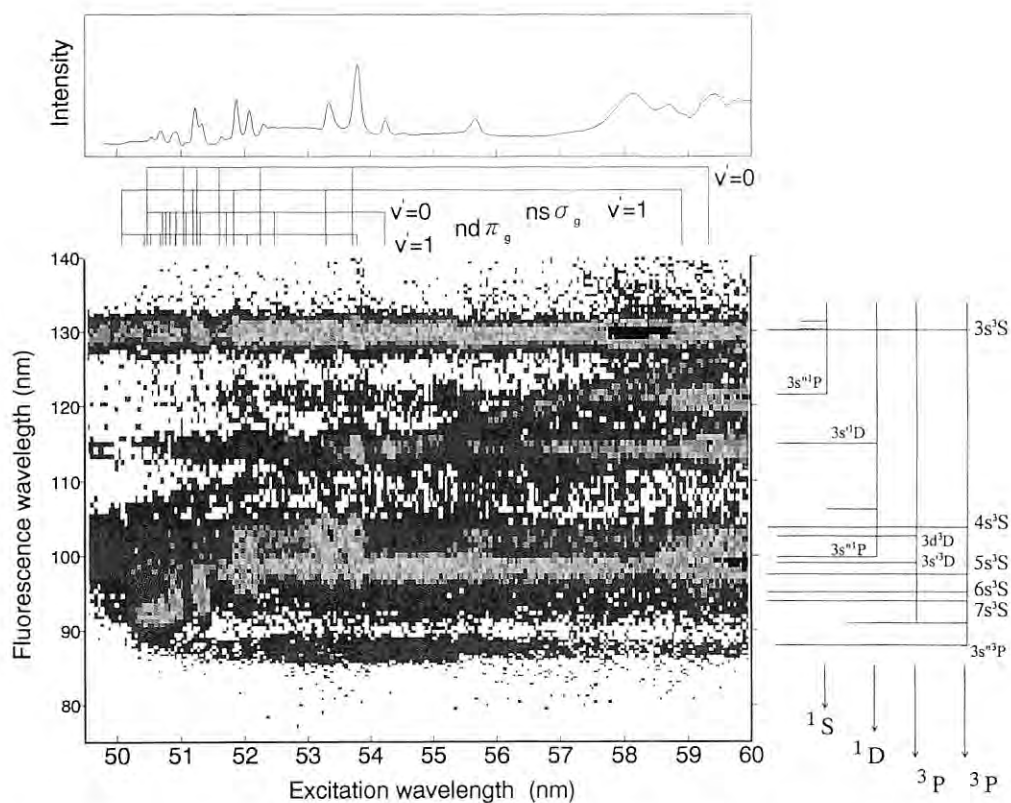


Fig. 3. Two-dimensional yield spectrum of the fluorescence radiation emitted from neutral O^+ atoms produced in the neutral photodissociation of O_2 molecules. Horizontal line structures present the partial fluorescence yields of $O I$ radiation lines. Yield spectrum of nondispersed fluorescence is shown in upper panel. M. Ukai, S. Machida, K. Kameta, M. Kitajima, N. Kouchi, Y. Hatano and K. Ito.

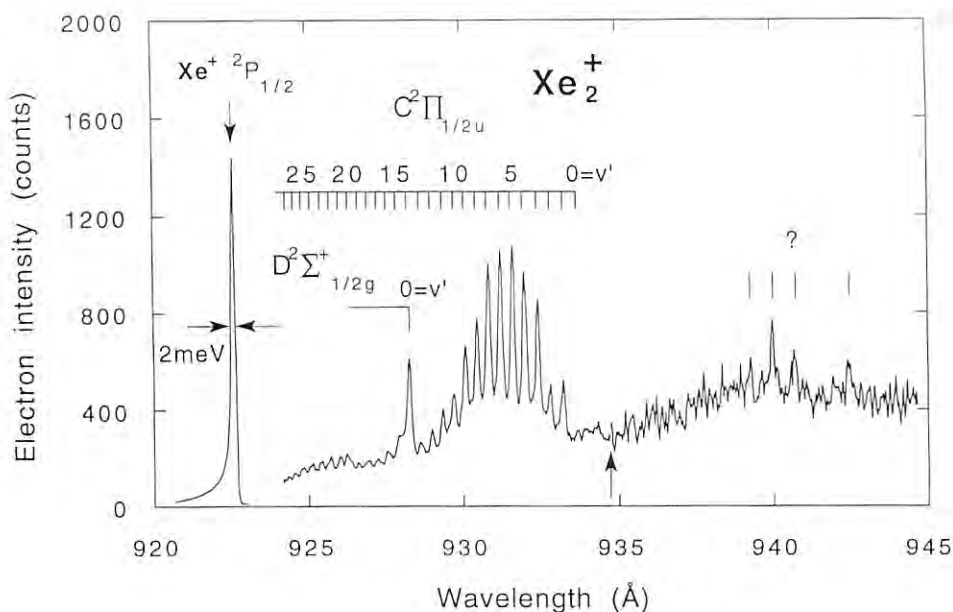


Fig. 4. Threshold photoelectron spectrum of Xe_2 in the region of 920-945 Å. Structures corresponding to the $C^2\Pi_{1/2u}$ and $D^2\Sigma^+_{1/2g}$ are identified in this region. Several unidentified structures are indicated by ticks. Y. Lu, Y. Morioka, T. Matsui, T. Tanaka, H. Yoshii, R.I. Hall, T. Hayaishi and K. Ito.

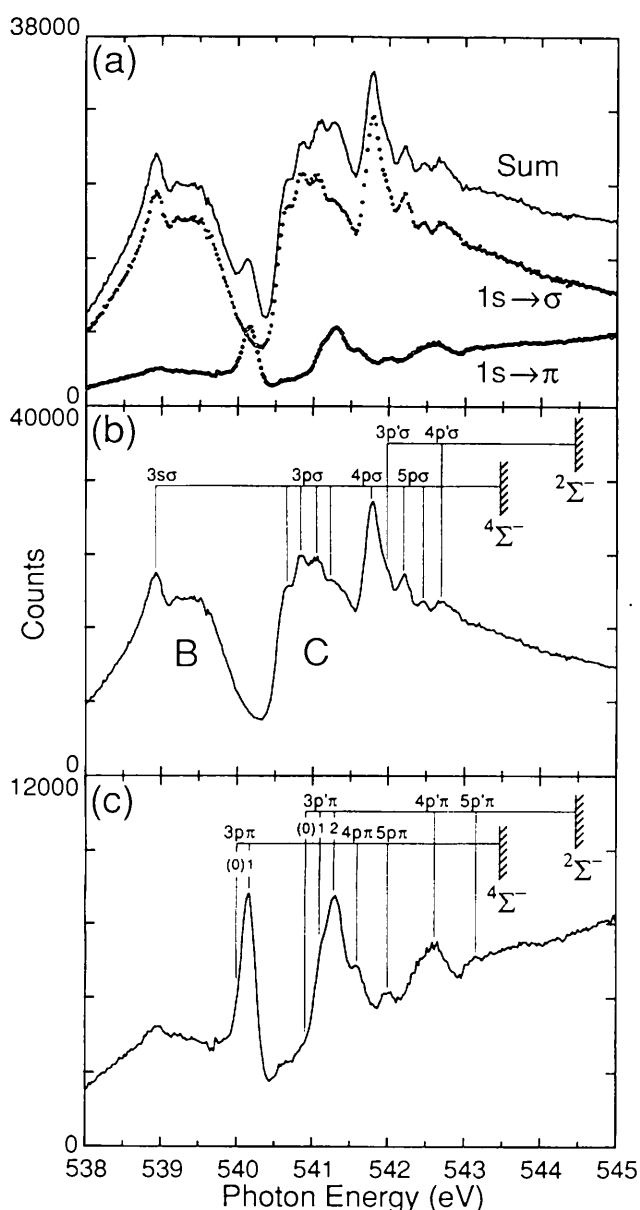


Fig. 5. High-resolution symmetry-resolved spectra of O₂ molecules. (a) symmetry-resolved spectra and their sum corresponding to the photo-absorption spectrum. (b) blowup of the $\Delta\Lambda = 0$ spectrum and (c) blowup of the $\Delta\Lambda = +1$ spectrum with the assignments of the Rydberg series. Anomalous vibrational progression is observed around the 3pσ state. A. Yagishita, E. Shigemasa and N. Kosugi.

Rydberg state is mixed with the $1s \rightarrow \sigma^*$ repulsive valence state with the same ion core ($4\Sigma^-$) and that the avoided curve crossing between the states enhances vibrational excitations. The resonance feature around 539.5 eV is attributed to the $1s \rightarrow \sigma^*$ ($2\Sigma^-$) state arising from the exchange splitting in the $1s \rightarrow \sigma^*$ va-

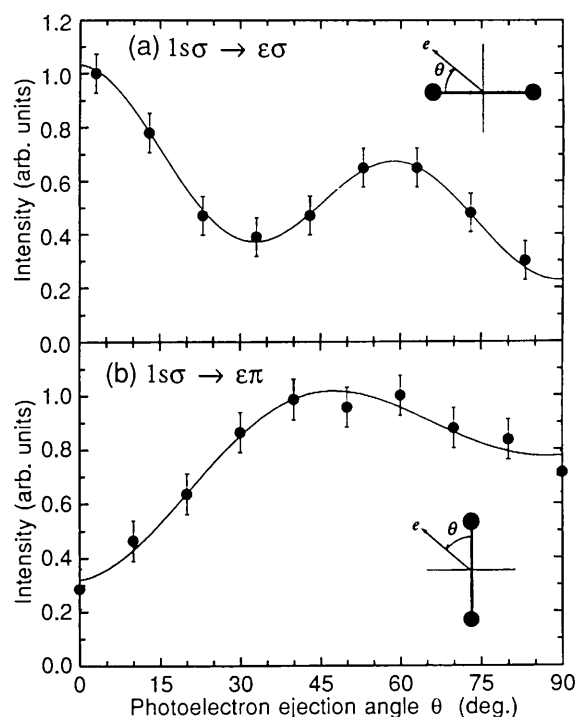


Fig. 6. Angular distributions of $1s\sigma$ photoelectrons from the spatially aligned N₂ molecules. (a) molecular axis is aligned parallel to the electric vector of the incident light and (b) molecular axis is aligned perpendicular to the electric vector. E. Shigemasa, J. Adachi, M. Oura and A. Yagishita.

lence excitations.

In order to determine angular distributions of photoelectrons from aligned molecules, one is faced with the technical difficulty of creating the alignment. The method adopted in this study made no attempt to physically align the molecules. Rather, the populations of molecules with the desired alignment were selected by detecting energetic ions ejected either parallel or perpendicular to the polarization vector. The angular distributions of $1s\sigma$ photoelectrons from spatially aligned N₂ molecules have been performed using an angle resolved photoelectron-photoion coincidence technique in the regions of the K-edge and σ^* shape resonance. The angular distribution pattern for the parallel transitions on the σ^* shape resonance is shown in Figure 6(a), and the one for the perpendicular transitions in Figure 6(b). As can be seen from Figure 6(a), for the parallel transitions the f-partial wave dominates due to the shape resonance effect. On the other hand, the p- and d-partial waves dominate for the perpendicular transitions (Figure 6(b)).

D. VUV AND SOFT X-RAY SPECTROSCOPY OF SOLIDS

1. BASIC TECHNIQUE OF THE RESEARCHES

With all the VUV and Soft-X-ray(SX) beamlines one can use monochromatized photons from 5 eV to 3 KeV. The low energy region below 1.5 KeV is mainly covered by grating monochromators, while the high energy region above 1.7 KeV is covered by double-crystal monochromators using Sb crystals.

One of the important actions to materials caused by the VUV and SX photons is excitations of core electrons of constituent atoms, which is usually exerted in the time scale much shorter than the time for relaxation by valence electrons, meaning that the most part of the excitation processes is completed before its side-effect propagates far from the atom concerned. In this context the core excitations are often called "local", "site-specific", or "atom selective" excitations.

However these photons can also excite valence electrons, some of which are not localized within an atom. Therefore the spectra obtained could in principle include effect due to delocalized excitations to some extent. The most important applications of this aspect is the angle-resolved photoelectron spectroscopy to determine the band structure of materials with translational symmetry.

High resolution spectroscopy with core excitations also gives information on non-local aspect of valence relaxation in the following way. With a very high energy resolution, ΔE , one can see a long time scale, Δt , which allows, for example, a non-local screening to occur. In other words a small ΔE generally corresponds to a small wave number, Δk , giving information on a larger size of the real space. That is why most VUV and SX synchrotron radiation facilities in the world try to construct grating monochromators with very high resolution over 10^4 .

Then a powerful method to investigate both local and non-local aspects of core excitations is to tune the photon energy to a resonance level regardless whether the level is localized or delocalized. In fact the characteristics of the resonance level could be changed between the initial and the final states but it can in principle be clarified through analysis of the above resonance experiment. Actually the method is

called "resonance photoemission" in photoemission spectroscopy or "resonant Raman scattering" in emission spectroscopy, the former of which already has a long history of about 20 years, while the latter has only a few years of history in VUV and SX regions.

On the other hand, EXAFS or SEXSAFS is related to measurement of much larger energy scale and gives information on the atomic arrangement of the short range distance. At the Photon Factory this technique is mainly used with a double-crystal monochromator and sometimes combined with a standing-wave method for materials with periodicity.

2. SPECIAL FEATURES OF SYNCHROTRON RADIATION

2.1 Utilization of polarized synchrotron radiation

One of the important advantages of the synchrotron radiation is its excellent polarization characteristic. Usually radiation from a bending magnet or a linear undulator is linear polarized when observed in the orbital plane. Furthermore the Photon Factory has two helical undulators to produce circularly polarized radiation, one at the 2.5 GeV ring and the other at the TRISTAN Accumulation Ring (AR).

Using linear polarization, one can get information on the orientation of a molecule or direction of the spatial extension of the wave function concerned. This advantage has been utilized to determine the structure of molecules or the atomic arrangement of atoms adsorbed on a surface. For a gas phase molecule, linear polarization has been used also to characterize the electronic states related to fragmentation or decomposition of the molecule.

Circular polarization in the VUV and SX region has been used mainly for magnetic circular dichroism (MCD) of materials such as ferromagnets, ferrimagnets, magnetic multilayers, and even materials without any magnetic order in the ground state. Figure 1 shows the MCD spectra of a Ni-Pd alloy in the Ni 2p-3d excitation region measured at BL-NE1B¹⁾. In this method an external magnetic field is applied to a material, which induces polarization of a material to some extent even though the material does not have any magnetic orders in the ground state. For all of those materials the sum rule relating the magnetic

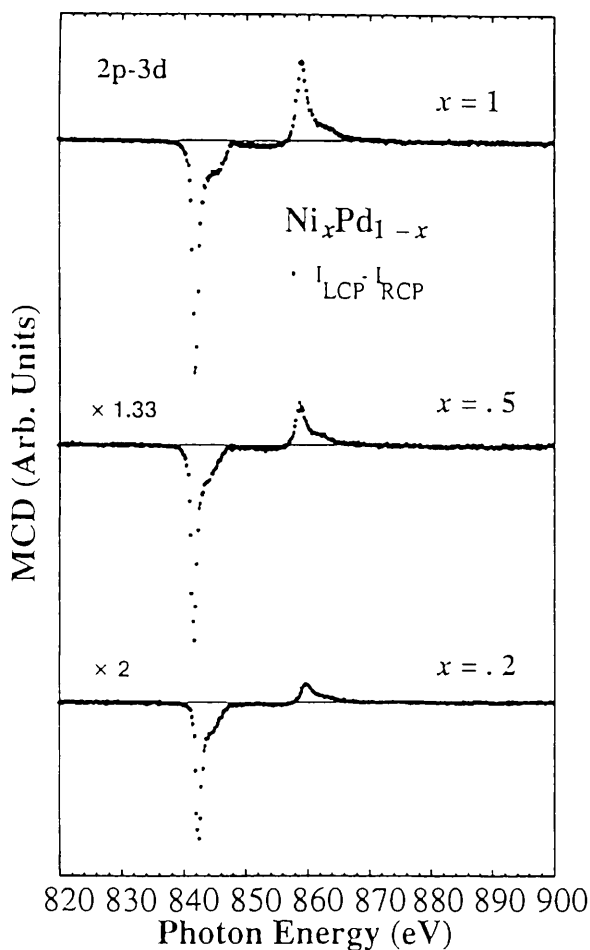


Fig. 1 The MCD spectra of Ni-Pd alloys in the Ni 2p \rightarrow 3d excitation region.

moment and the spectral intensity has been often used to analyze the results or decompose the spin and orbital moments. However it has been noticed that great care should be taken when applying the sum rule to the experimental results.

2.2 Utilization of the pulsed structure of synchrotron radiation

Because the PF ring has a revolution period of 560 nsec, one can observe a pulsed light signal with the above time separation in the single bunch mode. The bunch length in this mode is about 300 psec, which is short enough to observe decay or relaxation processes following core excitation with time constant longer than 1 nsec. With this advantage time-of-flight (TOF) measurements have been performed without using any optical shutter or chopper system, for instance, to investigate the dynamics of photode-

sorption processes occurring at molecules adsorbed on a surface. Figure 2 shows an example of such a measurements on polymethylmethacrylate (PMMA) thin films²⁾.

This technique could be used also in studies on relatively slow radiative decay of locally excited systems, which generally requires highly efficient second monochromator and a fast time-resolved emission detector. Though some measurements have been performed in the X-ray region (14.4 KeV) at the AR to investigate quantum beat appearing in nuclear Bragg scattering by a Fe⁵⁷ crystal, there have been very few examples in the VUV and SX regions.

3. PHYSICS OF SOLID STATE SPECTROSCOPY

3.1 Single electron states in solids: Band structure

Though various types of electron correlation effects have been known to play an important role in many "exotic" properties in solids, one of the basic

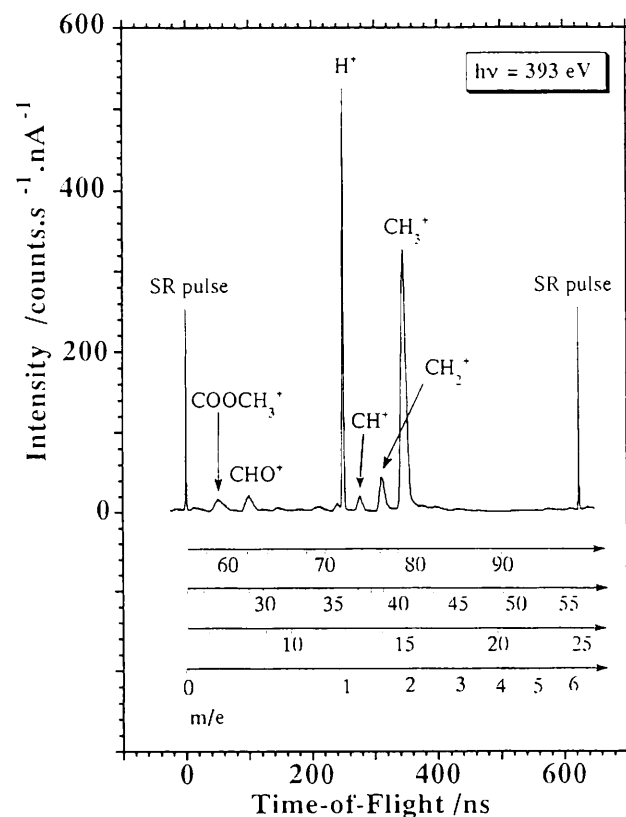


Fig. 2 The TOF measurement of PMMA thin film.

information on the electronic states in a solid or a surface is the apparent one-electron energy distribution described by the band structure. When the system has translational symmetry the energy has k dependence giving the corresponding energy dispersion, $E(k)$. It should be noted, however, that the obtained $E(k)$ is not the energy of an electron isolated from other electrons, and that it is rather a renormalized energy including the averaged effect induced by the presence or the motion of other electrons. Therefore the experimentally observed energy of a particular branch of the band has a non-vanishing energy width ΔE , corresponding to the inverse of the lifetime of the quasi-particle in the many-electron system. For the Fermi liquid system the energy width ΔE has been known to be proportional to the square of the binding energy, E_b , relative to the Fermi level when E_b is much smaller than the band width.

Quite recently great development of band calculation has made it possible to take electron correlation effects into account to some extent, and in some cases the relativistic effect causing the spin-orbit interactions. Therefore one can regard the results of the band calculation as the reference point from which further discussions continue.

Technically, photoemission spectroscopy with very high resolution on the valence band of metals and alloys is an important and essential experimental method to clarify the characteristics of electronic states near the Fermi level. The method has been adopted, for example, in the investigation of "heavy Fermion" systems or "Kondo insulators". From the results of the experiment one can deduce whether the electron correlation is really important or not.

3.2 Local electronic states without translational symmetry

Apparently, creation of a core hole induces some attractive force on valence electrons or even on the excited electrons. Here it is interesting to see that the above attractive force depends on the electronic states of valence electrons in the ground state. In fact, an electron which is more localized in the ground state feels larger attractive force due to the core hole. It often happens that there is some overlap between wave functions of the hole and a valence electron and this makes the attractive force dependent on the spin of the hole through exchange in-

teraction, which might be even more complicated if the spin-orbit interaction of the core hole is comparable to the exchange one.

Fortunately, however, the above situation allows us to adopt the atomic calculation for the starting point.

One of the important effects of the above uneven attractive forces acting on the valence electrons is that the states almost degenerate in the ground states may lose the degeneracy in the excited states. A good example can be found in a material with "valence fluctuation", where the state with valency n has almost the same energy with the state with valency $n + 1$. But because the created core hole gives different attractive forces on the two states, photoemission spectra of the core electrons generally add some satellite structures. Figure 3 shows an example of such a study on CeRu_2 measured with XPS technique³⁾.

In the time domain picture the above excited state is described as a non-stationary state oscillating from one state to another. When the oscillations with lower frequency are more important, the terminology "screened" states or "relaxed" states are often used. Strictly speaking "relaxation" of a system means some damping of the oscillations, through excitations of other quasi particles which are assumed to affect the system concerned from the *outside* of the system. However in most cases of high energy spectroscopy "relaxation" within the electronic system plays an essential role, because it is usually very difficult to observe real relaxations including lattice motions.

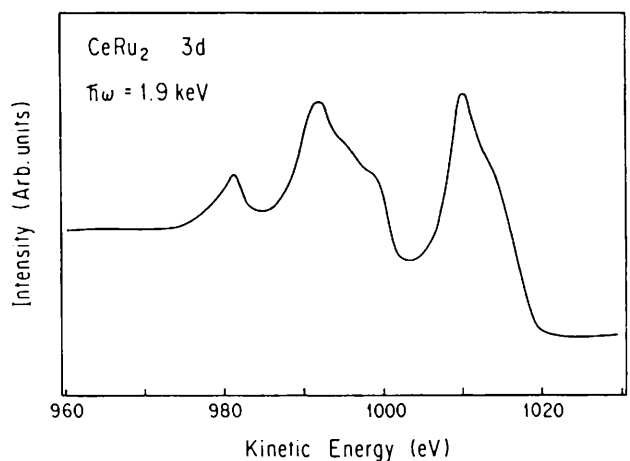


Fig. 3 The satellite structure of CeRu_2 measured with XPS technique.

3.3 Electron correlation

As mentioned in 3.1, some part of electron correlation effects in the ground state is renormalized in single-electron energy of the valence band. The other parts of the correlation effect are often concealed and do not appear as the dispersion curves of the band structure. They may appear as a separate structure like the “6 eV satellite” observed in the valence band photoemission spectra of Ni metal, where the number of 3d holes, 0.6, in the ground state is interpreted in terms of superposition of two almost degenerate configurations, such as $3d^9$ and $3d^{10}$. Figure 4 shows such an example, where the satellite is decomposed into atomic multiplets⁴⁾.

However an important difference compared to the case of uneven attractive forces is that the energy separation in the final state is caused by the repulsive energy between two electrons, which is often denoted symbolically by U . Roughly speaking the above separated satellite appears in the valence band structure when U is larger than the band width (or the inter-site electron transfer energy T). Here it is implicitly assumed that U works within a small spatial region corresponding to the size of constituent atoms. This means, that presence of many localized orbitals induced by the attractive force of an ion core, is an implicit but essential condition to give rise the above correlation satellite.

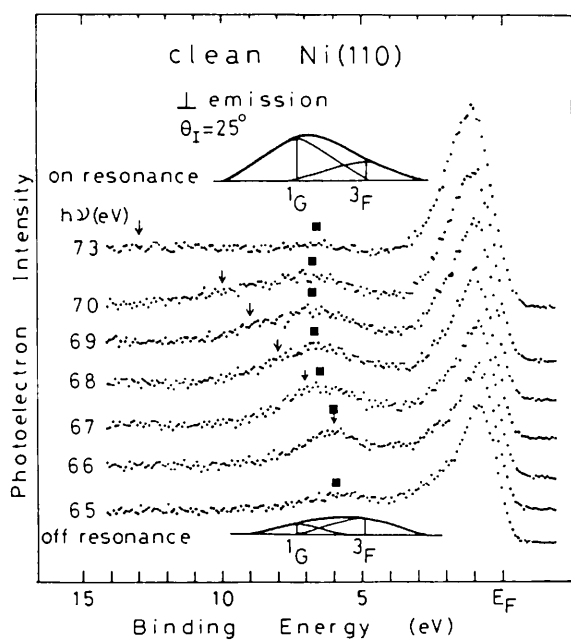


Fig. 4 The satellite structure of Ni metal.

4. EXAMPLE OF THE STUDY IN FY 1994

4.1 Photoemission spectroscopy

Some experiments have been carried out to obtain band dispersion $E(k)$ of SrTiO_3 with a proposal No. 93-G113, and that of $\text{Si}(001)2 \times 2\text{-Al}$ with a proposal No. 94-G189. The basic result in the former study was that the O 2p band can be described in terms of the single-electron picture. In the latter study, it was found that the dispersion curves of Al 2p band never intersect the Fermi level and one branch corresponds to the Al-Al dimer structure.

Gd-Lu multilayers were studied with 3d resonant XPS under a proposal No. 92-G146, where it was found that the satellite structure appearing in the 4f band of pure Gd disappeared in the multilayers indicating that the Gd 4f state is largely modified due to a long range effect induced by Lu layers. The disappearance of the satellite is interesting, because it shows the possibility that the origin of the satellite of pure Gd may be due to some unknown long range correlation effect. In most current theories, the correlation satellite is treated as a local effect such as the famous “6 eV satellite” in Ni metal, where two localized configurations, $3d^8$ and $3d^9L$ are considered in the excited states. On the other hand, it is well known that the observed correlation energy U is greatly reduced due to other correlation effect among d or f electrons. For example, Ni-Pd and Pd-Ag alloy systems studied at PF in 1988 showed that the “two hole bound state” is delocalized to some extent. Because the present system is a 4f system, the result might indicate break-down of the picture of local mixing between $4f^n$ and $4f^{n+1}L$ states.

CeB_6 has been a good target of the similar study because it would show the “Kondo peak” at low temperatures and it is a typical candidate of the “Kondo lattice” system. It has been studied with the energy resolution of 78 meV using the 4d-4f resonant photoemission technique under a proposal No. 93-G333. In the study, the spin-orbit splitting with 240 meV energy separation was observed together with a broad satellite structure at the binding energy of 2.4 eV. The spectra are shown in Fig. 5. The latter has been usually interpreted as “ $4f^0$ ” configuration, but the origin of the broadening is still puzzling, and the present result might suggest possibility of the band-like (delocalized) nature of 4f states in the ground

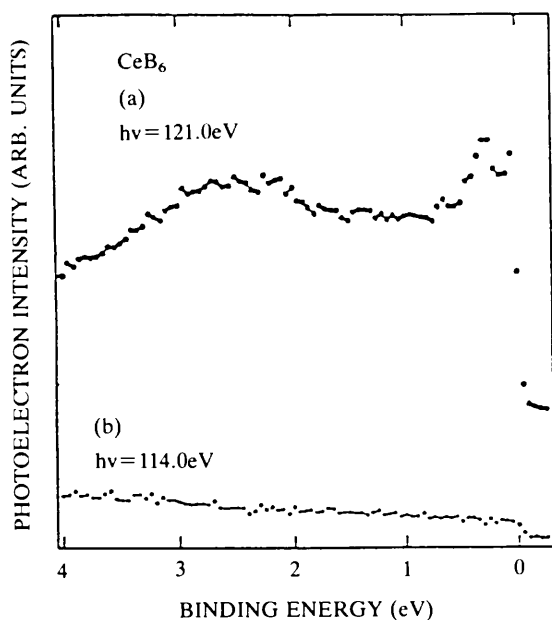


Fig. 5 The photoemission spectra of CeB_6

state, since the idea of the “Kondo lattice” needs coherence among 4f states belonging to different atoms.

A spin resolved photoemission study on Fe_7S_8 and Fe_7Se_8 has been performed under a proposal number 93-G335 at BL-19B. Both samples were found to show negative spin polarization near the Fermi level due to the Fe 3d minority band. The binding energies at which the change in the sign of the polarization occurs were found to be larger in FeS_8 than in FeSe_8 , indicating that the exchange splitting in the Fe 3d band is also larger in FeS_8 .

4.2 Absorption spectroscopy and magnetic circular dichroism

The absorption spectroscopy in the VUV and SX regions is divided into three categories, namely, EXAFS mainly for surface structural analysis, ordinary absorption measurement to investigate electronic states, and magnetic circular dichroism (MCD).

The first category was devoted to structural analysis of adsorbed atoms or molecules and the reconstructed layers of the substrate, where the polarization-dependent scattering processes have been taken into account to determine the orientation of the bondings. Many studies have been performed on various overlayers on various surfaces such as Ni(110), Ni(100), Ni(111), Cu(100), and Cu(111).

Among those a study on the adsorption and the decomposition of silane on Cu(111) under a proposal No. 94-G178 showed a drastic change of the structure dependent on the temperature. Because phase transitions on surfaces are of great interest, any temperature dependence of the surface structure should be studied by more number of users.

As an example of the second category, an O 1s absorption study was made under a proposal No. 93-G316 on $\text{Y}_{1-x}\text{Ca}_x\text{TiO}_3$, which is regarded as a Mott-Hubbard insulator for $x = 0$, and becomes a metal when $x > 0.4$. The results shown in Fig. 6 have suggested that the structure due to the Ti 3d t_{2g} orbital is enhanced when x is 0.4 or larger. This was interpreted in terms of creation of in-gap states with hole doping. In general, however, a change of the electronic states due to hole (or electron) doping in such a highly correlated system is very complicated and the creation of a in-gap state is not self-evident. In fact, the doped hole (or electron) may have some *itinerant* character, and can move in the solid accompanied by a very strong effect on other electrons *at each*

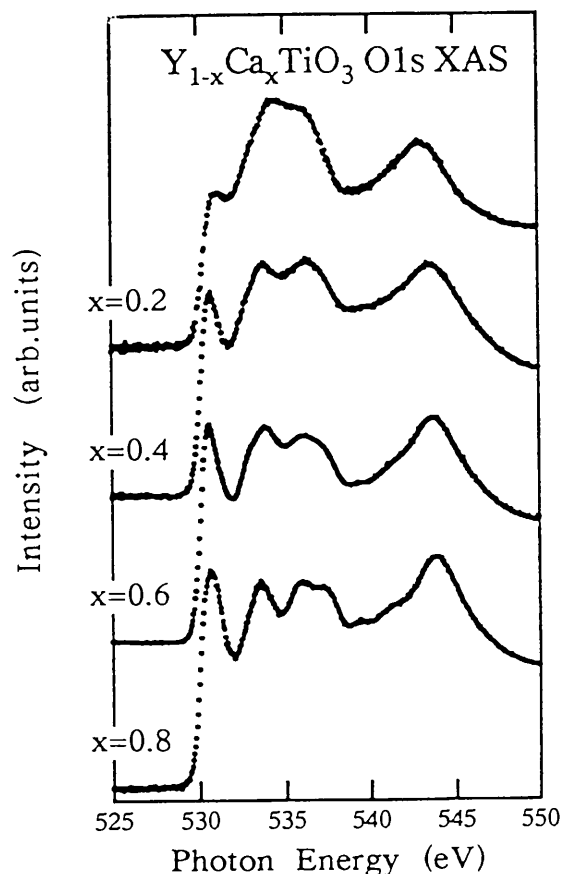


Fig. 6 O1s absorption spectra of $\text{Y}_{1-x}\text{Ca}_x\text{TiO}_3$

periodic site, and this also causes excitation of magnons possibly with a form of itinerant magnetic polarons. Therefore, a single-site model, such as the impurity Anderson model, or the cluster model, might not give a correct description of an “in-gap” state. In this sense the present results have given a subject of controversy as a topic of metal-insulator transition.

The MCD studies have been carried out by many groups on various materials. Among those the MCD study on KBr and RbBr excitons under a proposal No. 93-G340 is noteworthy because the specimens are non magnetic. They gave the estimated *g*-values of the excitons to check the validity of the band assignment. Significance of the study may also be stimulation of more exact relativistic band calculations for alkali halides.

4.3 Soft x-ray emission and Auger electron spectroscopy

The number of studies with soft x-ray emission or Auger electron spectroscopy have increased rapidly, not only because of the recent improvement of instrumentation for measurements of the secondary light, but also because of substantial enhancement of the brightness at the sample position, owing to developments in the beamline technology. Since the emission spectroscopy is useful for studying the valence band of a material, higher energy resolution of both the first and the second monochromators has more advantage, for example, to observe the detailed structures near the Fermi level of a metal. To accomplish high energy resolution of the second monochromator, the focused image on the specimen should be as small as possible at least along the direction of the dispersion by a grating, because the image works as the entrance slit. Actually there would be some compromise between the number of incoming photons and the energy resolution.

Probably the most significant advantage of the soft x-ray emission spectroscopy (SXES) is that, one does not have to worry so much about the vacuum environment, because the absorption length in the soft x-ray region, which is about several hundreds nm, is much longer than the escape depth of elastic photoelectrons, which is typically of the order of a few nm. This advantage could enable us to perform experiments, for example, on some high *T_c* super-

conductors having very unstable surfaces.

SXES is performed sometimes with resonant mode where the initial valence state of emission is modified by adding an extra electron. Even without the resonant mode, one can decompose the valence band of a compound or an alloy by tuning the photon energy to the core level of a particular atom, which is also an apparent advantage of SXES over the valence band photoemission spectroscopy. Therefore the resonant mode in the SXES is mainly utilized to investigate many-electron effects, which could not be described with a band picture.

The SXES study on LaCuO₄ and CuO has been carried out with the resonant mode under a proposal number of 93-G129. Because the specimens are regarded as “highly correlated system”, the main purpose of the study is to see any change in the hybridization between *d*⁹ and *d*¹⁰ \underline{L} configurations, and the results has shown that the hybridization as well as the emission band width is larger in LaCuO₄ due to the existence of apical oxygen atoms. In the experiment a curved crystal monochromator was used as the second monochromator.

The resonant SAXES and the Auger electron spectroscopy (AES) have been performed on SiO₂ in the Si 1s excitation region under a proposal number of 93-G128. The obtained Si 2p-1s emission spectra is shown in Fig. 7, where change in the emission in-

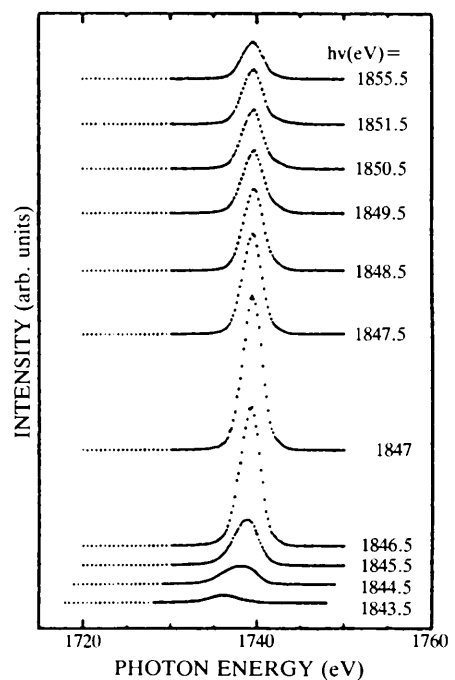


Fig. 7 Si 2p-1s emission spectra of SiO₂

tensity suggests existence of a resonant level within the unoccupied valence band. Figure 8 shows the resonant Auger spectra, where the components, N and N', with constant kinetic energies correspond to the normal Auger process with the excess energy carried by the photoelectron. There are also components, L and L', the energy shift of which is roughly proportional to the change in the incoming photon energy and they are interpreted as the "spectator Auger". This interpretation does not seem unique because a direct Si 1s resonant photoemission of a Si 2p electron accompanied by a shake-up of another 2p electron could also give the similar energy shift. In the latter case the electron excited from Si 1s level "participate" in the subsequent decay processes.

Though radiative decay and Auger decay are

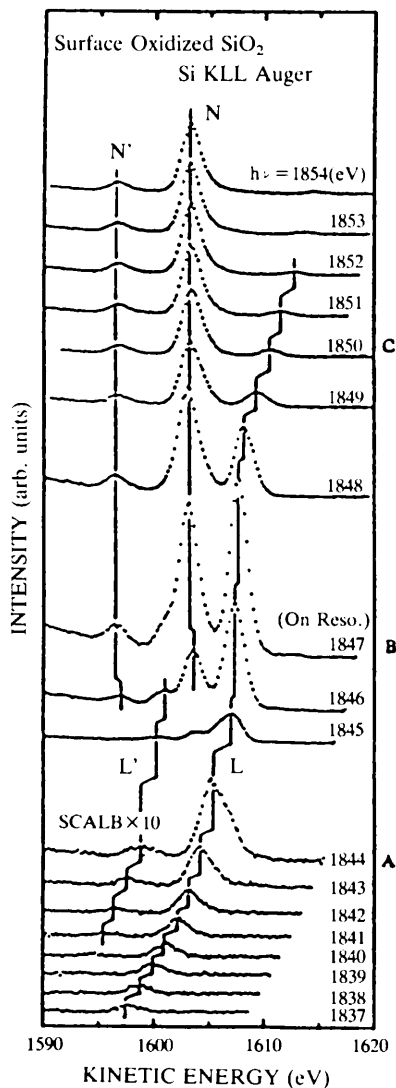


Fig. 8 The resonant Auger spectra of SiO₂

competing decay processes, both of them should be treated with a unified theoretical picture. When such a theory is presented in the future the present controversial interpretation of experimental results by SXES and AES will converge to be more definite, and these measurements will become just a powerful tool to investigate the detailed electronic structures of valence electrons of a material.

References

- 1) S.-Y. Park et al.: J. Phys. Soc. Jpn. **64** (1995) 934.
- 2) M. C. Kida-Tinone, Doctor thesis, Graduate University for Advanced Studies (1994).
- 3) T. Miyahara et al.: J. Phys. Soc. Jpn. **59** (1990) 3660.
- 4) Y. Sakisaka et al.: Pys. Rev. **B36** (1987) 6383.

E. X-RAY SCATTERING SPECTROSCOPY OF MAGNETIC MATERIALS

The topical experimental results concerned with the above subject at the last year are following experiments. One is a separation of the magnetic moment between the spin and orbital contribution on an actinide compound(UTe) by means of magnetic Compton scattering and magnetic Bragg scattering. The other is a success of the magnetic circular X-ray dichroism measurement at Pd L_{3,2}-edges in Fe-Pd alloys. The energies of these absorption edges are located at 3.1-3.4 keV.

1. X-RAY MAGNETIC SCATTERING STUDIES ON UTe

At actinide system (5f-electrons), there are various types of the magnetic ordering as to speak "almost localized" to "almost itinerant" or these mixture. In order to discuss such magnetic character, it is necessary to evaluate the degree of localization of the 5f-electrons, which will be reflected to the orbital magnetic moment. The separation of the magnetic moment between the spin and orbital contributions can be realized by magnetic X-ray scattering experiment by using the polarized synchrotron radiation

such as magnetic Compton scattering and magnetic Bragg scattering. For example, magnetic Compton scattering reflects only spin contribution μ_s , and therefore the orbital contribution μ_L of the magnetic moment can be estimated by a combination of magnetic Compton scattering experiments and the macroscopic total magnetization measurement; $\mu_{\text{total}} = \mu_s + \mu_L$.

The magnetic Compton scattering experiments were carried out at the beamline AR-NE1, whose insertion device is an elliptical multipole wiggler to get elliptically polarized high energy X-rays. The temperature of the sample was set 80 K. Figure 1(a) and (b) show the spectra of magnetic Compton scattered X-rays, $I_+ - I_-$, from Fe and UTe, respectively. Here I_+ and I_- are intensity profiles of the Compton scattered X-rays from the spin up(+) and the spin down(-) states. It must be noticed that the sign of $I_+ - I_-$ is positive for Fe, while negative for UTe. This fact shows directly the spin magnetization μ_s is anti-parallel to the bulk magnetization and also the value of the net spin moment μ_s (UTe) is $-1.57 \mu_B$. Together with the total magnetization; $\mu_{\text{total}} = 1.91 \mu_B$, the value of the orbital magnetization can be estimated as $\mu_L = 3.48 \mu_B$. Furthermore, the curve fitting analysis of the magnetic Compton profile (see Fig. 1(c)) gives the values of spin moment of the 5f component $\mu_s(5f)$ and the conductive s,p,d like electrons $\mu_s(s,p,d)$ as $-1.21 \mu_B$ and $-0.36 \mu_B$, respectively.

In a case of the magnetic Bragg scattering (especially non-resonant magnetic Bragg scattering), it is possible to obtain the separation at the magnetic form factors; $L(k)$, and $S(k)$. This is complementary to the magnetic Compton scattering experiments, because the latter gives us only the total spin magnetic moment: $\mu_s = 2S(0)$. The magnetic Bragg scattering experiments were carried out at the beamline PF-BL3C1 by using a white beam method. The method has been originally developed by Laundy et. al.. The experimental arrangement is schematically shown in Fig. 2(a). The incident beam on the sample is the synchrotron radiation above the orbital plane of the storage ring, because it is necessary to get an elliptically polarized white X-rays in this method. The scattering angle; $2\theta_B$, is fixed at 90 degree to reduce the intensity of the charge scattering and to enhance the magnetic scattering signal. The so called flipping ratio, which is defined as $(I_+ - I_-)/(I_+ + I_-)$, is expressed as $g_P \{L(k)(\cos \alpha + \sin \alpha) + 2S(k)\sin \alpha\} / n(k)$.

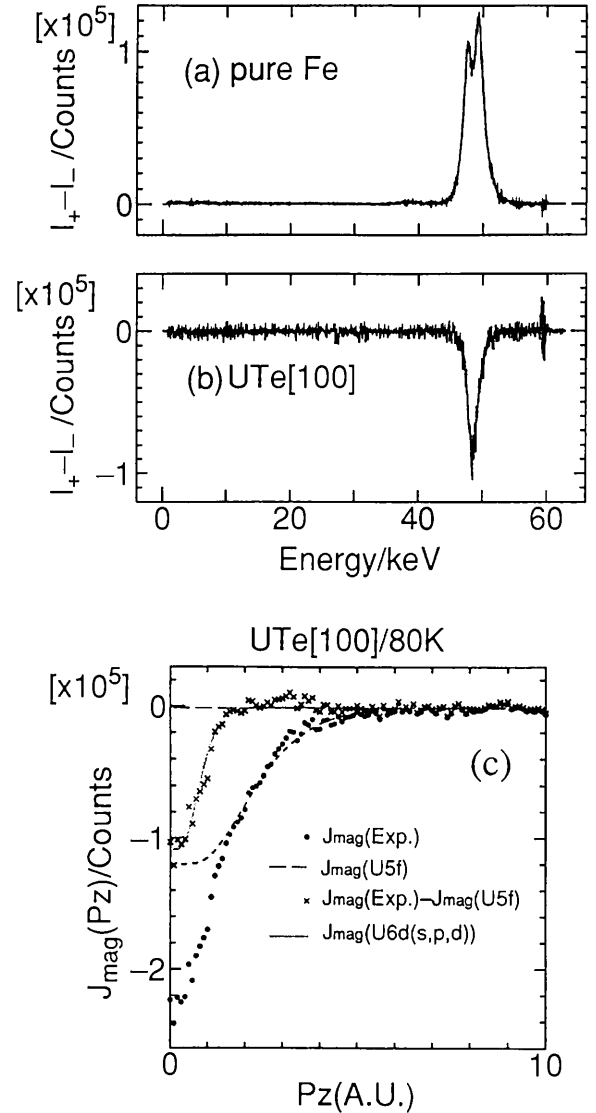


Fig. 1 (a), (b) Spectra of magnetic Compton scattered X-rays, $I_+ - I_-$, from Fe and UTe, respectively. From (b), the net spin moment $\mu_s(\text{UTe})$ can be estimated as $-1.57 \mu_B$. (c) Curve fitting analysis of the magnetic Compton profile on UTe. The values of spin moment of the 5f component $\mu_s(5f)$ and the conductive s,p,d like electrons $\mu_s(s,p,d)$ can be estimated as $-1.21 \mu_B$ and $-0.36 \mu_B$, respectively.

Here, g is the energy factor $g = E/mc^2$, f_P is the polarization factor; $f_P = P_c/(1-P_l)$, where P_c , (P_l) is the degree of the circular, (linear) polarization of the incident X-rays. $n(k)$ is the charge structure factor, and α is the angle of the direction of the flipping magnetic field respect to the direction of the incident X-rays. By choosing suitable values of α , it is possible to get the values of $L(k)$ and $S(k)$, independent-

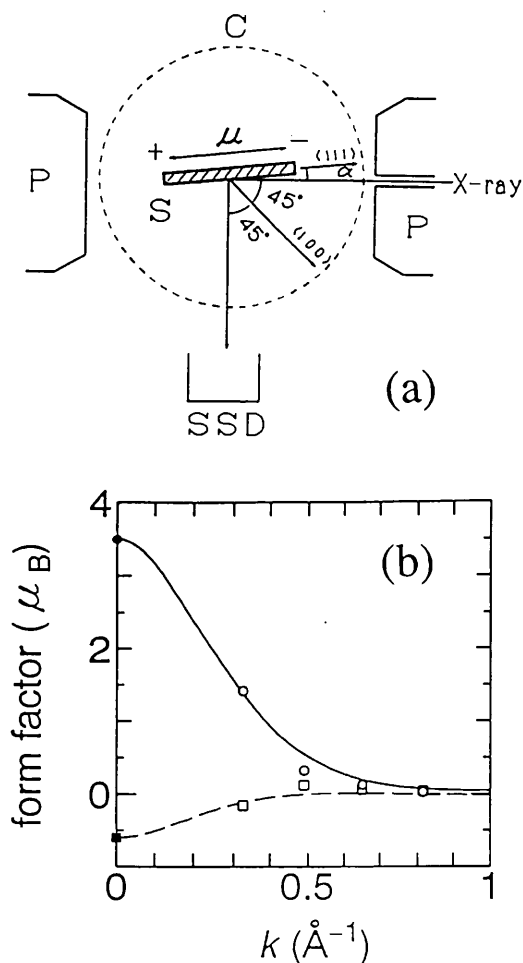


Fig. 2 (a) Schematic view of the experimental arrangement for magnetic Bragg scattering. The letters S, C, P and μ denote specimen, cryostat, pole piece of the magnet, and magnetic direction of the specimen, respectively. (b) Open circles and squares are the obtained form factors of the orbital and the spin magnetic moments in UTe, and the solid (broken) line is the calculated form factors of the orbital (spin) magnetic moment for U^{3+} ion under a dipole approximation, respectively. Full circle and square are the total orbital and spin magnetic moments obtained by the above magnetic Compton scattering experiment.

ly. Figure 2(b) shows the results of the orbital and spin form factors (circles and squares), and also shows the calculated form factors of $L(k)$ and $S(k)$ which are estimated from the dipole approximation from U^{3+} ion. From the figure, the following facts can be found. (1) UTe has the large orbital magnetic moment which is coupled anti-parallel to the spin

moment, and this is consistent to the above results by means of the magnetic Compton scattering. (2) The overall shapes of the $L(k)$ and $S(k)$ are not much different from those of the calculated ones for ionic state, however the experimental $L(k)$ and $S(k)$ show more rapid fall off than the calculated ones. This feature indicates that the orbital and spin magnetic moments of the 5f electrons are spatially spread out in UTe more than those in ionic state. This kind of a systematic X-ray scattering studies from various magnetic materials (actinide compounds etc.) will be progressed in a future.

2. MAGNETIC CIRCULAR X-RAY DICHOISM MEASUREMENT AT Pd $L_{3,2}$ -EDGES IN Fe-Pd ALLOYS

Magnetic circular dichroism (MCD) has attracted much attention as a useful tool for investigation of local magnetic states in ferromagnetic or ferrimagnetic materials. The MCD measurement using hard X-ray (photon energy > 6 keV) and VUV, soft X-rays (0.1-1.5 keV) have been made in various magnetic materials. However, in an intermediate energy region of 1.5-6 keV where the $L_{3,2}$ -edges of 4d transition metal and the $M_{5,4}$ -edge of 5f actinide are located, there is no MCD measurement because of the following problems: One is the attenuation of X-ray intensity by air, and the other is a deterioration of the degree of circular polarization due to the monochromator. Two years before, the beamline PF-BL28B has been constructed for circularly polarized X-rays including the above energy region, and now the beamline is opened for the MCD measurement in an above intermediate energy region without high vacuum system. Here, we describe the MCD measurements at Pd $L_{3,2}$ -edge in Fe-Pd alloys, whose energy range is located at 3.1-3.4 keV.

The measurement were made in fluorescent mode; the intensity of the fluorescent X-ray was measured by fluorescent ion chamber with flowing N_2 gas, while the incident beam intensity was monitored with an ion chamber with N_2 -He mixed gas. In order to minimize the absorption by air, the sample was mounted in an evacuated chamber and several tubes with flowing He gas were substituted for the air. Figure 3 shows the observed MCD spectra at the Pd $L_{3,2}$ -edges in the 67.1 and 40.3 atom % Pd-Fe alloys.

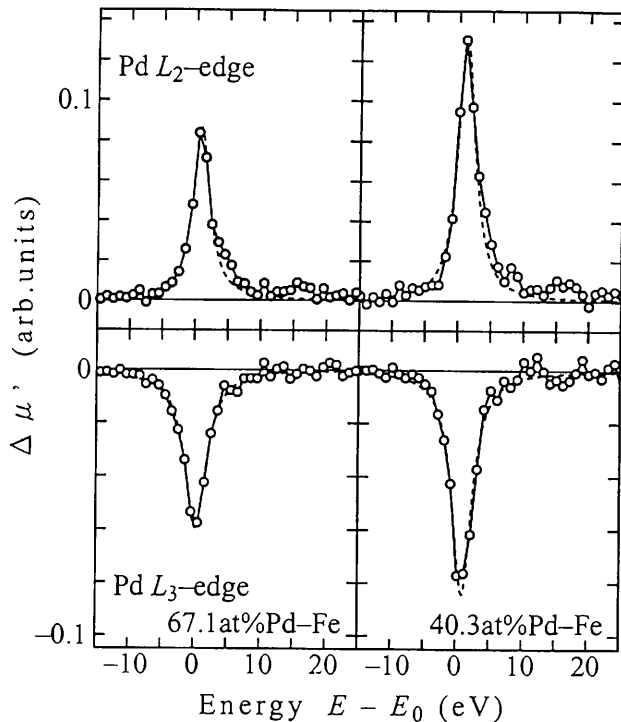


Fig. 3 MCD spectra at the Pd $L_{3,2}$ -edges in the 67.1 and 40.3 atom % Pd-Fe alloys.

The spectrum is negative (positive) at the Pd L_3 -edge (L_2 -edge), and the feature is common to the MCD spectra at the $L_{3,2}$ -edges of Pt in Fe-Pt alloys. The present results directly show the ferromagnetic ordering between the Fe 3d and Pd 4d magnetic moments. By using magneto-optical sum rules under the assumption that the magnetic dipole term can be neglected, the orbital moment is nearly equal to zero and the Pd 4d magnetic moment dominantly arises from spin character.

F. STRUCTURAL PROPERTIES OF CONDENSED MATTERS

1. X-RAY MAGNETIC BRAGG SCATTERING TOPOGRAPHY FROM Fe_3O_4

X-ray Bragg scattering topography gives us information of the crystal defect, strain distribution, domain structure etc. in a crystal. In the case of the domain structure on ferro-electric material, X-ray

topography reveals not only the presence of domain structure, but also the direction of the spontaneous polarization by using departures from Friedel's law which appears with the anomalous scattering. In the case of the domain structure on ferro- or ferri-magnetic materials, the main origin of the contrast in X-ray topography, however, is a strain contrast due to a magnetostriction, and it is impossible to reveal the direction of the spontaneous magnetization, M_s , within the charge scattering X-ray topography.

Recently, X-ray magnetic Bragg scattering measurement techniques have rapidly developed by using synchrotron radiation. Especially, the flipping ratio of the magnetic Bragg scattering intensity can be enhanced by using a resonant effect. Therefore, it is possible to see the direction of the spontaneous magnetization, if we take an X-ray magnetic Bragg scattering topography. Here, we present the first methodological success of X-ray magnetic Bragg scattering topography from an Fe_3O_4 single crystal, and determine the direction of M_s from the topographic image.

The experiment was carried out at the beamline 15B. Figure 1 shows the result of the topographs. Figure 1(a), (b), and (c) are (444), (606), and (800) X-ray topographs which are taken by 6.858 keV X-rays in order to characterize the domain formation in the sample. The energy of the incident X-rays is 253eV lower than the Fe K-absorption edge. Therefore, the main contribution in these topographs can be considered as charge scattering. In Fig. 1(b) and (c), domain boundaries can be seen as vertical white and black lines. On the other hand, there is no vertical line image in Fig. 1(a). The origin of this boundary image is considered as an orientation contrast of 109° domain due to the magnetostriction.

Then, the energy of the incident X-rays was tuned to the Fe K-edge to get a resonant magnetic Bragg scattering topography. The obtained topograph is shown in Fig. 1(d). It is possible to see some vertical stripe images, which corresponds well to the domain itself. This domain contrast is due to the X-ray magnetic Bragg scattering, and the direction of the magnetization in the black stripe image corresponds to a downward direction. Finally, the magnetization direction of each domain can be determined as the solid arrow in Fig. 1(e).

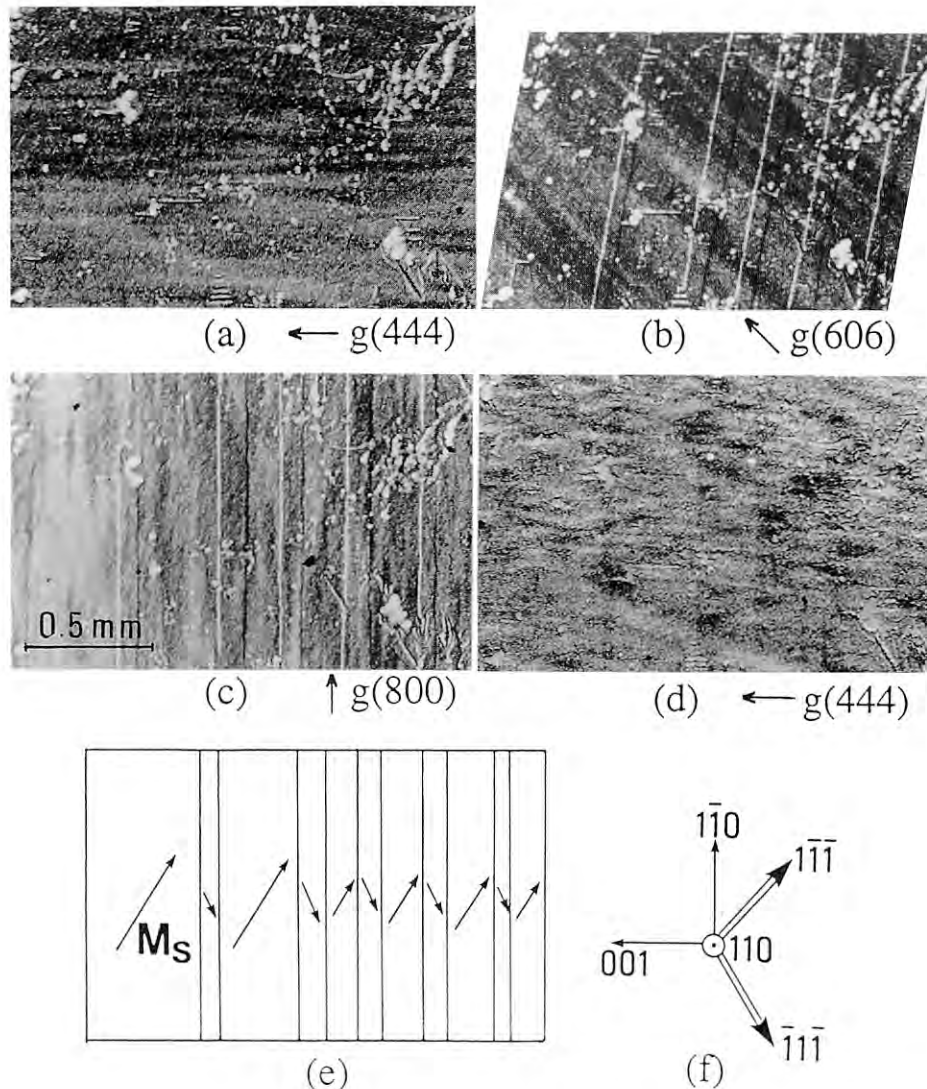


Fig. 1 (a), (b), and (c) are (444), (606), and (800) X-ray topographs which are taken by using 6.858 keV X-rays in order to characterize the domain formation in the sample. (d) (444) resonant magnetic Bragg scattering topograph. (e) Schematic view of the domain formation, and the direction of M_s is determined as solid lines by (d). (f) Directions of the crystal axes in this figure.

Reference

- 1) H. Kawata and K. Mori, Rev. Sci. Instrum. **66** (1995) 1407.

2. MICRO-AREA DIFFRACTION SYSTEM USING POLYCHROMATIC SR

For crystallographic studies of micrometer-sized area of larger specimen, an equipment and software system (micro-area Laue system; MAL) has been developed by making brief modification of the system

for a submicrometer-sized crystal particle using an imaging plate (IP; Fuji Co. LTD.) as a two-dimensional detector with its read out system. This development was carried out at beamline 4B of the Photon Factory. By this method, crystallographic information can be obtained from the exact same area of samples as is probed by optical microscopy, EPMA or micro Raman spectroscopy.

Due to the limited space around beamline 4B, a micro-beam is produced by using a micro-pinhole. Those with diameters of 2.4, 3.5 and $8\mu\text{m}$ full width at the half maximum are now available. The experi-

ment is carried out in vacuum to minimize background level caused by air scattering. The IP detector covers -60 to 165 degrees in two-theta with a cylindrical camera radius of 100 mm.

The software system includes (a) assignment of indices, (b) simulation of Laue pattern, (c) refinement of crystal orientation, (d) calculation of integrated intensities, (e) absorption collection and (f) structure refinement based on intensities of Laue spots.

One of the recent results of an application of MAL to unknown carbonaceous material in a thin section of ureilite (a kind of meteorite) is briefly introduced in below.

On ureilite, it is characteristic that there are carbonaceous materials in boundaries of mineral grains

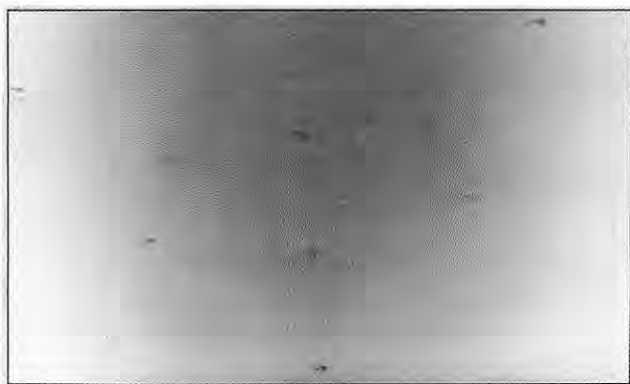


Fig. 2(a) Laue pattern of micrometer-sized diamond in a thin section of ureilite.

as veins. Eight polymorphism of inorganic carbonaceous material have been reported. By an application of micro Raman spectroscopy to the carbonaceous vein, it is suggested that there are some materials related to diamond or lonsdalite. Then MAL was applied to unknown sample with dimension of $2 \times 1 \mu\text{m}$ and Laue pattern (Fig. 2(a)) was obtained for 60 min. exposure with the ring current from 358 to 353 mA (2.5 GeV). By assignment of indices and subsequent simulation of the Laue pattern (Fig. 2(b)), the unknown material is determined to be diamond. An isotropic temperature factor has been refined to be $0.19(3) \text{ \AA}^2$ based on twelve Laue intensities.

Reference

- 1) K. Ohsumi, K. Hagiya, M. Miyamoto, Y. Kojima, M. Ohmasa (in preparatin).

3. Fe^{2+} AND Fe^{3+} IONS DISTRIBUTION IN MAGNETITE, DISTINGUISHABLE BY X-RAY ANOMALOUS SCATTERING

It has been recognized that a chemical shift of XANES spectra occurs among different valence states and is related to anomalous scattering. Using the XANES absorption spectra at the Fe K edge of iron oxides, a chemical shift of about 5 eV was observed between ferrous and ferric ions. The

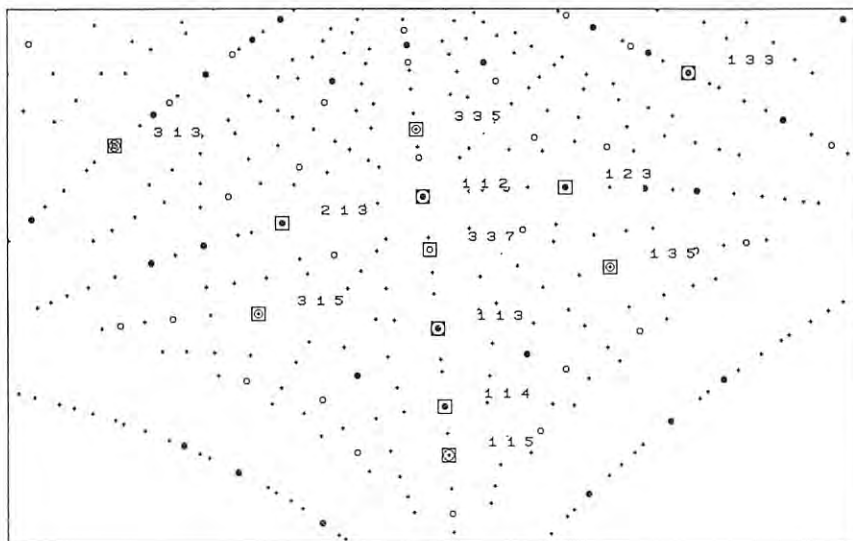


Fig. 2(b) Simulated Laue pattern of diamond in the same orientation as Fig. 2(a).

magnetite (Fe_3O_4) spectrum lies about 2 eV higher than FeO one. Similar to the Kramers-Krönig transformation, the Cromer and Liberman's calculation was applied to estimate experimental f' by substituting the observed cross-section data. The results shows that the maximum difference in experimental f' between ferrous and ferric ions are about 2.5 at the longer wavelength side near the Fe^{2+} edge. Selecting a wavelength to give the different f' values, the technique promises the possibility of distinguishing ions of the same elements in a mixed valence crystal. X-ray intensity data for a single crystal of magnetite were collected using a four-circle diffractometer at BL-10A. The experimental f' values are independent from the refinement procedure and can be estimated in advance. The structure calculation using f' possibly gives a model in an ionic state and extracts well the distribution of valence electrons. The introduction of f' into the difference-Fourier method gives valence-difference contrast for the same atomic species in a mixed valence crystal and therefore a schematic distribution of ions (Fig. 3).

Reference

- 1) S. Sasaki, Rev. Sci. Instrum. **66** (1995) 1573.

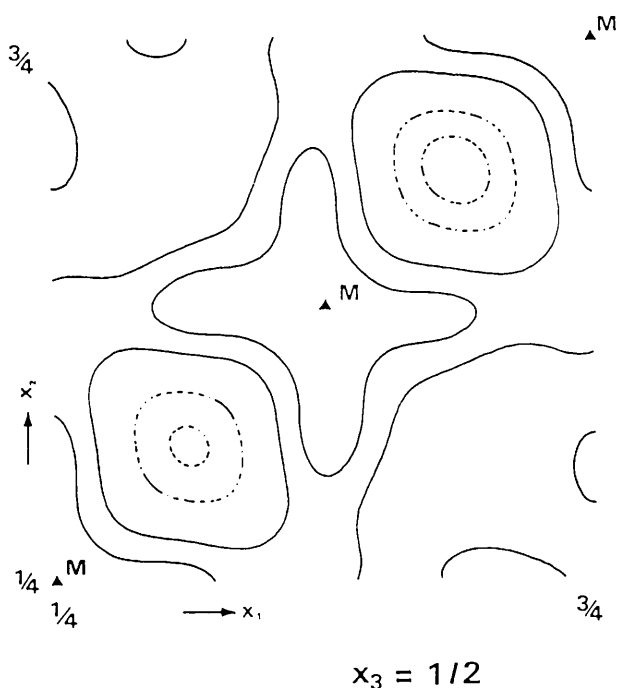


Fig. 3 Valence-contrast map of magnetite at $l = 1.7452 \text{ \AA}$. Fe^{3+} and Fe^{2+} may concentrate in positive and negative (dashed) regions. $\text{Dr} = 0.1 \text{ e \AA}^{-3}$; M= the B site.

4. CRYSTAL STRUCTURE OF ENDOHEDRAL METALLO-FULLERENE $\text{La}@\text{C}_{82}$

Endohedral Metallofullerenes are a very attractive materials in relation to the electronic state of metal and carbon cage. Some experimental results so far suggested that a metal atom position is inside of the carbon cage, but they are not the direct evidence of the endohedral structure. The inside position of the metal atom was elucidated by means of the x-ray diffraction (XRD) at the beam line BL-6B.

In the previous XRD study of $\text{La}@\text{C}_{82}$ with some solvent, the solvent makes the crystal structure analysis so complicated that the precise position of La could not determined. In the present study the solvent-free powder crystals of $\text{La}@\text{C}_{82}$ have been successfully prepared by the sublimation method. An imaging plate was used as a detector. Figure 4 shows the XRD spectrum of $\text{La}@\text{C}_{82}$ at room temperature. All diffraction peaks can be assigned to the major crystals with the f.c.c. lattice and the minor crystals with the hexagonal lattice. The lattice constant was determined as $a = 15.82 \text{ \AA}$ for the f.c.c. crystal, and $a = 11.14 \text{ \AA}$ and $c = 18.40 \text{ \AA}$ for the hexagonal crystal. These values are reasonable as a nearly closed pack of C_{82} molecules. The model calculation, in which the La atom is located inside the carbon cage, could reproduced the experimental spectrum; the R-factor is about 11%.

Reference

- 1) H. Suematsu, Y. Murakami, H. Kawada, Y. Fujii, N. Hamaya, O. Shimomura, K. Kikuchi, Y. Achiba and I. Ikemoto: Mat. Res. Soc. Symp. Proc. **349** (1993) 213.

5. SOLUTION X-RAY SCATTERING STUDY FOR THE STRUCTURE AND FUNCTION OF CALMODULIN-PEPTIDE COMPLEXES

Solution X-ray scattering (SOXS) using synchrotron radiation as an X-ray source has been applied to reveal the structure/function of calmodulin which regulates many cellular processes in a Ca^{2+} -dependent manner. The crystal structure of Ca^{2+} -saturated calmodulin is a dumbbell shape molecule in which N-lobe is connected with C-lobe by a long central linker as shown in Fig.5A. A series of SOXS

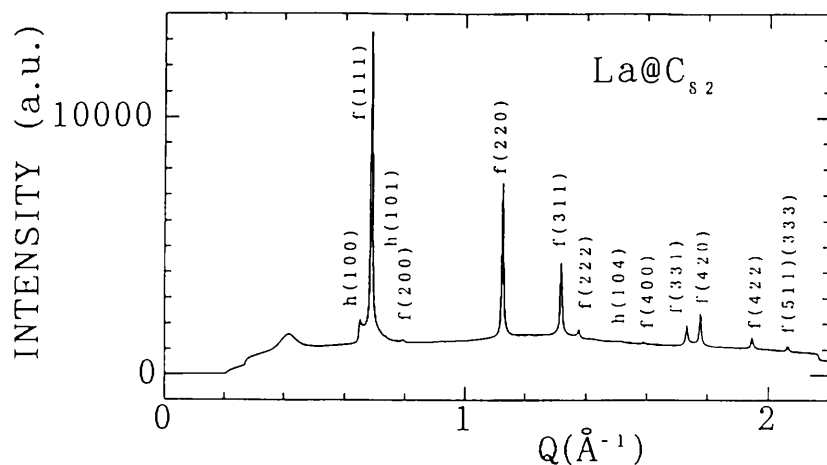


Fig. 4 The powder X-ray diffraction spectrum of La@C₈₂ at room temperature.

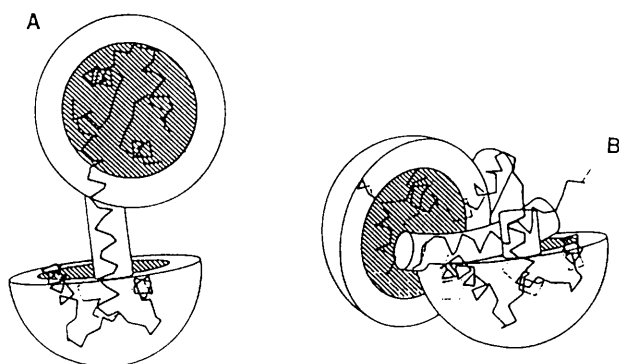


Fig. 5A : Crystal structure of calmodulin.
B : Solution structure of calmodulin bound to a peptide.

data indicate that the solution structure of calmodulin with or without Ca²⁺ is essentially a dumbbell-like structure.

The molecular structure of the complex of Ca²⁺-saturated calmodulin with mastoparan (a calmodulin binding peptide of INLKALAALAKKIL in the sequence), however, is not a dumbbell but a compact structure by a band in central linker region as shown in Fig.5B. Furthermore, the structure of Ca²⁺-saturated calmodulin with other peptides, substance P (a neurotransmitter of RPKPQQFFGLM in the sequence) and gramicidin S (an antimicrobial peptide of cyclo (-Val-Orn-Leu-D-Phe-Pro)₂ in the sequence) has been analyzed. The binding of each peptide brings the structural change of calmodulin from a dumbbell to a compact ovoid structure. Considering the sequence of the peptides, amphiphilic property, but not amphiphilic alpha-helical structure, of the peptides may be critical to stabilize the bending

structure of calmodulin molecule.

A further study with other peptides like myosin light chain kinase, calcineurin, etc., proceeds to reveal the structure and function of calmodulin.

Reference

- 1) R.H. Kretsinger, Science, 258 (1992) 50.

6. POST FCC STRUCTURE OF SOME LANTANIDES UNDER PRESSURE

Trivalent lanthanides are known to show common crystal structure sequence hcp → Sm-type → dhcp → fcc as a function of increasing pressure. This sequence is generally accepted as a result of the increase of electron transfer from s to d bands with pressure. Report of second-order like transition of La and Pr based on the resistivity measurement followed by the observation of a new high pressure structure having distortive character by high pressure X-ray diffraction study. Recent systematic investigation revealed that the distorted structure is the fifth common structure of lanthanides, but the structure has not been determined due to lack of precise intensity data. Recently the structure of this distorted structure was successfully determined for Pr, La and Nd by synchrotron X-ray diffraction measurement. Diffraction experiment was performed at BL-6B with a combination of a diamond anvil cell and an imaging plate. Obtained data was analyzed by Rietveld method. Followed by careful checks of two dimensional profile on the imaging plate, a few potential structures have been examined based on the diffraction profile.

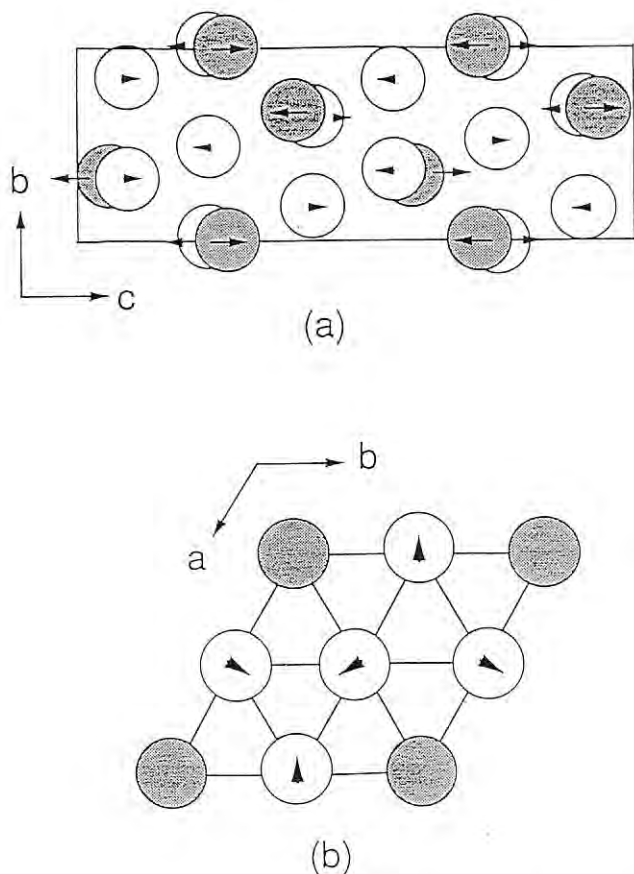


Fig. 6(a),(b) Rhombohedral structure of Pr (R3m). Arrows denote the displacements of atoms from fcc structure.

After several trials, the space group R3m (D_{3d}^5) was found to give the smallest R-factors. In this structure as shown in Fig. 6(a) and (b), Pr atoms occupy two independent atomic positions with three positional parameters: $6c : (0, 0, z_1)$ and $18h : (x, -x, z_2)$ in the hexagonal representation. The distorted fcc structure is obtained when $x = 0.5$ and $z_1 = z_2 = 0.25$. The atomic positional parameters were refined to be $a = 6.4655(4)\text{\AA}$ and $c = 16.085(8)\text{\AA}$, $z_1 = 0.2719(7)$, $x = 0.5080(6)$ and $z_2 = 0.2428(5)$. Global R factors are $R_{wp} = 2.94\%$, $R_p = 2.10\%$ and $R_e = 1.86\%$, and phase-dependent R-factors are $R_1 = 0.62\%$ and $R_F = 0.29\%$ for Pr. The goodness-of-fit indicator $S = R_{wp}/R_e = 1.58$ shows a fairly low value.

The distortion of the lattice can be explained by the amplitude of the static displacement, $\epsilon = x - 1/2$, $\delta_1 = z_1 - 1/4$ and $\delta_2 = z_2 - 1/4$. The continuous character of fcc-rhombohedral transition is clearly seen in Fig. 7 where ϵ , δ_1 and δ_2 are plotted as a function of pressure. It should be noted in Fig. 7 that over the whole stability field if the rhombohedral phase $-\delta_2$ is approximately equal to ϵ and one-third of δ_1 . The relationship $\delta_2 = -\epsilon = -(1/3)\delta_1$ can be derived from the interrelation between the amplitude of atomic displacement given by a linear combination of three TA phonon modes, having an equal amplitude, with wave vectors at the L point of the Brillouin zone of the fcc lattice. This is consistent with the fact that the unit cell volume of the rhom-

Table 1 Selected specifications for the horizontal parallel slits.

	HPS1	HPS2
Angular aperture($^\circ$)	0.032	0.065
Transmission efficiency(%)	67	80
Spacing between the two foils (mm)	0.1	0.2
Number of foils	167	100
Foil material	Stainless steel	
Foil thickness (mm)	0.05	
Foil length (mm)	353	
Effective window size (mm ²)	15(width) \times 25(height)	

Table 2 Comparison of peak maximum intensities and FWHM's in various settings for the slit system.

Slit	Peak maximum intensity (counts s ⁻¹)	FWHM ($^\circ$)
HPS1	14223	0.0319
HPS2	24236	0.0582
RS=0.1mm	1655	0.0385
RS=0.2mm	5199	0.0564
RS=0.5mm	15348	0.1153

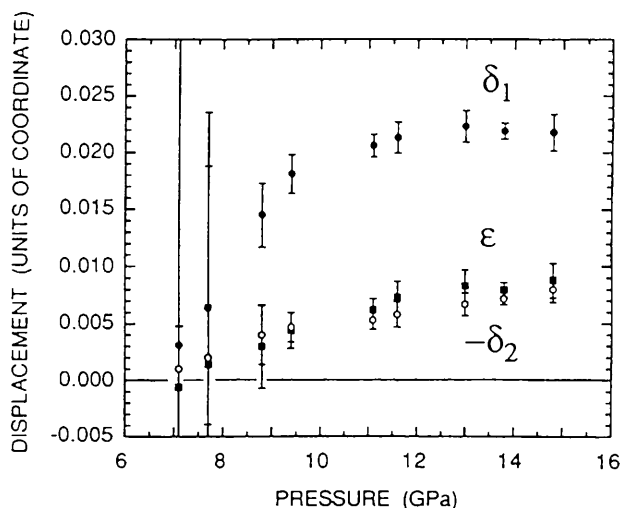


Fig. 7 Pressure dependence of static atomic displacement, ϵ (solid square), δ_1 (solid circle), and $-\delta_2$ (open circle) in rhombohedral structure.

bohedral phase is eight times larger than that of the undistorted fcc phase. These facts imply that the fcc-rhombohedral phase transition is associated with the softening of the TA phonon mode at the L point of the Brilluoin zone. The same pressure dependence for the static atomic displacement are found for La and Nd.

Reference

- 1) N. Hamaya, Y. Sakamoto, H. Fujihisa, Y. Fujii, K. Takemura, T. Kikegawa and O. Shimomura, High-Pressure Science and Technology-1993, ed. S.C. Schmit, J.W. Shaner, G.A. Samara and M. Ross. (AIP Press, New York, 1994), p. 457.

G. PROPERTIES OF SOLID SURFACES AND ADSORBATES

1. XAFS STUDIES FOR ADSORBATE STRUCTURES AND BONDINGS

XAFS (X-ray Absorption Fine Structure) spectroscopy is an ideal technique for characterizing structural and electronic properties of surface adsorbates. A local structure around an X-ray absorbing atom can be derived from EXAFS oscillations, which

includes interatomic distances in the adsorbed molecules as well as adsorption sites of the single crystal surfaces. NEXAFS arises from electronic transitions from a core to unoccupied molecular orbitals, which gives us information on electronic properties and adsorption behavior such as charge transfer, molecular dissociation and orientation.

At the Photon Factory, many adsorption systems of sulfur-containing molecules on nickel or copper single crystal surfaces have been investigated in these 5 years¹⁻⁵). Among them, the initial adsorption behavior of sulfur dioxide molecules on Ni(100) surface is described here as a typical example of the recent results.

Adsorption of SO₂ on metal surfaces has recently become an attractive subject, because it is a principal air pollutant. Since the molecule plays a stronger π acceptor role than CO, the structures and electronic properties in the initial adsorption of SO₂ are quite interesting. Orientation of the molecules in the submonolayer state should depend on whether the molecule acts as a π acceptor or a σ donor. All the previous studies have concluded that the molecular plane of adsorbed SO₂ is perpendicular to the metal surface, implying that the σ donor nature dominates the adsorption geometries. In contrast to the previous results, sulfur K-edge NEXAFS and EXAFS results (see Fig. 1) obtained at BL-11B⁶) and oxygen K-edge NEXAFS spectra together with UPS data taken at BL-7A⁷) for the SO₂/Ni(100) system indicate that the SO₂ molecule adsorbs on Ni(100) surface through the charge transfer from the nickel metal to the π^* molecular orbitals with its molecular plane parallel to the surface. Similar adsorption geometries are also found on Ni(111)⁶) and Ni(110)⁸) surfaces but a quite different structure has been estimated on Cu(100) where oxygen atoms are directly bonded to the copper substrate instead of sulfur with the O-S bond inclined by 60° from the surface normal. Details of all the experimental results are described in the Users' Reports section of this book.

This dissimilarity might be derived from different energy levels of the metal d bands: Ni 3d orbitals lie at the Fermi level, leading to the strong interaction with SO₂ π^* orbitals, while the deeper 3d bands of Cu could have much less interaction.

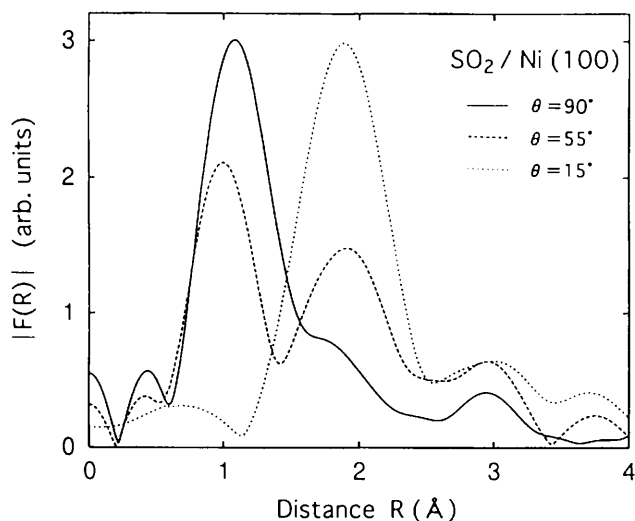


Fig. 1 Fourier transforms of the sulfur K-edge EXAFS oscillation functions for submonolayer adsorption system $\text{SO}_2/\text{Ni}(100)$ taken at X-ray incidence angles of $\theta = 90^\circ$ (normal incidence), 55° and 15° . There appear two peaks at 1.1 Å and 1.9 Å, which can be ascribed to S-O and S-Ni bonds, respectively, and the interatomic distances are determined as 1.51 ± 0.03 Å and 2.18 ± 0.03 Å. From the polarization dependence of the two features, it is concluded that the S-O bond is lying flat on the surface and S atom locates at the bridge site of the Ni(100) surface.

References

- 1) Y. Takata, T. Yokoyama, S. Yagi, N. Happo, H. Sato, K. Seki, T. Ohta, Y. Kitajima and H. Kuroda, *Surf. Sci.* **259** (1991) 266.
- 2) Y. Takata, Y. Kitajima, H. Aga, S. Yagi, T. Asahi, T. Yokoyama, K. Tanaka and T. Ohta, *Jpn. J. Appl. Phys. Suppl.* **32-2** (1993) 350.
- 3) S. Yagi, Y. Takata, Y. Kitajima, T. Asahi, H. Aga, T. Yokoyama and T. Ohta, *Jpn. J. Appl. Phys. Suppl.* **32-2** (1993) 353.
- 4) S. Yagi, T. Yokoyama, Y. Kitajima, Y. Takata, T. Kanazawa, A. Imanishi and T. Ohta, *Surf. Sci.* **311** (1994) 172.
- 5) S. Yagi, S. Takenaka, T. Yokoyama, Y. Kitajima, A. Imanishi and T. Ohta, *Surf. Sci.* **325** (1995) 68.
- 6) T. Yokoyama, S. Terada, S. Yagi, A. Imanishi, S. Takenaka, Y. Kitajima and T. Ohta, *Surf. Sci.* **324** (1995) 25.
- 7) T. Yokoyama, A. Imanishi, S. Terada, H. Namba, Y. Kitajima and T. Ohta, *Surf. Sci.* **334** (1995) 88.

- 8) S. Terada, A. Imanishi, T. Yokoyama, S. Takenaka, Y. Kitajima and T. Ohta, *Surf. Sci.* **336** (1995) 55.

2. ABSOLUTE X-RAY REFLECTIVITY MEASUREMENT FROM THE $\text{Si}(111)\sqrt{3} \times \sqrt{3}$ -Bi SURFACES

The recent advance of synchrotron radiation has enabled surface X-ray diffraction (SXD) method to investigate crystal surface structure. A lot of information on surface structures has been obtained by measuring diffraction intensity along reciprocal lattice rods. One of the results of SXD measurements made at PF is structure determination of the $\text{Si}(111)\sqrt{3} \times \sqrt{3}$ -Bi surface. The conclusion based on the kinematical data analysis is that the $\text{Si}(111)\sqrt{3} \times \sqrt{3}$ -Bi system forms the so-called milk-stool structure in which the Bi coverage is 1 ML and each adsorbed Bi atom is located nearly right above the Si atom in the first layer of the crystal substrate.^{1,2)} Thus SXD has become an effective method for surface structure analysis.

The present theme on SXD is how to get more refined information on matters such as coverage of adsorbed atoms, surface roughness, thermal vibration, etc. The absolute reflectivity measurement is a powerful tool for this requirement because the data analysis is made in unique intensity scale and the result contains less uncertainty than that of the conventional data analysis.

From the viewpoint of the absolute reflectivity, the measurement of the $\text{Si}(111)\sqrt{3} \times \sqrt{3}$ -Bi surface was retried at BL-10C recently since a controversy occurred on this system: a simple structure with the 1/3-ML Bi coverage was obtained by low-energy electron diffraction (LEED)^{3,4)} and scanning tunneling microscope (STM)⁵⁾ and a honeycomb structure with the 2/3-ML Bi coverage was obtained by X-ray standing wave and STM.⁶⁾ The absolute reflectivity measurement can definitely distinguish these structures because the reflectivity drastically changes according to the coverage of Bi atoms. Fig. 2 shows the reflectivities from the $\text{Si}(111)\sqrt{3} \times \sqrt{3}$ -Bi surfaces in different phases that were measured along 00 reciprocal lattice rod. Fitting curves in the figure are calculated on the basis of the dynamical theory developed for SXD.^{7,8)} The fitting result is that the high-reflectivity phase corresponds to the milk-stool

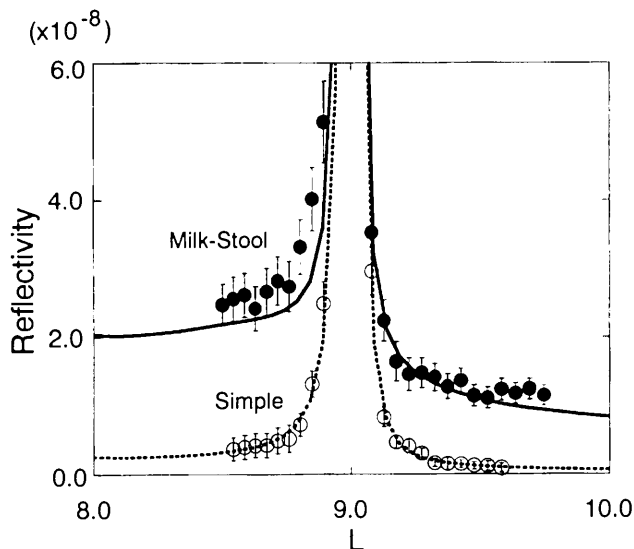


Fig. 2 X-ray reflectivities from the Si(111) $\sqrt{3}\times\sqrt{3}$ -Bi surfaces measured along 00 reciprocal lattice rod and fitting curves. The fitting results show that the high-reflectivity phase corresponds to the milk-stool structure with coverage of 1 and the low-reflectivity phase corresponds to the simple structure with coverage of 1/3.

structure and the low-reflectivity phase corresponds to the simple structure. This result clearly rejects the honeycomb structure model. The good agreement between experiment and theory indicates the efficiency of this method for SXD data analysis.

References

- 1) T. Takahashi, K. Izumi, T. Ishikawa and S. Kikuta, *Surf. Sci.* **183** (1987) L302.
- 2) T. Takahashi, S. Nakatani, T. Ishikawa and S. Kikuta, *Surf. Sci.* **191** (1987) L825.
- 3) K.J. Wan, T. Guo, W.K. Ford and J.C. Hermanson, *Phys. Rev. B* **44** (1991) 3471.
- 4) K.J. Wan, T. Guo, W.K. Ford and J.C. Hermanson, *Surf. Sci.* **261** (1992) 69.
- 5) R. Shioda, A. Kawazu, A.A. Baski, C.F. Quate and J. Nogami, *Phys. Rev. B* **48** (1993) 4895.
- 6) J.C. Woicik, G.E. Franklin, C. Liu, R.E. Martinez, I.S. Hwang, M.J. Bedzyk, J.R. Patel and J.A. Golovchenko, *Phys. Rev. B* **50** (1994) 12246.
- 7) S. Nakatani and T. Takahashi, *Surf. Sci.* **311** (1994) 433.
- 8) T. Takahashi and S. Nakatani, *Surf. Sci.* **326** (1995) 347.

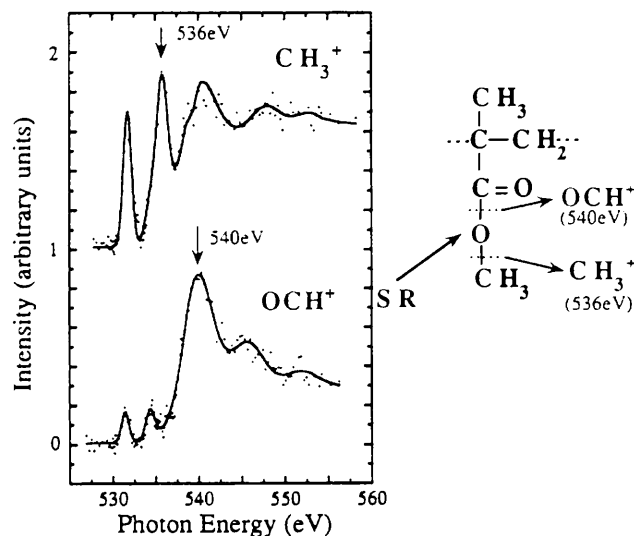


Fig. 3 Photon stimulated ion desorption yield spectra of CH_3^+ and OCH^+ ions in the near oxygen K-edge region from PMMA. The yields of CH_3^+ and OCH^+ increase at 536 eV and 540 eV, respectively. This indicates that O-CH₃ and C-O-CH₃ bond breakings are favored at 536 eV and 540 eV due to the O 1s $\rightarrow \sigma^*$ (O-CH₃) and the O 1s $\rightarrow \sigma^*$ (C-O-CH₃) transitions, respectively.

3. SITE SPECIFIC FRAGMENTATION OF POLYMER THIN FILMS

The excitation energy dependence of the photon stimulated ion desorption from thin films of polymethylmethacrylate (PMMA) has been measured in the 250-600 eV range to investigate the primary steps in radiation induced fragmentation reactions using monochromatic pulsed-synchrotron radiation at BL-13C. Site specific reactions were observed for the first time at the surface of polymer films.¹⁾ These site specific reactions were detected by the characteristic differences in the partial ion yield spectra of PMMA. The most intense ions produced from PMMA correspond to CH_3^+ and H^+ ions. The CH^+ , CH_2^+ , OCH^+ and COOCH_3^+ ions are also observed in considerable intensities. Using soft X-rays, ion desorption mechanism of PMMA was shown to be directly related to the scission of bonding after the excitation of 1s core electrons at specific atomic sites to unoccupied orbitals localized at the bonding responsible for the ion generation. For example, as shown in Fig. 3, the efficient production of CH_3^+ and OCH^+ ions observed at 536 eV and 540 eV can

be explained by excitations of the methoxy O 1s electron to unoccupied σ^* (O-CH₃) and σ^* (C-OCH₃) orbitals that favor the breaking of the methoxy group O-CH₃ bonding and the carbonyl-methoxy C-OCH₃ bonding, respectively.

Using monochromatic synchrotron radiation, we can selectively promote the core electron excitation of specific atoms in molecule. These site selective excitations can be used to control the fragmentation of molecules.

References

- 1) M.C.K. Tinone, K. Tanaka, J. Maruyama, N. Ueno, M. Imamura and N. Matsubayashi, *J. Chem. Phys.* **100** (1994) 5988.



Fig.1 Schematic drawing of ARP. (From K. Fukuyama of Osaka University)

H. STRUCTURES AND FUNCTIONS OF PROTEINS

A number of crystal structures of biological macromolecules have been determined on the basis of diffraction data obtained with Weissenberg cameras for macromolecular crystal¹⁾ at the Photon Factory. Most of them have been reported in authoritative journals. They are widely diverse in function, such as oxidoreductases, transferases, hydroxylases, lyases, DNA-binding proteins, cytokines, storage proteins, toxins, inhibitors and viruses. We will review some of them in the present article.

1. FUNGAL PEROXIDASE

The crystal structure of fungal peroxidase (H₂O₂ Oxidoreductase) from *Arthromyces ramosus* (ARP) has been determined at 1.9 Å resolution by Kunishima *et al.*²⁾ Tertiary structure of the enzyme is schematically shown by a ribbon drawing in Fig.1. The overall tertiary structure of ARP is similar to that of yeast cytochrome *c* peroxidase (CCP) and that of lignin peroxidase (LiP). Relative to CCP, ARP and LiP each have an extension of approximately 40 residues at the carboxy terminus. The orientation of the imidazole ring of the distal histidine at 56 relative to the heme group in ARP differs significantly from that of in LiP. The structure of access channel to the

distal side of the heme of ARP is markedly different from that of LiP. This may effect in the differences in substrate specificity between ARP and LiP.

2. HYDOXYLASE

The crystal structure of hydroxylase protein of methane monooxygenase (MMO) system from *Methylococcus capsulatus* determined at 2.2Å resolution by Rosenzweig *et al.*³⁾ provided a novel protein structure and revealed the geometry of the catalytic di-iron core as in Fig.2. The two iron atoms are bridged by exogenous hydroxide and acetate ligands and further coordinated by four glutamate residues, two histidine residues and water molecules. This structure is different from the well-known di-nuclear iron center of [2Fe-2S]. The di-nuclear iron center of MMO hydroxylase lies in a hydrophobic active-site cavity for binding methane.

3. L-LACTATE DEHYDROGENASE

Two conformational states of *l*-lactate dehydrogenase within the same crystal provided an explanation for the molecular mechanism of enzyme

eight-stranded β -barrel and may form a Schiff base intermediate with a N-acetylneuraminic acid molecule.

Three-dimensional structures of two plant β -glucan endohydrolases with distinct substrate specificities have been determined by Varghese *et al.*⁸⁾. One of them, (1 \rightarrow 3)- β -glucanase, can hydrolyze (1 \rightarrow 3)- and (1 \rightarrow 3, 1 \rightarrow 6)- β glucan of fungal cell wall and may therefore contribute to plant defense strategies, while the other, (1 \rightarrow 3, 1 \rightarrow 3)- β -glucanase, functions in plant cell wall hydrolysis during mobilization of the endosperm in germinating grain or during the growth of vegetative tissues. Both enzymes are α/β -barrel structures and their backbones are structurally very similar. The catalytic amino acid residues are located within deep grooves which bind substrates. Amino acid substitutions within the groove may result in wide divergence of function.

6. β -GALACTOSIDASE

β -galactosidase, the most commonly used in molecular biology, folds into five sequential domains, with an extended segment at the amino terminus. Three-dimensional structure of β -galactosidase from *E. coli* determined at 3.5Å resolution by Jacobson *et al.*⁹⁾ is a tetramer with 222-point symmetry. This enzyme hydrolyzes β (1-4) linkages of β -galactosides. The tetramer structure of this enzyme is shown in Fig.5. The β -galactosidase monomer folds into five sequential domains, with an extended segment at the

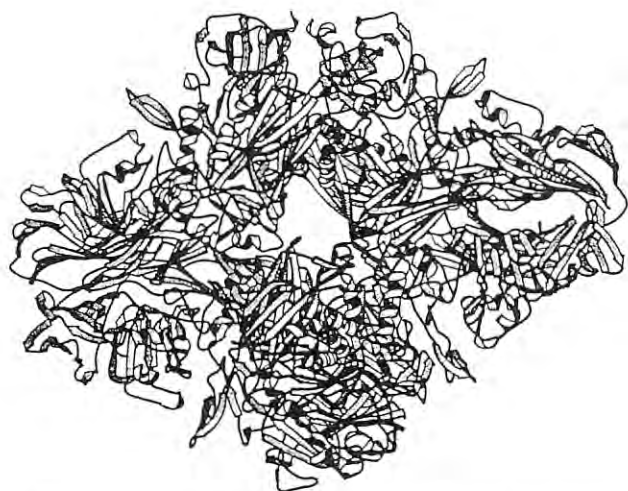


Fig. 5 Ribbon drawing of β -galactosidase tetramer with 222 symmetry. (From Jacobson *et al.*⁹⁾)

amino terminus. The first domain corresponds to a jelly-roll β -barrel as is often found in virus coat proteins. The second domain has a fold similar to immunoglobulin constant domains. The third domain forms a α/β -barrel and contains the catalytic site. The fourth domain is identical to the second domain in folding topology. The fifth domain has a novel 18-stranded, antiparallel sandwich.

7. PERTUSSIS TOXIN-SUGAR COMPLEX

Pertussis toxin-sugar complex provides a model for receptor binding. The crystal structures of pertussis toxin (PT) and PT-oligosaccharide complex have been determined both at 3.5Å resolution by Stein *et al.*¹⁰⁾ and by Stein *et al.*¹¹⁾, respectively. PT is a virulence factor of *Bordetella pertussis*, the etiological agent of whooping cough. The catalytically active (A) domain of the toxin comprises subunit S1, and the binding (B) domain, which recognizes receptors on the surface of eukaryotic cell, comprises five subunits, S2, S3, two copies of S4 and S5. The structure of PT-sugar complex is shown by the ribbon representation in Fig.6. The enzymatic A-subunit (S1) at the top of the molecule is pyramid-shaped, and the cell-recognizing B domain forms a disk-like base with approximate five-fold symmetry. The carboxy-terminal \sim 100 residues of S2 and S3, both copies of S4, and S5 have similar folds, consist of six antiparallel β -strands forming a closed β -barrel, capped by an α -helix between the fourth and fifth strands. Car-

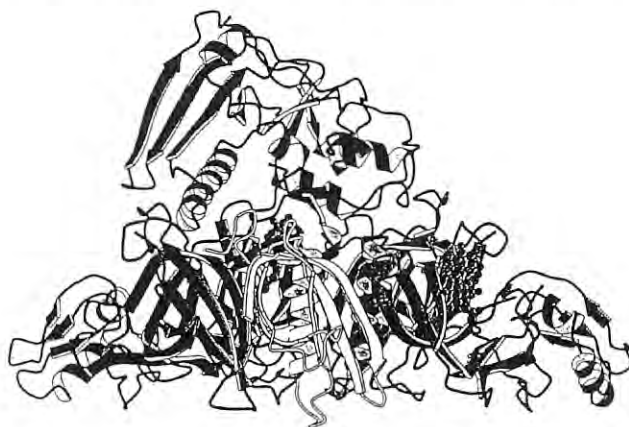


Fig. 6 Schematic drawing of the PT-sugar complex. Polypeptide chains and sugars are shown by ribbons and balls, respectively. (Reprinted from Stein *et al.*¹¹⁾. Copyright permission of the Nature.)

bohydrate was bound at equivalent sites on S2 and S3. The PT-sugar complex has provided a model for the interaction of the toxin with a cell surface receptor. Identification of amino acid residues involved in the receptor binding will provide the design of genetically inactivated toxins for use in new acellular whooping cough vaccines.

8. A VIRAL PROTEASE

A viral protease has a fold similar to chymotrypsin. The crystal structure of picornaviral 3C cysteine protease has been determined at 2.3Å resolution by Allaire *et al.*¹²⁾. Picornaviral proteins are expressed by direct translation of genomic RNA to a single, large protein precursor. The viral polyproteins is processed into the mature proteins by the 3C enzyme. The overall structure stereoscopically shown in Fig.7 suggests that an inter-molecular cleavage releases the 3C enzyme and that there is an active proteinase in the polyprotein.

9. STRUCTURE ANALYSES OF CRYSTALS WITH VERY LARGE ASYMMETRIC UNIT

Three of the protein crystals described in this review have very large asymmetric units. MMO hydroxylase crystal belonging to $P2_12_12_1$ with unit cell dimensions $a=62.6\text{\AA}$, $b=110.1\text{\AA}$, $c=333.5\text{\AA}$, has an $\alpha 2 \beta 2 \gamma 2$ dimer structure with Mw of 251K in an

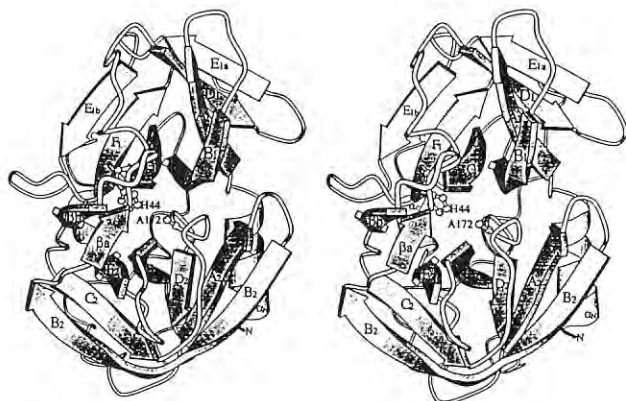


Fig. 7 Stereoscopic ribbon drawing of the picornaviral 3C proteinase structure. (Reprinted from Allaire *et al.*¹²⁾. Copyright permission of the Nature.)

asymmetric unit, therefore V_m is 2.3. The crystal structure analysis of MMO hydroxylase was initiated by the multiple isomorphous replacement (MIR) method, and MIR phases were improved and extended by solvent flattening and non-crystallographic two-fold averaging.

The crystal of *E. coli* β -galactosidase with four tetramer (each of Mw465K) per asymmetric unit belongs to $P2_1$ with cell dimensions $a=107.9\text{\AA}$, $b=207.5\text{\AA}$, $c=509.5\text{\AA}$ and $\beta=94.7$, and with $V_m=3.1$. Initial MIR phases, which were of poor quality, were refined and extended by iterative cycles of non-crystallographic 16-fold averaging¹¹⁾.

PT with a total MW of 105K was crystallized in space group $P2_12_12_1$ with unit cell dimensions $a=163.8\text{\AA}$, $b=98.2\text{\AA}$, and $c=194.5\text{\AA}$. The asymmetric unit contains two molecules related by non-crystallographic two-fold axis. V_m of the crystal is as high as 3.7. The crystal structure was solved by MIR method, followed by phase improvement using solvent flattening and two-fold averaging. Final phases were obtained at 2.9Å resolution.

The crystal structure of tobacco necrosis virus (TNV) consisting of 180 copies of protein subunits and an RNA has been determined at 5Å resolution by Bando *et al.*¹³⁾. Initial phases were determined at 8Å resolution by molecular replacement with an icosahedral asymmetric unit of southern bean mosaic virus with $T=3$ symmetry, and they were improved and extended by non-crystallographic five-fold averaging. Secondary structures were clearly assigned in the 5Å resolution map. Amino acid residues which form specific hydrogen bonds with nucleic acid bases tend to lie inside the virus to recognize the RNA.

Intensity data accurately collected with synchrotron radiation effected in success in initial phasing by MIR method and in phase improvement and extension by non-crystallographic symmetry averaging.

(T. Tsukihara, Tokushima Univ.)

References

- 1) N. Sakabe, *J. Appl. Cryst.* **16** (1983) 542.
- 2) N. Kunishima, K. Fukuyama, H. Matsubara, H. Hatanaka, Y. Shibano and T. Amachi, *J. Mol. Biol.* **235** (1994) 331.
- 3) A.C. Rosenweig, C.A. Frederick, S.J. Lippard and P. Nordlung, *Nature* **366** (1993) 537.
- 4) S. Iwata, K. Kamata, S. Yoshida, T. Minowa

- and T. Ohta, *Nature, Structural Biology* **1** (1994) 176.
- 5) T. Senda, T. Shimizu, S. Matsuda, G. Kawano, H. Shimizu, K.T. Nakamura and Y. Mitsui, *EMBO J.* **11** (1992) 3193.
 - 6) Y. Mitsui, T. Senda, T. Shimizu, S. Matsuda and J. Utsumi, *Pharmacology and Therapeutics.* **58** (1993) 93.
 - 7) T. Izard, M.C. Lawrence, R.L. Malby, G.G. Lilley and P.M. Colman, *Structure* **2** (1994) 361.
 - 8) J.H. Varghese, T.P.J. Garrett, P.M. Colman, L. Chen, P.B. Hoj and G.B. Fincher, *Proc. Natl. Acad. Sci. USA* **91** (1994) 2785.
 - 9) R.H. Jacobson, X-J. Zhang, R.F. DuBose and B.W. Matthews, *Nature* **369** (1994)761.
 - 10) P.E. Stein, A. Boodhoo, G.D. Armstrong, S.T. Cockle, M.H. Klein and R.J. Read, *Structure* **2** (1994) 45.
 - 11) P.E. Stein, A. Boodhoo, G.D. Armstrong, L.D. Heerze, S.T. Cockle, M.H. Klein and R.J. Read, *Nature, Structural Biology* **1** (1994) 591.
 - 12) M. Allaire, M.M. Chernaia, B.A. Malcolm, and M.N.G. James, *Nature* **369** (1994) 72.
 - 13) M. Bando, Y. Morimoto, T. Sato, T. Tsukhara, Y. Yokota, K. Fukuyama and H. Matsubara, *Acta Cryst.* **D50** (1994) 878.

I. RADIOBIOLOGY USING SYNCHROTRON RADIATION

1. INTRODUCTION

1.1 Radiobiological processes

Radiobiological effects are induced with energy deposited by radiation. The total amount of energy required to show lethality on humans is as low as that which can raise the body temperature by only one thousandth in degrees centigrade. A variety of processes are included in exhibiting radiobiological effects, some of which are familiar to physicists, some to chemists and others to biologists. In this sense, radiobiology can be said to be interdisciplinary. Today, radiobiology is attracting much attention, not only due to basic scientific interest, but also due to the practical points of view, such as the

radiotherapy of cancer using heavy particles, or protection from environmental radiation of low dose rates.

Most of the energy of the radiation is transferred to the molecules via secondary electrons, and each energy deposition events are discrete. Amount of energy deposited with each event has a very wide distribution, having an average of 30 or 40 eV. One may realize that the essence of radiobiological action lies in the discrete energy deposition event and spatial distribution of these events. To quantitatively represent this energy deposition density, the "linear energy transfer" (LET) is defined as the amount of energy deposited per unit length of a track of charged particles, such as secondary electrons. Heavy particles exhibit high LET, while Compton electrons generated by high-energy photons show a low LET. The irradiation of very low-dose radiation over the course of many years from environmental radionuclides is an extreme case from the viewpoint of energy deposition. In both cases, the distribution of energy deposition affects the biological consequences. In order to predict these effects logically, we need to completely understand what the consequences from each energy deposition events are, and how the difference in the distribution of the events affects the final results.

1.2 Usefulness of synchrotron radiation in radiobiology research, especially in the study of the initial processes

In order to answer the above questions experimentally, we need to be able to deposit any amount of energy that we desire into biological samples. One way would be to irradiate low-energy monochromatic photons. Since vacuum ultraviolet photons of about 40 nm wavelength would give an energy quantum of about 30eV around an absorption site, we could study the processes and their efficiencies in producing molecular changes induced with this energy. We can control the amount of energy deposited to molecules. In more energetic regions, monochromatic soft X-rays are absorbed photoelectrically, mainly by K-shell electrons of the oxygen in water molecules contained in living cells, and produce a shower of almost monoenergetic electrons in the cells. By changing the photon energy, we can change the energy of electrons, since the energy of

the photoelectrons is equal to the energy of the photon minus the binding energy of the K-shell electrons of oxygen. Electrons exhibit different LET depending upon their energy. This means that we can study the LET dependence of biological efficiency, in other words, dependence on the spatial distribution of the energy deposition event. From this point of view, we require a tunable light source which is sufficiently strong even after monochromatized. Synchrotron radiation is the only strong light source having a continuous spectrum from infrared to X-rays.

1.3 Inner-shell photoabsorption and the Auger effect

When an inner-shell electron absorbs an X-ray photon and is ionized or excited (inner-shell ionization/excitation), an electron in the next inner shell falls into the lower inner shell to fill the hole. The energy released from this transition causes the ejection of another electron (Auger electron) in the next inner shell, leaving two holes in the shell (Auger process). Other Auger processes can occur successively to fill the two holes until the outermost shell is reached, and finally several electrons are emitted from the atom and the atom itself becomes multiply ionized. This Auger cascade is considered to produce highly localized energy deposition events around the photoabsorption site, and also considered as an extreme case of high LET radiation. Production of serious molecular changes around the Auger site is now expected as a powerful tool for radiation therapy of cancer. The biological effects of an Auger cascade have been studied with radionuclides which decay through the electron-capture process. Monochromatized synchrotron radiation enabled us to study the effect of inner-shell photoabsorption, followed by the Auger process, at any atom we desire, which includes phosphorus in deoxyribonucleic acid (DNA) and halogen atoms artificially incorporated into DNA. Furthermore, it is known that the photoelectric absorption cross section strongly depends upon both the energy and the absorbing element. The most drastic changes can be observed across the absorption edge of the K-shell of elements. A difference of several eV in the photon energy causes about a one-order difference in the absorption cross section. This means that we can select the photon-absorbing element by choosing the irradiation photon energy, which may lead to the

damage production around the photoabsorption site.

2. SOME OF THE RESULTS OBTAINED RECENTLY

2.1 Amount of energy to produce double strand breaks in DNA

DNA is a long molecule composed of two complementary chain of polynucleotide and the most important molecule in the cell since the genetic information of the living cell is coded on a moiety (base) in the constituting unit (nucleotide). Molecular changes or damages in the DNA are known to cause cell death or induction of genetic changes. When irradiated with ionizing radiation, cell death is considered to be caused by the strand breaks of DNA. There are two types of strand breaks, namely, single strand break (SSB) and double strand break (DSB). SSB is scarcely lethal, since almost all of them are repaired by the enzymatic reaction in the cell (repair activity). Amount of energy required to produce DSB is the most fundamental parameter in the radiobiological processes, since it might give some clues to the mechanism of DSB production, and presumably of the cell death.

Using a plasmid DNA as a specimen, a group lead by Prof. Hieda (Rikkyo Univ) has been investigating the energy dependence of the production yields of SSB and of DSB¹⁾. They irradiated the plasmid samples in dry state in the energy region between 60 and 550 eV at BL-12C. Plasmid having SSB and DSB can easily be analyzed quantitatively by gel electrophoresis technique. Results are shown in Fig. 1, along with the accumulated data obtained at BL-27A²⁾ and elsewhere³⁾. Absorption spectrum of DNA estimated with spectroscopic data is also shown for comparison. Action spectra for the production of SSB and DSB look very similar to the absorption spectrum of DNA in the energy region below 60 eV, although the cross sections for DSB are less than one-hundredth of those for SSB. This may suggest that the production mechanisms for DSB and SSB do not change in the energy region below 60 eV. It was surprising that DSB can be produced with the energy as low as 8 eV. Also seen in Fig. 1 is that the cross sections of DSB and SSB increased with the photon energy while the absorption cross section decreases

with the energy in the region above 60 eV. Values for SSB greater than the absorption means that one photoabsorption event produces more than one SSB, possibly by the energetic secondary electrons. Ratio of the cross section of DSB against SSB is plotted as a function of the photon energy in Fig. 2. The ratio was almost constant below 60 eV and above 500 eV. Between two energy regions, the ratio increased with the photon energy. This could be explained either by the increase of the yield for DSB or by the decrease for SSB. Taking into consideration that the yield for

SSB per absorbed energy seems to be constant, the former would be considered more likely. More efficient reaction channel for DSB seems to open above several hundred eV, which might cause the production of biologically significant amount of DSB. In summary, it was revealed that i) 8 eV is enough to produce DSB and ii) DSB can be produced more efficiently with the energy above 200-300 eV, which may correlate with the energy required for cell death. Obtained data, however, are still in the preliminary stage and further studies are necessary which include the experiments in wet or aqueous conditions.

2.2 Photon energy dependence of radical yield in water

The mechanism of biological enhancement with densely ionizing radiation such as Auger-emitting isotopes and heavy-particle radiation, as well as low energy X-rays, has been one of the hot topics in radiobiology. Among the various processes to be investigated in radiobiology, chemical reactions involving water radicals are basically important in aqueous systems, since they may determine the yields of various molecular changes which may lead to biological effects. From this point of view, the oxidation yield of ferrous ion in aqueous solution was investigated after irradiation with monochromatic synchrotron soft X-rays. This oxidative reaction is well known as a Fricke dosimeter, the yield of which can be expressed as a linear combination of the yields of water radicals produced by the radiation energy. Many studies have determined the oxidation yield of the ferrous ion with various X-ray energies above 7 keV. Below 7 keV only one experimental datum has been reported at 1.5 keV⁴⁾, suggesting that the yield decreases along with a lower photon energy. Theoretical simulations of the photon energy dependence of the oxidation yield have also shown that the yield decreases along with a lower energy photon or electron energy with a minimum at around 1 keV. This is considered to be due to an increase in the recombination probability of water radicals in a densely ionized area. A few years ago, data at X-ray energies of 13.6 and 8.86 keV were reported using synchrotron radiation at the Photon Factory⁵⁾. Recently more data were taken at eleven energy points from 10 keV down to 1.8 keV utilizing the advantage of the com-

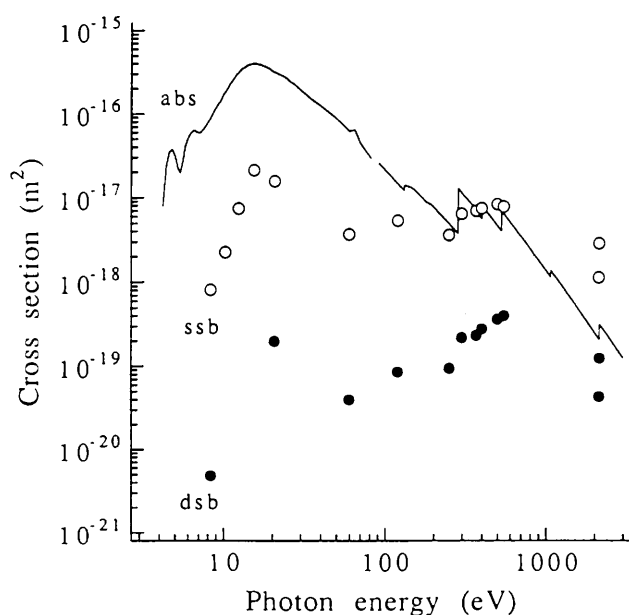


Fig. 1 Production cross sections for SSB and DSB. Solid curve represents the estimated absorption cross section of the DNA molecule.

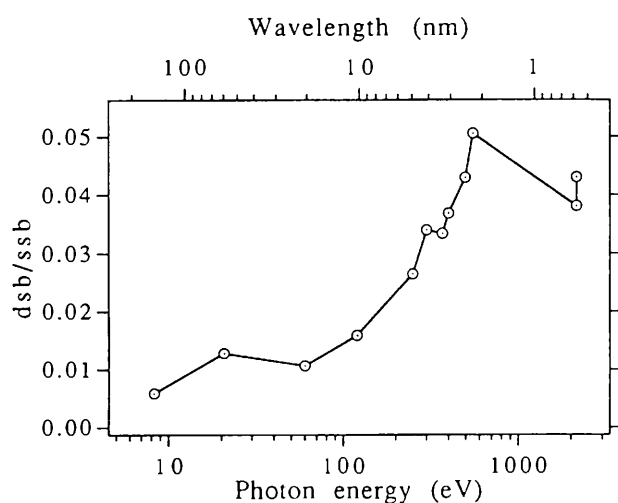


Fig. 2 Ratio of production cross section of DSB against SSB.

plete tunability of synchrotron radiation.

The standard ferrous sulfate solution (Fricke solution) containing 0.4 M sulfuric acid, 1.0 mM ferrous sulfate and 1.0 mM sodium chloride was prepared with distilled, doubledeionized and ultrafiltered water (~ 18 MW/cm resistance). The ferrous sulfate solution was prepared one day prior to use in order to assure oxygen saturation and to avoid any high background due to auto-oxidation. The white synchrotron X-rays were monochromatized with either one of two types of double-crystal monochromators, depending upon the X-ray energy used. Monochromatic X-rays having energies lower than 5 keV as well as those higher than 6 keV were obtained by using the monochromators of InSb (BL-27A) and Si (BL27B), respectively. Monochromatized X-rays were led out into atmosphere through polyimido film windows for irradiating sample solutions. Photon energies used are 1.800, 1.907, 2.153 (the K-absorption edge of phosphorus), 2.466 (below the Kabsorption edge of sulfur), 2.472 (the K-absorption edge of sulfur), 2.480 (above the K-absorption edge of sulfur), 3.100 and 4.038 (the K-absorption edge of calcium) keV at BL-27A, and 7.093(below the K-absorption edge of iron), 7.129 (above the K-absorption edge of iron), and 10.00 keV at BL-27B. One hundred ml of a ferrous sulfate solution was put in a sample chamber, which is made of acrylic resin and has a mylar-film window of 5 mm thickness, through which samples were exposed to soft X-rays. The X-ray beam size was adjusted to be smaller than the window size of the sample chamber. The solutions were stirred with a glass-coated iron piece during irradiation. A pair of samples in these chambers was always prepared in each irradiation experiment: one was exposed to X-rays; the other was only stirred and used as an unirradiated control. Since the ferric ion has a characteristic absorption peak at 304 nm, the optical densities of irradiated and unirradiated solutions were immediately measured using a spectrophotometer at 304 nm with micro-quartz cells.

The exposure rate of X-rays was measured by a specially made free-air ionization chamber at the both stations. The actual X-ray exposures to the samples were obtained with the integrated output of the monitors, which were calibrated with this free-air ionization chamber. In the examined X-ray region, especially lower than 4 keV, the attenuation of the

X-rays in air must be considered based on the practical reasons mentioned below. In the case of 1.8 keV X-rays, the intensity was reduced to $1/e$ of its incident value in only 10 mm of air. Therefore, the exposure rate measured by the ionizing chamber was corrected using the linear absorption coefficient of air in order to estimate the exposure rate at the sample position. Attention was also paid to the third-order harmonics contained in the monochromatized X-rays using such crystals as Si (111) or InSb (111). Especially, the contamination of higher order X-rays in X-rays below 2 keV must be carefully excluded in order to accurately estimate the exposure. Careful measurements of third-order harmonics showed that the third-harmonics components were negligible at the sample surface at these three energies, although the component was more than half at the center of the ionization chamber in the case of 1.8 keV X-rays. Absorbed dose in the sample was calculated with the mass-energy absorption coefficient of air, $(\mu_{en/r})_{air}$, and the average energy (33.73 J/C) required to produce an ion pair in air. In the case of X-rays higher than 7 keV, a sample thickness of 2 mm is not sufficient to completely absorb the incident photons. In these cases, the transmittance of the 2 mm thick solution was measured for each X-ray energy

Good linear relationships were obtained in the dose response curves for all of the examined X-rays. The yields of the produced ferric ion were determined from the slope of these response curves. The uncertainties were evaluated based on the errors in each measurement. Figure 3 shows plots of the obtained yields as a function of the incident X-ray energy. The yield decreased along with a decrease in the X-ray energy. The values reported in other studies are also plotted in Fig. 3 for a comparison, which include the values recommended by the ICRU (1970)⁶⁾, those theoretically calculated for electrons⁷⁾, those by theoretically calculated using a spur-diffusion model for photons⁸⁾, the value experimentally determined at 1.5 keV using Al Ka X-rays⁴⁾, and those experimentally determined at 8.86 keV and 13.55 keV using monochromatic synchrotron X-rays⁵⁾. It is shown that energy dependence of the yield is similar to that by Yamaguchi⁸⁾ rather than by Magee and Chatterjee⁷⁾, although the obtained values are almost the same as the latter at about 2.5 keV. In the energy region tested lie the

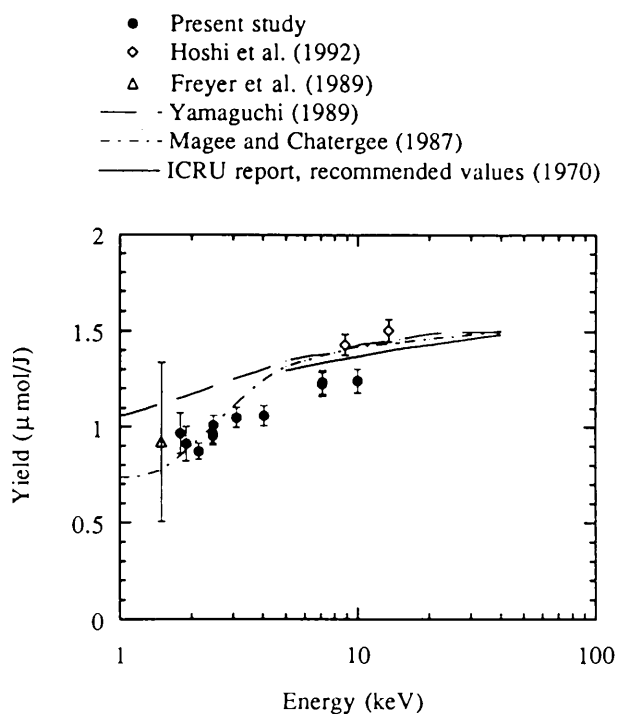


Fig. 3 Yield of the ferric ion as a function of the incident X-ray energy. The values reported on other studies^{6,7,8)} are also plotted for a comparison.

absorption edges of the iron K-shell and the sulfur K-shell. Effect of the absorption edge of these elements were not detected. This is considered to be due to the small atomic fraction of these elements in the sample solutions. The accuracy of the obtained oxidation yield was estimated from the errors of each measurement in the experimental procedure. Taking all of the uncertainties into consideration, the total errors of the obtained values were between 11.1% for 1.8 keV and 5.3% for 2.47 keV.

Low-energy photons were reported to exhibit a higher lethality similar to high-LET radiation by using characteristic X-rays such as those of carbon and of aluminum. Low-energy photons were absorbed exclusively via photoelectric effects and produced low-energy photoelectrons. Low-energy electrons are known to have high LET. The higher lethality of soft X-rays has been regarded as being due to the action of high-LET, low-energy photoelectrons. Present data that the oxidation yield of the ferrous ion decreases along with the energy of X-ray photons is in good agreement with those reported using heavy ions. This is the first systematic data experimentally obtained that soft X-rays have a high-LET nature in

radiation chemical reactions, and might link knowledge concerning the high LET of photoelectrons and the higher lethality of soft X-rays reported by other groups. Since the oxidation of ferrous ion occurs in reactions with diffusive water radicals, the higher biological effectiveness of high-LET radiation could not be explained based on the action of these radicals. Reactions between the highly reactive species, such as radicals, in an energy-deposited region are considered to cause a decrease in the diffusive radical yields, which can contribute to the oxidation of the ferrous ion. It might be necessary to consider the reactions which occur before the radicals diffuse out from the excited, spur- or blob-like regions, or the core regions of the heavy ions, in order to explain the higher biological effectiveness. One way to look into these excited regions on the nanometer scale might be to use concentrated solutions as samples where the solute molecule could participate in the reactions occurring in the concerned region. Watanabe et al.⁹⁾ reported that there exists a concentration dependence in the degradation yield of ATP in concentrated aqueous solutions. This might reflect the reaction specific to the region to which the radiation energy is densely deposited. Very few studies have been reported so far on radiation chemistry using concentrated solutions, especially with high-LET radiation. It might be necessary to work on radiation chemistry with concentrated aqueous solutions as a model of intracellular conditions in order to elucidate the mechanisms of high-LET radiation.

References

- 1) K. Hieda, *Int. J. Radiat. Biol.* **66** (1994) 561.
- 2) K. Hieda, T. Hirono, A. Azami, M. Suzuki, Y. Furusawa, H. Maezawa, N. Usami, A. Yokoya and K. Kobayashi, *Int. J. Radiat. Biol.* (1995) submitted.
- 3) K. Hieda, K. Suzuki, T. Hirono, M. Suzuki and Y. Furusawa, *J. Radiat. Res.* **35** (1994) 104.
- 4) J.P. Freyer, M.E. Schillaci and M.R. Raju, *Int. J. Radiat. Biol.* **56** (1989) 885.
- 5) M. Hoshi, S. Uehara, O. Yamamoto, S. Sawada, T. Asao, K. Kobayashi, H. Maezawa, Y. Furusawa, K. Hieda and T. Yamada, *Int. J. Radiat. Biol.* **61** (1992) 21.
- 6) International Commission on Radiation Units and Measurements, Report No. 17 (1970) (ICRU, Washington, DC).

- 7) J.L. Magee and A. Chatterjee, *J. Phys. Chem.* **82** (1978) 2219.
- 8) H. Yamaguchi, *Radiat. Phys. Chem.* **34** (1989) 801.
- 9) R. Watanabe, M. Ishikawa, K. Kobayashi, and K. Takakura, *Biophysical Aspects of Auger Processes*, AAPM Symposium Series No.8 (1992) 24.

J. X-RAY MICROBEAMS AND X-RAY MICROSCOPY

This section covers topics on hard X-ray microbeams for X-ray diffraction / scattering and X-ray fluorescence experiments, soft X-ray microscopy for the imaging of biological samples and photoelectron microscopy for the material characterization. The imaging and micro-analysis are key words of these research fields and have made remarkable advances during the past decade due to developments of both high brilliance synchrotron radiation sources and X-ray optical elements.

1. HARD X-RAY MICROBEAMS

1.1 Brief summary

Owing to a growing need for the material characterization over a small region in both basic researches and applications and the realization of practically-useful X-ray microbeam systems at SR facilities, synchrotron hard X-ray microprobes have been applied to X-ray diffraction/scattering studies and X-ray spectroscopy. To apply the X-ray microbeam system to the characterization of practical samples, not only the beam size but also other characteristics, such as a photon flux, an energy range, an energy resolution, an angular divergence and a polarization, are crucial. At the PF, X-ray microbeam systems having a few μ m beam size are now open to scientists. Furthermore, a few groups have succeeded in developing microbeam systems having the sub- μ m beam size. The following is a brief summary of activities on the hard X-ray microbeam.

Three types of X-ray microbeams are in use on

BL-4A. (1) The monochromatic X-ray microbeam system using Kirkpatrick-Baez optics¹⁾ has been open to researchers and used for X-ray fluorescence trace element analysis of biological and geological samples, micro-XAFS, surface analysis and X-ray micro-diffraction studies of liquid crystals. The beam size is typically about $5 \times 5 \mu\text{m}^2$ and can be reduced down to about $2.5 \times 2.5 \mu\text{m}^2$. (2) The continuum X-ray microbeam using a simple slit system has been used for X-ray fluorescence analysis over a small region. (3) An ellipsoidal mirror system combined with a pinhole is also effective to focus monochromatic X-rays to the beam size ranging from a few hundred μ m to a few μm^2 . Trace element analysis and chemical state analysis were performed with this system for the characterization of synthetic diamond crystals³⁾.

On BL-4B, K. Ohsumi and his group have developed techniques for the crystal structure determination of the microcrystal and over a micro-region of inhomogeneous samples using the Laue method in combination with continuum X-rays⁴⁾. In micro-area X-ray diffraction, a few μ m beam size was obtained by a micro-pinhole.

S. Aoki et al. have evaluated a paraboloidal mirror using partially coherent X-rays on BL-6C. Their system used highly collimated and highly monochromatized beams and attained a several μ m beam size.

On BL-8C, both elliptical mirrors and cylindrically bent multilayers were developed as focusing elements of Kirkpatrick-Baez optics for the sub- μ m spatial resolution X-ray microscope. The dark-field imaging, i.e. the detection of diffracted, scattered and fluorescent X-rays from the sample, has been performed to improve the sensitivity⁵⁾. Another Kirkpatrick-Baez focusing system was used for the X-ray diffraction studies of polycrystalline materials⁶⁾. The evaluation of a sputtered-sliced Fresnel zone plate has been performed on BL-8C⁷⁾ and the beam size of less than $1 \mu\text{m}$ was obtained.

X-ray scattering topography has been developed by Y. Chikaura et al.⁸⁾ and attained a spatial resolution of a few μm at BL-15B.

On BL-16X, a sub- μ m monochromatic X-ray microprobe using newly designed Kirkpatrick-Baez optics has been developed for the spectroscopic and diffraction studies over a small region. Owing to the high brilliance of the multipole wiggler source, the

useful photon flux for the diffraction and spectroscopic studies was obtained even with the small beam size.

1.2 Characterization of liquid crystals by X-ray μ -diffraction

Recently, a great deal of study has been made for cells consisting of thin layer of ferroelectric smectic-C liquid crystal (FLC) between solid plates. When the cell is thin enough, typically a few μm , it shows high-speed, bistable electro-optical switching between orientational states stabilized by surface interaction. This surface stabilized ferroelectric liquid crystal (SSFLC) cell attracted much attention because of the growing need for the display device application and the interest in studies on the interaction between the molecule or the layer and the external electric field. The layer structure in the SSFLC cell is characterized by the “chevron” structure. The SSFLC samples, when viewed with a polarized-optical microscope, exhibit a so-called zigzag defect in addition to the domain structure as shown in Fig.1(a). The zigzag defect is a local layer structure (LLS) defect and corresponds to walls between the two possible chevron directions. The zigzag defect consists of broad and narrow walls which run perpendicular and nearly parallel to the rubbing direction, respectively. The widths of walls depend on the cell thickness and are about $38\ \mu\text{m}$ and $6\ \mu\text{m}$ for the broad and narrow walls in $6\ \mu\text{m}$ thick cell, respectively. The proposed LLS at the broad wall is schematically shown in Fig.1(b). But no one has confirmed the LLS at the boundary directly.

The small angle X-ray micro-diffraction experiments using monochromatic X-ray microbeam system on BL-4A revealed the LLS over a small region for the first time. The experimental arrangement is shown in Fig.2. The advantages of this microbeam system for the characterization of SSFLC cells are both the small angular divergence (less than $0.7\ \text{mrad}$) and the small beam size (less than $5\ \mu\text{m}$). Special attention was paid to the alignment of the center of θ rotation to the X-ray focusing point. An optical microscope with a pair of polarizers was useful for both the alignment of the system and the *in situ* observation of the sample cell. The sample cell was mounted on the X-Z translation stages for the positioning.

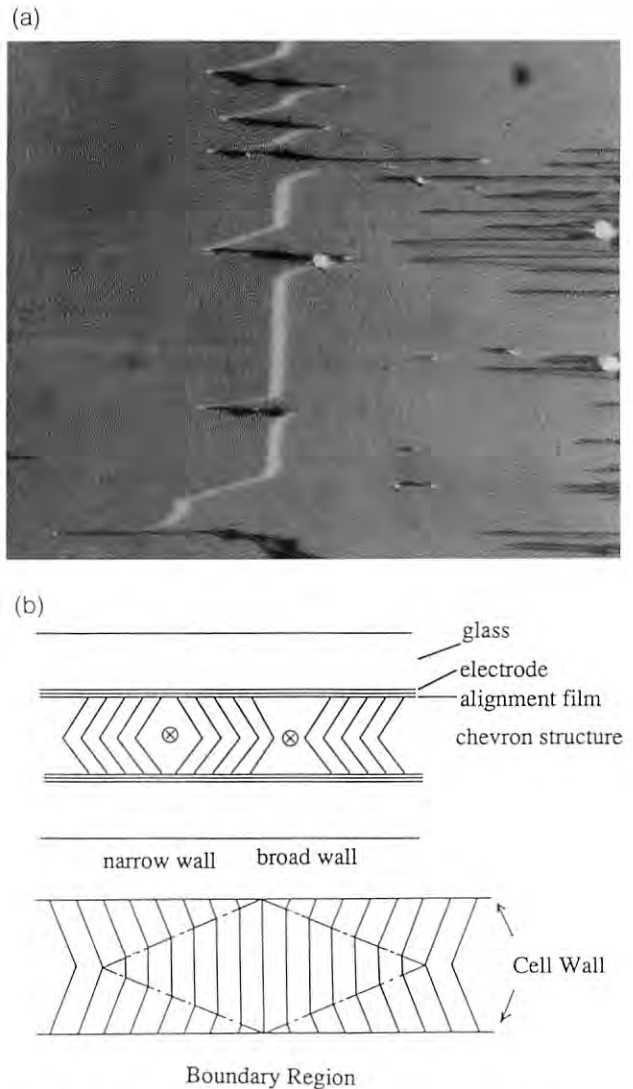


Fig. 1 (a) A polarized optical micrograph of a surface stabilized ferroelectric liquid crystal cell. (b) The chevron layer structure of the SSFLC cell and the proposed local layer structure at the broad wall.

The sample used was CS-1014 (Chisso). The sample cell was prepared by sandwiching the FLC material between two glass plates of $80\ \mu\text{m}$ thick with thin ITO electrodes on which the polyvinylalcohol layer was coated and unidirectionally rubbed. The smectic layer normal was parallel to the rubbing direction. The thicknesses of sample cells ranged from $1.5\ \mu\text{m}$ to $10\ \mu\text{m}$. Since the layer normal was set horizontally, the θ -scan (rocking curve) revealed the inclination of the layer normal to the bounding plate and the χ -scan (obtained by a position sensitive proportional counter without the scan) corresponded to the layer bending along the layer. With

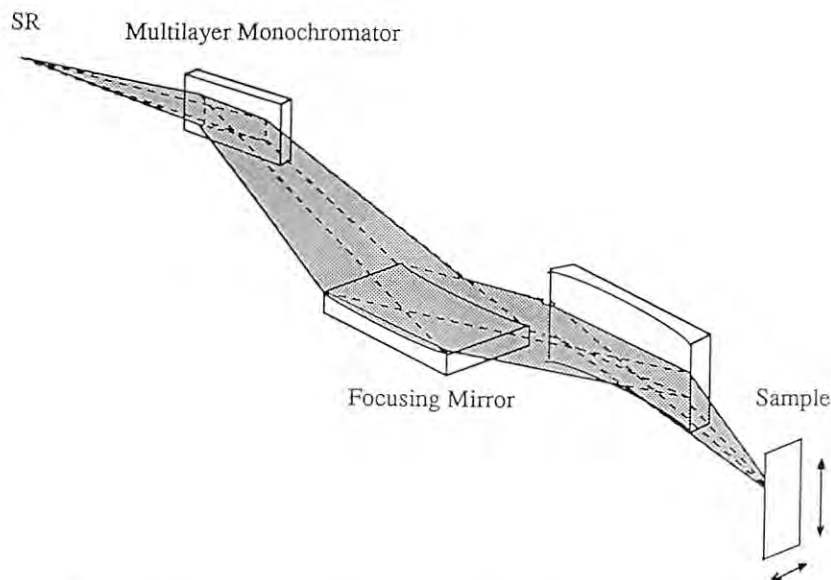


Fig. 2 The schematic representation of a hard X-ray microbeam system at BL-4A.

the fine positioning of the sample, the LLS over a small region can be determined directly and precisely.

The LLSs of the broad and narrow walls were characterized by X-ray μ diffraction. At the broad wall, the LLS changed from the chevron to the bookshelf similar to the proposed structure as shown in the Fig.1(b). The detailed analysis, however, revealed fine structures which were related with the LLS deformation at the wall⁹⁾. The LLS response of SSFLC to the electric field was also measured. Fig.3 shows the dependence of rocking curves on the applied voltage obtained at the broad wall center. With an increasing applied voltage, the peak corresponding to the bookshelf structure (around $\theta = 0^\circ$) became stronger in the intensity and narrower in the FWHM. Since integrated intensities of diffracted X-rays and the width of the broad wall itself remained constant, it was suggested that the rearrangement of the LLS was induced due to the applied voltage. More detailed description is given in the users' report section. In preliminary experiments for the characterization of the narrow wall, the LLS exhibited the bent bookshelf structure. It was also found that there were a few types of LLSs depending on the shape of the narrow wall. Further investigation on the narrow wall is now in progress.

These direct measurements of the SSFLC cells reveal the LLS in the thin cell, which has been speculated only by the indirect method.

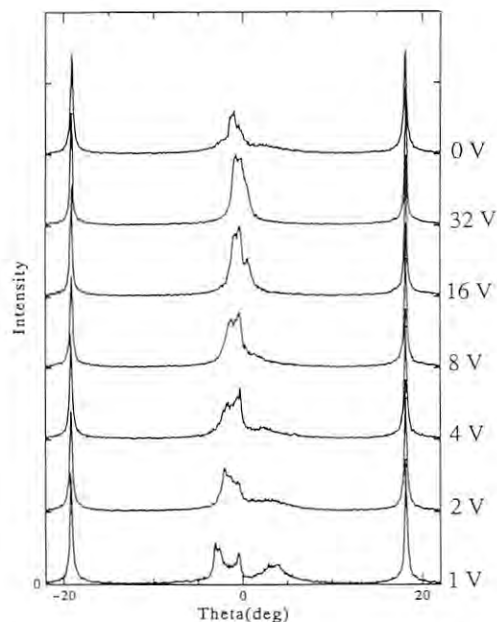


Fig. 3 A series of rocking curves obtained at the broad wall as a function of applied voltages.

1.3 X-ray fluorescence analysis using X-ray microbeam

Trace element analysis over a small region and the imaging of the trace element distribution in inhomogeneous samples are interesting applications of the X-ray microprobe.

Hair analysis for trace element concentrations has attracted much interest among researchers in

topics such as toxicology, nutrition, forensic science and environmental technology due to the possibility that trace element levels in hair reflect those in the other parts of the body. Most human hair analysis were carried out for bulk hair. One of the problems on hair analysis is the origin of trace elements: endogenous (incorporated from the body) or exogenous (attached from the environment). The two-dimensional elemental imaging of the cross section of human hair is valuable to elucidate these problems. The X-ray microbeam technique is most suitable for this purpose because of its high sensitivity and its non-destructive nature. Preliminary experiments were done for human hair to demonstrate the capability of the X-ray microprobe¹⁾. Recently, systematic analysis of human hair is in progress to investigate the environmental effect to the human body¹⁰⁾.

Hairs of metal smelter workers were analyzed. For Pb smelter workers, the amount of Pb was high near the surface of the hair compared to the inside. Results are in good agreement with the exogenous model, i.e. the high Pb concentration could be caused by fumes of Pb. To further investigate the endogenous and exogenous nature of elements, Hg distributions in hair of rats were measured. Methyl mercury chloride was given to rats every day for 5 consecutive days. The correspondence between the Hg levels in the blood and in hair was confirmed by flameless atomic absorption spectrometry, suggesting that the Hg concentration in hair is closely related with that in blood. Cross sections of the rat hair (25 μ m thick) were measured by the SR X-ray microbeam. XRF imaging revealed the selective accumulation of Hg in the cortex (inner part of the hair): therefore the endogenous origin was confirmed. On the contrary, the exogenous exposure of human hair to a Pb environment resulted in the Pb accumulation in the cuticle (surface of the hair). Thus, SR X-ray microbeam analysis is effective to distinguish between the endogenous and exogenous origins of trace elements in hair.

The excess or depletion of trace elements sometimes correlates with several kind of diseases. Intoxication is caused by the ingestion of toxic elements followed by the accumulation at various biological organs and tissues. The study on the interaction of toxic metals and essential elements is important to understand the impact of toxic metals on the biomedical system. For example, the correlation between

Hg and other elements suggested the interaction between Hg and the metalloenzyme system. To further investigate the correlation among elements, elemental analysis with a high spatial resolution and a high sensitivity is necessary.

Hg is a nephrotoxic metal and thought to cause more serious damage to the proximal convoluted tubules than to the distal tubule. To clarify the relation between the trace element such as Zn and the morphological change in kidney of a rat after exposure to Hg, SR-XRF elemental imaging technique was used. Since SR-XRF imaging analysis is nondestructive, histochemical staining by the method of periodic acid Schiff reaction (PAS) was performed after the XRF measurement. Using X-ray microbeam analysis, the relationship between toxic metal distribution and the renal tubular cell damage was successfully revealed. The experimental details are described in the users' report section.

2. SOFT X-RAY MICROSCOPY

2.1 A scanning soft X-ray photoelectron microscope using circularly polarized radiation

Magnetic circular dichroism (MCD) measurements in an X-ray region are actively performed at SR facilities to study magnetism of magnetic thin films and bulks including alloys. The current MCD measurements give spectroscopic information mostly as an averaged value over the whole irradiated area of a sample. If a microscopic technique is introduced, magnetic domains with different magnetization direction can be imaged by the contrast arising from the MCD.

A scanning photoelectron microscope using an X-ray focusing optical system with a zone plate has been developed on the beamline AR-NE1B by Y.Kagoshima et al¹¹⁾. It aims at the imaging of magnetic domains as well as the position and element specific spectromicroscopy of magnetic materials using circular polarization with a spatial resolution approaching several tens nm in the near future.

Figure 4 shows an optical arrangement of a scanning X-ray microscope. The circularly polarized radiation was produced under a helical undulator operation mode of the insertion device, EMPW #NE1. The undulator radiation was monochromatized by

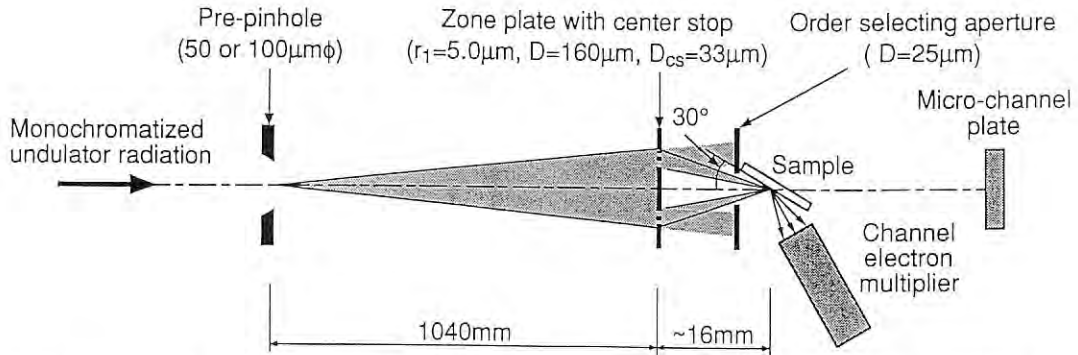


Fig. 4 A top view of an optical arrangement of a scanning X-ray microscope using circularly polarized radiation at the NE1B.

the NE1B -SGM and then post-focused. There was a pre-pinhole (PPH) at the post-focused point to collimate the X-ray beam. Regarding PPH as a secondary source, the X-ray beam was focused onto a sample by a reduction optical system using a zone plate. The spatial resolution was simply determined by a size of PPH and the reduction ratio of the optical system. The focused beam was incident at an angle of 30° from the surface of the sample to obtain the MCD contrast because the magnetization direction of the sample was in plane. Photoelectron yield was counted using a channel electron multiplier. All elements except for the scanning unit were mounted inside a vacuum chamber.

A resolution test has been made using a copper #2000 mesh as a sample. The PPH was $50 \mu\text{m} \phi$. A criterion of 90%-10% intensity in an edge scan profile gives the resolution of $\sim 1.2 \mu\text{m}$, which is in good agreement with the ideal value of $\sim 0.9 \mu\text{m}$.

A piece of video tape was used as a magnetic sample. Its evaporated magnetic layer composing of cobalt and nickel (Co:Ni = 80:20) was overcoated by a 20-nm thick CoO layer and several-nm thick organic lubrication layer as a surface. The CoO does not exhibit the MCD contrast because it is antiferromagnetic. A magnetic pattern was recorded in a piece of video tape using an audio recording head. The pattern consisted of magnetic domains with alternating in-plane magnetization direction. The width of domains was $20 \mu\text{m}$. A surface of the tape was sputtered using an ion gun until the MCD contrast appeared. Fig.5(a) shows a microscopic image of the pattern taken at the L_2 absorption edge of cobalt (793 eV) by the right circularly polarized light. The observed pattern exactly corresponds to the recorded one. Fig.5(b) is an illustration of Fig.5(a). It

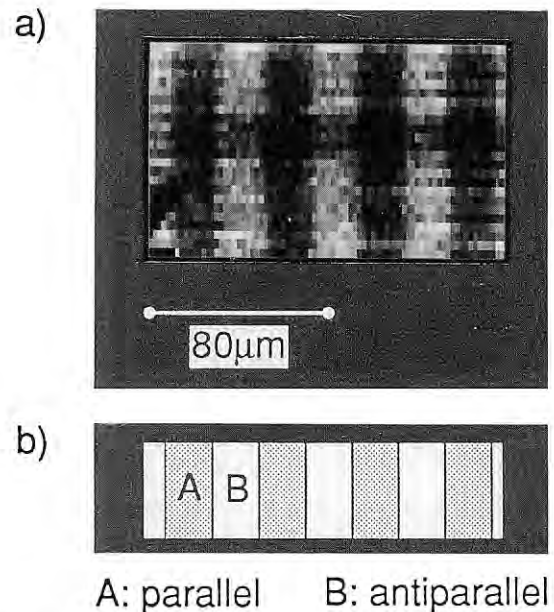


Fig. 5 (a) A microscopic image of the magnetic pattern taken at the L_2 absorption edge of cobalt (793 eV) and with right circularly polarized light. (b) Illustration of (a). In (a), a pixel number, a pixel pitch and a gate time are $80(\text{H}) \times 24(\text{V})$, $2 \mu\text{m}(\text{H}) \times 4 \mu\text{m}(\text{V})$ and 1 sec., respectively. The width of domains recorded was $20 \mu\text{m}$. The photon spin and magnetization direction are parallel in dark (weak) zones, while antiparallel in bright (intense) zones, respectively.

explains the relation between the photon spin and the local magnetization direction of the domains. Namely, the photon spin and magnetization direction are parallel in dark (weak) zones of Fig.5(a), while antiparallel in bright (intense) zones of Fig.5(a). Further, images at the L_3 edge (778 eV) and below

L₃ edge (770 eV) were also taken. It was found that the observed contrast was reversed between L₂ and L₃ edges and that no contrast was observed at 770 eV.

Thus, a scanning X-ray microscope is shown to be effective in imaging magnetic domains by means of the contrast arising from the MCD. Both smaller magnetic domains and higher contrast will be achieved with a proper sample preparation. Position specific spectroscopy will also be performed.

2.2 Zone plate soft X-ray microscope

Main object of the soft X-ray microscope is the imaging of the wet biological sample with the spatial resolution of less than a few tens of nm. In order to obtain the high contrast of the specimen and to avoid the severe absorption by the water, X-ray energies of "water window", which range from carbon (major element of biological specimen) to oxygen (water) K absorption edges, are usually used.

Undulator radiation from AR NE1B is most suitable for soft X-ray microscope owing to its high brilliance, high collimation and energy tunability. J.-D Wang et al. have been developed a microscope to fully utilize these advantages of undulator radiation¹²⁾.

For imaging application, monochromatic illumination of the zone plate is essential to avoid chromatic aberration. A spherical grating monochromator was introduced instead of the conventional linear zone plate monochromator because of the matching to the undulator source characteristics and the heat load problem. An objective zone plate having a well defined fine zone is indispensable to obtain a high resolution and good quality image. The objective zone plate used had 50 nm finest zone and was fabricated by IBM in collaboration between Lawrence Berkeley Lab. and IBM. In a high resolution zone plate microscope, the alignment of the objective zone plate, the pinhole and the sample needs careful adjustment. A visible light pre-focus unit has been developed and introduced into a vacuum chamber of the X-ray microscope. As a result, the X-ray optical system of the microscope can be adjusted easily, quickly and precisely. The experimental results shows that the diffraction limited resolution of 55 nm was realized with this microscope. Recently they succeeded in observing some



Fig. 6 Magnified image of dry diatoms. The X-ray wavelength was 2.37 nm. The magnification of the X-ray optical system was about 1020. The exposure time was about 2 min. A scale mark is 1 μ m.

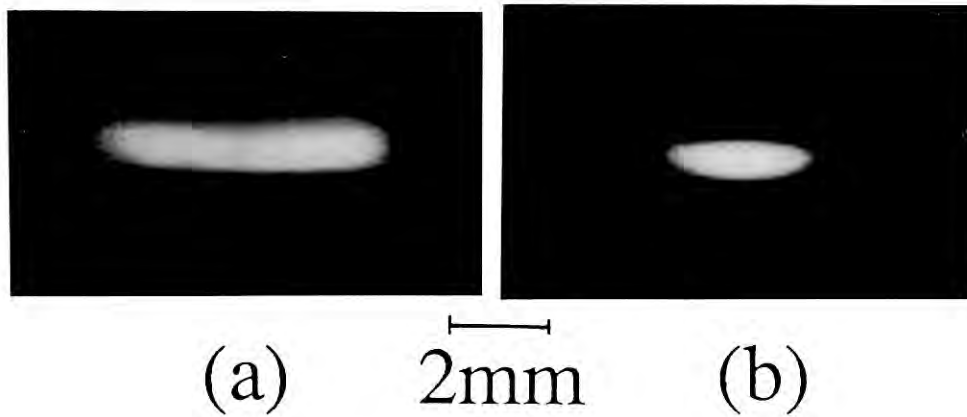
dry biological specimen. Fig. 6 shows a full-field image of diatom.

Reference

- 1) A. Iida and T. Noma, Nucl. Instrum. and Methods B82 (1993) 129.
- 2) S. Hayakawa, A. Iida, S. Aoki and Y. Gohshi, PF Activity Report #10 (1992) 57.
- 3) M. Wakatsuki, S. Hayakawa, S. Aoki, Y. Gohshi and A. Iida, New Diamond Science and Technology (1991) 143.
- 4) K. Ohsumi, K. Hagiya, M. Uchida, N. Suda, M. Miyamoto, M. Kitamura and M. Ohmasa, Rev. Sci. Instrum. 66 (1995) 1448.
- 5) Y. Suzuki and F. Uchida, Rev. Sci. Instrum. 66 (1995) 1469.
- 6) T. Hirano, F. Higashi and K. Usami, Rev. Sci. Instrum. 63 (1992) 5602.
- 7) N. Kamijo, S. Tamura, Y. Suzuki and H. Kihara, Rev. Sci. Instrum. 66 (1995) 2132.
- 8) Y. Chikaura, Y. Suzuki and H. Kii, PF Activity Report #11 (1993) 358.

- 9) A. Iida, T. Noma and K. Hirano, *Ferroelectrics* **149** (1993) 117.
- 10) N. Shimojo, K. Tabata, G. Sun, S. Homma and I. Nakai, *PF Activity Report # 11* (1993) 55, this volume.
- 11) Y. Kagoshima, T. Miyahara, M. Ando, J.-D. Wang and S. Aoki, *Rev. Sci. Instrum.* **66** (1995) 1534.
- 12) J.-D. Wang, Y. Kagoshima, T. Miyahara, M. Ando, S. Aoki, E. Anderson, D. Attwood and D. Kern, *Rev. Sci. Instrum.* **66** (1995) 1401.

Experimental Facilities



Images of the monochromatized 60keV X-rays at (a) under focusing point and (b) focusing point of AR-NE1A1

You can jump to the article by clicking its title.

CONTENTS

	Page
A. BEAMLINES	E - 1
1. NEW BEAMLINE IN OPERATION	E - 1
1.1 BL-12C Preliminary Performance Test of the Monochromator for a New XAFS Beamline	E - 1
2. BEAMLINES UNDER CONSTRUCTION AND PLANNING	E - 1
2.1 BL-4C Improvement of Optical Elements	E - 1
2.2 BL-4B Separation to two stations (BL-4B1 and 4B2) with focusing optics	E - 1
2.3 BL-18C powder diffraction at non-ambient conditions	E - 2
3. IMPROVEMENT OF BEAMLINES	E - 3
3.1 BL-16A	E - 3
3.2 BL-16 A new monochromator for the undulator	E - 3
3.3 New doubly bent crystal monochromator at AR-NE1A1	E - 4
4. LONG HORIZONTAL PARALLEL SLITS FOR POWDER DIFFRACTION	E - 5
B. NEW INSTRUMENTATION	E - 6
1. CURRENT STATUS OF HIGH RESOLUTION PHOTOEMISSION FACILITY	E - 6
2. THE TITANIUM SAPPHIRE/DYE LASER SYSTEM	E - 7
3. SCANNING X-RAY MICROSCOPE USING CIRCULARLY POLARIZED RADIATION AT THE NE-1B FOR THE OBSERVATION OF FERROMAGNETIC DOMAINS	E - 8

A. BEAMLINES

1. NEW BEAMLINE IN OPERATION

1.1 BL-12C Preliminary Performance Test of the Monochromator for a New XAFS Beamline

Main components of a new XAFS beamline (BL-12C) have been delivered in FY 1993. The outline of the beamline was described in the previous volume.¹⁾ The double crystal monochromator had been designed to improve the angular linearity of the Bragg angle and the parallelism of two crystals. The crystal holders were designed as light as possible and the first crystal was placed at the center of rotation.

The mechanical performance of the double crystal monochromator was tested by using an autocollimator. The linearity was better than 0.004° between 7 and 50° , which is better than 0.006° observed at BL-7C.²⁾ Especially the backlash decreased from 0.003° to 0.001° . The variation of the parallelism between two crystals is a key performance of the double crystal monochromator for XAFS experiments and it was also tested. The result is shown in Fig. 1. It was within 10 arcsec within usually used angular range, which is much better than that observed at BL-6B (40 arcsec). The data for BL-6B was taken when it was delivered and it is improved after that (14 arcsec).

The optical components were aligned and tested during the summer shutdown period. The performance of the beamline will be tested during the autumn beamtime of 1994, and the results will be re-

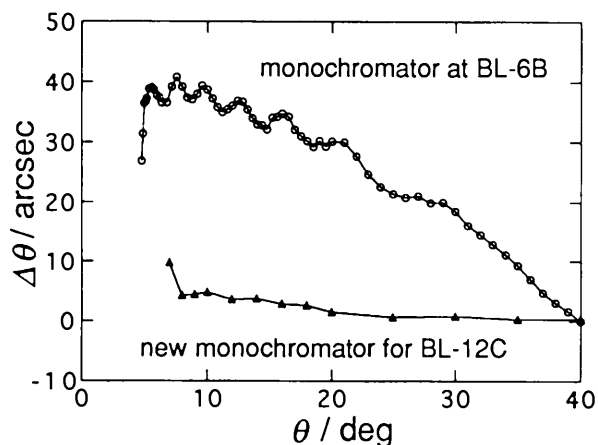


Fig. 1 The variation of the parallelism between two crystals against 2θ .

ported in the next volume.

References

- 1) Photon Factory Activity Report 1993, # 11, I-4 (1994).
- 2) M. Nomura, A. Koyama and M. Sakurai, KEK Report, 91-1. (1991).

2. BEAMLINES UNDER CONSTRUCTION AND PLANNING

2.1 BL-4C Improvement of Optical Elements

BL-4C will be mainly used for x-ray diffraction experiments using a 6-circle diffractometer after April of 1995, since the present XAFS activities at BL-4C will be transferred to BL-12C. New experiments of X-ray magnetic Bragg scattering will be started as well as the experiments of X-ray diffuse scattering.

Optical elements of BL-4C are to be improved during the summer shutdown of 1995. The present sagittal focusing monochromator is replaced by a flat double-crystal monochromator and a focusing mirror, which ensures a high photon density and a good energy tunability. Figure 2 shows the layout the BL-4. The monochromator and mirror are placed between BL-4A and -4B₁ hutches. A one-meter long rhodium-coated silicon mirror focuses the monochromatic beam of 6 to 25 KeV at the sample position.

The beam line is to be opened for public use at the end of 1995.

2.2 BL-4B Separation to two stations (BL-4B1 and 4B2) with focusing optics

For a long while, BL-4B has been in charge of both powder diffractometer and X-ray camera for submicrometer-sized crystal in the modes of Laue and Weissenberg method. Recent rise of the demand for usage of both equipments caused frequent replacement and their adjustment to the SR beam. In order to save the time, BL-4B is to be separated to two tandem experimental stations (Fig. 2).

For the Laue methods, the nearer to the light source is preferable, the camera is located in BL-4B1 at the distance of 29m from the source.

An X-ray mirror for BL-4B2 is installed in the

beamline just after the monochromator at the distance of 18m from the source and horizontally focuses the monochromatized X-ray beam to 13mm in full width at the half maximum in horizontal plane on the powder sample. This new optics is expected to gain 5 times higher that of non-focusing.

The reconstruction of the beamline is scheduled to carry out in the summer shutdown of 1995, and the commissioning of both equipments is going to start at the end of 1995.

2.3 BL-18C powder diffraction at non-ambient conditions

BL-18C is newly designed for powder diffraction experiments at non-ambient conditions such as high pressure and/or low temperature. Diffraction intensity from sample at such conditions is weak, so that high x-ray intensities are required to obtain reliable intensity data. For this purpose, a focused optics is adopted in contrast to the standard powder diffraction beam line. The new beam line, shown in Fig. 3, consists of a double-crystal monochromator and horizontal and vertical focusing mirrors.

The double-crystal monochromator is of a fixed-exit type, equipped with two flat crystal. The second crystal is long enough to receive a monochromatized beam by the first crystal without a translational motion in the x-ray direction. The position of the first crystal is adjusted in the vertical direction to keep beam height constant. This design of the monochromator is the same for BL-4C. Mirrors are of a fixed concave type without bending mechanism, and made of SiO_2 with Pt coating, and the critical energy is designed to be 25keV. The mirror size is designed to have a divergence from sample side of 1 mrad. The horizontal mirror locates at 18.4m from the source and the radius is 1070m, and the vertical mirror is located at 18.9m and the radius is 760m, while the sample position is 21.5m from the source. The focused beam size is expected to be $50 \mu\text{m}$ in vertical direction and $100 \mu\text{m}$ in the horizontal direction.

A diamond-anvil high-pressure cell or a He-flow type cryostat (able to cool down to 10K) is attached to a vertical-type single axis goniometer. Diffracted X-rays are recorded on a round-type imaging plate, and can be read out in three minutes. For more precise measurements, a flat-type imaging plate is also

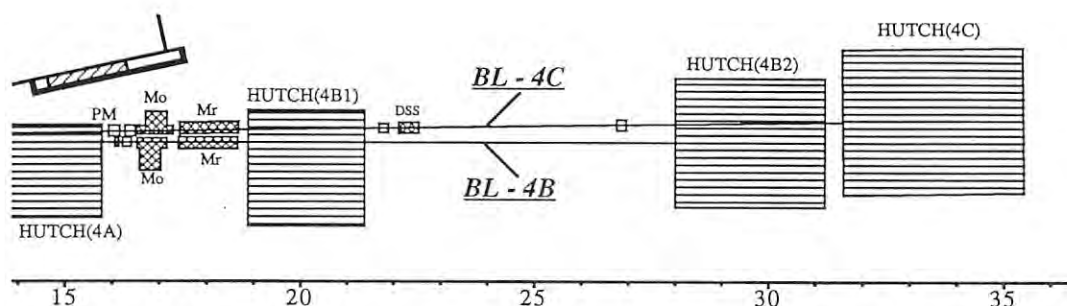


Fig. 2 New layout of BL-4B and -4C. PM: beam position monitor; Mo: double-crystal monochromator; Mr: focusing mirror; DSS: downstream shutter.

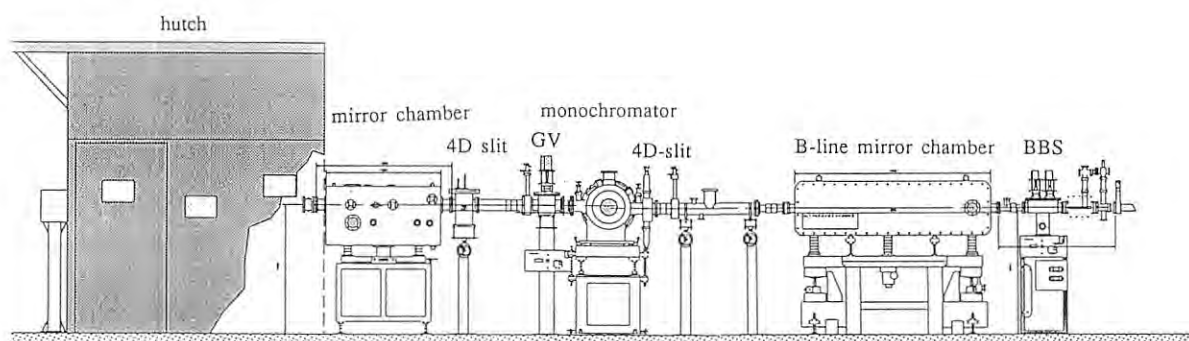


Fig. 3 Layout of BL-18C (side view).

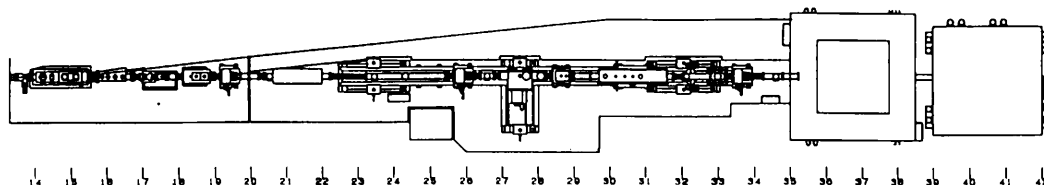


Fig. 4 The layout of BL-16A.

available. In future, an X-ray CCD camera will be equipped for more quick measurement. This diffractometer is constructed in cooperation with Tokyo Univ. and NIRIM. The station will be opened for public use from 1996.

3. IMPROVEMENT OF BEAMLINES

3.1 BL-16A

BL-16A has been reconstructed as a beam line to provide general purpose hard X-rays from the 53-pole MPW. This beam line can be used for both white and monochromatic X-rays (5-25 keV). The layout of the beam line is shown in Fig. 4. The collimating mirror and fluorescence screen # 1 will be installed in the summer of 1995. The monochromator is located at 27.5 meters from the source, and the 3:1 focusing point (36.7 meter) is in the A1 hatch. The main improvements of the beam line layout are as follows.

- 1) The whole beam line is covered with radiation shielding consisting of 5mm Pb sandwiched by Fe. Then the individual optical element does not need to be shielded by Pb sheets and it is become easy to access for the maintenance.
- 2) The Be-windows, the BBS and the slit are installed upstream of the collimating mirror. Then the heat load irradiated to the mirror reduces to about 1/5, because the low energy component of synchrotron radiation (SR) is filtered by the Be-window and the graphite filters installed just upstream of the window.
- 3) Components downstream from the collimating mirror to the slit # 3 are mounted on an inclination stage in order to adjust these components to fit the inclined angle of the SR beam reflected by the mirror. The height of the stage can be easily adjusted with the aid of several fluorescence screens.

In addition to the modification of the beam line layout, we improved the design of crystal. The pre-

vious crystal had semi-circular water channels with a width of 0.6 mm below the irradiated surface, and the thickness of the fins between these channels were 1 mm. In this case, because of thermal deformation, the measured Si(111) rocking curve peak height at 300 mA was about 70% of the value extrapolated from the low current data for 8.3 keV monochromatic X-rays. The Si(333) rocking curve widths (FWHM) was about 9 arcsec.

In the new one (Fig. 5), the channel width is 0.1 mm and the fin width is 0.2 mm. The performance of this new micro-channel crystal is as follows; The Si(333) rocking curve widths (FWHM) become about 5 arcsec at almost the same condition as above, and the deterioration of the total flux for the Si(111) fundamental reflection seen at the previous crystal can not be observed.

Using the sagittal focusing of the second crystal, the monochromatic beam is gathered to 2.4 mm FWHM in horizontal at the focusing point, and the photon flux of 0.7×10^{13} photons/sec is achieved at an energy of 8.3 keV and a ring current of 300 mA.

3.2 BL-16 A new monochromator for the undulator

During the last decade there has been a great

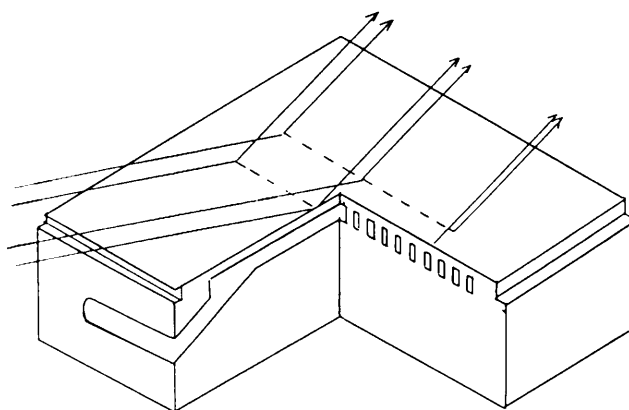


Fig. 5 A sketch of the directly water-cooled monochromator crystal with a micro-channel.

demand for high-resolution and high-throughput monochromators in the far ultraviolet and soft x-ray regions. Recently the installation of undulators in storage rings has emphasized the various scientific possibilities in these energy regions. To meet the demand, a design study on monochromators for the undulator beam line BL-16 has been carried out. A 24-m spherical grating monochromator (24-m SGM) has been proposed and its construction has been started.

The design concept of the 24-m SGM is based on the so-called Dragon monochromator. The layout of optical elements is schematically shown in Fig. 6. The beam line consists of a Kirkpatrick-Baez pre-mirror system, a 24-m spherical grating monochromator with a movable exit slit, and refocusing mirrors. Undulator radiation is focused horizontally by the first cylindrical mirror M_0 with $3/5$ demagnification. The second mirror M_1 is a spherical mirror, which focuses vertically with $1/10$ demagnification onto an entrance slit. With three gratings of 400 l/mm, 900 l/mm, and 2000 l/mm, the 24-m SGM covers the photon energy range from 40 to 600 eV.

The analytical results for the resolving power with an entrance slit width of $50 \mu\text{m}$ are shown in Fig. 7, together with main contributions to the resolution limit. Here a figure slope error of 0.2 arcsec for each grating is assumed. In the low energy regions, the considerable contribution of the coma aberration is seen. To reduce the coma, one has only to close an aperture suitably. It is expected that the 24-m SGM can cover the entire energy range with a resolving power of more than 10000, if the figure slope error of the gratings is less than 0.2 arcsec.

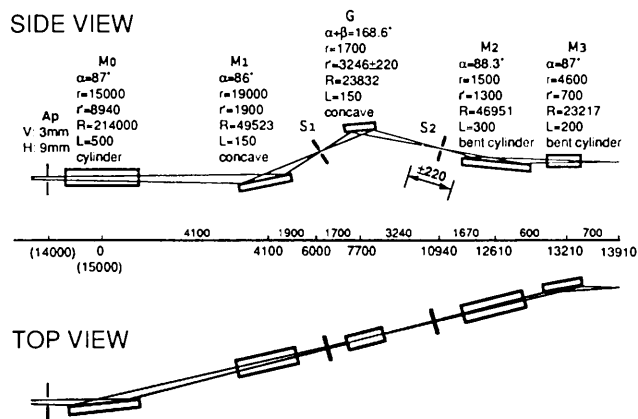


Fig. 6 Schematic layout of the 24-m SGM for the undulator at BL-16.

From a separated estimation for the throughput of the whole beam line, it is found that the photon flux of more than 10^{10} photons/sec is achievable with a resolving power of 10000 in the entire photon energy range.

3.3 New doubly bent crystal monochromator at AR-NE1A1

A new doubly bent crystal monochromator has been installed at the beamline AR-NE1A1, which is the dedicated beamline for Compton scattering experiments. The previous monochromator for this beam line was a quasi-doubly bent crystal monochromator which comprised an array of 20 pieces of singly-bent crystals. By using the previous monochromator, we could get a focused X-ray beam at 60 keV as the size of 2 mm height and 8 mm width, whose energy resolution and flux were about 90 eV and 6×10^{12} photons/sec. Various Compton scattering experiments have been done by using this monochromator for 5 years.

Recently, however, the sophisticated Compton scattering experiments need much better focusing at the sample position and much better energy resolution without losing any flux, in order to observe the Compton scattering from small samples, to reduce the back ground, and to get much better momentum space resolution. In order to achieve the above performance, we started to design the new doubly bent

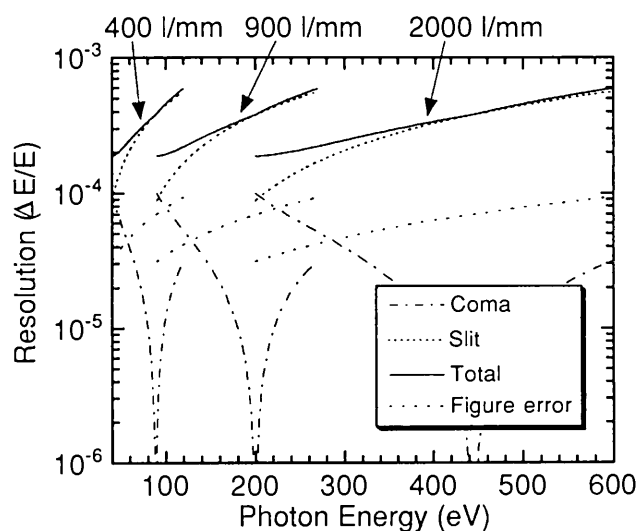


Fig. 7 Various resolution limits as a function of photon energy.

monolithic crystal monochromator one year ago, and it has been successfully installed into the beamline.

Figure 8 shows the schematic view of this new monochromator. Its mechanical system is similar to an usual bent cylindrical X-ray mirror. The monolithic Silicon (111) crystal is mounted on a water cooled cylindrically polished copper crystal holder with liquid Ga-In alloy between them, in order to get good thermal and also mechanical contacts. The sagittal bending radius of the holder, R_s , is 508 mm and the surface is coated by Ni metal to avoid damage by Ga-In alloy. Then the holder is mounted on a bender to make a meridian radius, R_m , to be 596 m as shown in Fig. 8. The shape of the crystal is 3 mm \times 75 mm \times 200 mm (thickness, width, and length) with 0.6 mm wide channels to make an weak linkage as shown in Fig. 8. The remained lib width is 1.2 mm. The thickness of 3 mm is important to avoid a crystal strain which is introduced by the contact with the crystal holder.

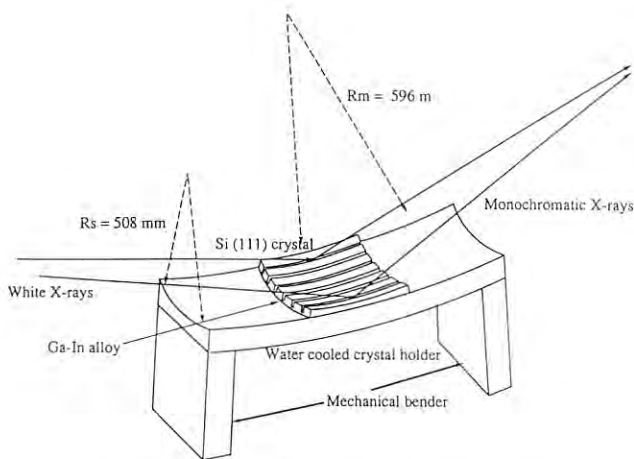


Fig. 8 Schematic view of the new doubly bent crystal monochromator.

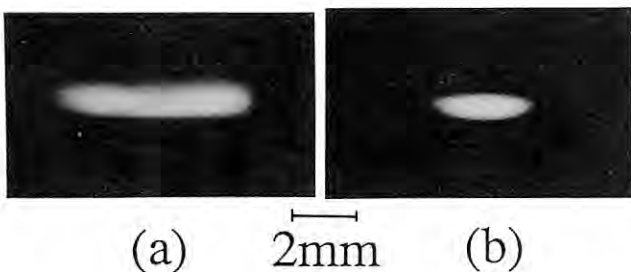


Fig. 9 Images of the monochromatized 60keV X-rays at (a) under focusing point and (b) focusing point, respectively.

Figure 9(a) and (b) show the image of the monochromatized 60 keV X-rays at 34000 mm from the source (under-focusing point) and at 37700 mm from the source (the focusing point), respectively. At the focusing point, the beam size is 0.5 mm in height and 2.0 mm in width. The flux of the above focused beam was 5×10^{12} photons/sec. The energy resolution of the monochromator was about 60eV at 59.38 keV.

The new monochromator gives one order higher brightness at the sample position and also better energy resolution than those by the previous monochromator. Then the over all momentum resolution for the high resolution Compton scattering experiment is expected to become 0.09 a.u.. The back ground can be reduced to 1/3, because it is possible to insert a fine slit after the analyzer crystal without losing any Compton scattering signal.

4. LONG HORIZONTAL PARALLEL SLITS FOR POWDER DIFFRACTION

The parallel-beam optics using synchrotron radiation has an advantage for high-resolution powder diffraction experiments. For this purpose, a crystal analyzer or a horizontal parallel slits (hereafter called HPS) is effectively used on the diffracted beam side. The former gives higher angular resolution, while the latter is advantageous in obtaining high intensity.

The HPS consist of a number of long thin foils stacked parallel at very narrow spacing. The angular spacing can be chosen by selecting the foil length and the spacing between foils. The high precision of assembly is required in constructing the HPS, which determine the limit of angular resolution. After the first report on the HPS in 1986¹⁾, many HPS system have been developed at various synchrotron radiation facilities including the Photon Factory. The highest resolution so far obtained is 0.038° with 300 mm slit length²⁾.

Recently a HPS system aimed at better resolution with high intensity has been performed³⁾. The main purpose is to achieve the angular resolution of 0.03° and to stack the foils 25 mm height, which required for asymmetric 2-theta scanning at fixed incident angle. Two sets of HPS (hereafter HPS1 and HPS2) were constructed, the specification of which are listed in Table 1. These HPSs were tested com-

binning with a powder diffractometer at BL-4B using CeO₂ as a test material. Table 2 gives a comparison of the peak maximum intensity and the FWHM of the (111) reflection observed in various slit settings. The intensity is decreased to about one third at each time of narrowing the receiving slit from 0.5 mm to 0.2 mm and then to 0.1 mm. On the other hand, the intensity is decreased to 59% by replacing HPS2 with HPS1. This relative efficiency is thought to be quite reasonable compared with the ideal value when the technical difficulty of stacking 167 very long thin foils of stainless steel in parallel.

Variations of FWHM with 2θ, observed with HPS1 and HPS2 for the reflection from CeO₂, are shown in Fig. 10. FWHM for the (200) reflection at 2θ = 32.810° gave the minimum of 0.03° for HPS1, achieving the primary purpose of the present study. The variations were well fitted to Caglioti-Paoletti-Ricci formula as follows;

$H(2\theta) = (0.0028\tan^2\theta - 0.0008\tan\theta + 0.0010)^{1/2}$ for HPS1, and

$H(2\theta) = (0.0038\tan^2\theta + 0.0012\tan\theta + 0.0027)^{1/2}$ for HPS2.

These newly developed HPSs will be used together with the diffractometer at BL-4B2 which will be dedicatedly used for powder diffraction experiment.

Table 1 Selected specifications for the horizontal parallel slits.

	HPS1	HPS2
Angular aperture (°)	0.032	0.065
Transmission efficiency (%)	67	80
Spacing between the two foils (mm)	0.1	0.2
Number of foils	167	100
Foil material	Stainless steel	
Foil thickness (mm)	0.05	
Foil length (mm)	353	
Effective window size (mm ²)	15 (width) × 25 (height)	

Table 2 Comparison of peak maximum intensities and FWHM's in various settings for the slit system.

Slit	Peak maximum intensity (counts s ⁻¹)	FWHM (°)
HPS1	14223	0.0319
HPS2	24236	0.0582
RS = 0.1 mm	1655	0.0385
RS = 0.2 mm	5199	0.0564
RS = 0.5 mm	15348	0.1153

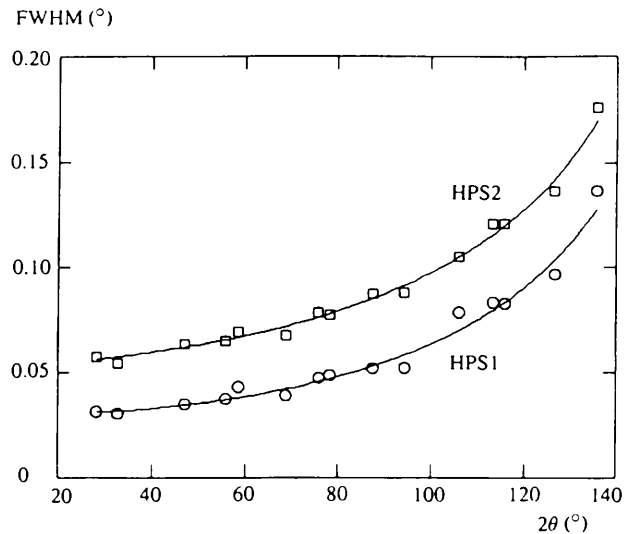


Fig. 10 Variations of FWHM with 2θ observed with HPS1 and HPS2 for the reflection from CeO₂.

References

- 1) W. Parrish, M. Hart, C.G. Erickson, N. Masciocchi and T.C. Huag, *Adv. X-ray Anal.* **29** (1986) 243.
- 2) M. Takata, M. Kisono, M. Sakata, and S. Sasaki, *Photon Factory Activity Report # 11*(1994) 39.
- 3) H. Toraya, M. Takata, H. Hibino, J. Yoshino and K. Ohsumi, *J. Synchrotron Rad.* **2**(1995) 143.

B. NEW INSTRUMENTATION

1. CURRENT STATUS OF HIGH RESOLUTION PHOTOEMISSION FACILITY

Recently, high performance of monochromators have made it possible to do extreme high energy resolution photoabsorption spectroscopies at BL-2B, BL-3B and BL-20A. The installation of a high resolution electron analyzer is thus proposed for the extreme high resolution photoemission spectroscopy. The system consists of a SCIENTA SES-200 electron analyzer with a 200mm hemispherical analyzer, pre-focusing lenses and a two-dimensional detection system(Fig.11). High resolution photoemission measurements are expected to give a total resolution

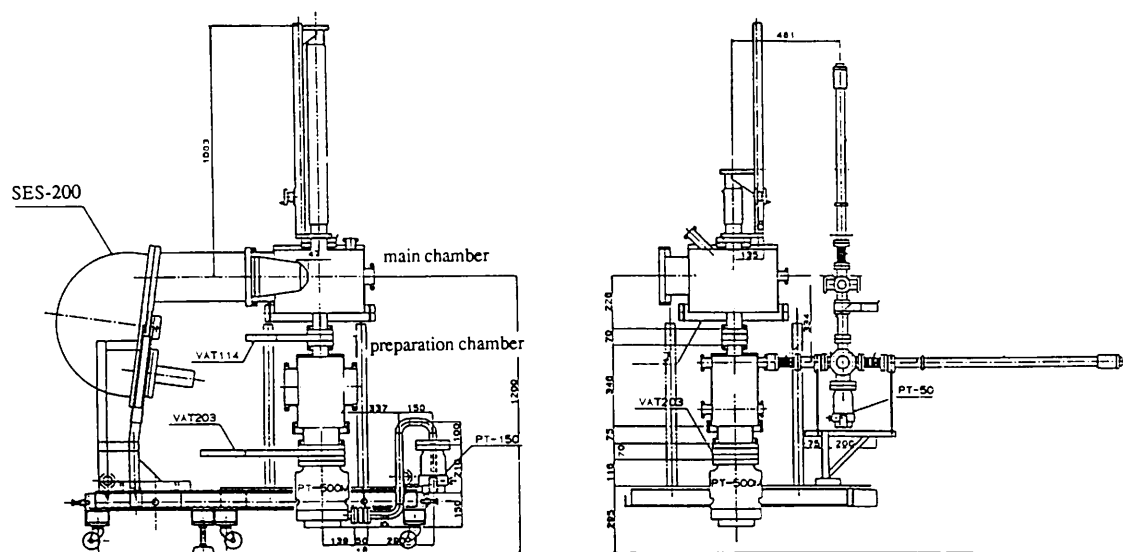


Fig. 11 Side (left) and top (right) views of a high resolution electron analyzer for the extreme high resolution photoemission spectroscopy.

of better than 10meV for low-photon energy UPS in the valence band and the Fermi-edge regions. After the special proposal for this purpose was accepted in June 1994, the construction of the vacuum chamber and analyzer was started.

As reported in the previous activity report, the main chamber is evacuated by tandem turbomolecular pumps (TMP) of 1500//s and 150//s, and the sample preparation chamber is pumped by a sputter ion pump. The resulting base pressure is less than 4×10^{-11} Torr in the main chamber when the analyzer chamber is not connected. The vacuum system is controlled by a systematic controller with a vacuum interlock for safety reasons.

In addition, the main chamber is equipped with a He-flow-type cryostat (High-Tran UHV183-IS-102) for cooling sample down to about 10K. It takes about an hour to cool down sample to the saturated temperature. Such a very low temperature is really necessary for high resolution photoemission spectroscopy, because of broadening effect due to lattice vibrations. An UV-lamp (PHI) is also available in order to calibrate various properties of the SES-200 analyzer.

The sample preparation chamber is equipped with a diamond file for cleaning sample surface. It will be possible to attach LEED-AES optics to ICF 203 flange, not only for checking the degree of contamination but also for the study of single crystals or

adsorbates on crystal surfaces.

2. THE TITANIUM SAPPHIRE/DYE LASER SYSTEM

A laser system for experiments combining synchrotron radiation and laser photons has been installed. The primary purpose is to study photoionization of laser excited gas phase metal vapours at BL-3B. However, proposals for other types of experiments as well as usage at nearby beamlines are also welcomed. It is currently located under the BL-3B platform and consists of the following components.

1. Coherent Radiation 899-21 single mode stabilized ring titanium-sapphire and dye lasers: The wavelength coverage with the currently available optics sets range from 530 nm to 700 nm (dye configuration) and 690 nm to 1000 nm (Ti-Sapphire configuration). Single mode power from 400 mW to 1.2 W is available, depending on the wavelength.
2. Coherent Radiation Innova 400-15 Ar laser: This is for the pumping of CR 899-21, but can be also used by itself. Power: 15 W multi-line visible, 7 W for 514 nm single line.
3. Accessories:
 - Burleigh wave meter (resolution $\Delta\lambda=0.001$ nm).
 - Coherent Radiation spectrum analyzer (FSR = 7.5 GHz).
 - Newport optical table (3m \times 1.2m).

3. SCANNING X-RAY MICROSCOPE USING CIRCULARLY POLARIZED RADIATION AT THE NE-1B FOR THE OBSERVATION OF FERROMAGNETIC DOMAINS

A scanning x-ray microscope using X-ray focusing optical system with a zone plate was constructed in the beamline NE-1B. It aims at the imaging of magnetic domains as well as the position and element specific spectromicroscopy of magnetic materials using circular polarization with a spatial resolution approaching several tens nano-meters in the future.

Figure 12(a) shows an optical arrangement of the scanning x-ray microscope. The circularly polarized radiation is produced under a helical undulator operation mode of the EMPW # NE1¹⁾. The undulator radiation is monochromatized by the NE1B-SGM²⁾ and then post-focused. There is a pre-pinhole (PPH) at the post-focused point to collimate the X-ray beam. Regarding PPH as a secondary light source, the X-ray beam is focused onto a sample by a reduction optical system using a zone plate (ZP). The spatial resolution is simply determined by the

size of PPH and the reduction ratio of the optical system. As we can select one of several PPH's, the appropriate spatial resolution can be chosen. The focused beam is incident at an angle of 30° from the surface of the sample to obtain the MCD contrast because the magnetization direction of the sample is in plane. Photoelectron yield is counted using a channel electron multiplier. A micro-channel plate (MCP) is used to monitor the x-ray image for the optical alignment. A scanning unit consists of x-y coarse stages driven by pulse motors and x-y fine stages driven by piezoelectric actuators. The structure of a single fine stage is a monolithic parallel spring stage with flexure hinges and a magnification lever. The lever magnifies a motion of a piezoelectric actuator with a magnification ratio of 2. The fine stages can scan the sample two dimensionally with the smallest step of 10 nm. The specifications of the scanning unit are summarized in Table 3. Figure 12(b) shows a schematic top view of the apparatus. All elements except for the scanning unit are mounted inside a vacuum chamber. The sample is connected to the scanning unit through the flexible welded bellows. The position of the order selecting

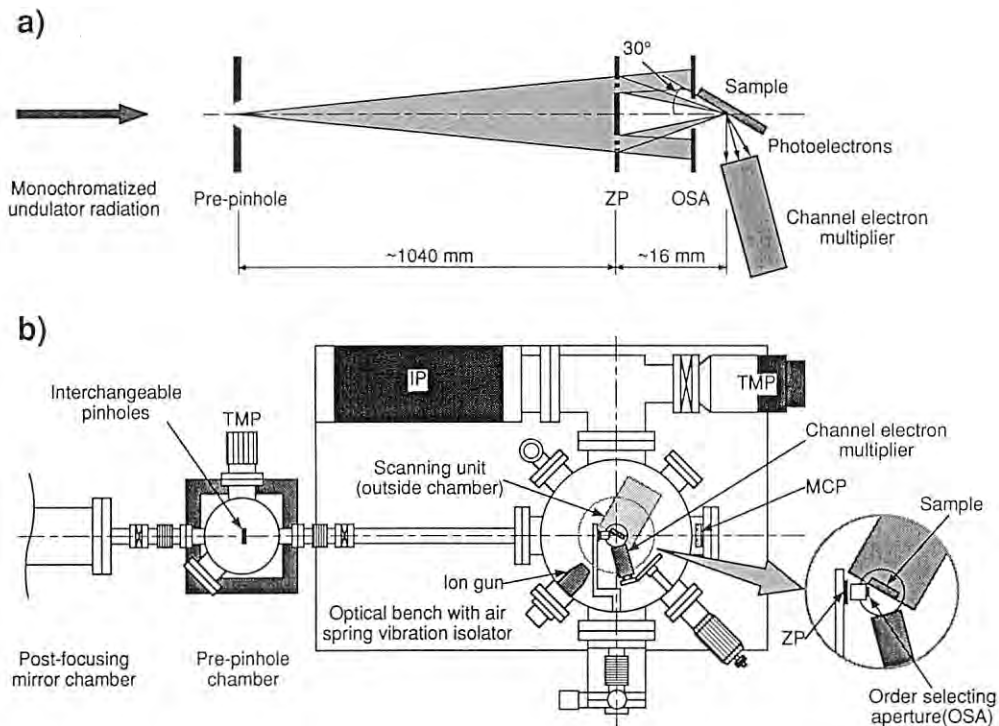


Fig. 12 Schematic (a) optical arrangement and (b) top view of the apparatus of a scanning x-ray microscope at the NE-1B.

Table 3 Specifications of a scanning unit

Coarse stages	Step width	Repeatability	Movable range
	0.5 μm /pulse	$\pm 1\mu\text{m}$	$\pm 12.5\text{mm}$
Fine stages	Resolution	Movable range	
	(operated with linear encoder) 10 nm	$\pm 45\mu\text{m}$	

aperture (OSA) is fixed, while ZP can be aligned using the manipulator. The surface of the sample can be sputtered using an ion gun. Measuring the photoelectron yield (I) and the incident intensity (I_0), the sample is scanned two dimensionally. The I_0 is at present the photoelectric current of the final mirror, M6, of the beamline²⁾. The two dimensional distribution of the normalized photoelectron yield (I/I_0) is displayed as an microscopic image.

A resolution test was made using a copper # 2000 mesh as a sample. The PPH was 50 μm ϕ . The photon energy was tuned to the L_3 absorption edge of copper (933 eV), at which the ideal spatial resolution was $\sim 0.9 \mu\text{m}$. A vertical line scan profile of an image of a wire of the mesh is shown in Fig.13. A criterion of 90%-10% intensity in an edge scan profile gave the resolution of $\sim 1.2 \mu\text{m}$, which was in good agreement with the ideal value of $\sim 0.9 \mu\text{m}$. The resolution was limited by the photon flux. The results of the observation of the magnetic domains is also shown somewhere of this volume and elsewhere³⁾.

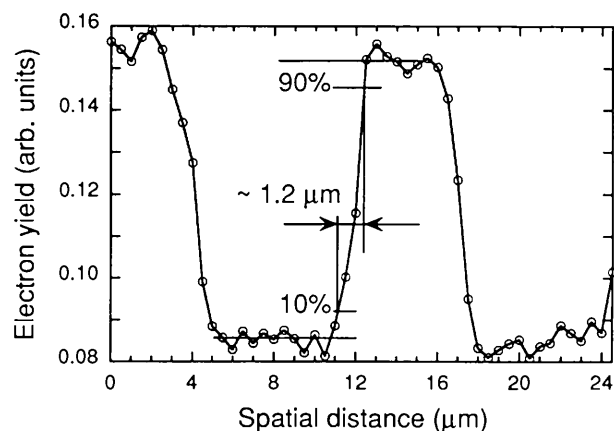


Fig. 13 A vertical line scan profile of an image of a wire of the mesh. The resolution was evaluated to be $\sim 1.2 \mu\text{m}$.

References

- 1) S. Yamamoto, H. Kawata, H. Kitamura, M. Ando, N. Sakai, and N. Shiotani, Phys. Rev. Lett. **62**, (1989) 2672, S. Yamamoto, T. Shioya, S. Sasaki and H. Kitamura, Rev. Sci. Instrum. **60** (1989) 1834.
- 2) Y. Kagoshima, T. Miyahara, S. Yamamoto, H. Kitamura, S. Muto, S.-Y. Park and J.-D. Wang, Rev. Sci. Instrum. **66** (1995) 1696.
- 3) Y. Kagoshima, T. Miyahara, M. Ando, J.-D. Wang and S. Aoki, Rev. Sci. Instrum. **66** (1995) 1534.

List of Experimental Stations

Experimental Station	Contact person
BL-1 [NTT]	
A Solid surface analysis	M. Oshima
[PF]	
B	K. Kobayashi
C	K. Tanaka
BL-2 (Undulator)	
A Soft X-ray spectroscopy	Y. Kitajima
B1 Soft X-ray microscopy	Y. Azuma
B2 Soft X-ray spectroscopy	Y. Azuma
BL-3	
A X-ray diffraction and scattering	M. Tanaka
B VUV and soft X-ray spectroscopy	E. Shigemasa
C1 X-ray diffraction	T. Matsushita
C2 X-ray topography in milli-Kelvin region (for solid helium)	T. Nakajima
BL-4	
A Trace element analysis, X-ray microprobe	A. Iida
B Liquid/melt structure analysis, powder diffraction, micro-crystal structure analysis	K. Ohsumi
C X-ray diffuse scattering, fluorescent EXAFS	Y. Murakami
BL-6	
A Macromolecular crystallography by Weissenberg camera	N. Watanabe
B X-ray spectroscopy and diffraction	M. Nomura
C1 X-ray diffraction at low temperatures	T. Nakajima
C2 Accurate lattice spacing measurement	M. Ando
BL-7 [The Research Center for Spectrochemistry, The Univ. of Tokyo]	
A Soft X-ray photoelectron spectroscopy	H. Namba
B Surface photochemical reaction and angle resolved photoelectron spectroscopy	H. Namba
[PF]	
C X-ray spectroscopy and diffraction	M. Nomura
BL-8 [Hitachi]	
A Soft X-ray spectroscopy	Y. Hirai
B EXAFS	A. Nakano
C1 X-ray lithography	M. Itou
C2 X-ray tomography and X-ray microscopy	K. Usami
BL-9 [NEC]	
A X-ray lithography	K. Suzuki
B Photochemical reaction	I. Nishiyama
C EXAFS and X-ray topography/diffraction	J. Mizuki
BL-10	
A X-ray diffraction/scattering, crystal structure analysis	M. Tanaka
B XAFS	N. Usami
C Small-angle X-ray scattering of enzymes, surface diffraction	K. Kobayashi
BL-11	
A Soft X-ray spectroscopy	T. Sekitani
B Surface EXAFS, soft X-ray spectroscopy	Y. Kitajima
C VUV spectroscopy (solid state)	H. Kato
D Angle-resolved photoelectron spectroscopy	H. Kato

Experimental Station	Contact person
BL-12	
A Soft X-ray spectroscopy (under construction)	K. Tanaka
B VUV high-resolution spectroscopy	K. Ito
C Photochemical reaction XAFS (from July 1994)	M. Nomura
BL-13 (Multipole wiggler/Undulator) [Research team for advanced materials*]	
A Accurate lattice parameter measurement	K. Nakayama
B1 Surface-sensitive XAFS, X-ray diffraction	H. Oyanagi
B2 High pressure & high temperature X-ray diffraction	O. Shimomura
C Soft X-ray photoemission spectroscopy and XAFS	H. Shimada
BL-14 (Vertical wiggler)	
A Crystal structure analysis, EXAFS	S. Kishimoto
B High-precision X-ray optics	K. Hirano
C General purpose (X-rays)	O. Shimomura
BL-15	
A Small-angle X-ray scattering of muscle and alloys	Y. Amemiya
B White X-ray topography and X-ray magnetic bragg scattering	H. Kawata
C High-resolution X-ray diffraction	K. Hirano
BL-16 (Multipole wiggler/Undulator)	
A General purpose (X-rays)	K. Takeshita
U Soft X-ray spectroscopy	E. Shigemasa
BL-17 [Fujitsu]	
A XAFS	S. Komiya
B Photochemical vapor deposition	S. Komiya
C Grazing incident X-ray diffraction, X-ray fluorescence analysis	S. Komiya
BL-18 [The Institute for Solid State Physics, The Univ. of Tokyo]	
A Angle-resolved photoelectron spectroscopy of surfaces and interfaces [PF]	A. Kakizaki
B Macromolecular crystallography (Weissenberg and Laue)	N. Watanabe
BL-19 (Revolver undulator) [The Institute for Solid State Physics, The Univ. of Tokyo]	
A Spin-resolved photoelectron spectroscopy (Mott detector)	A. Kakizaki
B Spin-resolved photoelectron spectroscopy (SPLEED) Soft X-ray emission spectroscopy	A. Kakizaki
BL-20 [PF]	
A VUV spectroscopy [Australia]	K. Ito
B White and monochromatic beam general purpose X-ray station	G. Foran
BL-21 [Light Source Division]	
Beam position monitoring	T. Katsura
BL-27 (Beamline for experiments using radioisotopes, under construction)	
A Radiation biology, Soft X-ray photoelectron spectroscopy	K. Kobayashi
B Radiation biology, X-ray diffuse scattering	K. Kobayashi
BL-28 (Multipole wiggler/Undulator)	
A VUV and soft X-ray spectroscopy with circularly polarized undulator radiation	T. Miyahara
B Spectroscopy and scattering with polarized X-rays	T. Iwazumi

Experimental Station	Contact person
AR-NE1 (EMPW#NE1)	
A1 High resolution Compton and magnetic Compton scattering	H. Kawata
A2 Spectroscopy and scattering with circularly polarized X-rays	T. Iwazumi
B Spectroscopy and microscopy with circularly polarized soft X-rays	Y. Kagoshima
AR-NE3 (Undulator#NE3)	
A1 Nuclear resonant scattering	X. Zhang
A2 Surface and interface diffraction	H. Sugiyama
AR-NE5	
A Angiography and X-ray computed tomography	K. Hyodo
C High pressure and high temperature X-ray diffraction	T. Kikegawa
AR-NE9	
A In desing	M. Ando
B Vacuum science and technology	K. Kanazawa

* National Laboratory of Metrology, National Institute of Researches in Inorganic Materials, Electrotechnical Laboratory, National Institute of Materials and Chemical Research, The Institute of Physics and Chemical Research

X-ray Beamline Optics

Branch Beam Line	Acceptance Horiz. (mrad)	Beam Size (H×V)	Photon Flux at Sample Position	Type of Monochromator	Energy Resolution ($\Delta E/E$)×10 ⁻⁴	Photon Energy (keV)	Mirror	Reference
BL-3A	4	100×5 4×0.1		Double Crystal Si(111) Sagittal Focusing	~ 2	4 ~ 25	Collimating and Focusing Mirrors (Fused Quartz)	1, 2, 3, 4 5, 6
BL-3C1/C2	2	20×4		None		4 ~ 30	None	7, 8, 9
BL-4A	6	50×4 4×1		Double Crystal Sagittal Focusing	~ 2	4 ~ 20	None	10
BL-4B	4.5	50×5		Double Crystal Si(111)	~ 2	4 ~ 35	None	11
BL-4C	4	4×1		Double Crystal Si(111) Sagittal Focusing	~ 2	4 ~ 20	None	12
BL-6A	4	2.5×1		Bent Si(111) ($\alpha = 0, 6.0^\circ, 7.8^\circ, 9.5^\circ, 11.4^\circ, 13.7^\circ, 16.5^\circ$)		5 ~ 25	Bent Plane Fused Quartz	13
BL-6B	4	8×1	1×10 ¹⁰ /6mm ² (8 keV, 300 mA) (1×10 ¹¹ when focused)	Double Crystal Si(220), Si(111), Si(311) Sagittal Focusing with Si(111)	~ 2	4 ~ 25 (4 ~ 13)	None	14, 15, 16
BL-6C1	4	37×5		None		8 ~ 30		7, 8, 17, 18
BL-6C2	0.5	5×5		Channel-Cut Si (111)	7.5	8 ~ 12	None	
BL-7C	4	8×1	1×10 ¹⁰ /6mm ² (8 keV, 300 mA) (1×10 ¹¹ when focused)	Double Crystal Si (111) Sagittal Focusing	~ 2	4 ~ 20 (4 ~ 13)	Double Mirror Fused Quartz Focusing	14, 15, 16
BL-8C1/C2	5	50×5	6×10 ⁸ mm ² (10 keV, 300 mA) Si (111)	Channel-Cut Si(220), Si(111), Si(400)	~ 2	5 ~ 40	None	
BL-9A	5	25×25				1.2 ~ 3.1	SiC	
BL-9C	5	150×5		Double Crystal Si(111) Sagittal Focusing	~ 2	5 ~ 25	None	
BL-10A	1	10×3		Si(111), Si(220) Ge(111), InSb(111) Quartz(100), PG(002) Curved Si(111) ($\alpha \sim 4^\circ, 8^\circ$)	50 ~ 5	5 ~ 25	None	19

Branch Beam Line	Acceptance Horiz. (mrad)	Beam Size (H×V)	Photon Flux at Sample Position	Type of Monochromator	Energy Resolution ($\Delta E/E$)×10 ⁻⁴	Photon Energy (keV)	Mirror	Reference
BL-10B	2	8×1	1×10 ⁹ /7mm ² (10 keV, 300 mA)	Channel-Cut Si(311)	1	6 ~ 30	None	
BL-10C	4	6×1.5 (8 keV, 100 mA)	~10 ¹⁰ /9mm ² Si(111)	Double Crystal	2	4 ~ 10	Bent Cylinder	
BL-12C	2	1.3×0.6	5×10 ¹⁰ /1mm ²) (8.0 keV,) 300mA W.Si(111)	Double Crystal Si(111) Si(311)	~ 2	6~23	Bent Cylinder	
BL-13A	1			Double Crystal Si(220)	~ 0.1	4 ~ 30	None	
BL-13B1/B2	4	4×1		Double Crystal Si(111), Si(220) Sagittal Focusing	~ 2	4 ~ 30	Bent Plane Fused Quartz	
BL-14A	1.28 (Vertical)	5×38		Double Crystal Si (111) Si (311) Si (553)	2	5.1 ~ 19.1 9.9 ~ 35.6 22.7 ~ 84.5	Bent Cylinder for Vertical Focusing, Pt-coated Fused Quartz	20
BL-14B	2.2	5×30		Double Crystal Si(111), Si(220), Si(311)	2	5.2 ~ 57	None	
BL-14C	1.3	10×40		Double Crystal Si(111), Si(220)	2	5.5 ~ 69	None	
BL-15A	2	0.7×0.8 at focus	9×10 ¹⁰ /6mm ² (8.0 keV, 150 mA)	Bent Crystal Ge(111) ($\alpha = 8.0^\circ$)	~ 10	5.6 ~ 12.4	Bent Plane, Fused Quartz	21
BL-15B	0.14	5×5		None		3.5 ~ 34	None	
BL-15C	2	60×6		Double Crystal Si(111)		4 ~ 30	None	
BL-16A	4	4×1		Double Crystal Si(111) Sagittal Focusing	~ 2	4 ~ 35		
BL-17A	4	100×10		Double Crystal Si(111)	~ 2	5 ~ 13	None	22
BL-17C	1	20×5		Double Crystal Si (111)	~ 2	5 ~ 13	None	23
BL-18B	2	1.2×0.4	1.1×10 ¹⁰ (12.4 keV, 300 mA) Si(111)	Double Crystal Si (111) Si (220) Ge (111) Ge (220)	~ 2	6 ~ 30	Bent Cylinder Fused Quartz, Pt-coated	24

Branch Beam Line	Acceptance Horiz. (mrad)	Beam Size (H × V)	Photon Flux at Sample Position	Type of Monochromator	Energy Resolution ($\Delta E/E$) × 10 ⁻⁴	Photon Energy (keV)	Mirror	Reference
BL-20B	2	26 × 3		Channel Cut Si (111)	~ 2	4 ~ 25	None	25
BL-27B	4	100 × 10		Double Crystal Si (111)	~ 2	4 ~ 20	None	
BL-28B	4 × 0.2	2.4 × 0.3	3 × 10 ¹⁰ (9 keV, 300 mA) Si (220) Pc ~ 0.5	Double Crystal Si (111) Si (220) InSb (111)	3 (at 6.3 keV)	2 ~ 10	Pre-mirror Bent Cylinder Si Pt- & Ni-coated Post-mirror Bent Plane Fused Quartz Pt- & Ni-coated	26
NE-1A1	2	8 × 3	1 × 10 ¹⁰ (60.0 keV)	Double Bent Crystal Si(111)	0.15	0.25 × 10⁻⁴		
NE-1A2	2	80 × 4 3 × 4 3 × 0.5		Double Crystal Si(111) Single Focusing Si(111) Sagittal Focusing + Bent Mirror	2	6 ~ 28		
NE-3A1 3A2	H:0.3 V:0.03	15 × 2	1 × 10 ³ (14.4 keV)	Double Crystal Si(111) with fine monochromator of Si with Single Crystal ⁵⁷ Fe ₂ O ₃ (777)	1 5 × 10 ⁻³ 1 × 10 ⁻⁷	5 ~ 25		
NE-5A	10	150 × 8	5 × 10 ⁸ (33.2 keV)	Asym. Cut Single Crystal Si(311) or Si(511) ($\alpha = 4^\circ \sim 6^\circ$) Double Crystal Si(111)	0.6 1	20 ~ 60 20 ~ 50		27, 28
NE-5C	3	60 × 5	Si (111)	Double Crystal	1	30 ~ 100		29
NE-9A	5			not fixed Si (111)				
NE-9B	10		10 × 3	White beam				

References

- 1) K. Kawasaki et al., Rev. Sci. Instrum. **63** (1992) 1029.
- 2) K. Kawasaki et al., Rev. Sci. Instrum. **63** (1992) 1047.
- 3) T. Mori and S. Sasaki, Rev. Sci. Instrum. **66** (1995) 1.
- 4) PF-News, Vol. 9, No. 4 (1992).
- 5) Photon Factory Activity Report 1989 #7, I-1 (1990).
- 6) Photon Factory Activity Report 1990 #8, I-1 (1991).
- 7) T. Nakajima et al., Nucl. Instr. Meth. **A261**, (1987) 308.
- 8) T. Nakajima et al., Rev. Sci. Instrum. **66** (1995) 1400.
- 9) Photon Factory Activity Report 1989 #9, I-12 (1990).
- 10) A. Iida et al., Rev. Sci. Instrum. **66** (1995) 1373.
- 11) K. Ohsumi et al., Rev. Sci. Instrum. **66** (1995) 1448.
- 12) H. Iwasaki et al., Rev. Sci. Instrum. **60** (1989) 2406.
- 13) N. Sakabe et al., Rev. Sci. Instrum. **66** (1995) 1276.
- 14) M. Nomura and A. Koyama, KEK Report 93-1 (1993).
- 15) M. Nomura et al., KEK Report 91-1 (1990).
- 16) M. Nomura and A. Koyama, ed. by S.S.Hasnain, E. Horwood, Chichester **667** (1991).
- 17) Photon Factory Activity Report 1982/83, V-25 (1984).
- 18) Photon Factory Activity Report 1988 #6, I-16 (1989).
- 19) Photon Factory Activity Report 1982/3, V-7 (1984).
- 20) Y. Satow and Y. Iitaka., Rev. Sci. Instrum. **60** (1989) 2390.
- 21) Y. Amemiya et al., Nucl. Instr. Meth. **208** (1983) 471.
- 22) Photon Factory Activity Report 1988 #6, I-15 (1989).
- 23) Y. Horii et al., Rev. Sci. Instrum **66** (1995) 1370.
- 24) N. Watanabe et al., Rev. Sci. Instrum. **66** (1995) 1824.
- 25) R.F. Gareet et al., Rev. Sci. Instrum. **66** (1995) 1351.
- 26) T. Iwazumi et al., Rev. Sci. Instrum. **66** (1995) 1691.
- 27) K. Hyodo et al., Handbook on SR4 (1991) 55.
- 28) Y. Itai et al., Rev. Sci. Instrum. **66** (1995) 1385.
- 29) T. Kikegawa et al., Rev. Sci. Instrum **66** (1995) 1335.

VUV and Soft X-ray Monochromators

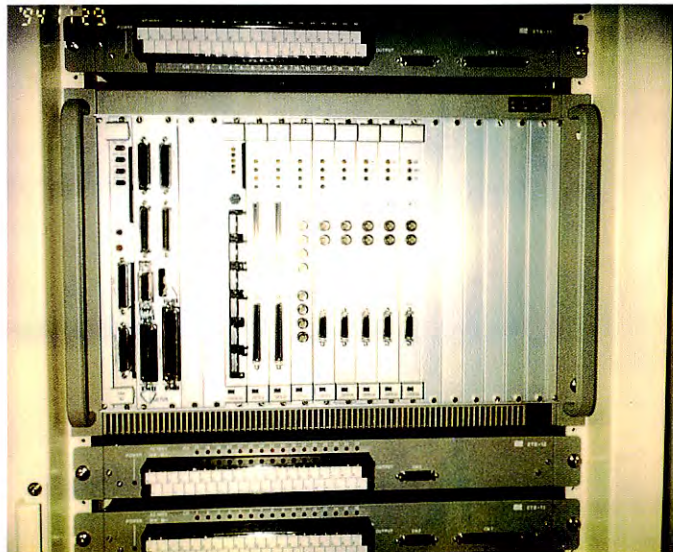
Branch Beamline	Acceptance Horiz./Vert. (mrad)	Type of Monochromator	Grating Groove density (l/mm)	Photon Energy (eV)	Beam Size (mm)	Typical Resolution ($\lambda/\Delta\lambda$)	Reference
BL-7B (RCS)	6 4	1m Seya-Namioka	1200 2400	5 ~ 50	1 × 1	1000	1
BL-11C	4.8 3	1m Seya-Namioka	1200	4 ~ 35	~1 ϕ	1000	2
BL-12B	5 3.6	6.65 m Off-Plane Eagle	1200 4800	5 ~ 30	---	2.5×10^5	3,4
BL-20A	28 5	3m Normal Incidence	1200 2400	5 ~ 40	2 × 1	3×10^4	5
BL-1A (NTT)	4 0.5	Grating/Crystal	1200 2400	50 ~ 900	4 × 1	500	6
BL-1B	1.2 4	----	----	----	----	----	
BL-1C'	2 4	----	----	----	----	----	
BL-2B2 Undulator	K = 0.55 ~ 2.2 $\lambda_u = 6$ cm	10 m Grazing Incidence $\alpha = 89^\circ$	1200 2400	250 ~ 1600	< 0.2 ϕ	500 ~ 5000	7, 8, 9
BL-3B	10 2	Grazing Incidence R = 24 m $\alpha + \beta = 165^\circ$	200 600 1800	10 ~ 280	< 2 ϕ	200 ~ 3000	10, 11
BL-7A (RCS)	6 1	Plane Grating	1200 2400	10 ~ 1000	2 × 1	500	12
BL-8A (Hitachi)	0.5 1	Varied-space Plane Grating	800 2400	40 ~ 1800	5 × 1	1000	13
BL-11A	1 0.5	2 m Grazing Incidence $\alpha = 88^\circ$ Grasshopper Mark VII	600 1200 2400	40 ~ 1000	< 1 ϕ	200 ~ 2000	14
BL-11D	1.5 2	Grazing Incidence R = 2 m $\alpha + \beta = 154^\circ$	600 1200 2400	20 ~ 150	1.5 ϕ	100 ~ 1500	15
BL-13C Undulator	K = 0.3 ~ 4.2 $\lambda_u = 18$ cm	Grazing Incidence R = 50 m $\alpha + \beta = 173.2^\circ$	750	140 ~ 1000	5 × 1	1000 ~ 6000	16, 17
BL-16U Undulator	K = 0.5 ~ 5.75 $\lambda_u = 12$ cm	2 m Grazing Incidence $\alpha = 87^\circ$	1200 2400	40 ~ 600	----	1400 ~ 2500	18, 19
BL-18A (ISSP)	2 2	Grazing Incidence R = 3 m $\alpha + \beta = 160^\circ$ R = 6.65 m $\alpha + \beta = 167.5^\circ$	300 600 1200 500	7 ~ 150	< 1 ϕ	1000 ~ 2000	20
BL-19A Revolver Undulator (ISSP)	K = 1.0 ~ 9.0 $\lambda_u = 16.4$ cm	Grazing Incidence R = 2 m $\alpha + \beta = 160^\circ$ R = 4 m $\alpha + \beta = 170^\circ$	600 1200 600 1200	12 ~ 250	< 0.7 ϕ	1000	21, 22

Branch Beamline	Acceptance Horiz./Vert. (mrad)	Type of Monochromator	Grating Groove density (l/mm)	Photon Energy (eV)	Beam Size (mm)	Typical Resolution ($\lambda/\Delta\lambda$)	Reference
BL-19B Revolver Undulator (ISSP)	$K = 0.5 \sim 1.25$ $\lambda_u = 5 \text{ cm}$ $K = 0.5 \sim 2.5$ $\lambda_u = 7.2 \text{ cm}$ $K = 1.0 \sim 5.0$ $\lambda_u = 10 \text{ cm}$	Varied-space Plane Grating	800 2400	10 ~ 1200	$< 0.5 \phi$	1500~4000	22
BL-28A Undulator	$K_x = 0.5 \sim 3$ $K_y = 0.5 \sim 0.75$ $\lambda_u = 16 \text{ cm}$	Grazig Incidence $R = 2 \text{ m}$ $\alpha + \beta = 160^\circ$ $R = 4 \text{ m}$ $\alpha + \beta = 170^\circ$	600 1200 600 1200	15 ~ 250	$< 0.5 \phi$	1000	23
BL-1A (NTT)	4 0.5	Grating/Crystal InSb (111) Si (111)	----	1800 ~ 4000	4×1	2000	6
BL-2A Undulator	$K = 0.5 \sim 2.2$ $\lambda_u = 6 \text{ cm}$	Double Crystal InSb (111) Si (111)	----	1760 ~ 5000	2ϕ	5000	7, 24
BL-8B (Hitachi)	3 0.5	Double Crystal InSb (111) Si (311)	----	1700 ~ 14000	1.9×0.5	5000	----
BL-11B	4 0.6	Double Crystal InSb (111)	----	1760 ~ 3650	8×1	2000	25, 26
BL-27A	5 0.5	Double Crystal InSb (111)	----	1800 ~ 6000		2000	
BL-1B (NTT)	1.2 4	Plane Mirror	----	----	5×1	----	
BL-1C (NTT)	2 4	Toroidal Mirror	----	----	3×5	----	27
BL-2B1 Undulator	$K = 0.55 \sim 2.2$ $\lambda_u = 6 \text{ cm}$	Zone Plate	----	400 ~ 830	$\sim 0.01\phi$	50	28, 29, 30
BL-9A (NEC)	5 0.3	Oscillating Mirror	----	----	----	----	31
BL-9B (NEC)	10	Plane + Toroidal Mirrors	----	----	15×20	----	31
BL-12C	5 1	Toroidal + Multilayer Mirrors	Rh - Si 21 Layers Rh - C 21 Layers	80 ~ 103 89 ~ 124	2×1	12 15	32
BL-17B (Fujitsu)	8 1	Toroidal Mirror	----	----	10×1	----	
NE-1B	~ 0.2 0.02	Grazig Incidence $R = 10 \text{ m}$ $\beta = 89^\circ$	1200 2400	250 ~ 1800	$\sim 0.8 \times 0.2$	5000 400eV, slit: $10_{\mu\text{m}} - 10_{\mu\text{m}}$	33

References

- 1) H. Namba et al., Rev. Sci. Instrum. **60** (1989) 1917.
- 2) Photon Factory Activity Report 1982/1983 V-15 (1984).
- 3) K. Ito et al., Appl. Opt. **25** (1986) 837.
- 4) K. Ito et al., Appl. Opt. **28** (1989) 1813.
- 5) K. Ito et al., Rev. Sci. Instrum. **66** (1995) 2119.
- 6) T. Kawamura et al., Rev. Sci. Instrum. **60** (1989) 1928.
- 7) H. Maezawa et al., Nucl. Instrum. and Meth. **A246** (1986) 310.
- 8) H. Maezawa et al., Rev. Sci. Instrum. **60** (1989) 1889.
- 9) A. Yagishita et al., Rev. Sci. Instrum. **63** (1992) 1351.
- 10) A. Yagishita et al., KEK Preprint 90-132 (1990).
- 11) S. Masui et al., Rev. Sci. Instrum. **63** (1992) 1330.
- 12) H. Namba et al., Rev. Sci. Instrum. **60** (1989) 1909.
- 13) M. Itou et al., Appl. Opt. **28** (1989) 146.
- 14) M. Yanagihara et al., KEK Report 84-17 (1984).
- 15) T. Miyahara et al., Jpn. J. Appl. Phys. **24** (1985) 293.
- 16) M. Matsubayashi et al., Rev. Sci. Instrum. **63** (1992) 1363.
- 17) H. Shimada et al., Rev. Sci. Instrum. **66** (1995) 1780.
- 18) Y. Muramatsu and H. Maezawa, Rev. Sci. Instrum. **60** (1989) 2078.
- 19) Y. Muramatsu et al., Rev. Sci. Instrum. **63** (1992) 1305.
- 20) S. Suzuki et al., Activity Report of SRL-ISSP 60 (1989).
- 21) A. Kakizaki et al., Rev. Sci. Instrum. **63** (1992) 1289.
- 22) S. Shin et al., Rev. Sci. Instrum. **66** (1995) 1584.
- 23) A. Kakizaki et al., Rev. Sci. Instrum. **60** (1989) 367.
- 24) Y. Kagoshima et al., Rev. Sci. Instrum. **63** (1992) 1289.
- 25) Y. Kitajima et al., Rev. Sci. Instrum. **63** (1992) 886; T. Ohta et al., Nucl. Instrum. and Meth. A **246** (1986) 373.
- 26) M. Funabashi et al., Rev. Sci. Instrum. **60** (1989) 1983.
- 27) T. Urisu et al., Rev. Sci. Instrum. **60** (1989) 2157.
- 28) Y. Kagoshima et al., Jpn. J. Appl. Phys. **29** (1989) L 172.
- 29) Y. Kagoshima et al., Rev. Sci. Instrum. **60** (1989) 2448.
- 30) Y. Kagoshima et al., Rev. Sci. Instrum. **63** (1992) 605.
- 31) Photon Factory Activity Report 1988 #6, I-13 (1989).
- 32) Photon Factory Activity Report 1988 #6, I-11 (1989).
- 33) Y. Kagoshima et al., Rev. Sci. Instrum. **66** (1995) 1696.

Accelerator Operations, Researches and Developments



The VME system used for global feedback

You can jump to the article by clicking its title.

CONTENTS

	Page
A. INJECTOR LINAC	A - 1
B. PF STORAGE RING	A - 2
1. SUMMARY OF THE STORAGE-RING OPERATIONS	A - 2
2. EMITTANCE UPGRADE PROGRAM	A - 4
2.1 Field Measurement of Model Magnets for a High-Brilliance Configuration (II)	A - 4
2.2 Performance Test of the Global Feedback DSP Board	A - 6
3. STORAGE RING SPECIFICATIONS	A - 7
C. TRISTAN ACCUMULATION RING	A - 17
1. SPECIFICATIONS OF THE TRISTAN ACCUMULATION RING	A - 17

A. INJECTOR LINAC

During this period, the linac has been stably operated with a total operation time of 5,322.5 hours and a high operation rate of 99.1%. Operation statistics for this period are listed in Table 1. There was no severe failure which took comparatively long recovering time during this run.

Table 1 Operation and failure time during this period.

Date	Operation time (hrs)	Failure time (hrs)	Operation rate (%)
FY1993			
Sep. 27 - Nov. 10	1036.0	17.1	98.3
Nov. 16 - Dec. 24	899.5	7.7	99.1
Feb. 8 - Mar. 31	1235.0	7.0	99.4
FY1994			
Apr.1 - July 1	2152.0	14.8	99.3
total	5322.5	46.6	99.1

The cumulative usage hours of klystrons and the averaged fault rate with averaged applied anode voltage are shown in Tables 2 and 3, respectively. Cumulative status of klystrons up to the end of this term are summarized in Table 4.

Table 3 Averaged fault rate and averaged applied voltage to klystrons.

Period	Fault rate (/daytube)	Applied voltage (kV)	Total operation (tube days)
1985/8-1986/7	1.0	238	5,600
1986/8-1987/7	1.0	239	7,740
1987/8-1988/7	1.0	240	9,990
1988/8-1989/7	0.6	241	10,510
1989/8-1990/7	0.3	244	10,690
1990/8-1991/7	0.2	246	10,750
1991/8-1992/7	0.1	248	10,140
1992/8-1993/7	0.1	247	10,010
1993/8-1994/7	0.1	245	10,580

Table 2 Cumulative usage hours of klystrons during the past years.

Period	Total	Unused	Failed		Living		MTBF
	No. of tubes	No. of tubes	No. of tubes	Mean age (hours)	No. of tubes	Av. op. time (hours)	(hours)
up to 1985/7	79	2	28	3,600	49	6,200	13,400
up to 1986/7	91	3	39	4,400	49	7,400	13,100
up to 1987/7	106	4	52	4,400	50	9,600	13,600
up to 1988/7	120	2	67	4,500	51	11,400	13,500
up to 1989/7	140	5	82	6,400	53	12,400	14,400
up to 1990/7	158	6	98	8,500	54	11,200	14,700
up to 1991/7	176	14	107	10,100	55	11,100	15,800
up to 1992/7	191	24	113	10,800	54	13,400	17,100
up to 1993/7	203	19	123	10,800	56	15,300	17,700
up to 1994/7	217	30	130	10,900	57	17,800	18,700

Table 4 Cumulative status of klystrons up to July 1994 corresponding to the year of production. Unused tubes are those which have never been used in the klystron gallery. STB(stand-by) tubes are those which have been used in the gallery and can be used there again.

Year of product	Total No. of tubes	Unused No. of tubes	Living				Failed				Cumulative operation (tube-hours)	MTBF (hours)		
			No. of (STB tubes)	Working	Av.op.time (hours)	e-	e+	No. of tubes (arc)	Causes (window others)	Mean age (hours)				
1987	7	0	5	0	5	0	33,220	2	0	1	1	16,748	199,594	99,797
1988	20	1	14	3	8	3	24,380	5	0	4	1	14,961	416,128	83,226
1989	18	1	10	0	9	1	24,306	7	0	5	2	12,002	327,079	46,726
1990	18	6	7	1	5	1	17,318	5	0	4	1	10,773	175,087	35,017
1991	15	5	5	0	4	1	6,258	5	0	4	1	4,411	53,343	10,669
1992	12	2	10	1	8	1	6,816	0	0	0	0	—	68,163	—
1993	14	13	1	0	1	0	2,224	0	0	0	0	—	2,224	—
total	104	28	52	5	40	7	18,719	24	0	18	6	11,176	1,241,618	51,734

B. PF STORAGE RING

1. SUMMARY OF THE STORAGE-RING OPERATIONS

A summary of the operation times of the storage ring is given in Fig. 1. Table 5(a) shows the operation statistics for the fiscal year 1993, and (b) those of between March 28 and December 22, 1994. Machine-failure times are given in Fig. 2. The injection intervals and average currents are given in Fig. 3. The initial stored current is 370 mA for user-runs and the beam lifetime is 70-80 hours at 300 mA. The average stored current is about 320 mA during 24-hours of operation. In single-bunch runs, initial current is 65 mA and the beam lifetime at 50 mA is 20-30 hours. During single-bunch runs, as a beam current in the main bucket decays, number of positrons in the next bunch gradually increases. In the PF storage ring, a cleaning of the beams in the next buckets routinely takes place by continuous running of the RF knock-out with the vertical scrapers at the straight section B04-B05. The ratio of the satellite bunch to the main one was maintained less than 10^{-6} during the routine user-runs. Figure 4 is a plot of $I \tau$ (beam current \times lifetime), which is being maintained at around 1400-1500 A-min.

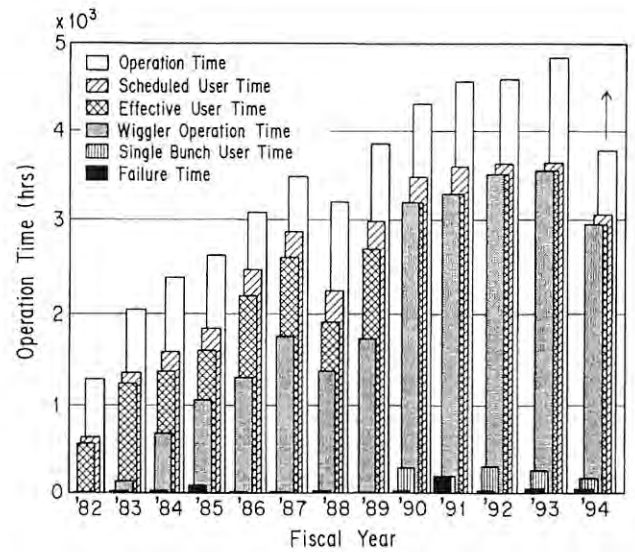


Fig. 1 Operation times of the storage ring.

Table 5(a) Statistics of the storage ring operation during fiscal year 1993.

	Multi-bunch	Single-bunch	Total
Ring Operation Time (hours)	—	—	4908.0
Scheduled user time (hours)	3435.0	312.0	3747.0
Net user time T (hours)	3328.2	228.7	3556.9
Time used for injection (hours)	69.1	15.1	84.2
Integrated current in T (A-hours)	1075.0	13.8	1088.8
Average current in T (mA)	323.0	47.9	—
Number of injections	179	28	207
Interval between injections (hours)	18.6	10.3	—

Table 5(b) Statistics between March 28 and December 22, 1994.

	Multi-bunch	Single-bunch	Total
Ring Operation Time (hours)	—	—	3772.0
Scheduled user time (hours)	2904.0	114	3048.0
Net user time T (hours)	2830.8	133.4	2964.2
Time used for injection (hours)	69.5	9.7	79.2
Integrated current in T (A-hours)	871.3	6.4	877.7
Average current in T (mA)	307.8	47.8	—
Number of injections	143	12	155
Interval between injections (hours)	19.8	11.1	—

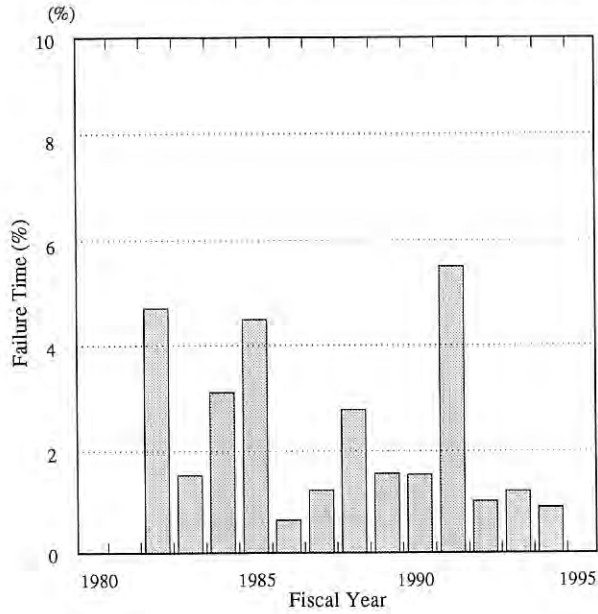


Fig. 2 Rate of failure time of the storage ring operation.

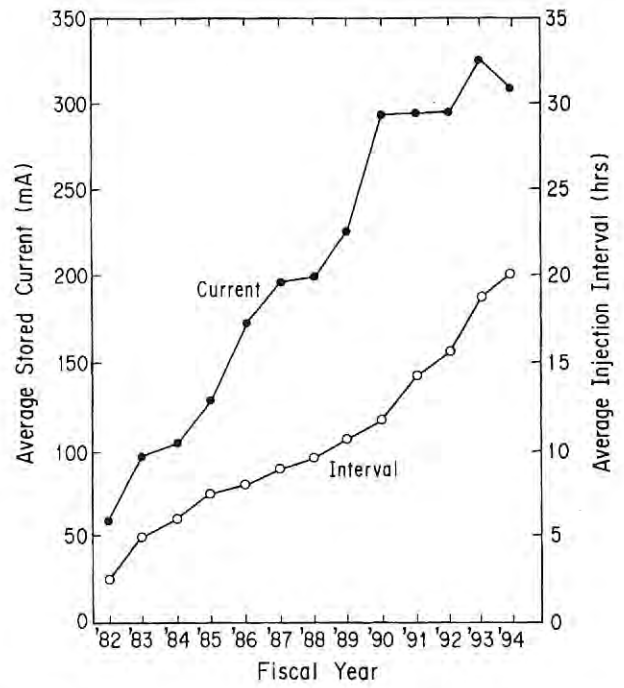


Fig. 3 Average stored currents and injection intervals.

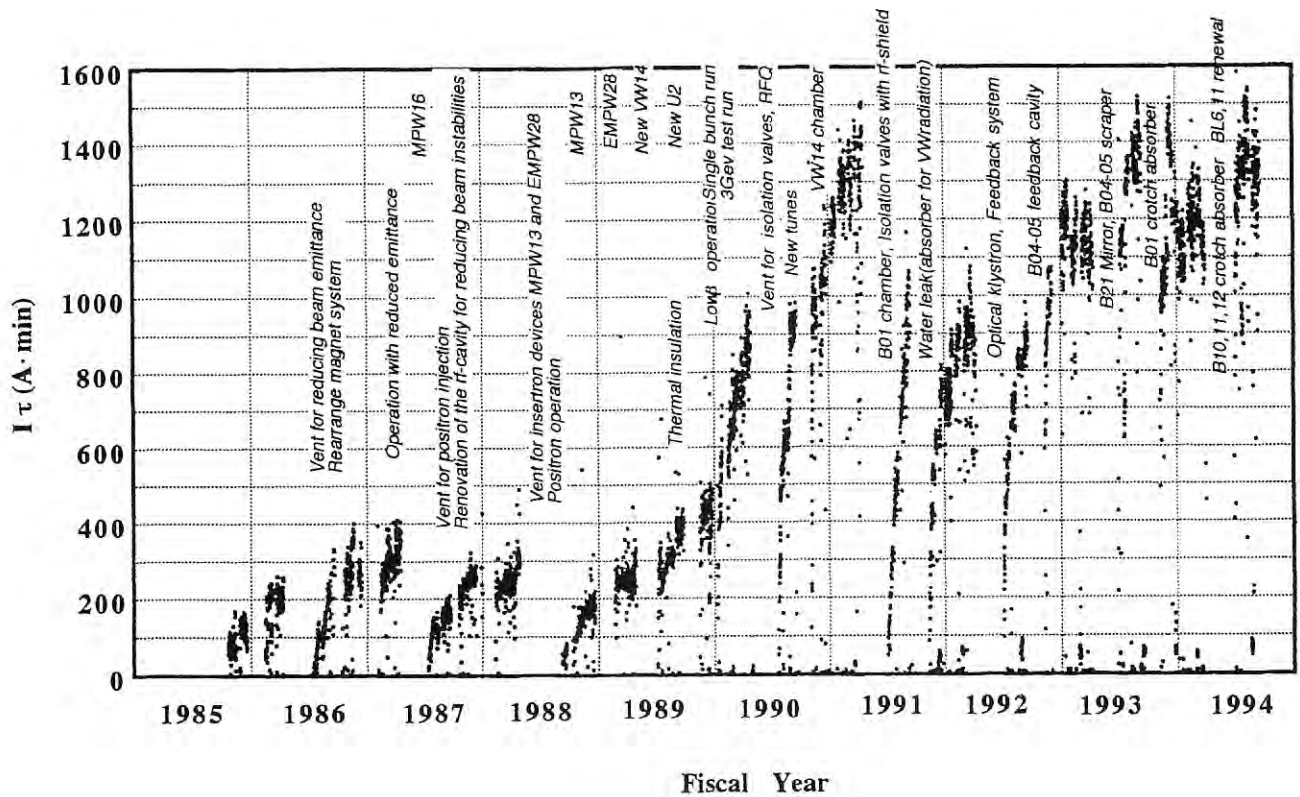


Fig. 4 Plot of $I\tau$

The FEL-research in the VUV-region is underway at the PF storage ring using BL02. A gain measurement at 177 nm is our present goal. For the gain measurement, we will use 6th-harmonics of a Nd-YAG laser light as an external coherent light of 177 nm, which is successfully produced with a high peak power in 1993 by using a nonlinear-optical crystal system. An optical pass to transport the incident 177 nm light from the laser source to the optical klystron will be constructed during 1995 by using three LiF lenses. This optical system will create laser-beam having a waist of 500 μm in diameter at the center of the optical klystron. A precise matching on the incident laser-beam and the circulating positron-beam is required both for their positions and timings. Measurement errors in the positions of the positron beams should be less than 50 μm at the center of the optical klystron. We are attempting to know the positron-beam positions by measuring the profiles and angles of the spontaneous emission using an optical system installed in the downstream. During 1994, we tried the measurements by a system using VUV-lenses. However, the position error was in an order of 100 μm due to chromatic aberration. In order to improve the measurement error, a spherical-mirror system will be installed in the downstream of the optical klystron in February of 1995.

Since 1988, positrons have been used for the routine-user runs at the PF storage ring. Under the electron operations, various destructive effects in the beam quality have been observed due to both ion trapping and micro-particle trapping, such as sudden beam loss and lifetime deterioration. These phenomena have never been observed with positron beams. However, a strange vertical instability was observed. Properties of the instability are as follows: (1) it is a coupled-bunch oscillation with multi-modes; (2) the threshold current is very low, 15- 20 mA without octupole fields; and (3) the distribution of the betatron sidebands is broad. To suppress this beam instability, we must add octupole fields. The reason why such an instability appears only under positrons was not understood long time. The puzzle is finally solved and more studies for the instability cures are undergoing.

2. EMITTANCE UPGRADE PROGRAM

An emittance upgrade program is in progress, whose detail is described in ref. 1. By doubling and

reinforcing the quadrupoles and sextupoles in the normal cells, the emittance can be reduced to 27 nm-rad, which is about one fifth of the present value (130 nm-rad).

To realize this emittance upgrade, about one third of the ring will be reconstructed. All the quadrupoles and sextupoles in the normal cells will be replaced with new and reinforced ones. The vacuum chambers including BPM's in the normal cells will be modified to be matched with the small bores of the new magnets. Injection kickers will be reinforced to be matched with the new optics. The front ends of the SR beam lines in the normal cells will be modified to be matched with the new configuration of the magnets.

To cure the beam instabilities, RF cavities will be replaced with damped type ones. A transverse feedback system is also under developing. Since the orbit stability is much more important for the low emittance lattice, the present orbit feedback system will be reinforced to be faster and more accurate.

In 1997, the ring will be shut down for 9 months. To finish all the reconstruction work within this rather short period, the fabrication of the accelerator components has started in 1994, and will be finished in 1996. The reconstruction work of the front ends of the SR beam lines has already started and will be finished before 1997, preceding the reconstruction works of the ring.

1) M. Katoh et al, Rev. Sci. Instrum. 66(2) 1995.

2.1 Field Measurement of Model Magnets for a High-Brilliance Configuration (II)

We have measured the field gradient of the model magnets for a high-brilliance configuration using a harmonic coil method. This method has the following advantages compared with the previous search coil one: it enables us to measure the higher multipole field components, and a shift of the magnetic field center, and so on.

In the last year the harmonic coil measurement system was newly constructed. The schematic view and specifications are shown in Fig. 5 and Table 6. We installed two kinds of coils: one is a long coil for measurement of an integrated field gradient and the other is a short coil for measurement of a field gradient around a center of the magnet. A coil cylinder supported by chacking collets is rotated by a motor

with an inverter control. A rotating speed is available to change from 10 to 100 rpm. An angular position signal which triggers the integration of the induced voltage is read out from an angular encoder mounted in one side of the coil. The data acquisition is made by a digital integrator circuit controlled by an on-line computer. The alignment between the center of the coil and the geometric centers of the magnets is done using a level scope and a special target made for the alignment.

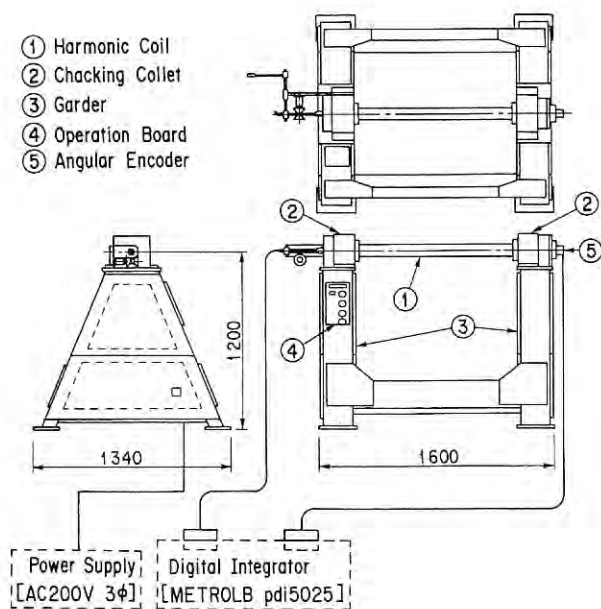


Fig. 5 The Schematic view of the harmonic coil measurement system

Table 6 Specifications of the harmonic coil

Coil	
General	
bobbin diameter	74.6 (mm)
length	1532 (mm)
weight	6 (kg)
Long Coil	
radius	29.9 (mm)
length	1000 (mm)
turn number	10
Short Coil	
radius	29.5 (mm)
length	20 (mm)
turn number	50
Angular Encoder	
resolution	6000 pulse/turn
DC Motor	
Rotating speed	10 – 100 rpm (inverter control)

The preliminary results measured by a long coil are shown in Fig. 6 for the quadrupole magnets, and in Fig. 7 for the sextupole magnets, respectively. Figures (a) show the pattern of the integration of the induced voltage (v_s) to the angular position (θ), which is displayed by the following equation:

$$v_s(\theta) = \sum_n \{b_n \cos(n\theta) + a_n \sin(n\theta)\}$$

$$b_n = \frac{2\pi \cdot N \cdot B_{normal}^{(n-1)} l}{r^n \cdot n! \cdot T}, a_n = \frac{2\pi \cdot N \cdot B_{skew}^{(n-1)} l}{r^n \cdot n! \cdot T}$$

Here, n is a harmonic number, r is a coil radius, N is a coil turn number, $B^{(n-1)} l$ is an integrated field strength, and T is an angular position number. Figures (b) show a harmonic coefficients, b_n , calculated through a Fourier analysis. The dodecapole component ($n = 6$) is reasonably larger than the other higher multipole one in the quadrupole magnet, but it will be compensated with

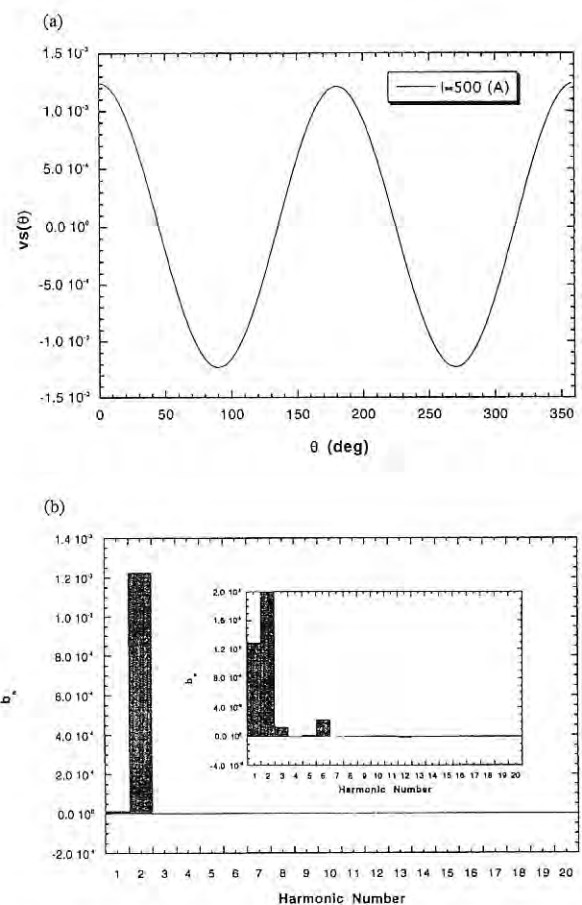


Fig. 6 (a) An angular pattern of the integration of the induced voltage to the quadrupole magnet measured at a current of 500 A; (b) a harmonic coefficients, b_n , calculated through a Fourier analysis.

end-shims. The sextupole component ($n = 3$) is also observed. Although the octupole ($n = 4$) and decapole component ($n = 5$) are observed in the sextupole magnet, but they are quite small.

The field measurement is now in progress for the preparation of more than 60 magnets employed in the high-brilliance configuration.

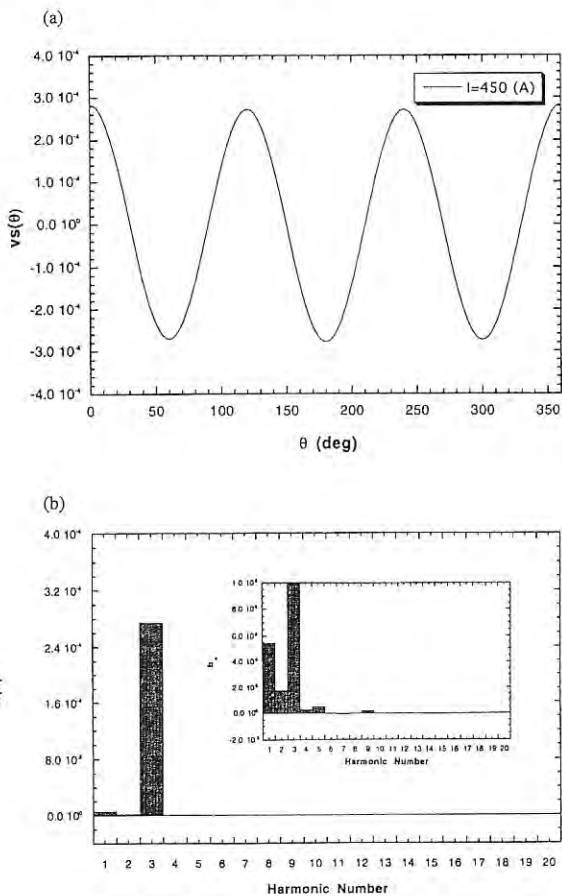


Fig. 7 (a) An angular pattern of the integration of the induced voltage to the sextupole magnet measured at a current of 450 A; (b) a harmonic coefficients, b_n , calculated through a Fourier analysis.

2.2 Performance Test of the Global Feedback DSP Board

A fast global feedback system is planned in order to obtain good beam stability for the vertical direction in a high-brilliance configuration.¹⁾ This system is expected to correct orbit fluctuations up to 50 Hz. A VME system was adopted for fast feedback control; it contains a DSP board with two 32-bit floating-point

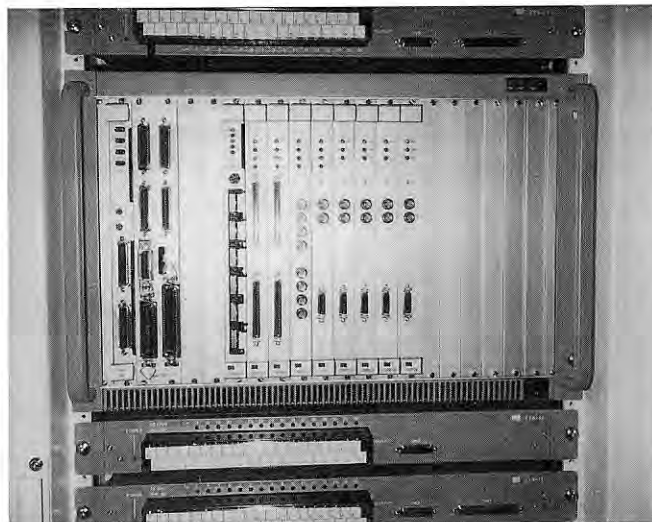


Fig. 8 Photograph of the VME system used for the global feedback

DSPs (Texas Instruments TMS320C40s), a CPU board and some kinds of I/O boards in a VME crate. Fig. 8 shows a photograph of the VME system. The DSP board is linked with the I/O boards through an I/O bus in order to control the beam position monitors (BPMs) and the vertical steering magnets; it is also connected through a VME bus to the CPU board, which is interfaced with a UNIX workstation by Ethernet. The CPU board intermediates between the DSP board and the workstation for download of DSP programs and transfer of feedback data.

The computation performance of the DSP board was tested using a DSP program which simulates the global feedback computation (not including the I/O control). This program contains the following parts:

- 1) Calculation of the horizontal and vertical positions based on electrode-voltage data of the BPMs and a quality check of the position data,
- 2) Calculation of the steering-magnet currents based on the vertical-position data,
- 3) Calculation for the PID (proportional, integral and derivative) control in order to improve the feedback performance,
- 4) Communication of the electrode-voltage data and the horizontal-position data between the main and sub DSPs.

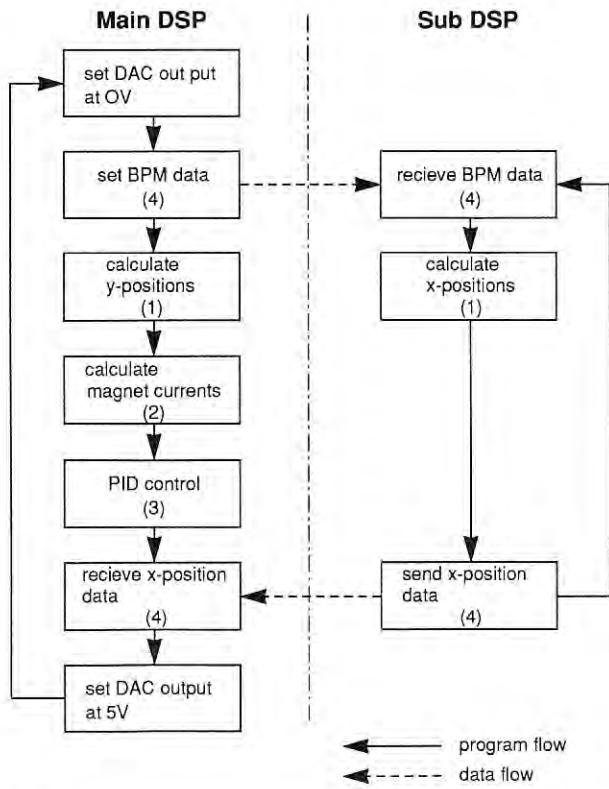


Fig. 9 Flow chart of a DSP program simulating the global feedback computation

Figure 9 shows a flow chart of the program. In this program, the numbers of the BPMs and the vertical steering magnets were assumed to be 65 and 28. Parts (1), (3) and (4) were coded in C-language and Part (2) in assembly language. Parallel C (from 3L Ltd.) was used as an optimizing C compiler, assembler and linker to reduce the consumed time for Part (1) by parallel programming of the two DSPs. Part (4) means that the sub DSP has to take the electrode-voltage data from the main DSP directly connected with the outside of the DSP board and return the calculated horizontal-position data to it. The communication speed between the two DSPs is 20 MBytes/s, except for the software overhead. The program forced the main DSP to change the output voltage of a DAC board before and after one computation cycle. Therefore, the total computation time was easily obtained by observing the DAC output level with an oscilloscope. The consumed time for each part was also measured in the same manner. The results are summarized in Table 7. Since the I/O control time is kept within 1 ms, the total computation time (555 μ s) is sufficiently short for the global

Table 7 Measured DSP computation time

(1) Position calculation (x&y)	305 μ s
(2) Magnet current calculation (y)	100 μ s
(3) PID control (y)	25 μ s
(4) Data communication	125 μ s
Total	555 μs

feedback with a planned sampling time of 2 ms. It was also confirmed that the total computation time is almost unchanged in parallel programming when the horizontal global feedback computation is added to Parts (2) to (4). This suggests that we can join the horizontal global feedback to the vertical one without changing the sampling time, if necessary.

1) Photon Factory Activity Report 1993 R-8.

3. STORAGE RING SPECIFICATIONS

This section contains major specifications of the 2.5 GeV PF ring to provide quick and handy information for users and machine physicists.

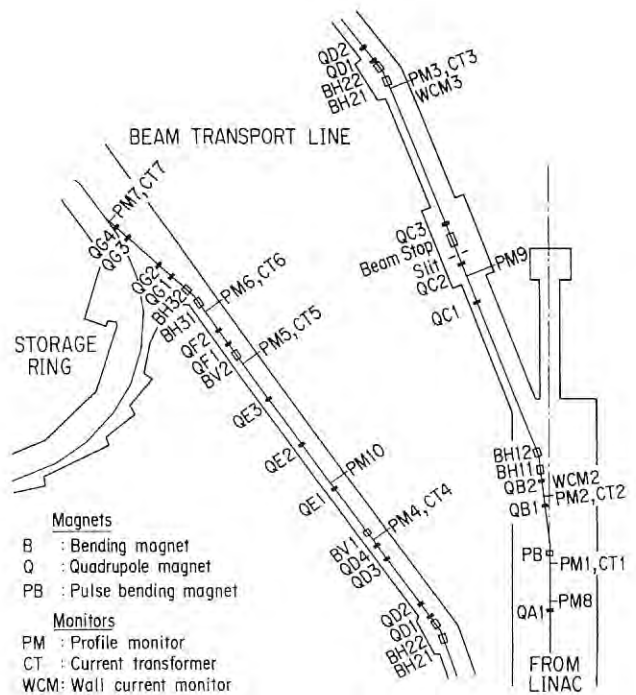


Fig. 10 Beam transport line.

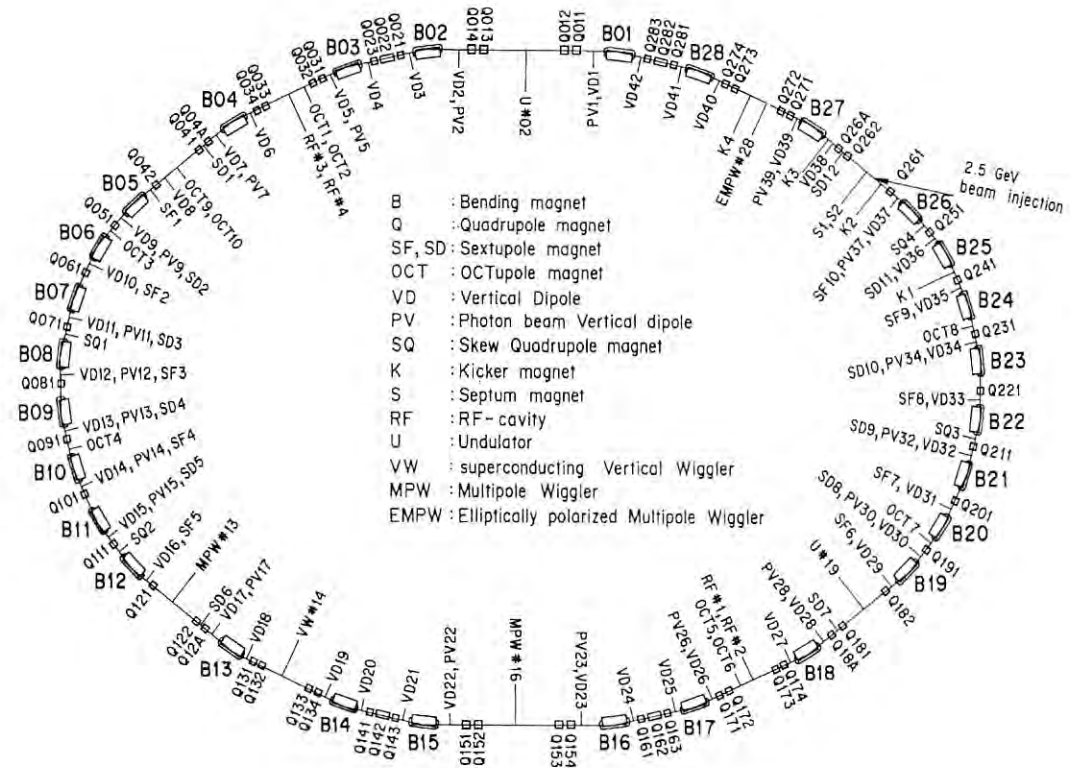


Fig. 11 Ring lattice components.

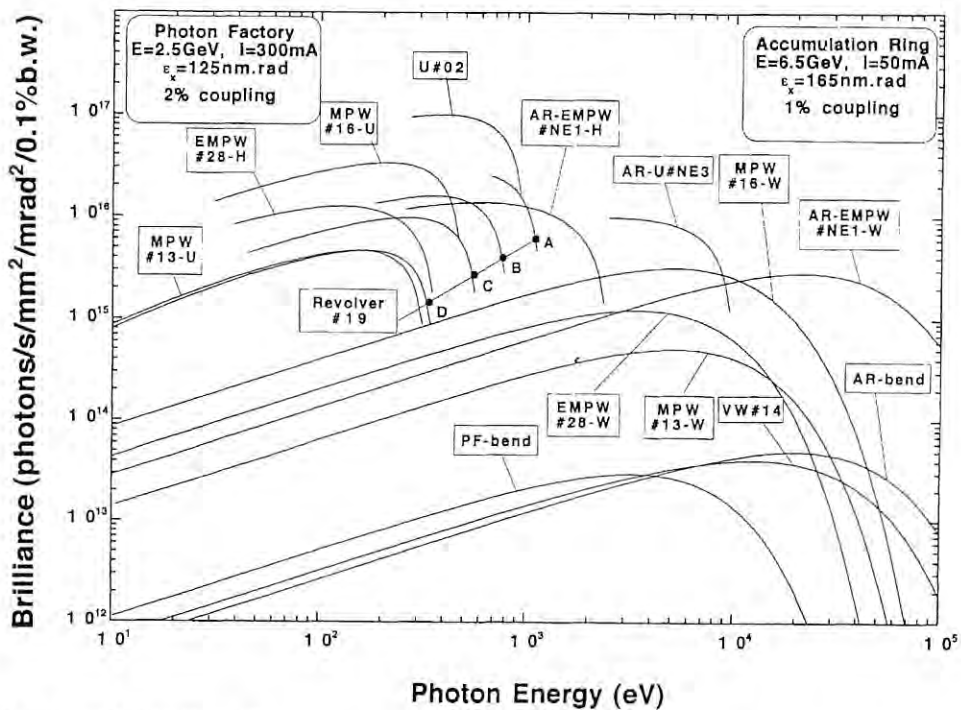


Fig. 12 Synchrotron radiation spectra. Brilliance of radiation vs. photon energy for the insertion devices (U#02, MPW#13, VW#14, MPW#16, Revolver#19 and EMPW#28) and the bending magnet (Bend) of the PF, and for the insertion device (EMPW#NE1) of the AR. The name of each source is assigned in Table C-4. Several insertion devices have both undulator and wiggler modes, which are denoted by U or W, respectively. The spectral curve of each undulator (or undulator mode of multipole wiggler) is a locus of the peak of the first harmonic within the allowable range of K-parameter. Spectra of Revolver#19 are shown for four kinds of period lengths.

Table 8 Insertion devices

Calculated spectral performances of the bend source and 6 insertion devices at the Photon Factory. E/I: beam energy and current, λ_u : period length, N: number of periods, L: length of undulator or wiggler, G_y (G_x): minimum vertical (horizontal) gap height, B_y (B_x): maximum vertical (horizontal) magnetic field, P: pure configuration, H: hybrid configuration, S.C.: superconducting magnet, $\sigma_{x,y}$: horizontal or vertical beam size, $\sigma_{x',y'}$: horizontal or vertical beam divergence, K_x (K_y): horizontal (vertical) deflection parameter, ϵ_r / ϵ_c : photon energy of the first harmonic (critical energy in the case of bend source or wiggler), $\Delta \epsilon / \epsilon$: relative bandwidth, Pc: degree of circular polarization, \mathcal{D} : photon flux in unit solid angle (photons / s \cdot mrad² \cdot 0.1%b.w.), \mathcal{B} : brilliance (photons / s \cdot mm² \cdot mrad² \cdot 0.1%b.w.), P_T : total radiated power, $dP/d\Omega$: power in unit solid angle. Different operating modes of undulator and wiggler are denoted by -U and -W, respectively.

Name	E/I GeV/mA	λ_u cm	N	L m	G_y (G_x) cm	B_y (B_x) T	Type of magnet	σ_x mm	σ_y mm	$\sigma_{x'}$ mrad	$\sigma_{y'}$ mrad	K_x (K_y)	ϵ_r / ϵ_c keV	$\Delta \epsilon / \epsilon$	\mathcal{D}	\mathcal{B}	P_T kW	$dP/d\Omega$ kW / mrad ²
Bend								0.74	0.26	0.38	0.037		4.0		3.5E13	2.9E13		0.060
U#02		6.0	60	3.6	2.8	0.4	H (NdFeB)	0.78	0.11	0.16	0.022	2.25	0.28	0.029	5.2E16	9.7E16	0.68	2.7
MPW#13-W		18.0	13	2.5	2.7	1.5	H (NdFeB)	1.66	0.17	0.15	0.019	25.0	6.2		9.7E14	4.9E14	6.7	2.6
-U												2.0	0.108	0.086	5.7E15	3.2E15	.042	0.19
VW#14					5.0	5.0	S.C.	1.05	.096	0.16	0.025		20.8		2.2E13	3.4E13		0.18
MPW#16-W	2.5 / 300	12.0	26	3.1	1.9	1.5	H (NdFeB)	0.78	0.11	0.16	0.022	16.8	6.2		1.8E15	3.1E15	8.3	4.9
-U												2.0	0.162	0.050	1.6E16	2.8E16	0.12	0.52
Revolver		5.0	46	2.3	3.0	0.28	H (NdFeB)	1.66	0.17	0.15	0.019	1.3	0.637	0.021	4.1E16	2.3E16	0.21	1.27
#19		7.2	32		0.41		H (NdFeB)					2.7	0.176	0.039	2.1E16	1.2E16	0.44	1.54
		10.0	23		0.53		H (NdFeB)					5.0	0.0436	0.047	6.9E15	3.8E15	0.78	1.53
		16.4	14		0.62		P (NdFeB)					9.5	0.0078	0.066	1.2E15	6.3E14	1.05	1.09
EMPW#28		16.0	12	1.9	3 (11)	1 (0.2)	P (NdFeB)	1.05	.096	0.16	0.025							
-W												15 (1)	4.2 (Pc=89%)		2.5E14	3.4E14	2.3	0.38
-U												1 (1)	.18 (Pc=99%)	0.11	6.3E15	9.8E15	0.02	0.058

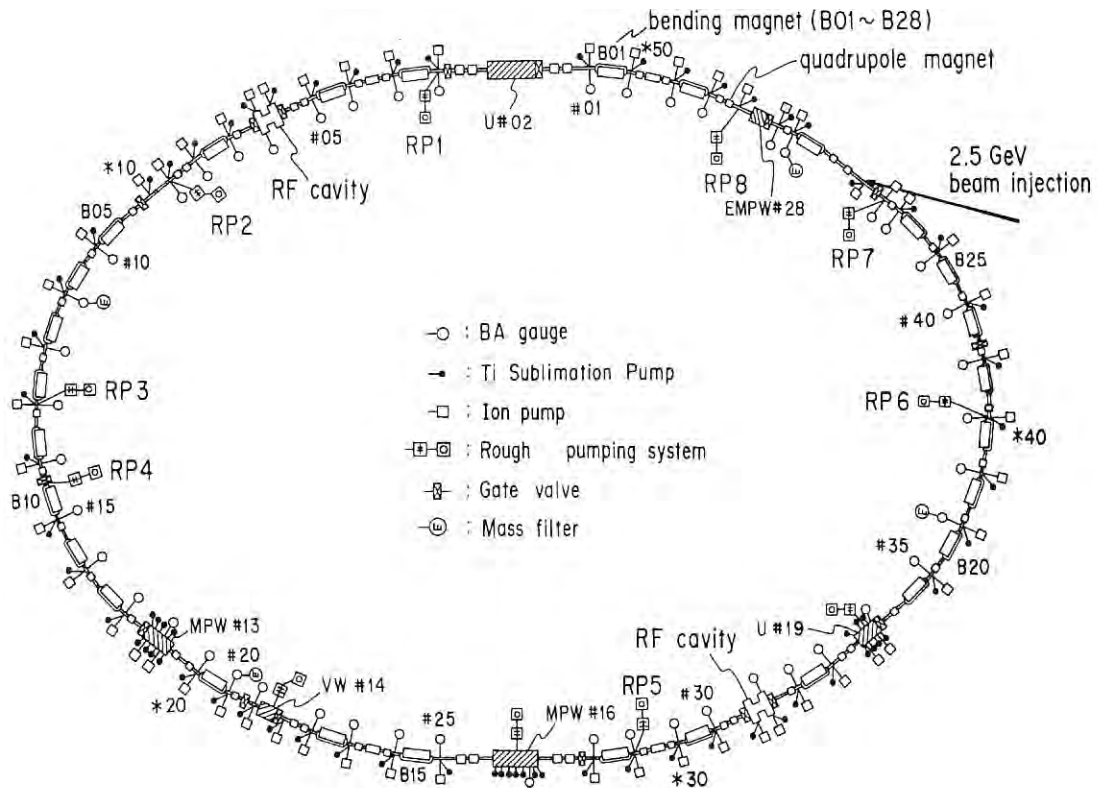


Fig. 13 Vacuum system components.

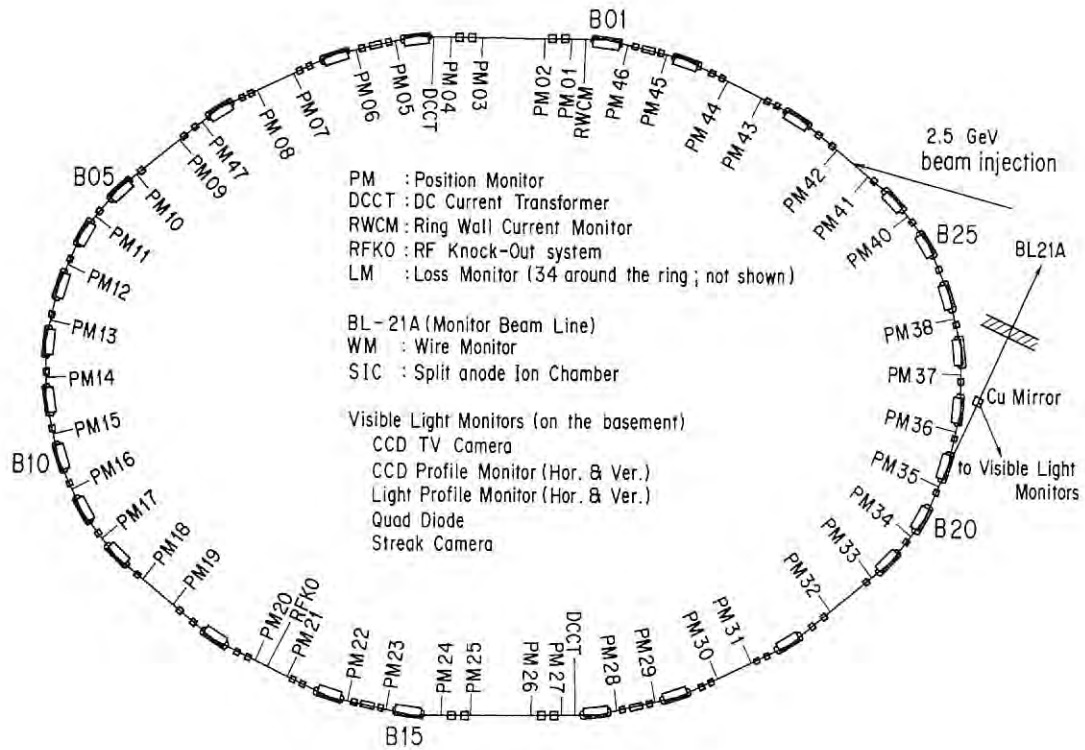


Fig. 14 Beam monitors.

Table 9 General parameters of the storage ring.

Energy	2.5 GeV	(0.75 GeV to 3 GeV)
Initial stored current	(multi-bunch)	350 mA (max 500 mA)
	(single bunch)	60 mA (max 104 mA)
Emittance	130nm-rad(horizontal) ~2nm-rad(vertical)	
Circumference	187m	(bending radius=8.66m)
RF frequency	500MHz	(harmonic number=312)
Injection	2.5GeV Linac	(positron/electron)
Beam lifetime	60 h (at 300 mA)	$I\tau \geq 18 \text{ A}\cdot\text{h}$ (at ~250 mA ~ 350 mA)
Vacuum pressure	$\geq 3 \times 10^{-10}$ Torr (at 300mA) $P/I \sim 8 \times 10^{-10}$ Torr/A (at ~250 mA ~ 350 mA) $\sim 3 \times 10^{-11}$ Torr (at 0 mA)	
Insertion devices	Superconducting vertical wiggler 5T 60 period undulator $K=1.78\sim 0.1$ 26 period multipole wiggler/undulator 1.5T~0.04T Four way revolver type undulator 14 period multipole wiggler Elliptically polarized multipole wiggler	
SR channels	SR experiment 22 Beam diagnosis 3	

Table 10 Beam parameters.

Horizontal tune ν_x	8.45
Vertical tune ν_y	3.30
Compaction factor α	0.015
Natural chromaticity ξ_x	-15.8
ξ_y	-8.6
Bunch length σ_z	1.5cm
Transverse damping time	7.8msec
Longitudinal damping time	3.9msec
Energy spread 7.3×10^{-4}	
Radiation loss (without insertion devices)	400keV

Table 11 Principal parameters of the accelerator system.

Magnet system

	number of magnets	number of power supplies
Bending	28	1
Quadrupole	58	12
Sextupole	22	2
Octupole	11	10
Skew quadrupole	4	4
Dodecapole	6	6
Vertical steering	42	42
Photon beam steering	20	20
Others		
Backleg winding of bending magnet	28	
Electric shunt for tune compensation	12	

RF system

Number of RF stations	4
Number of klystrons	4 (180kW/klystron)
Number of RF cavities	4 (single cell cavity)
Shunt impedance	32M Ω (four cavities)
Unloaded Q	39000
Total power dissipated in cavity wall	89kW
Total cavity gap voltage	1.7MV
Synchrotron frequency	37kHz

Vacuum system

main pumping system		
pump	pumping speed	number
SIP (Sputter Ion Pump)	128 l/sec	54
DIP (Distributed Ion Pump)	150 l/sec	26
Ti sublimation	_____	71
NEG (Non-Evaporable Getter)	_____	2

total effective pumping speed = 2×10^4 l/sec (for CO)

Rough pumping system		
TMP (Turbo Molecular Pump)	pumping speed	number
	300 l/sec	12

Measurement

	number
B-A gauge	48
mass filter	4
cold cathode gauge	16(for baking)

Sector gate valve

	number
all metal with RF shield	5
all metal without RF shield	1
Viton seal with RF shield	10

Injection system

Septum magnet

name	Septum I (S1)	Septum II (S2)
core material		laminated silicon steel (passive type)
length [mm]	1500	1000
maximum current [A]	6000	6000
deflection angle [degree]	7.0	5.0
pulse width [msec]	88	60

Kicker magnet

name	K1, K2, K3, K4
core material	ferrite (window frame type)
core length [mm]	300
maximum current [A]	3500
maximum deflection angle [mrad]	4.4
pulse width [msec]	5

Superconducting vertical wiggler

Maximum field strength on the beam orbit	5 Tesla
Magnet gap	66 mm
Magnet pole size (widthxheight)	40 mm × 260 mm
Number of magnetic poles arranged every 200 mm	5 poles
Rated exciting current	220 A at 5 Tesla
Superconducting wire	NbTi : Cu 1 : 1 size 1.70 × 0.85 mm ²
Cross section of coils	65 mm × 70 mm
Number of turn	2520
Liquid helium consumption in the permanent current mode	0.1 L/h
Damping rate of the permanent current	1.4 × 10 ⁻⁵ /h
Inductance	1.31 H/coil

FEL oscillator

1. General	
target wavelength	177 nm
FEL gain	18 %
cavity loss	12 %
net FEL gain	6 %
2. Storage ring	
beam energy	0.75 GeV
number of bunches	4
bunch length(2s)	60 psec
peak current	30 A
beam emittance	15 nm-rad
energy spread	3.5 × 10 ⁻⁴
accelerating frequency(f_{rf})	500.1 MHz
3. Optical klystron	
periodic length	9 cm
number of periods	19+19
max. magnetic field	0.7 tesla
max. deflection parameter	5.9
optimum N_d	210
FEL gain	0.6 %/amp
4. Optical cavity	
type	Fabry Perot
cavity length	23.38 m
mirror 1(UHV Al)	R=92%
mirror 2(MgF ₂ multilayer)	R=96%
cavity loss at 1770 Å	12 %
5. Laser system	
mode-lock YAG laser	
mode-lock frequency	83.35 MHz (= $f_{rf}/6$)
regenerative YAG amplifier	
repetition rate	50 Hz
pulse energy at 5320 Å	15 mJ
pulse duration	80 psec
Harmonic generation	
harmonic material	Xe or Cd vapor
max. pulse power	1 kW

Table 12 Beam size and divergence at source point.

location	σ_x [mm]	σ_y [mm]	σ'_x [mrad]	σ'_y [mrad]
B15&B01	0.34	0.16	0.41	0.033
B02&B16	0.60	0.13	0.38	0.033
B03&B17	0.43	0.22	0.32	0.018
B04&B18	0.52	0.18	0.29	0.045
B05&B19	1.26	0.21	0.39	0.037
B06&B20	0.85	0.25	0.38	0.037
B07&B21	1.26	0.21	0.39	0.037
B08&B22	0.85	0.25	0.38	0.037
B09&B23	1.26	0.21	0.39	0.037
B10&B24	0.85	0.25	0.38	0.037
B11&B25	1.26	0.21	0.39	0.037
B12&B26	0.85	0.25	0.38	0.037
B13&B27	0.44	0.23	0.31	0.045
B14&B28	0.50	0.20	0.30	0.018

Table 13 Summary of Beamline (front-ends) in FY 1993.

Beamline	Affiliation	Source	Spectral range	Status
BL-1	NTT	bending magnet (B1)	VUV and soft X-ray	in operation
BL-2	KEK-PF	60-period permanent magnet undulator	Soft-X-ray	in operation
BL-3	KEK-PF	bending magnet (B2 & B3)	VUV and X-ray	in operation
BL-4	KEK-PF	bending magnet (B4)	X-ray	in operation
BL-5	KEK-PF	permanent magnet wiggler/undulator (under design)	-	under installation
BL-6	KEK-PF	bending magnet (B6)	X-ray	in operation
BL-7	University of Tokyo	bending magnet (B7)	VUV and X-ray	in operation
BL-8	Hitachi Ltd.	bending magnet (B8)	VUV and X-ray	in operation
BL-9	Nippon Electrical Co. (NEC)	bending magnet (B9)	VUV and X-ray	in operation
BL-10	KEK-PF	bending magnet (B10)	X-ray	in operation
BL-11	KEK-PF	bending magnet (B11)	VUV and soft X-ray	in operation
BL-12	KEK-PF	bending magnet (B12)	VUV and soft X-ray	in operation
BL-13	KEK-PF	27-pole wiggler	Soft and hard X-ray	in operation
BL-14	KEK-PF	superconducting vertical wiggler	Hard X-ray	in operation
BL-15	KEK-PF	bending magnet (B15)	X-ray	in operation
BL-16	KEK-PF	53-pole permanent magnet wiggler/undulator	Soft and hard X-ray	in operation
BL-17	Fujitsu Ltd.	bending magnet (B16 & B17)	VUV and X-ray	in operation
BL-18	ISSP and KEK-PF	bending magnet (B18)	VUV	in operation
BL-19	ISSP and KEK-PF	permanent magnet multi-undulator	VUV	in operation
BL-20	KEK-PF	bending magnet (B20)	VUV and X-ray	in operation
BL-21	KEK-PF	bending magnet (B21)	White, visible, and X-ray	in operation
BL-27	KEK-PF	bending magnet (B27)	Soft X-ray and X-ray	in operation
BL-28	KEK-PF	25-pole permanent magnet wiggler/undulator	Circularly polarized VUV and soft X-ray	in operation

C. TRISTAN ACCUMULATION RING

TRISTAN accumulation ring, AR, is a storage accelerator which accelerates electrons or positrons from 2.5 GeV to 8 GeV and transfers them to TRISTAN main colliding ring (MR). In the intervals of the MR-injection AR is operated with the electron beam of 6.5 GeV as a synchrotron radiation source. Typically it takes one hour for MR-injection. Following two hours are used for SR experiments. At present AR has four beam lines, BL-NE1, -NE3, -NE5 and -NE9. BL-NE1 accepts SR from a ellipsoidal multipole wiggler and BL-NE3 does it from an X-ray undulator. The remaining two beam lines transport SR from the bending magnets in the normal cells. Table 14 shows the machine parameters of AR.

Table 14 Machine parameters of TRISTAN AR.

Energy	6.5 GeV
Natural emittance	293 nm rad
Circumference	377 m
RF frequency	508.6 MHz
Bending radius	23.2 m
Energy loss per turn	6.66 MeV
Damping time	
horizontal	2.5 ms
vertical	2.5 ms
longitudinal	1.2 ms
Natural bunch length	18.6 mm
Momentum compaction factor	0.0129
Natural chromaticity	
horizontal	-14.3
vertical	-13.1
Stored current	40 mA
The number of bunches	1
Beam lifetime	240 min.

Table 15 summarizes the operation statistics of AR in this year. Two failures which took up the most part of the failure-time occurred in the vacuum system. One was the leak in a ceramic chamber of a direct current transformer and the other the leak on a beryllium window which separates the vacuum system of AR from that of a beam transport line for the positron-injection.

AR has been suffered from sudden shortening of beam lifetime which occurs about once or twice a day. To investigate whether this shortening occurs in the positron-accumulation or not, AR was operated using the positron beam about four days. Shortening of beam lifetime never occurred in this period. This seems to support a speculation where it is caused by trapped dusts by the electron beam. An experiment, in which minute particles are dusted artificially on the beam, is planned next year.

Table 15 Operation statistics of TRISTAN AR (From Oct. 1993 to Sep. 1994).

	Time(hr)
SR experiment and MR injection for physics experiment	4048.0
MR injection for machine study and beam tuning	703.5
Machine study and beam tuning for AR	178.0
Failure	86.5
Others	188.0
Total	5204.0

1. SPECIFICATIONS OF THE TRISTAN ACCUMULATION RING

Table 16 summarizes principal parameters of a bend source and insertion devices and Fig. 15 shows calculated spectral performance.

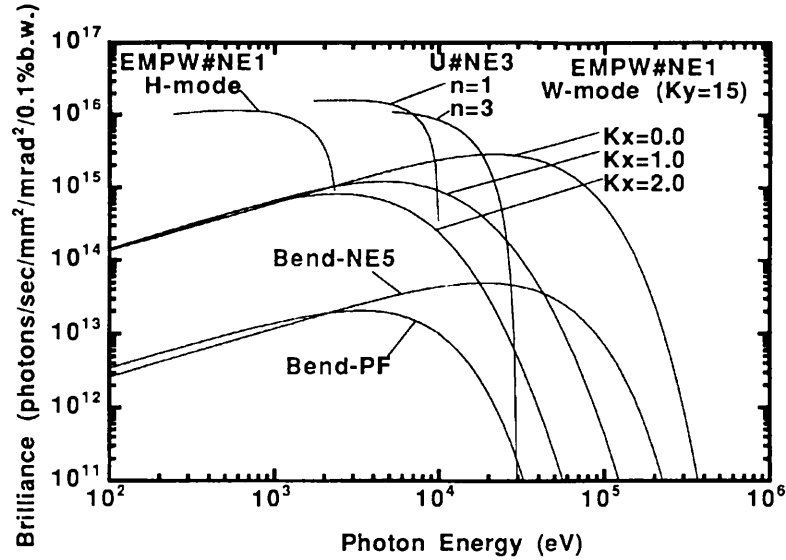


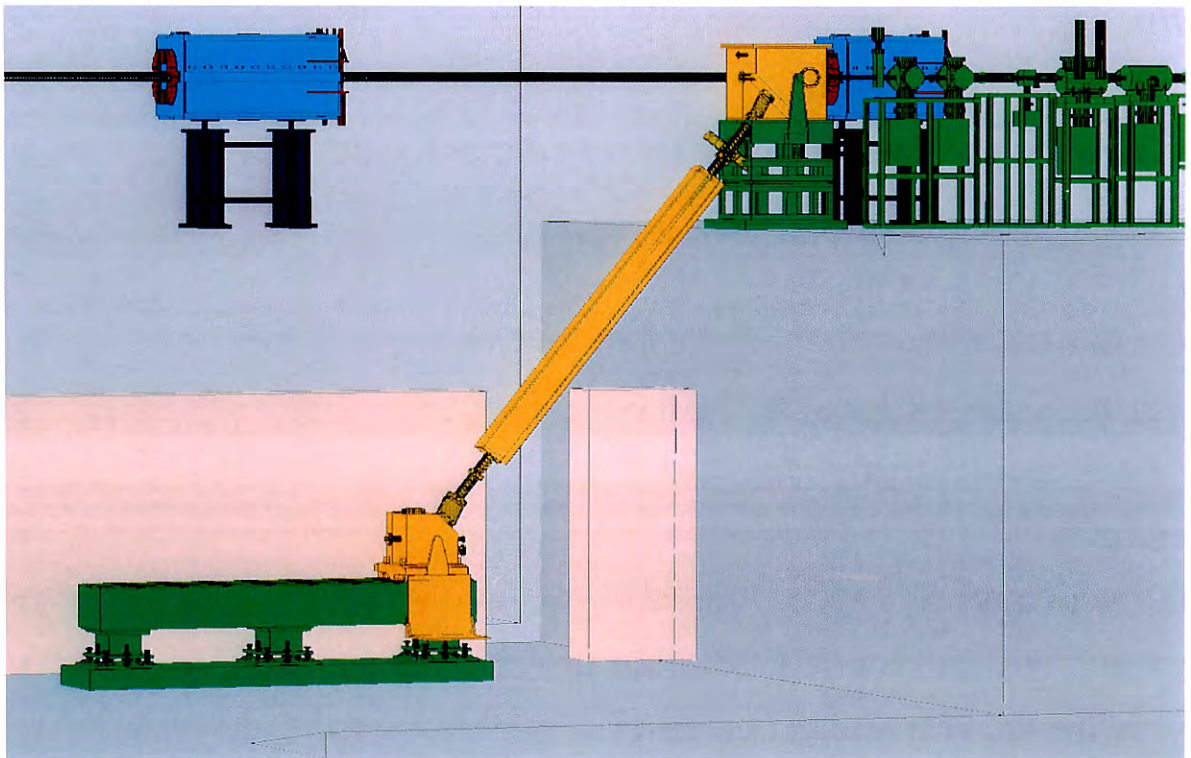
Fig. 15 Synchrotron radiation spectra.

Brilliance of radiation vs. photon energy for the insertion devices (EMPW#NE1 and U#NE3) and the bending magnet (Bend-NE5,NE9) of the AR. The name of each source is assigned in Table 7. EMPW#NE1 has both a helical undulator and wiggler modes, which are denoted by H or W, respectively. The spectral curve of each undulator (or a helical undulator mode of EMPW) is a locus of the peak of the harmonics within the allowable range of K-parameter.

Table 16 Calculated spectral performance of the bend source and insertion devices at the TRISTAN Accumulation Ring. E/I: beam energy and current, λ_u : period length, N: number of periods, L: length of undulator or wiggler, G_v (G_h): minimum vertical (horizontal) gap, B_v (B_h): maximum vertical (horizontal) magnetic field, P: pure configuration, H: hybrid configuration, σ_x , σ_y : horizontal and vertical beam size, $\sigma_{x'}$, $\sigma_{y'}$: horizontal and vertical beam divergence, K_x (K_y): horizontal (vertical) deflection parameter, ϵ_1/ϵ_c : photon energy of the first harmonic (critical energy in the case of bend source or wiggler), $\Delta\epsilon/\epsilon$: relative bandwidth, Pc: degree of circular polarization, D: photon flux in a unit solid angle (photons /s · mrad² · 0.1%b.w.), B: brilliance (photons/s · mm² · mrad² · 0.1%b.w.), P_T: total radiated power, dP/dΩ: power in a unit solid angle. Different operation modes of a helical undulator and a wiggler are denoted by -H and -W, respectively.

Name	Bend-NE5,NE9	EMPW#NE1	-W	-H	U#NE3	
E/I GeV/mA	6.5/50	6.5/50			6.5/50	
λ_u cm		16.0			4.0	
N		21			90	
L m		3.4			3.6	
G _v (G _h)		3 (11)			1.0	
B _v (B _h)		1 (0.2)			0.83	
Type of magnet		P (NdFeB)			P (NdFeB)	
σ_x mm	0.8	1.14			1.24	
σ_y mm	0.15	0.079			0.121	
$\sigma_{x'}$ mrad	0.45	0.14			1.24	
$\sigma_{y'}$ mrad	0.023	0.021			0.018	
K _x (K _y)			15 (1)	1 (1)	1.5	3.1
ϵ_1/ϵ_c keV	26.3		28 (Pc=83%)	1.2 (Pc=97%)	4.68	
$\Delta\epsilon/\epsilon$				0.12	0.064	
D	3.5×10^{13}		5.3×10^{14}	5.4×10^{15}	1.4×10^{16}	
B	4.7×10^{13}		8.8×10^{14}	9.5×10^{15}	1.5×10^{16}	
P _T kW			4.5	0.04	0.78	3.3
dP/dΩ kW/mrad ²	0.38		5.6	0.49	8.95	35

Projects



A computer sketch of the double-crystal monochromator for the beamline BL-BW-TL which will be installed in the MR tunnel. Yellow components correspond to the double-crystal monochromator, green to other beamline components and light blue to the MR.

You can jump to the article by clicking its title.

CONTENTS

	Page
A. THE TRISTAN SUPER LIGHT FACILITY	P - 1
1. INTRODUCTION	P - 1
2. ACCELERATOR PLAN FOR A LIGHT-SOURCE STUDY IN THE AUTUMN OF 1995	P - 2
3. SUPER-BRILLIANT X-RAY UNDULATOR FOR THE TRISTAN SUPER LIGHT FACILITY	P - 5
4. BEAMLINER AND RELATED RESEARCH AND DEVELOPMENT	P - 8
5. PROPOSALS OF SR EXPERIMENTS	P - 11
B. VUV-FEL	P - 20
1. VUV-FEL AT THE PF RING	P - 20
2. LOW ENERGY OPERATION OF THE PF RING AT 0.75 GEV.	P - 20
3. FEL OSCILLATOR	P - 20
4. SPONTANEOUS EMISSION	P - 21
5. FEL GAIN	P - 21
6. THE LASER SYSTEM AND BEAMLINER	P - 22
7. MONITOR SYSTEM	P - 22
C. KEKB	P - 23
1. OVERVIEW	P - 23
2. HIGH-POWER TEST OF A NEW-TYPE RF PULSE COMPRESSOR	P - 25
3. 50-MW KLYSTRON DEVELOPMENT	P - 26
4. RF DRIVE SYSTEM	P - 27
5. HIGH-CURRENT SINGLE-BUNCH BEAM ACCELERATION	P - 28
6. BEAM-POSITION MONITOR	P - 29
D. SLOW-POSITRON SOURCE	P - 30
1. SLOW-POSITRON BEAM INTENSITY	P - 30
2. POSITRON MODERATOR	P - 30
3. POSITRON RE-EMISSION MICROSCOPE	P - 31
4. HIGH-VOLTAGE APPLYING TEST	P - 31

A. THE TRISTAN SUPER LIGHT FACILITY

1. INTRODUCTION

The director of KEK has changed a future plan to employ Main Ring tunnel from for the Tristan Super Light Facility (TSLF) to the b-factory. The synchrotron-radiation community will thus have to await another few decades, for instance, to use that tunnel in the far future for a super-brilliant light source. As a consequence, the budget requirement to the Monbusho for converting the Main Ring into a super-brilliant light source has been cancelled. Nevertheless, the Tristan Accelerator department has made a very kind decision that they should be happy to let the synchrotron-radiation community use the Main Ring as a super-brilliant light source for the moment until its full conversion into a b-factory ring commences in 1996; as a matter of fact, the high-energy community will need some time to analyze their data shortly after the current high-energy physics programme is finished. The accelerator group is likely to greatly appreciate what we do with the ring, because those who need very high luminosity are very much interested in achieving low-emittance operation using the current machine, and measuring its emittance, in which crystal optics as a new technology will be adopted. Thus, both the Tristan Super Light Facility (TSLF) and the Tristan Accelerator Department agreed that we should proceed with this project as a joint one.

As a result, the Accelerator Department said that they would be happy to support both the construction of the machine and its operation for three months for synchrotron-radiation science. This means that although only the least modification will be made due to the short time available, the machine will be modified so that it can still provide a small emittance of 5 nm.rad. Also, in order to minimize expenditures and the time spent for preparation, not a new and detached experimental hall outside the ring, but a semi-detached and shielded experimental area, should be prepared on the same level as the orbit. However, since no such convenient space has been found on the same level, we will attempt to temporarily use a small storage space at a fourth basement as an experimental area that is close to one of the three Tristan detectors; a first piece of the monochromator will be located at the third basement, while the second will be at the fourth basement, 4.5

meters below the third. Because of such a big height difference, if a big range of photon energies is required, a very long rail is needed in the case of housing a single piece of crystal. In order to accommodate a second monochromator chamber and steel base plates for experiments in a relatively small space, various pieces of crystals, each of which corresponds to each photon energy range, should be prepared.

Almost at the end of 1993 an article on the "Applications of Synchrotron Radiation Using a Test Beamline at the Tristan Main Ring" by Masami Ando and Seishi Kikuta was published (in Japanese) in Journal of the Synchrotron Radiation Society of Japan, Vol.6, No.4 (1993) p.113-119 in order to explain the ongoing TSLF project.

On January 11th, 1994, at the PF symposium 5 representatives of research teams presented tentative proposals about their research programmes. Those five subjects are as follows:

- 1) Small-Angle Scattering of a Single Muscle Fibre by Naoto Yagi;
- 2) Parametric Scattering by Kazumichi Namikawa;
- 3) Mössbauer Scattering by Seishi Kikuta;
- 4) Solid Phase Crystal Growth by Irradiation of Synchrotron Radiation by Fumio Sato; and
- 5) Brilliant Submicron Beam Production and Its Applications by Yoshio Suzuki.

The design of an associated beamline was nearly completed at the beginning of 1994, and floppy diskettes of their drawings were passed on to the KEK machine shop. The inner diameter of the beamline was to be 30 mm in order to reduce the cost and its potential capability as an acoustic delay. Liquid-nitrogen cooling was adopted because such a high power density of synchrotron radiation onto a monochromator crystal piece of silicon can only be removed by liquid nitrogen.

The 1st US-Japan Discussion Meeting was held at SLAC on May 27-28th concerning the collaboration of Linac Coherent Light Source development. Organization was undertaken by Herman Winick and Gerhard Materlik at SSRL. Due to the upgrade schedule of the PF 2.5-GeV linac, since a positron beam will not be available when our test experiment is carried out in 1995, an electron beam will be provided so that, without changing the polarity of the dipole magnets, synchrotron radiation from a clockwise orbit of an electron beam can be used. In addition, due to the structure of the building of the Tsukuba Experiment Point it is the best place for our test experiments.

A workshop on the utilization of the MR super brilliant light source was held on July 7th, 1994. It was to exchange knowledge concerning machine physics of the MR and application sciences utilizing superbright synchrotron radiation. That was jointly arranged by Masakazu Yoshioka from Tristan and Susumu Kamada from TSLF.

The 5th International Conference on Synchrotron Radiation Instrumentation (SRI'94) was held on July 21st at New York State University, where an invited talk on "Science — Trend and Trial towards a Fourth Generation Light Source Started from the PF Ring and through the AR and the MR" was presented by Masami Ando. It is going to be published in the proceedings of SRI'94 in Rev. Sci. Instrum.

On August 8th, 1994 the MR Committee in the second phase was started; its members were changed slightly. The new assignments include Koji Takata and Motohiro Kihara, while the others, such as Toshiaki Ohta, Seishi Kikuta (chairman), Shigeru Sato, Norihiro Shiotani, Yoshihiko Hatano, Kotaro Hieda, Kazumasa Ohsumi, Susumu Kamada, Yoshitaka Kimura, Hisashi Kobayakawa, Isamu Sato, Tadashi Matsushita, and Masami Ando, will remain for another two years. The Committee announced a call for proposals for test experiments.

On the occasion of the KEK Open House on September 11th a visual demonstration of the magnetic field using the same permanent magnets as those used in the insertion device for the MR was presented by Shigeru Yamamoto.

M. Ando

2. ACCELERATOR PLAN¹⁾ FOR A LIGHT-SOURCE STUDY IN THE AUTUMN OF 1995

For the sake of light-source development and research programs using it, three-month operation with a beam is scheduled for the autumn of 1995.

The lattice will be modified so as to enable the installation of a 5.4m long undulator and to achieve a very low-emittance beam of 5nm at 10 GeV. Emittance damping wigglers will enhance the radiation-damping rate, which will stabilize the coherent beam instabilities as well as reduce the emittance more.

A considerable number of accelerating cavities will be removed from the ring in order to minimize the

impedance of the higher order modes of the cavities that may cause coupled-bunch instabilities and limit the intensity of the stored beam.

For the stability of the light beam, a local feedback system will be applied to the electron orbit in the MR.

To measure the beam emittance in an independent way, visible synchrotron light from a bending magnet and 100-keV X-rays from an undulator will be utilized as well as the Compton scattering of laser photons from the beam electrons.

2.1 Lattice Modification, Damping Wigglers and Dynamic Aperture

The modification plan of the lattice is illustrated in Fig. 1 along with the optics parameters resulting from the modification. The following are the main motives for the modification:

In order to achieve a low emittance, the betatron phase in a normal cell will be increased from $\pi/3$ to $\pi/2$ in both the horizontal and vertical directions.

To make a free space for installing an undulator, two B magnets (5.86m long) will be replaced by short ones.

To remove any obstacles to the light beam line.

To operate the MR without superconducting magnets.

In high-energy physics operation, the wiggler magnets work so as to increase the beam emittance. By tuning the dispersion function there to zero, the same wiggler magnets will work to decrease the emittance, as given in Table 1. At the same time, the wiggler magnets will make the damping time short and help to suppress any collective beam instabilities.

Table 1 Major beam parameters for the MR light-source study.

	units		
beam energy	10	GeV	
normal cell phase(H/V)	90°/90°		
momentum compaction	7.2×10^{-4}		
accelerating voltage	36	MV	
wiggler magnets	OFF	ON	
energy loss in a turn	3.8	6.5	MeV
energy spread in a beam	0.59	1.1	$\times 10^{-3}$
natural bunch length	4.5	8.5	mm
natural emittance	7.0	5.1	nm

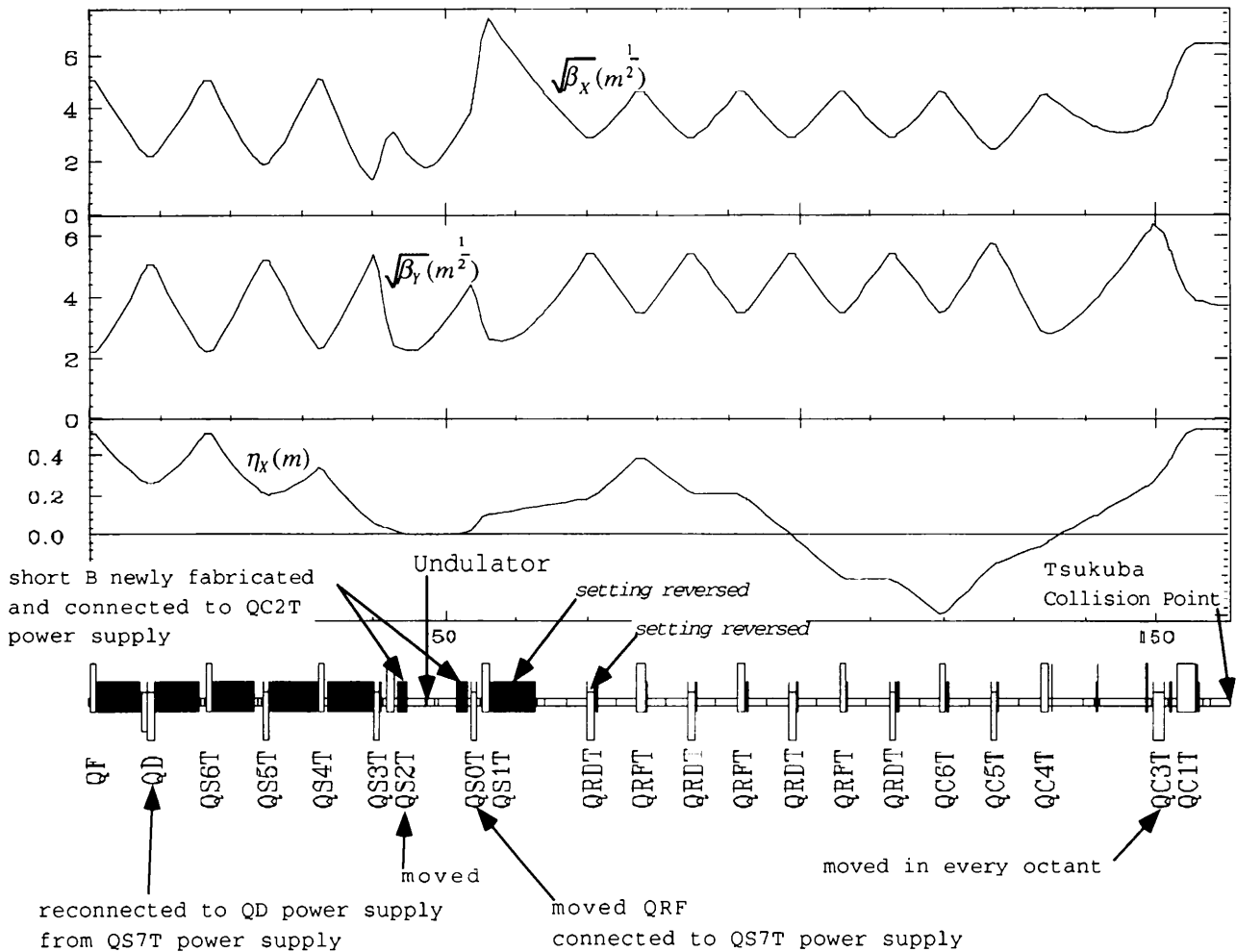


Fig. 1 MR lattice modification plan and the optics parameters for the undulator installation.

In the chromaticity correction, sextupoles are to be arranged in pairs having the same strength. In each pair, sextupoles will be placed at the interval of the betatron π phase both horizontally and vertically, and will never be interleaved with other sextupoles. Any non-linear effects of the sextupoles will be automatically cancelled out in each pair with this arrangement, so that the dynamic aperture will be kept large.^{2,3,4)}

2.2 Instabilities and Lifetime

The APS-type cavity currently in use was examined from the view point of coupled-bunch instabilities, by which the beam current of the MR must be limited. The most dangerous higher mode of the cavity was found to be the TM₁₁₀ mode (horizontal). Figure 2 shows the real part of the coupling impedance of the TM₁₁₀ mode (horizontal), obtained by fitting the

measured data with two resonators. The growth rate of the coupled-bunch instability is estimated in Fig. 3 for an 8-GeV injection beam.

The radiation-damping rate at 8 GeV (21 sec⁻¹) is not sufficient to overcome the growth rate of the coupled-bunch instability. However, the head-tail damping rate in the MR⁴⁾ is more than 10-times larger than the radiation-damping rate, and can suppress the coupled-bunch instability. To facilitate this process, the important issues are the chromaticity tuning and the temperature control of the cavity cooling water as well as the removal of any unnecessary cavities.

The bunch number is chosen to be less than 8, so that the bunch spacing is sufficiently long for the research programs. A rather high bunch current will enhance the head-tail damping; on the other hand, the effects of intra-beam scattering must be carefully checked. As shown in Fig. 4, the Touschek effect on the

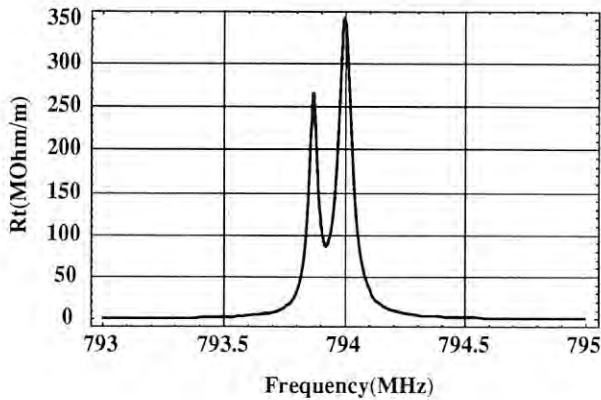


Fig. 2 TN110 (horizontal) impedance of the APS-type cavities.

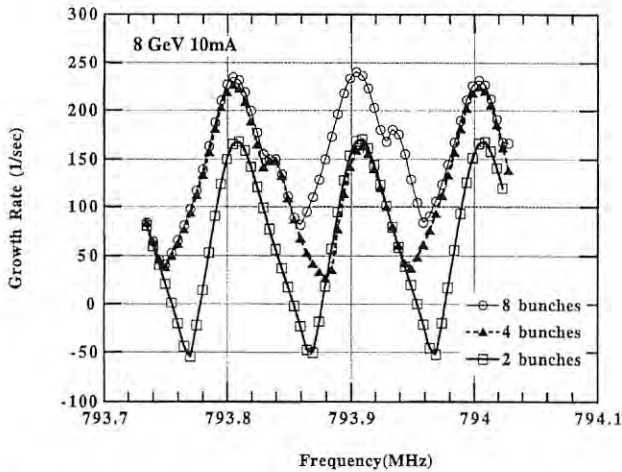


Fig. 3 Estimated growth rate of the coupled-bunch instability induced by the TM110 (horizontal) mode.

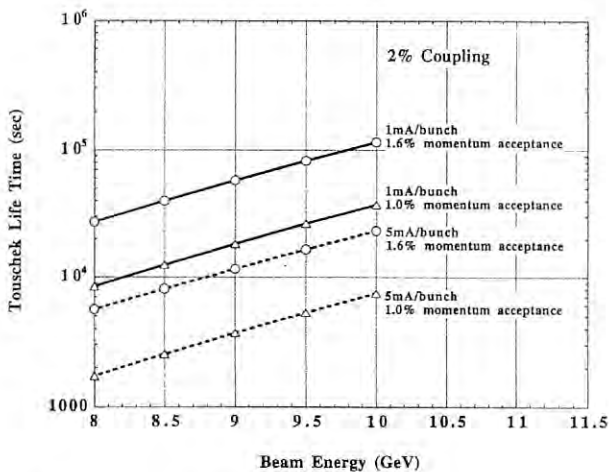


Fig. 4 Touschek lifetime.

beam life is not negligibly small, especially at an 8-GeV injection energy. However, the situation at the injection energy can be improved by increasing the wiggler field.

The beam life will also be limited by scattering with residual gas in the vacuum chambers, especially in those chambers which will be newly installed into the locations of the removed cavities. Alkaline cleaning (NaOH) of the chamber surface is under preparation so as to improve the vacuum pressure when being irradiated with synchrotron light.

2.3 Orbit Stability and Feedback

Table 2 lists the requirements on the orbit stability for possible research programs in the MR light-source study.

Based on the data for slow orbit movement measured over a period of 8 hours, the MR electron orbit is expected to change by $48\mu\text{m}$ and $94\mu\text{m}$ in the horizontal and vertical positions, respectively, and by $14\mu\text{rad}$ and $21\mu\text{rad}$ in the horizontal and vertical angles, respectively, at the location of the undulator. The fast orbit movement (3~100Hz) was also measured, and is expected to satisfy the stability requirements.

To suppress the slow orbit movement, an orbit feedback system is being prepared that comprises single-pass beam-position monitors, horizontal and vertical steering magnets and a feedback circuit. An analysis of the feedback system gives a feedback gain of 14dB at 4Hz when the beam position is measured every 5msec.

This feedback system will keep the orbit movement within the stability requirements for all research programs.

Table 2 Requirements on the orbit stability.

research program	position (μm)	angle (μrad)
(Vertical direction stability requirements)		
(a) X-ray diffraction on single muscle fibers	± 500	± 10
(b) formation of micro beam and its application	± 5	± 10
(c) crystallization process by SR irradiation	± 500	± 5
(d) X-ray parametric scattering	± 500	± 5
(e) Mössbauer spectroscopy	± 500	± 5
(Horizontal direction stability requirements)		
(a), (b), (c), (d) and (e)	± 1500	± 15

2.4 Emittance Measurement

In a light-source study at the MR the achievement of a very low emittance is a key issue, and must be confirmed in a reliable way. Three methods have been proposed, as presented in the following with comments. All of them are being prepared to make emittance measurements of the MR beam.

Visible light has a much longer wavelength (typically 500nm) than the emittance of the MR beam (5nm in the horizontal and several % of this in the vertical). However, a beam-size measurement is marginally possible, owing to the wide opening angle (942 μ rad) of the synchrotron radiation from the bending magnet. The resolution (42 μ m) is comparable to the vertical beam size when the emittance coupling is several %.

The wavelength of a 100-keV x-ray is sufficiently short for measuring the MR emittance with high precision. It will be obtained from the 5th harmonics of the undulator radiation ($K=0.3$). The final resolution may deteriorate somewhat because of a deformation of the first crystal due to the heat load and mechanical stress of the cooling water.

The measuring system of the spin-polarization already in use will be used for the emittance measurement. This system measures the emittance by detecting the angular distribution of the Compton scattering of laser photons from the electron beam.

S. Kamada

References

- 1) S.Kamada, et al., the SRI'94 proceedings.
- 2) K.Oide and H.Koiso, Phys. Rev. **E47** (1993) 2010 .
- 3) Y.Funakoshi, KEK Preprint 94-72.
- 4) S.Kamada, KEK Preprint 94-176.

3. SUPER-BRILLIANT X-RAY UNDULATOR FOR THE TRISTAN SUPER LIGHT FACILITY

3.1 Prototype Undulator XU#MR0

In order to develop a construction method for very long undulators, which will be required in the original TSLF plan,¹⁾ we have been carrying out various R&D studies by building a prototype undulator (named XU#MR0 : see Table 3 and Fig. 5), which comprises

three precise standardized-unit undulators.²⁾ Each standardized-unit (1.8m long) is placed very precisely on a rigid common frame to form a 5.4-m undulator. We adopted a pure-Halbach type configuration of NdFeB magnets (remanent field, $B_r=12.8$ kG; coercivity, $iH_c=17$ kOe). The selection of the period ($\lambda_u=4.5$ cm) was made so that a Mössbauer energy of ^{57}Fe (=14.4keV) could be obtained at the first harmonic under 10-GeV operation of the MR.

Since the support structure of the XU#MR0 is shaped like the letter "C", it can be installed without breaking the vacuum of the MR. In order to standardize the mechanical structure of the XU#MR0 and to make it applicable to various magnetic specifications, the following items were considered.

Table 3 Parameters of XU#MR0.

Magnetic structure	Pure configuration
Magnetic material	NdFeB ($B_r=12.8$ kG, $iH_c=17$ kOe)
Period length	$\lambda_u=4.5$ cm
Number of periods	120 [=3 \times (40/unit undulator)]
Magnet length	5.4m [=3 \times (1.8m/unit undulator)]
Maximum peak field	$B=2.64$ kG
Maximum K	$K=1.11$
Range of magnet gap	3~50cm
Aperture	2.4cm

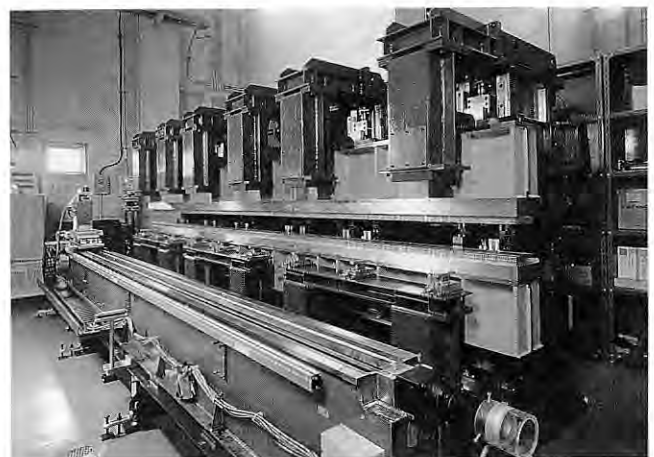


Fig. 5 Photograph of the XU#MR0.

Adoption of a spring system

In the present support structure the magnetic attractive force tends to violate parallelism between the upper and lower girders on which the magnets are attached. In order to eliminate this, both girders are equipped with special spring systems from the open side of the letter "C" to share the magnetic force. Each system has a set of springs; the stiffer springs work at progressively closer gaps to support the load.²⁾ Although the load shows an exponential dependence on the gap, it can be approximated by the force-gap relation of the present spring system.

Optimization of magnet-mounting girders

In order to optimize the stiffness of the girders and to suppress the distortion within an allowable range, we need to know the maximum force applied to them. Figure 6 shows the maximum magnetic field at a minimum gap of 3cm as a function of the magnetic period length (λ_u). Although the longer λ_u gives a higher field and a larger distortion, its increase can be limited by limiting the maximum value of K . If the undulator radiation is characterized by K values of less than 5, the maximum field is limited to below 6.5kG at $\lambda_u=8.3$ cm, as shown in Fig. 6. This value of the magnetic field gives a maximum attractive force of 1400kgf.; the distortion is suppressed below $1\mu\text{m}$ regardless of λ_u , by adopting the present design of the girders, whose height is 35cm.

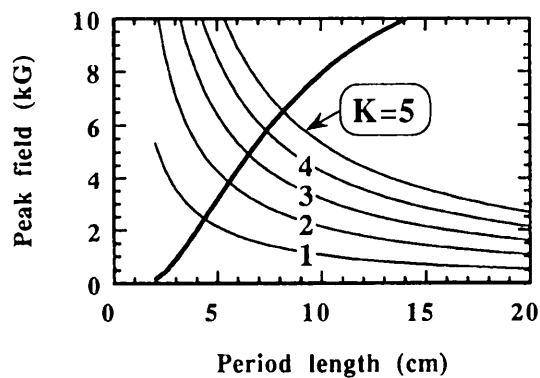


Fig. 6 Maximum magnetic field given as a function of λ_u (a bold line). The relations of the magnetic field and λ_u with a constant K value are also shown (thin lines). The maximum field is limited to below 6.5kG at $\lambda_u=8.3$ cm under the condition of K values less than 5.

Flexibility for selection of λ_u

The selection of λ_u is constrained by the reducibility of the girder length with respect to $\lambda_u/4$ for the pure configuration and $\lambda_u/2$ for the hybrid configuration. A girder length of 1.8m was selected due to this viewpoint: in the pure configuration, the allowable values of λ_u , from 4 to 12cm are 4.0, 4.5, 4.8, 5.0, 6.0, 7.2, 7.5, 8.0, 9.0, 9.6, 10.0, and 12.0cm. For the easy selection of any of these period lengths we can use a set of parallel plates. Each set has holes through which the magnets are bolted onto the plates. The pitch of these holes fits only a particular λ_u .

Besides the above items, relaxation of the thermal expansion should be one of the most significant problems when we construct very long undulators, especially in making the vacuum chamber for the out-of-vacuum configuration. This problem seems to be resolved by adopting an in-vacuum configuration of the magnets, which is also allowed by the present design of the structure of the XU#MR0.¹⁾

The magnetic field of the XU#MR0 is optimized so that the electron orbit is close to an ideal sinusoidal curve. For this purpose, the kick-angle of electrons at each magnetic pole is adjusted on the basis of a precise magnetic measurement using a Hall generator and a precise three-axis translation stage. As a coarse adjustment, the magnets at a pole having a larger kick-angle (usually a higher field strength) were exchanged with those at another pole having a smaller one (a lower strength). For a fine adjustment, disk-shaped magnet chips were used in order to decrease the scatter of the kick-angles. Each holder which mounts the magnet block has holes in which these chips are embedded

As a criterion for field optimization we used the following conditions concerning the deflection angle (θ_{def}) and the effective amplitude (δ) of the envelope of the electron orbit in order to obtain good transverse coherence of the radiation: $\theta_{def} \leq \sigma_r' = (\lambda / N\lambda_u)^{1/2}$, and $\delta \leq \sigma_r = (\lambda N\lambda_u)^{1/2} / 4\pi$. Here, σ_r' is the divergence angle of the undulator radiation, having a wavelength of λ from a single electron; σ_r is the corresponding size of the radiation. We adopted a value of $\sigma_r' = 4 \mu\text{rad}$ as the critical deflection angle, and one of $\sigma_r = 1.8\mu\text{m}$ as the critical amplitude, since we designed the XU#MR0 so that its first harmonic could be tuned at 14.4keV (0.86A in terms of λ) when $K=0.97$. The optimization was performed fairly successfully, and the deflections of the envelope became less than $0.2\mu\text{rad}$ and the amplitude less than $1\mu\text{m}$.

The variation in the ambient magnetic field, which mainly comes from changes in the accelerator operation and from geomagnetism, is crucial for the fine magnetic adjustment mentioned here. We devised a correction system for such a variation, and installed it in the XU#MR0. This system comprises a detector using Hall generators and correction coils wound round the upper and lower magnet arrays of the XU#MR0. The details have been given elsewhere.³⁾

3.2 Practical Source for the SR Test Experiments in 1995

Although our original plan for converting the MR was not finally approved, we will be able to carry out the SR test experiments using the MR in the autumn of 1995. The XU#MR0 will be used for these experiments as a super-brilliant x-ray source. Although the MR will not be completely converted, compared to the original TSLF, we will be able to obtain a natural-beam emittance of 5nm-rad at the MR's operation energy of 10GeV, owing to an adequate and minimum modification of the MR lattice for the creation of a free space for installing the XU#MR0. The spectrum obtained in this case is also shown in Fig. 7. A calculation shows that the XU#MR0 is able to produce quasi-monochromatic x-rays as the first harmonic with a brilliance of 1.0×10^{18} [photons/s/mm²/mrad²/0.1% bandwidth] in the case of $K=0.97$ at 14.4keV, when the MR is operated at 10GeV and 10mA. By combining 8- and 10-GeV operations, a photon energy from 8.4 to 21keV can be covered by the first harmonic, and that from 25 to 60keV can be covered by the 3rd harmonic.

In order to install the XU#MR0 into the MR for test experiments, some modification of the common frame of the XU#MR0 is required, since the beam-path height of the installation point available in the present conversion of the MR is lower than that planned in an original TSLF. We have already reissued a slim version of the common frame, and reassembled three unit undulators on it. The effects of this reconstruction on the magnetic field of the XU#MR0 are negligibly small since reconnection of the unit undulators is made carefully with an accuracy of $\pm 10\mu\text{m}$, as shown in Fig. 8.

This also shows that magnetic measurements and adjustments for the long undulators can be made by longitudinal connections of those for the short parts, which comprise several unit undulators. In this case the measurements and adjustments for neighboring

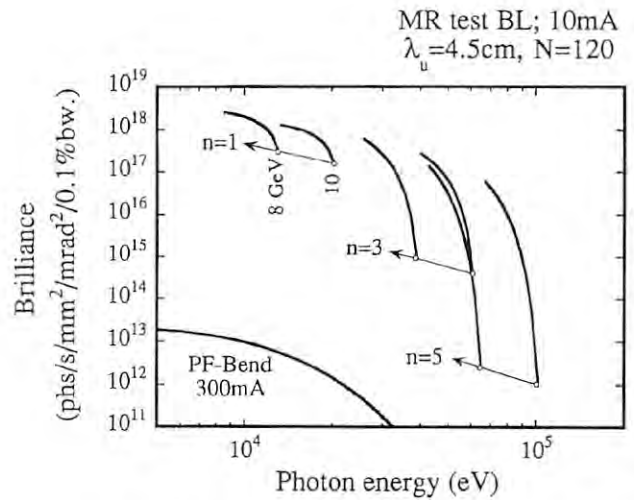


Fig. 7 Brilliance of radiation from the XU#MR0 in the cases of 8- and 10-GeV operation of the MR with the beam current of 10mA. Each curve shows the locus of the peak position of the n-th harmonic when K decreases from its maximum.

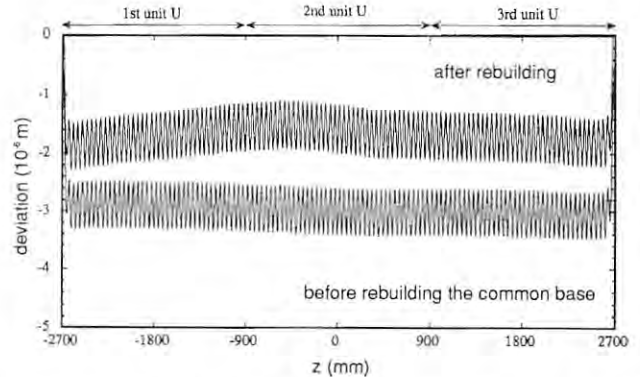


Fig. 8 Magnetic field of the XU#MR0 after rebuilding the common frame, in terms of the electron orbit in it, is compared with that before rebuilding.

parts will be done successively; at least one unit undulator between the first and second short parts will be measured twice as the last unit of the first part and as the first unit of the second part. By using this scheme construction of long undulators will be made effectively since installation of the long undulator to an accelerator and the magnetic adjustment will be done simultaneously by installing the parts for which the magnetic adjustment is completed, prior to the uncompleted parts.

S. Yamamoto

References

- 1) The Tristan Super Light Facility; Conceptual Design Report 1992, KEK Progress Report No. 92-1 (1993).
- 2) S.Yamamoto et al., Rev. Scientific Instrum. 66 (1995) 1996.
- 3) S.Yamamoto, Proceedings of the international workshop on magnetic measurements of insertion devices, ANL/APS/TM-13, 186 (1993).

4. BEAMLINE AND RELATED RESEARCH AND DEVELOPMENT

4.1 Present Status of the Beamline BL-BW-TL

In the previous report we described the basic design of a test beamline (BL-BW-TL) constructed for a feasibility study of the SR experiments at the Tristan MR. After that, the construction of the test beamline has progressed at a tentative place for the examination. The design of the beamline has been improved as the plan for the feasibility study has become concrete. Here, we mainly describe modifications of the design and the present status of the BL-BW-TL.

In this beamline, super-brilliant radiation having a high heat load from the XU#MR0 has to be handled. The MR will be operated at 10GeV, 10mA and 1, 2, 4 and 8 bunches with an emittance of around 5nmrad. A

lower emittance than that of third-generation light sources, such as SPring8, ESRF and APS, will be realized, and, thus, even more brilliant X-rays than those in case of a single bunch operation will be obtained from the undulator (XU#MR0) in the X-ray region. As a typical value, the brilliance will be 2.6×10^{18} photons/s/mrad²/mm²/0.1% band width at 14.4keV, as the first harmonic when $K = 0.95$ in the case of 10GeV and 10mA operation of the MR. Table 4 gives the characteristics of radiation from the XU#MR0, which is obtained when K is at the maximum value of 1.07, and the MR is operated at 10GeV with a ring current of 10mA and an emittance coupling ratio of 1%. As design parameters of each beamline component, the highest heat-load condition coming from the 100mA operation of the MR which 10GeV has been considered.

The design of the beamline was modified as follows:

- a) A fast closing valve (FCV) is not installed, because there will be no probability of accidental vacuum leaks at the lower reaches of the beamline for the short period of SR experiment, which is about 3 months. Actually, there has been no accidental vacuum leak at which the FCV has to work at the PF during this decade. Even if an accidental leak occurs, the ordinary gate-valve system will be able to take care of it because of the very long and low conductive vacuum pipes of the beamline.

Table 4 Characteristics of undulator radiation from the XU#MR0, which is at the maximum K value of 1.07, and when the MR is operated at 10GeV with a ring current of 10mA and an emittance coupling ratio of 1%.

Total power		220 W
Power density		22.2 kW/mrad ²
Source size (horizontal / vertical)*		292 / 35 μm
Beam divergence (horizontal / vertical)*, **		71 / 19 μrad
Power divergence (horizontal / vertical)*		127 / 74 μrad
Beam size at each position from the source point (horizontal / vertical)*, **	(at 17m)	1.5 / 0.36 mm
	(at 50m)	3.8 / 1.0 mm
	(at 85m)	6.3 / 1.7 mm
Power size at each position from the source point (horizontal / vertical)*	(at 17m)	2.5 / 1.3 mm
	(at 50m)	6.7 / 3.8 mm
	(at 85m)	11 / 6.4 mm
Power flux at each position from the source point	(at 17m)	76.8 W/mm ²
	(at 50m)	8.9 W/mm ²
	(at 85m)	3.1 W/mm ²

*: These values are twice standard deviations.

** : These are values for the first harmonic (13.4 keV).

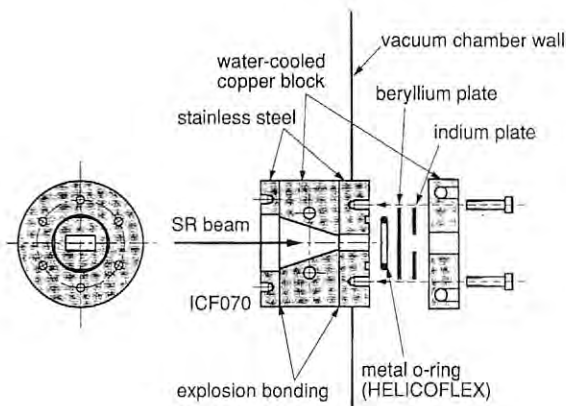


Fig. 9 Schematic structure of a beryllium window for vacuum isolation.

- b) A schematic structure of a beryllium window for vacuum isolation is shown in Fig. 9. A beryllium plate is mechanically fixed onto a water-cooled copper block. It is thermally contacted to a copper block through the indium medium from one side; from the other side a metal o-ring is used for vacuum sealing.

Most of the beamline components have already been made, and have been assembled at a tentative place. We are testing the motion of shutters, slits and beam-position monitors in a vacuum.

H. Sugiyama

4.2 Design and Construction of the Double-Crystal Monochromator for the Beamline

The double-crystal monochromator on the BL-BW-TL has a special structure, because the SR beam is led to the experimental station after it is kicked down by a first-piece crystal, which is set on the third basement; the second one is in the experimental station on the fourth basement, as shown in Fig. 10. The available range of the Bragg angle of this monochromator is limited from 18 to 26 degrees because of a height difference of 4.5m between the incident and out-going beams and the allowed restricted space. We need to exchange diffraction orders or crystals relevantly so as to obtain photons of the required energy, as shown in Fig. 11.

The first crystal is to be cooled by liquid nitrogen in a vacuum. The second crystal goniometer, together with the vacuum chamber, can be moved along the SR

Tristan Tsukuba experimental hall

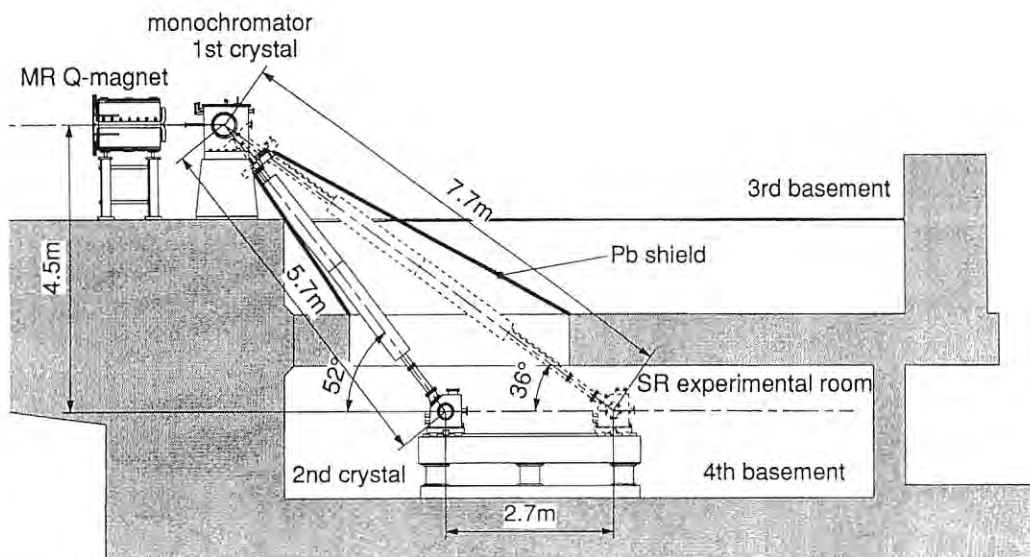


Fig. 10 Cross-sectional view of the SR experimental station including the double-crystal monochromator viewed from the center of the MR.

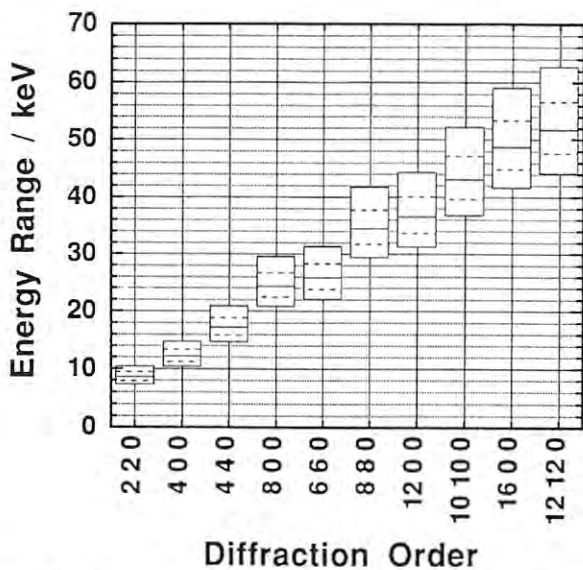


Fig. 11 Available energy range for each diffraction when the Bragg angle is limited from 18 to 26 degrees.

beam axis by about 2.7m on a rigid stage. The second crystal is also put in a vacuum isolated by beryllium windows. Welded bellows connect the first-crystal and second-crystal vacuum chambers. The length of the welded bellows can be altered by about 2m as the second-crystal chamber moves.

The ω -axes of the first-crystal and second-crystal goniometers and the linear movement of the second crystal of the monochromator are controlled by a feedback system with rotary or position encoders. The motions of each component are interlocked by computer control.

The feedback system for goniometers are able to control the ω -axis of HUBER's goniometer 420 even without a tangential bar with a relative accuracy of about 1/100arcsec. For this purpose we use a rotary encoder ROD 800 (HEIDENHAIN) and NANO DRIVE UNIT SF-1 (S.G INSTRUMENTS Co. LTD.) with an ordinary servo-motor in this system. We use HUBER's goniometers 430 and 420 for the double-crystal monochromator. The angle and energy divergence of the incident X-ray beam can be accurately measured by means of the double-crystal monochromator with this precise control system.

H. Sugiyama & Y. Higashi

4.3 X-Ray Microbeam

An X-ray microprobe has been expected to be a promising analytical tool for spectroscopic and structural studies of the elemental constitution of matter with spatial resolution. The detectable signals are fluorescent X-rays, photoelectrons, micro-X-ray diffraction, EXAFS and so on. Recent advances in X-ray optical elements have made it possible to design various types of X-ray microprobes.

Among them, grazing-incidence mirrors are the most convenient focusing elements because they can be used for a wide spectral range. Due to the large optical aberrations inherent to a single grazing-incidence mirror it was difficult to produce a small X-ray spot of less than one micron. In order to produce a much smaller microbeam these aberrations must be reduced. A Wolter type-I mirror is one of the best grazing-incidence mirrors which can considerably reduce aberrations. Figure 12 shows the parameters of the Wolter type-I mirror which is being developed for X-rays longer than 0.1nm. The Wolter mirror consists of one paraboloidal mirror and one hyperboloidal mirror which compensate the aberrations with each other. The optical alignment of the Wolter mirror becomes considerably easier compared with that of the paraboloidal mirror. Figure 13 shows the variation in the spot size of two mirror systems due to the axial displacement of the mirrors. If the complete 360-degree surface of revolution is used for focusing X-rays, it is theoretically possible to obtain a microbeam smaller than 10nm. A submicron X-ray microbeam will be obtained by using only a small part of the aperture.

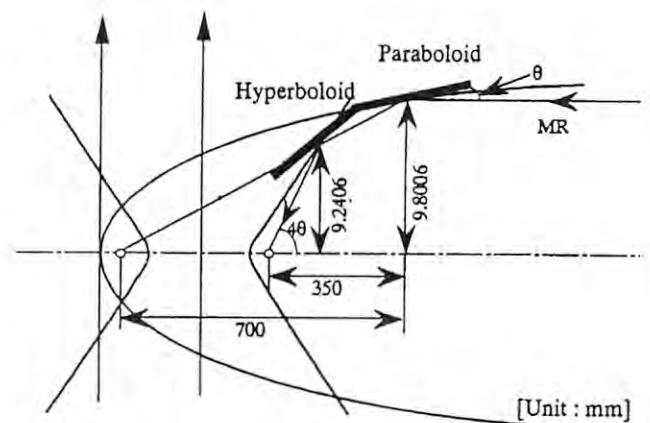


Fig. 12 Parameters of a wolter mirror.

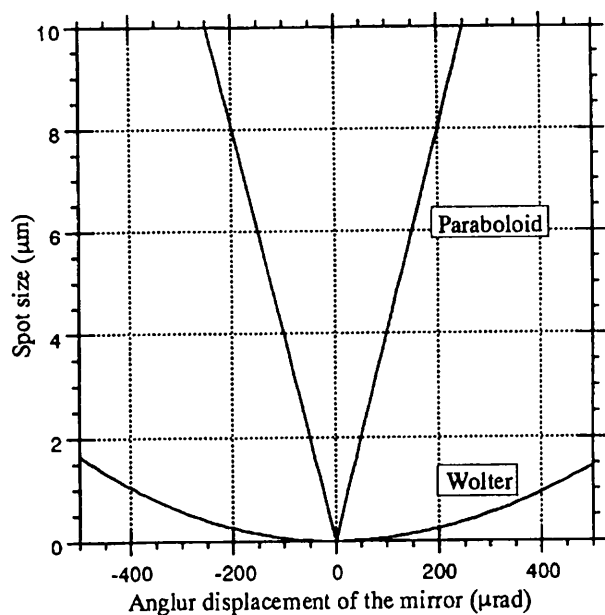


Fig. 13 Spot size with angular displacement of the mirror.

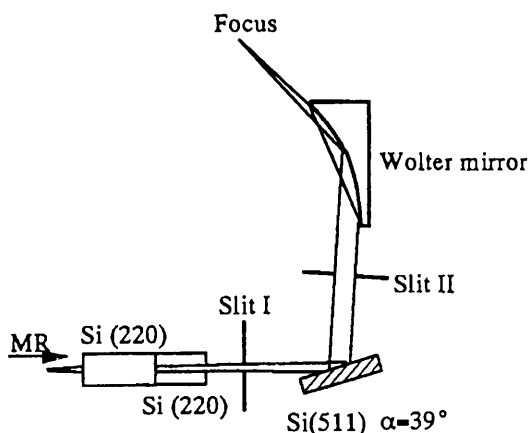


Fig. 14 X-ray microbeam optics.

This optical system does not require a very long source-to-mirror distance, which is usually required when an ellipsoidal mirror is used instead of a paraboloidal one. It only requires a collimated beam. A high collimation of better than 10 microradian can be accomplished by using a combination of Si crystals, that is, double-parallel crystals and an asymmetric one. This also produces a relatively large coherent area suitable for producing a diffraction-limited microbeam.

Some preliminary tests with a single paraboloidal mirror having a small aperture have been made at beamline 6C2 (see proposal No.93G110). A highly collimated X-ray beam having a horizontal divergence of about 6 microradian was obtained by combining a Si(311) channel-cut monochromator and a single Si(333). This beam divergence gave us a linear spatial coherence distance of about $24\mu\text{m}$ with an X-ray energy of 9keV. The figure error of the paraboloidal mirror was well examined by using a spatially coherent beam. The surface undulation of several microradians produced separate micro-spots in the focal plane. The final microbeam must be obtained by using the entrance mask of the mirror. Although the limited aperture of the mirror was small, the diffraction-limited micro-spot as small as $5\mu\text{m}$ was obtained.

A further improvement can be expected by using a higher collimation beam. An asymmetric Bragg reflection of Si(511) having a 39-degree difference between the crystal surface and the reflecting plane can produce a 9-keV sub-microradian divergent beam. The optical system which will be installed at MR is shown in Fig. 14. The spatially coherent area produced by this optics can be made larger than $100\mu\text{m}$. The final spot size will become sub-micron, or so.

S. Aoki, University of Tsukuba

5. PROPOSALS OF SR EXPERIMENTS

5.1 Mechano-Chemical X-Ray Diffraction Experiments on Single Skeletal Muscle Fibers

5.1.1 Scientific Background

Tension development in skeletal muscle is due to an interaction between two contractile proteins, actin and myosin. Myosin hydrolyses an ATP molecule, and uses its chemical energy to produce a contractile force in a muscle. Since actin and myosin molecules polymerize into a helical filamentous form and the filaments are arranged in a regular array in muscle cells, it is possible to study their structure in a muscle using an X-ray diffraction method. Especially, their structural changes during contraction can be studied by the time-resolved X-ray diffraction technique. This would provide a unique opportunity to investigate the relation between the structure and function of protein

molecules in living cells at a resolution of nanometers and microseconds. Since the size and periodicity of the molecular arrangement of actin and myosin filaments is on the order of nanometers, a small-angle diffraction technique is required.

A skeletal muscle comprises many elongated cells, called muscle fibers. In experiments of muscle physiology, an isolated fiber is commonly used as a specimen. In a whole-muscle preparation, the mechanical response that is recorded is an average of those from many fibers. At a high time resolution this hampers any accurate measurement, because each fiber has slightly different mechanical characteristics, and produces a different mechanical output. In order to study the mechanical behavior of muscle cells accurately, a measurement on a single fiber is essential.

In many of the X-ray diffraction studies on muscles made so far, the specimen was a whole muscle. This is because the diffraction from muscle, which is due to the contrast between proteins and water, which are made of light atoms, is weak. Thus, especially in time-resolved experiments, in order to collect enough photons in each time slot it has been necessary to use a whole muscle, which gives strong diffraction. Recently, because of the physiological requirement explained above, several X-ray diffraction experiments have been made on isolated single-muscle fibers, showing that the use of single fibers is essential in physiological studies of muscle. However, such experiments are still technically demanding compared with those using a whole muscle, because of the weak diffraction from a single fiber, which is only 100 μm in diameter.

Thus, intense synchrotron radiation from the Tristan main ring will be quite beneficial for X-ray diffraction experiments on single fibers. The most important advantage is its low emittance, which provides a small, parallel beam; since a single muscle fiber is only 100 μm in diameter, the cross-section of the X-ray beam should be similar in size to match it. The total flux of X-rays is also high, making it ideal for single-fiber experiments.

One drawback to using intense X-rays is radiation damage. It has been reported that a living single muscle fiber can survive in an X-ray beam of a conventional storage ring for only a few tens of seconds. However, we have found that a skinned muscle fiber is more resistant to radiation damage. Skinned fibers are also advantageous in that the chemical composition of the fluid around the contractile proteins can be easily

changed. This is useful in studying the relationship between chemical reactions and conformational changes of contractile proteins.

By using the intense synchrotron radiation from the Tristan ring and a small-angle X-ray diffraction technique, we have proposed to use a single skinned muscle fiber as a specimen and to study the structural changes in contractile proteins coupled with the force-generating process.

5.1.2 Experimental Setup

The X-rays will be provided by the double-monochromator which will be installed for general purposes. We are currently planning to use radiation from the ring run at 8 GeV. The monochromators will be tuned so as to pass 8.5 keV radiation, which has the highest intensity in radiation from the undulator. The estimated brilliance is *ca.* 6.3×10^{18} phs/s/mm²/mrad²/0.1%b.w.; a total flux of *ca.* 1×10^{14} will be provided in a cross-section of 6×1.7 mm (horizontal \times vertical) in 2s after the monochromators at the 10mm position from the source.

Immediately after this slit, a toroidal mirror will be placed. This mirror should have a focusing distance of 2.5 m vertically and 4.5 m horizontally. After the mirror, a 2-m vacuum pipe with quadrant slits at each end will be placed. These slits eliminate any X-rays parasitically scattered by the monochromators and the mirror; reduction of the low-angle background is essential for the proposed experiments.

The specimen (a single skinned skeletal muscle fiber) is placed just behind the second slits. The specimen is on a remotely controlled movable stage so that its position can be accurately adjusted to the beam.

Behind the specimen is a vacuum pipe of 2 m in length. The output diameter is 20 cm so that the small-angle diffraction pattern can be observed. The pipe is placed on a movable stage to adjust the position of the backstop, which is at the end of the pipe.

A detector is placed behind the vacuum pipe. Two kinds of detectors may be used: one is a rotating-drum type imaging plate detector; the other is an X-ray image intensifier coupled with a CCD video-camera. The former is a linear detector with a maximum time resolution of 27 msec; the latter is an area detector with a time resolution of 33 msec. These two detectors will be used according to the requirements of the physiological experiments.

5.1.3 Physiological Experiments

Currently, two experiments are being considered. One is a length-oscillation experiment. A single skinned fiber is connected to a motor; its length is changed sinusoidally at 0.5-4 kHz with an amplitude of a few %. Using the rotating-drum imaging plate detector, the intensity change of the meridional reflection from the thick filament at a 14.5 nm Bragg spacing is monitored during the oscillation of activated fibers. The intensity of this reflection is sensitive to any conformational change of the myosin cross-bridges, especially a conformational change along the direction of the filament, which may take place during force generation.

Another experiment makes use of caged-ATP which is a chemical compound that releases an ATP molecule upon photolysis. ATP, which is the energy source of muscle contraction, binds to myosin and modifies its interaction with actin. It is thus possible to study the kinetics of structural changes in the muscle proteins during force generation process using caged-ATP. All X-ray diffraction studies using caged-ATP have been made on a limited number of reflections, such as the equatorial reflections. We aim to record the full two-dimensional pattern using the X-ray image intensifier and the CCD video-camera to study any changes in other reflections, so that a more detailed analysis of the behavior of myosin heads and changes in the actin structure can be made.

*N. Yagi, Tohoku University and
K. Wakabayashi, Osaka University*

5.2 Hard X-ray Microprobe and Scanning Microscopy Experiment

5.2.1 Introduction

An X-ray microbeam is considered to be one of the keytechnologies in a third-generation high-brilliance SR source. Achieving an X-ray microprobe with a sub-micrometer spot size is expected to add a new dimension to various X-ray analysis methods, such as scanning microscopy, micro-diffraction, absorption spectroscopy and fluorescent X-ray analysis. Hard X-ray microbeam projects are planned and progressing in third-generation SR facilities. A high-brilliance X-ray

source is indispensable for microprobe experiments, because the flux of the microbeam is limited by the source brilliance, due to emittance conservation in the optical system. We have tried to generate a hard X-ray microbeam at the PF 2.5-GeV storage ring bending magnet station,¹⁻⁴⁾ and recently achieved a sub-micrometer focused beam size. However, the beam intensity is far from that needed for practical use (only about 10^2 cps- 10^4 cps). By using TSLF, a much higher beam intensity of about 10^9 cps is expected.

Micro-structures in semiconductors (LSI) and magnetic storage are on the sub-micrometer scale at present, and will approach $0.1\mu\text{m}$ in the future. These sub-micrometer structures are usually observed and inspected using a scanning electron microscope. However, only the surface regions can be detected by an electron probe, and radiation damage is very serious. The hard X-ray microprobe has the following advantages:

- 1) large penetration and low radiation damage;
- 2) low-background noise: trace-element mapping, and mono-atomic layers are easily detected by a fluorescent X-ray analysis;
- 3) micro-XAFS (X-ray absorption fine structure) spectroscopy for structure analyses of small samples or small areas in samples. Chemical state imaging by utilizing the absorption-edge chemical shift and/or differences in XAFS is possible using a wavelength-tunable microprobe. The magnetic domain and Bloch wall can be observed by using magnetic circular dichroism (MCD). However, MCD imaging is not possible at TSLF because of the planer undulator source.

5.2.2 Experimental Plans for X-ray Microprobe

By utilizing the above-mentioned advantages, we are planning the following experiments at TSLF:

- 1) Dislocation and impurity imaging for single-crystalline semiconductor materials. For instance, the relation between the lattice strain (or dislocation) and deposited pattern (or impurity mapping) can be studied by simultaneous imaging with scanning-diffraction topography and trace-element analysis by fluorescent X-ray spectroscopy.⁵⁾ It is also possible to analyze the chemical state of a small region of interest on the μm scale size by means of a micro-XAFS technique.

- 2) Observation of the domain structure in a monolayer polymer film as Langmuir-Blodgett films by means of trace-element mapping. The sensitivity for trace elements will be much higher than 10^{12} atoms/cm², and a submicron resolution will also be achieved by using TSLF. It will also be possible to measure 3-dimensional mapping of metal atoms using the fluorescent X-ray interference method.⁶⁾ The domain structures of over-turning in Langmuir-Blodgett monolayer films may be detectable by this method.

5.2.3 Experimental Setup for TSLF Hard X-ray Microprobe

We are now developing three types of optical devices for a hard X-ray microprobe, and an evaluation of the optical elements is now being performed at experimental station BL-8C2 of the PF 2.5-GeV storage ring: elliptical Kirkpatrick-Baez (KB) optics with total-reflection mirrors, bent-cylinder KB optics with multilayer mirrors, and sputtered-sliced Fresnel zone plate (FZP) optics. Here, we describe these candidates of optical systems for TSLF microprobe experiments.

1. Elliptical KB Total Reflection Optics¹⁻³⁾

A schematic diagram of the elliptical KB optics is shown in Fig.15. The elliptical KB optics use a pair of elliptical cylinder-shaped mirrors arranged in the Kirkpatrick-Baez configuration. An X-ray beam from the light source (*S*) is focused by a pair of elliptical cylinder-shaped mirrors (*M*₁ and *M*₂). The first mirror (*M*₁) focuses the beam in the vertical direction and the second mirror (*M*₂) focuses the beam horizontally. A demagnified image of the light source is generated at the focal point (*F*) where the samples are set. In the grazing-incidence optics, the focused spot size is limited mainly by a strong astigmatism and a spherical aberration. Compared with the Wolter mirror, the elliptical KB optics have a strong coma and field distortion (or field obliquity). However, their on-axis focusing properties are nearly perfect, *i.e.*, radiation from a point source is focused on a point by the elliptical KB mirror system. Therefore, diffraction-limit-focusing can be achieved if light sources with a sufficiently small source size are available and the optical elements have sufficient accuracy.

In a preliminary experiment at the bending magnet beam line (BL-8C) of the PF 2.5-GeV storage ring, a

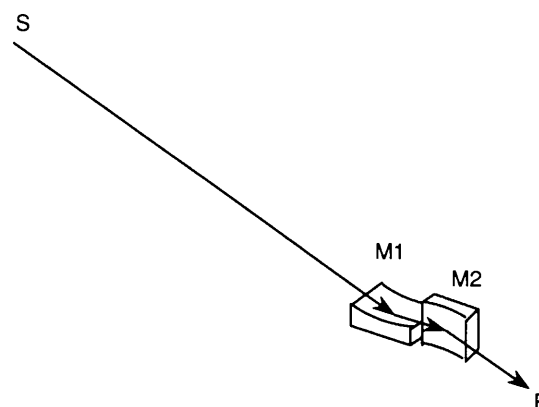


Fig. 15 Schematic diagram of elliptical Kirkpatrick-Baez microprobe. S, X-ray source; M1 and M2; elliptical; Mirrors; and F, focal point.

focused spot size of about $1\mu\text{m}$ was achieved at 6keV, and a periodic resolution test pattern with a $0.6\mu\text{m}$ line and space was resolved in a scanning-microscopy experiment.^{2,3)} The design values of a microprobe with an elliptical KB mirror system for the TRISTAN test beamline is listed in Table 5. The results of Monte-Carlo ray-trace-simulation are shown in Fig. 16. The effects of the depth of the undulator source were evaluated in the ray-trace-simulation by changing the distance between the source and the focal point. When the distance was changed by $\pm 10\text{m}$, no significant deformation or motion of the focused beam was found, as shown in Fig. 16.

2. Multilayer KB optics

KB optics with a cylindrically bent multilayer reflector have been developed and tested at BL-8C2, and a focused beam size of 1.2 micron has been achieved at an X-ray energy of 10keV (unpublished data).

3. FZP optics

A sputtered-sliced FZP fabricated by Kamijio and Tamura⁴⁾ at Osaka National Institute has been tested, and a focused beam size of $0.9\mu\text{m}$ has been achieved at an X-ray energy of 8 keV. However, an FZP is not practical at the bending magnet beamline because of the low efficiency (about 4%) and small numerical aperture. The total photon flux available at the bending magnet station of the PF 2.5-GeV ring (BL-8C2) is much less than 10^3cps at present. However, a beam intensity higher than 10^6cps is expected at TSLF. The design parameters of FZP microprobe optics for TSLF are listed in Table 6.

Table 5 Design value of X-ray microprobe I (elliptical Kirkpatrick-Baez optics)

Optics:	single stage elliptical Kirkpatrick-Baez
Monochromator:	Si(220) double crystal $\delta\lambda/\lambda=6 \times 10^{-5}$
X-ray wavelength range:	from 1.0Å to 2.0Å
Source size (assumed):	0.3mm \times 0.05mm
Distance between source and focal point:	100m
Divergence of radiation accepted by mirrors:	0.9 μ rad \times 0.9 μ rad (half angle)
Focal length:	120mm for first mirror (M_1) 60mm for second mirror (M_2)
Mirror length:	60mm (both M_1 and M_2)
Average glancing angle:	3mrad
Critical wavelength:	0.9Å (copper mirror)
Nominal demagnification:	1.2×10^3 for M_1 0.6×10^3 for M_2
NA:	0.8×10^{-3} for M_1 1.8×10^{-3} for M_2
Calculated spot size (FWHM):	0.06 μ m \times 0.14 μ m
Diffraction limit:	60nm \times 30nm at 1.0Å 120nm \times 60nm at 2.0Å
Photon flux at sample point: ($B=2 \times 10^{18}$ photons/s/mm ² /mrad ² /0.1%bandwidth is assumed)	about 5×10^9 photons/s

Table 6 Design value of X-ray microprobe II (Fresnel zone plate optics)

Optics:	single stage Fresnel Zone Plate
Monochromator:	Si(220) double crystal $\delta\lambda/\lambda=6 \times 10^{-5}$
X-ray wavelength	1.54Å
Source size (assumed):	0.3mm \times 0.05mm
Distance between source and focal point:	100m
Divergence of radiation accepted by mirrors:	0.4 μ rad \times 0.4 μ rad (half angle)
Focal length:	132mm at 1.54Å
Diameter of FZP:	80 μ m
Nominal demagnification:	1.3×10^3
NA:	3×10^{-4}
Calculated spot size (by geometrical optics):	0.4 μ m \times 0.07 μ m
Diffraction limit:	0.31 μ m.
Photon flux at sample point: (Efficiency of 5% is assumed) ($B=2 \times 10^{18}$ photons/s/mm ² /mrad ² /0.1%bandwidth is assumed)	about 3×10^7 photons/s

4. Other setup for scanning microscopy experiments

A newly developed mechanism and electronics for microscopy have already been installed at BL-8C2. It has an optical element alignment stage with four degrees of freedom, 4 channel counters, 4 channel frame memories (512 \times 512 pixel), and an image-processing computer. These setups will be moved to the TSLF experimental station for microprobe experiments.

Y. Suzuki, Advanced Research Lab., Hitachi, Ltd.

References

- 1) Y. Suzuki et al., Jpn. J. Appl. Phys. **28** (1989) L1660.
- 2) Y. Suzuki and F. Uchida, Jpn. J. Appl. Phys. **30** (1991) 1127.
- 3) Y. Suzuki and F. Uchida, Rev. Sci. Instr. **63** (1992) 578.
- 4) N. Kamijio et al., to be published in Rev. Sci. Instr.
- 5) Y. Suzuki and F. Uchida, to be published in Rev. Sci. Instr.
- 6) Y. Suzuki and S. Hasegawa, Jpn. J. Appl. Phys. **32** (1993) 3261.

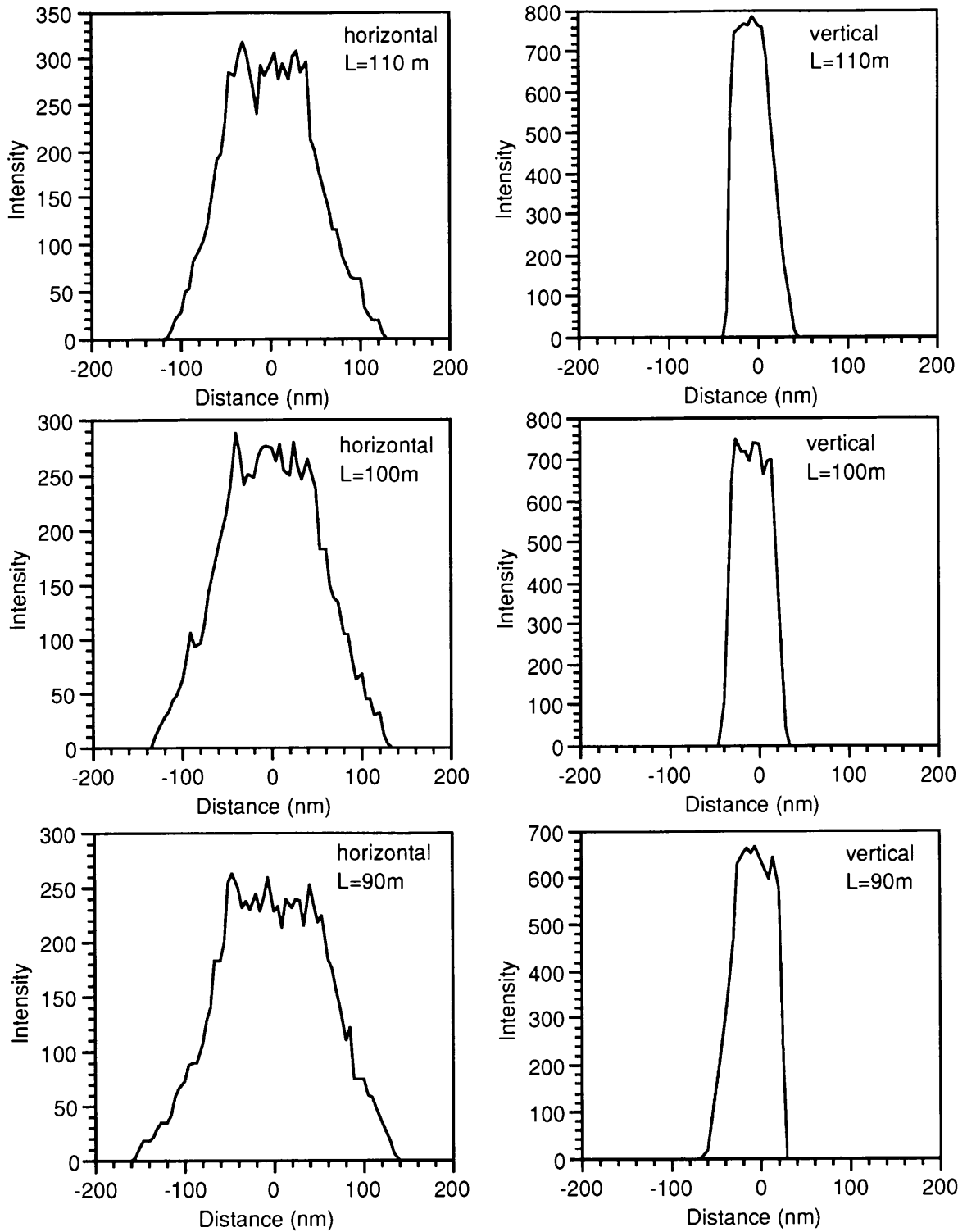


Fig. 16 Monte-Carlo ray trace simulation for elliptical Kirkpatrick-Baez optics. The design parameters are listed in table 1. L , source to focus distance. The focal spot is scarcely affected by the source motion along the optical axis.

5.3 SOLID-PHASE CRYSTALLIZATION OF SEMICONDUCTORS WITH X-RAY IRRADIATION

Solid-phase crystallization (SPC) of amorphous semiconductors by X-ray irradiation using synchrotron radiation is a promising technique for controlling the growth rate, selective growth and fabrication of nanostructures. From experiments for amorphous silicon (a-Si), it has been supposed that core-electron excitations by X-rays result in nonthermal atomic rearrangements which cause an enhancement of the SPC. However, the mechanism for nonthermal formation of this atomic structure has not been made clear.

Figure 17 shows the X-ray irradiation time dependence of the SPC of a-Si by post-thermal annealing. The a-Si specimens were irradiated by white X-rays at a substrate temperature of 40-50°C (BL-15B, 2.5GeV, ~300mA). Post-thermal annealing was performed at 600°C for 30 minutes for all specimens. The Raman parameters for the specimen are plotted against the irradiation time. It is clearly seen that the crystallinity increases along with the irradiation time up to 5hrs. This means that the structure change of the a-Si network is not saturated for this irradiation time, whereas the dangling-bond density tends to saturate after several minutes of irradiation. Therefore, it is necessary to confirm using more brilliant X-rays how much dosage of X-ray photons is required for a maximum enhancement of the SPC by this crystallization technique.

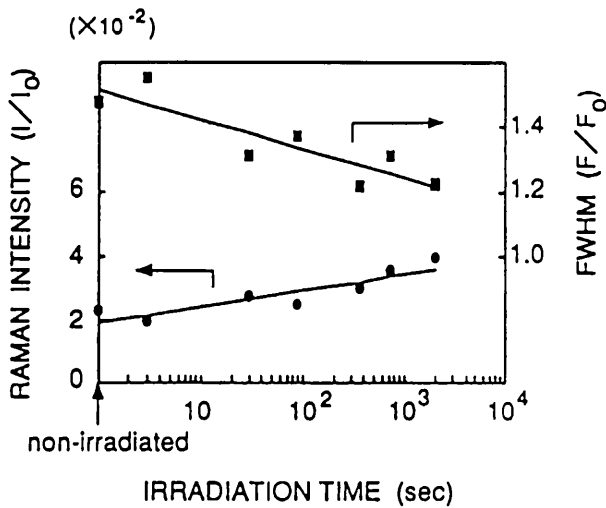


Fig. 17 Irradiation time dependence of Raman parameters for post-thermally annealed specimens.

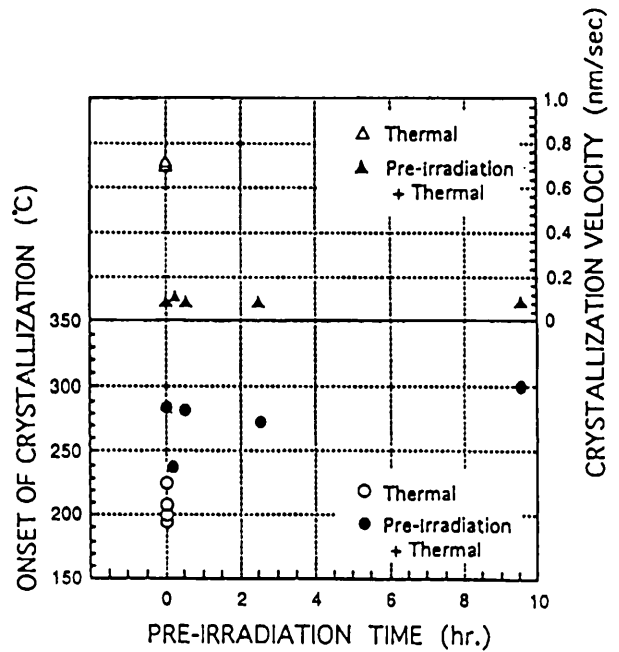


Fig. 18 Pre-irradiation time dependence of crystallization parameters of a-GaAs during in-situ annealing.

As for the nonthermal rearrangements of atoms by X-rays, the authors have considered the coulombic repulsion between multiply-ionized atoms, although the life of such ionized state is not known. Fig. 18 shows the X-ray irradiation effect on the solid-phase epitaxy of amorphous GaAs formed by heavy ion-implantation. (The irradiation conditions are the same as for Fig.17. In this case, in-situ annealing was performed.) It can be seen that both the onset temperature of epitaxy and the averaged growth velocity is lowered by X-ray irradiation. Since this effect does not depend on the pre-irradiation time, it can be supposed that X-ray photons break Ga-As bonds at the growing interface. (The solid-phase epitaxy of a-GaAs has been considered to be rate-limited by microscopic stoichiometry of GaAs at the growing interface.) For a selective treatment of compound semiconductors, it is necessary to clarify by experiments using monochromated X-rays as to whether this bond breaking is due to core-electron excitations or not.

F. Sato, NHK Science and Technical Research Labs.

5.4 X-RAY PARAMETRIC SCATTERING

X-ray quantum optics is an important subject in coherent X-ray physics which will be fully developed by using the X-ray FEL in the near future. Most of the characteristics of the quantum optics appear in non-linear optical phenomena. There have been few observations of X-ray non-linear phenomena. The nature of X-ray non-linear phenomena has yet to be revealed. Because of the poor coherency of synchrotron radiation at present, there is little hope to observe non-linear phenomena that include many X-ray photons. However, non-linear phenomena including laser photons and one X-ray photon can be observed. Investigations of this phenomena would lead to a better understanding of the characteristics common to X-ray non-linear phenomena.

X-ray spontaneous parametric scattering¹⁾ is a well-known quantum optical phenomenon; an incident X-ray field couples with a field due to a vacuum fluctuation through a higher order susceptibility of the material, resulting in two-photon scattering. These phenomena, in which both scattered photons are in the X-ray region,²⁾ or one photon is in the X-ray region and the other photon is in VUV region,³⁾ have already been observed. However, the case in which one of the two photons is in the optical region has not been observed yet because of its small scattering probability; it is on the order of 10^{-9} compared to that of photons scattering.⁴⁾ We can expect the emission of optical photons to occur as an induced process, provided an intense laser field exists. In this case, the scattering probability of that X-ray parametric scattering can be enhanced enormously. Estimating from laser assisted X-ray absorption under a 10^7 W/cm² laser field,⁵⁾ the scattering probability of the X-ray parametric scattering amounts to 10^{-4} of that of photon scattering.

Adopting a GGG single crystal as a sample, we presume such a resonance scattering process in which the 2p electron in Gd is excited into an empty 5d band; an intra-band transition then takes place by the stimulated emission of two optical photons; finally, the emission of an X-ray photon takes place. This process occurs effectively under so-called phase matching conditions, as follows:

$$\omega_{x'} = \omega_x - 2\omega_l, \quad (1)$$

and

$$k_{x'} = k_x - 2k_l + G. \quad (2)$$

Here, x and x' are the incident and scattered X-rays, respectively; l is the optical photon and G is a reciprocal-lattice vector. From eqs (1) and (2) we can expect a satellite to exist at the tail of a higher angle side of the Bragg scattering.

A more reliable experiment has recently been performed at an undulator beam line (AR NE-3) at KEK, which is operated in the single-bunch mode. Incident X-rays have been monochromated by a Si(111) double-crystal monochromator within a resolution of 1eV to an energy of 4.66eV; the double energy of the optical photon, is higher than the energy of the Gd L2 absorption maximum. Second higher harmonics of a pulsed Nd-YAG laser 50 Hz in repetition and 2 nsec in width have been utilized as the laser beam. Under the condition described above, the satellite has been expected to appear at a 268" higher angle side of the 444 Bragg reflection. The simultaneous irradiation of an X-ray beam and laser beam has been performed by referring to the ring control timing signal. The intensity profile has been measured with respect to the rotation of the crystal. Two kinds of the profiles have been measured simultaneously: one is gated by the laser Q-switch trigger; the other is ungated.

The gated profile normalized by the ungated profile exhibits an intensity enhancement at the region expected based on the phase-matching conditions. The width of the enhancement agrees well with that of the 444 Bragg reflection. The enhancement amounts to about 3% of the background intensity in this region. This value corresponds to 1×10^{-5} of the intensity of the 444 Bragg reflection. The scattering probability of the relevant phenomenon amounts to 10^{-4} of that of normal one-photon scattering if we consider the effective number of atoms contributing to the relevant structure factor. These results strongly suggest that the observed intensity enhancement is due to the X-ray parametric scattering induced by a strong laser field.

The advanced nature of the X-ray in Tristan Super Brilliant Light Facility is characterized by its ultra small beam size, super brilliance, very narrow pulse width and long pulse interval. As a result, a distinguished improvement in the spatial coherence is realized in TSLF radiation. Thus, the phase-matching condition is satisfied over a wide region of the crystal. The radiation damage is diminished by using a laser pulse as short as that of the X-ray pulse. This fact enables us to focus the laser beam upon the sample. In this case, the scattering probability increases bilinearly

to the laser-beam brilliance. These characteristics of the X-ray parametric scattering, stimulated by an intense laser field, enhances the scattered intensity. An energy analysis of the satellite reflection will be possible. Investigations of these characteristics reveal in the X-ray region the meaning of the concept peculiar to such nonlinear phenomena as the phase-matching condition, non-linear susceptibility and the temperature inversion in the induced process. These concepts are the key factors to open the field of the X-ray quantum optics when the X-ray FEL is realized in the near future.

K. Namikawa, Tokyo Gakugei University

References

- 1) I. Freund and B. F. Levine, Phys. Rev. Lett. **23** (1969) 854.
- 2) P. Eisenberger and S. L. McCall, Phys. Rev. Lett. **26** (1971) 684.
- 3) H. Danino and I. Freund, Phys. Rev. Lett. **46** (1981) 1127.
- 4) I. Freund, Phys. Rev. **A7** (1973) 1849.
- 5) I. Freund, Opt. Commun. **8** (1973) 401.

5.5 Photon Correlations in the X-ray Region

The high brilliance of synchrotron radiation from an undulator which is planned to be installed in the MR will enable us to obtain highly monochromatic X-rays (highly temporally coherent X-rays) by means of an ultrahigh-resolution nuclear monochromator or a high-resolution silicon monochromator. In addition, the source size in the MR is very small, and the spatial coherence of the beam is high. By using highly temporally and spatially coherent X-rays the observation of the photon correlations of the Hanbury Brown and Twiss type may be realizable in the X-ray region. It is expected to observe the bunching effect of X-ray photons. This experiment is also useful for characterizing the source size of synchrotron radiation. We are now developing instrumentation for this experiment, as follows.

5.5.1 Construction of a Precision Diffractometer System

A precision diffractometer system was designed and constructed. The mechanical design of the

diffractometer system is based on that constructed for studying nuclear resonant scattering at the TRISTAN Accumulation Ring. The diffractometer system comprises four-component goniometers, the main rotation axes of which have an accuracy of less than 0.1 arcsec and lie in the horizontal plane. Each component goniometer is mounted on a vertical (z direction) translation stage, which is assembled on a horizontal x-y stage attached to a cast-iron base. A precise slit system with an accuracy of 1 μm was also constructed, which is an important instrument for this experiment.

5.5.2 Ultrahigh Monochromatization of Synchrotron Radiation

5.5.2.1 Use of a Nuclear Monochromator

As a nuclear monochromator an α - $^{57}\text{Fe}_2\text{O}_3$ hematite crystal is planned to be used for this experiment. It provides an ultrahigh monochromatic beam with an energy width of less than 1 meV. Single crystals of ^{57}Fe -enriched α - $^{57}\text{Fe}_2\text{O}_3$ were grown by the PbO-V₂O₅ flux method; nearly perfect crystals were obtained. The maximum counting rate of nuclear Bragg scattering (14.4keV photons) using the best crystal with (777) reflection was as high as 2×10^4 cps, which was observed using synchrotron radiation from the TRISTAN Accumulation Ring.

5.5.2.2 Use of a High-Resolution Silicon Monochromator

Another candidate for monochromatization of synchrotron radiation is a silicon monochromator based on the usual Thomson scattering. Hitherto, an energy width down to about 10 meV has been achieved by using asymmetric reflection and extreme back-reflection. To obtain an energy width of about 100 meV a new type of silicon monochromator has been designed which will be operated under consecutive extreme asymmetric reflections. It will be worked well for synchrotron radiation source with a small size. If this monochromator is completed, it can be used more effectively for this experiment.

A nuclear monochromator of a $^{57}\text{Fe}_2\text{O}_3$ crystal or a high-resolution silicon monochromator is arranged in the precision goniometer system. After limiting the beam cross section by a precise slit, a highly monochromatized X-ray beam splits into two using diffraction by a silicon crystal. Two fast avalanche

photodiode detectors are arranged so as to detect photons coming from the crystal along two directions. The intensity fluctuations due to the arriving time of photons are measured.

S. Kikuta, University of Tokyo

B. VUV-FEL

1. VUV-FEL AT THE PF RING

Since 1992, development of a short-wavelength free electron laser (FEL) in a vacuum ultraviolet region has been made using a transverse optical klystron (TOK) located in the straight section, B01-B02, of the Photon Factory (PF) ring. For the first step, properties of the spontaneous emission obtained from the TOK were studied prior to the FEL gain experiment at 177 nm (the 6th harmonic of the Nd-YAG laser).

2. LOW ENERGY OPERATION OF THE PF RING AT 0.75 GEV.

For the FEL experiment, positron energy was lowered from the nominal energy of 2.5 GeV to 0.75 GeV. The beam parameters at 0.75 GeV are listed in Table 7. The RF feedback system was used to suppress the longitudinal beam instability for the FEL experiments.¹⁾

The bunch length of the positron beam was measured by the streak camera. As shown in Fig. 19, the bunch length becomes longer with the beam current, so that FEL gain may be reduced at the beam current higher than 5 mA (average current).

Table 7 Beam parameters at 0.75 GeV

beam energy	0.75GeV
number of bunches	1 or 4
beam emittance	~10nmrad (full coupling)
bunch length(2 σ)	60psec
peak current	20A
energy spread	~3.8*10 ⁻⁴
life time	~45 minutes
accelerating frequency	500.1MHz
injection energy	2.5GeV
time of reducing energy	~10 minutes

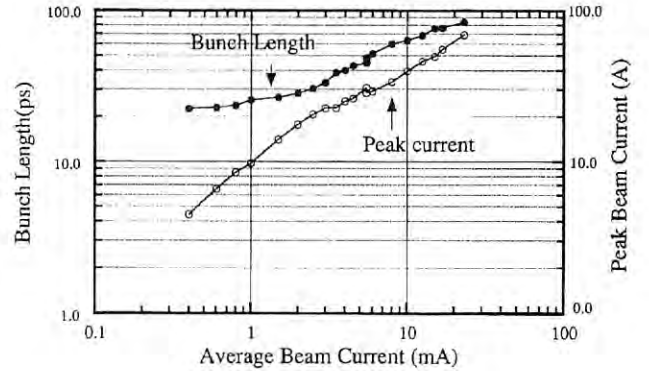


Fig. 19 The bunch length and peak beam current at 0.75GeV

3. FEL OSCILLATOR

The main parameters of the TOK are listed in Table 8. Fig. 20 shows the positron trajectory for various N_d values. The number, N_d , is given by

$$N_d = \frac{1}{2\lambda\gamma^2} \left[L_d + \frac{e^2}{m^2 c^2} \int_0^{L_d} \left\{ \int_0^u B(z) \right\}^2 du \right]$$

where L_d and $B(z)$ are the length and the magnetic field of the dispersive section of the TOK, respectively. The optimum N_d for the highest FEL gain depends on the energy spread as shown in the following equation;

$$(N_d)_{opt} = \frac{1}{4\pi \left(\frac{\delta_\gamma}{\gamma} \right)} - N_u$$

Table 8 Parameters of the TOK

periodic length	9cm
number of periods	19+19
max. magnetic field	0.7tesla
max. deflection parameter	5.9
N_d	90 to 200
length of dispersive section	38cm

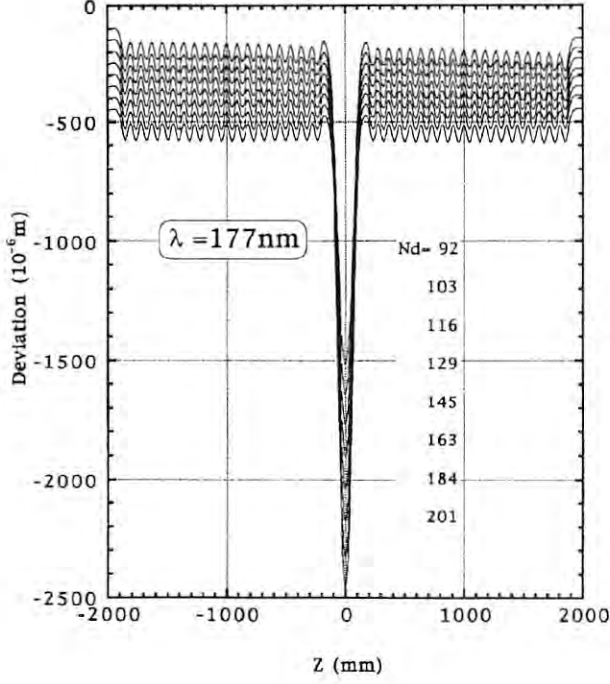


Fig. 20 Positron trajectory in the magnetic field of the TOK

4. SPONTANEOUS EMISSION

The spontaneous emission from the TOK was measured in the FEL beam line located at the downstairs of the straight section. Fig. 21a and 21b show the typical spectra for the betatron function, 5m and 1m, respectively. The TOK spectrum is given by

$$\left(\frac{d^2I}{d\Omega d\omega}\right)_{TOK} = 2\left(\frac{d^2I}{d\Omega d\omega}\right)_{undulator} \{1 + F_m \cos(\alpha)\}$$

$$\alpha = 2\pi(N_u + N_d) \frac{\lambda_1(177\text{nm})}{\lambda}$$

where F_m is a modulation factor giving the strength of oscillation in the TOK spectrum. The modulation factor is reduced by various inhomogeneous effects; for example, the energy spread ($\delta\gamma/\gamma$) and the angular spread of the positron beam. From the spectra observed, F_m is estimated as 0.58 at $\beta=5\text{m}$ and 0.46 at $\beta=1\text{m}$.

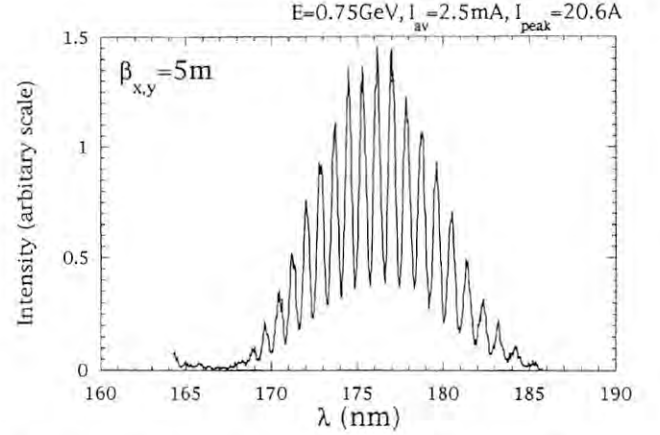


Fig. 21a Typical TOK spectrum obtained in the single bunch operation ($\beta=5\text{m}$)

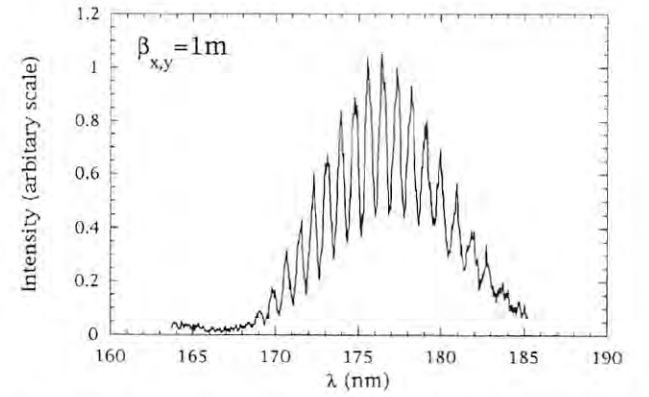


Fig. 21b Typical TOK spectrum obtained in the single bunch operation ($\beta=1\text{m}$)

5. FEL GAIN

According to the one-dimensional plane-wave approximation, the maximum FEL gain for the TOK can be obtained as

$$[G_{\max}(TOK)] \cong 0.926 \left(1 + \frac{N_d}{N_u}\right) F_m F_{\text{fill}} (8GU)$$

where GU is the FEL gain of a single undulator, and F_{fill} is a filling factor corresponding to the overlap of the positron and laser beams. We define F_{fill} as

$$F_{\text{fill}} = \frac{1}{1 + (2\sigma/w_0)^2}$$

where w_0 is the laser waist size and σ is the positron beam size at the center of the TOK. If the betatron function is set at 1m and a w_0 at $240\mu\text{m}$, the highest F_{fill} that can be obtained is 0.59. Therefore, the maximum FEL gain is expected to be 11.5% at the peak beam current of 20A. Considering the TEM_{00} mode laser beam, however, F_{fill} may be somewhat lower. So, the FEL gain may be also lowered to some extent.

6. THE LASER SYSTEM AND BEAMLIN

Table 9 shows the parameters of the laser system for the FEL gain experiment. The VUV laser at 177 nm is obtained by 6th-harmonic generation using an amplified Nd-YAG laser with three kinds of crystal; KTP, BBO, and KB5. Since the VUV laser is of multi-mode in the transverse direction, TEM_{00} mode should be selected by using a spatial filter. The beamline for the transportation of the VUV laser from the filter to

Table 9 Parameters of the laser system

mode-lock YAG laser	
mode-lock frequency	83.35MHz(=frf/6)
regenerative YAG amplifier	
repetition rate	50Hz
pulse energy at 10640Å	30mJ
pulse duration	80psec
Harmonic generation	
harmonic crystal	
SHG	KTP
THG	BBO
5HG	BBO
6HG	KB5
max.pulse power	~100KW

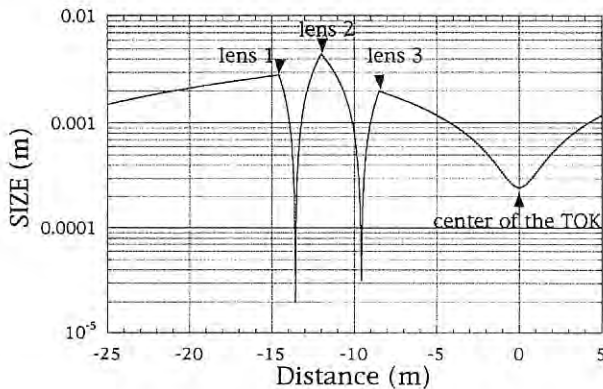


Fig. 22 Laser waist size in the FEL beamline

the TOK is composed of three LiF lenses with focal lengths of 1m, which should be located in the beamline so as to obtain a waist of $w_0=240\mu\text{m}$ at the center of the TOK. Fig. 22 shows the calculated laser beam size in the beamline. Waist size measurement will be made during the shutdown period next summer.

7. MONITOR SYSTEM

In the FEL gain experiment, spatial overlap between the positron beam bunch and the VUV laser is required. To realize that, a precise profile monitor is required. However, the spontaneous emission has longer wavelength radiations off axis, which may reduce accuracy in determining the central position of the radiation. To avoid such a problem we have developed a profile monitor having a monochromator system with an incident pinhole of $100\mu\text{m}$ in diameter. Therefore, we can obtain the precise central position of the spontaneous emission having a wavelength of 177 nm. Fig. 23 shows a profile of the spontaneous emission measured at 177 nm. The solid curves were obtained from the least squares fit of Gaussian distribution. In this measurement, the orbit of the positron beam was stabilized by the transverse feedback system composed of four steering magnets and two beam position monitors located at both ends of the TOK.

Reference

- 1) Photon Factory Activity Report #10(1992)p.R-5

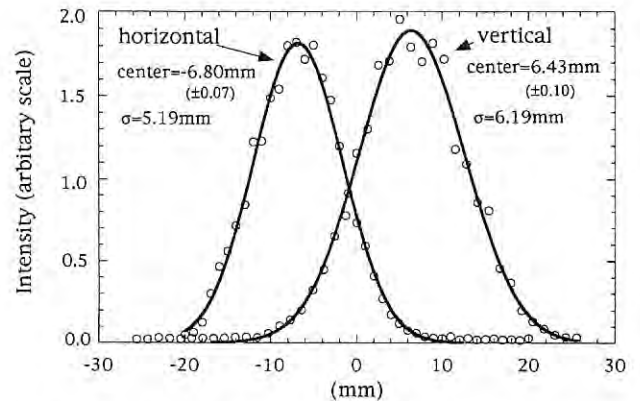


Fig. 23 Spatial profile of the TOK spontaneous emission

C. KEKB

1. OVERVIEW

The KEKB is an asymmetric, double-ring electron-positron collider, which will be optimized for detailed studies on the decay of B mesons. (The majority of the research topics is to study CP violation in the decay of neutral B mesons.) The KEKB will be built inside the existing tunnel for the TRISTAN main ring (MR). A schematic layout of KEKB is shown in Fig. 24. The high-energy ring (HER) will store electrons at 8 GeV, and the low-energy ring (LER) will store positrons at 3.5 GeV.

Two major goals of the upgrade of the Injector Linac (formerly 2.5 GeV) are:

- 1) To increase the energy of electrons and positrons so that they can be injected into the HER and LER of KEKB at full energy (8 and 3.5 GeV, respectively), and
- 2) to increase the bunch intensities of positrons by roughly one order for efficient fills.

Table 10 (1) through (4) show the parameters of the injector before and after the upgrade. The specific work involves the followings:

- 1) Successive replacement of the rf power sources with higher-power klystrons having rf pulse compressors.
- 2) A small extension of the total linac length.
- 3) Relocation of the positron production target so that positrons are produced with electrons at 3.7 GeV (formerly 0.25 GeV).

The pre-upgrade linac consists of six sectors, called P, 1, 2, 3, 4 and 5. A regular sector consists of eight accelerator units, each of which includes four 2-m

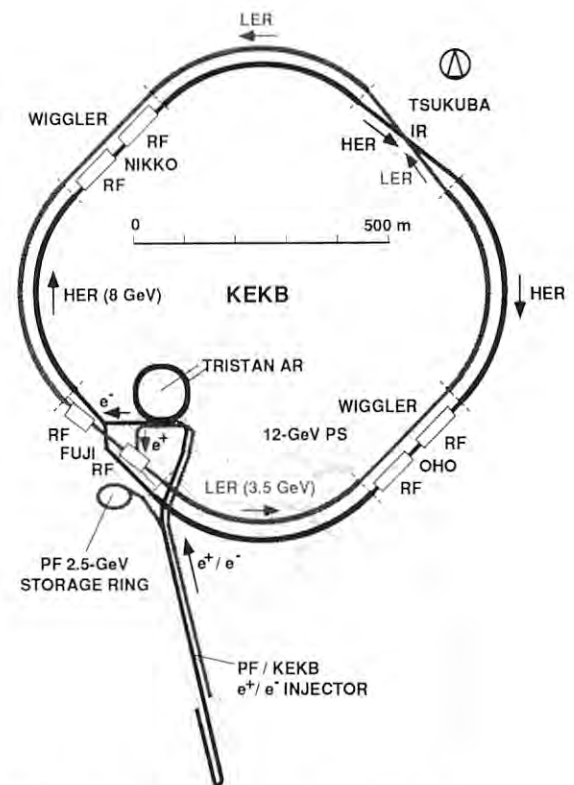


Fig. 24 A schematic plan view layout of KEKB.

accelerator guides. The accelerator guide in each unit is to be driven by divided rfs, fed by a klystron. In the upgrade, two new sectors will be added to the linac; they will be renamed A, B, C, 1, 2, 3, 4 and 5, as shown in Fig. 25. Sectors A, B and C are those to be newly built. Sector A will have a pre-injector to produce intense single bunches. It will include double sub-harmonic bunchers (SHBs), followed by three accelerator units. Sectors B and C are to be regular accelerating sectors. Sector 2 will be rebuilt so as to include a positron generator by moving Sector P to this

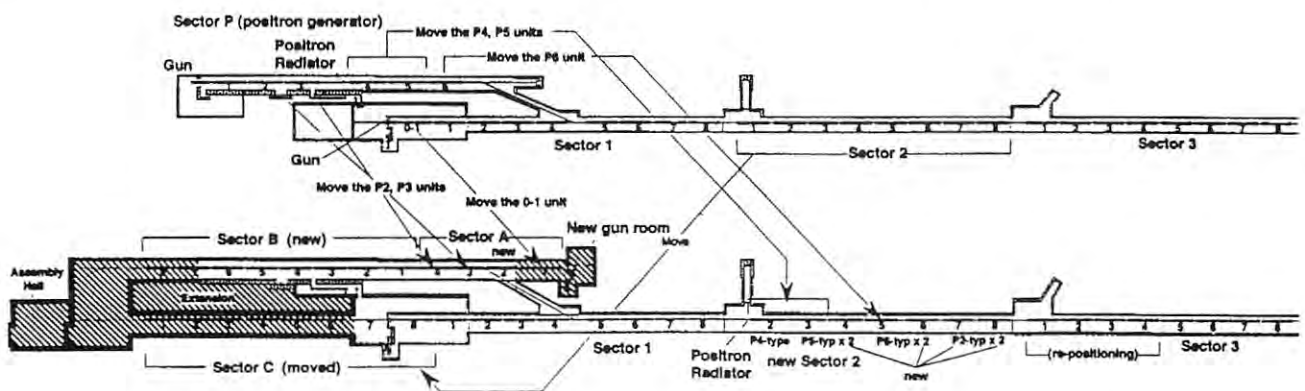


Fig. 25 The linac re-formation from the 2.5-GeV linac (upper) to the KEKB 8-GeV injector (lower).

Tables 10 Changes in the linac major parameters from the present to KEKB.

(1) INJECTION BEAM

	PRESENT	KEKB
energy [GeV]		
(e ⁻)	2.5	8.0
(e ⁺)	2.5	3.5
pulse length	< 2 ns	single bunch
bunch width (σ_z) [ps]	~5	~5
particle [$\times 10^9$]/pulse, (charge,[nC/pulse])		
(e ⁻)	2 (0.32)	8 (1.28)
(e ⁺)	0.2 (0.032)	4 (0.64)
pulse repetition [pps]	25	50
emittance [$\times 10^{-8}$ m]		
(e ⁻)	4	6.4
(e ⁺)	80	88
energy width [%]		
(e ⁻)	0.2	0.125
(e ⁺)	0.22	0.25

(3) PRE-INJECTOR

	PRESENT	KEKB
Gun		
type	triode	triode
norm. emit. [m]	5×10^{-6}	5×10^{-6}
1st-subharmonic buncher		
frequency [MHz]	119.00	114.24
field-strength [MV/m]	4	4
2nd-subharmonic buncher		
frequency [MHz]	—	571.20
field-strength [MV/m]	—	4
1st- and 2nd- prebuncher		
frequency [MHz]	2856	2856
phase velocity	0.7c	0.7c
Buncher		
frequency [MHz]	2856	2856
phase velocity	0.7c	0.7c
Output beam		
energy [MeV]	50	50
energy spread ($\sigma E/E$) [%]	0.6	0.6
norm. emit. [m]	$\sim 6 \times 10^{-5}$	$\sim 6 \times 10^{-5}$

(2) MAIN ACCELERATOR

	PRESENT	KEKB
frequency [MHz]	2856	2856
filling time [μ s]	0.5	0.5
structure	(T.W., $2\pi/3$ -mode, semi-C.G.)	
unit length [m]	9.6	9.6
number		
(total)	46	57
(before e ⁺ radiator)	3	26
(stand-by, energy-tuning)	~3+1	4+2
energy gain [MeV/unit]		
(w SLED)	—	160
(w/o SLED)	62.5	90
input rf power [MW] / unit	20	40
energy multiplication	—	1.8

(4) POSITRON PRODUCTION

	PRESENT	KEKB
Radiator		
material	Ta	W
thickness [mm]	8	16
diameter [mm]	8	8
Primary electron		
energy [GeV]	0.25	3.7
particle /pulse	1×10^{11}	6×10^{10}
(charge [nC]/pulse)	(16)	(10)
energy width [%]	0.45	0.45
Positron production rate (e ⁺ /e ⁻ GeV)		
after the solenoid [%]	6.5	6.5
final [%]	1.8	>1.8
Focusing system		
norm. acceptance [m]	6×10^{-3}	6×10^{-3}

location. In Sectors 1, 3, 4 and 5, the component layout will not be changed, or changed only slightly.

The pulse energy of the pulse modulators will be increased by a factor of two. This will be achieved by increasing the total capacitance of the PFN (pulse-forming network) while maintaining the same charging voltage. All of the 30-MW klystrons will be replaced by 50-MW types. Rf pulse-compressors will be installed at the klystron output with a small modification of the waveguide system and improvements in the vacuum system. The modulators

will be relocated to the old Sector P and Sector 2.

The number of accelerator units is to be increased from 46 to 57. The average energy gain of each unit will be 160 MeV by using an rf compressor. The full acceleration energy without beam loading will reach about 9 GeV. Extra energy over 8 GeV (13%) will be used to compensate for any gain loss due to defective units, energy-spread adjustment or energy tuning.

In the pre-upgrade, linac positrons are produced with 0.25 GeV primary electrons, where the production rate of positrons from electrons is to be 1.8% e⁺/e⁻ GeV⁻¹.

Assuming that the positron production yield is proportional to the primary electron energy, the expected positron charge after the upgrade will be 0.67 nC in each pulse, when primary electron pulses are 3.7 GeV and 10 nC .

2. HIGH-POWER TEST OF A NEW-TYPE RF PULSE COMPRESSOR

A high-power model of a new-type rf pulse compressor utilizing a coaxial traveling-wave resonator was fabricated and tested at high rf power level using the 46 MW klystron. A photograph of the high-power model of the pulse compressor is shown in Fig. 26. The cavity was assembled by silver and gold brazing. The surface flatness of the cavity inner wall is $0.1\mu\text{m}$. The measured rf characteristics of the cavity were as follows: the resonant frequency was 2.858 GHz, the Q -value (unloaded) was 4,800 and β was 2.7.

A schematic drawing of the high-power test setup is shown in Fig. 27. Before rf-conditioning, the entire system, including the waveguides, 3dB-hybrid and water loads were baked at 100°C for 4 hours. During rf-conditioning, the vacuum-pressure interlock used to stop the klystron was set at 2×10^{-4} Pa. After 240 hours of processing, the klystron output power reached 45MW with a pulse width of $3.8\mu\text{s}$ and a repetition rate of 25 pps. An example of the output waveform from

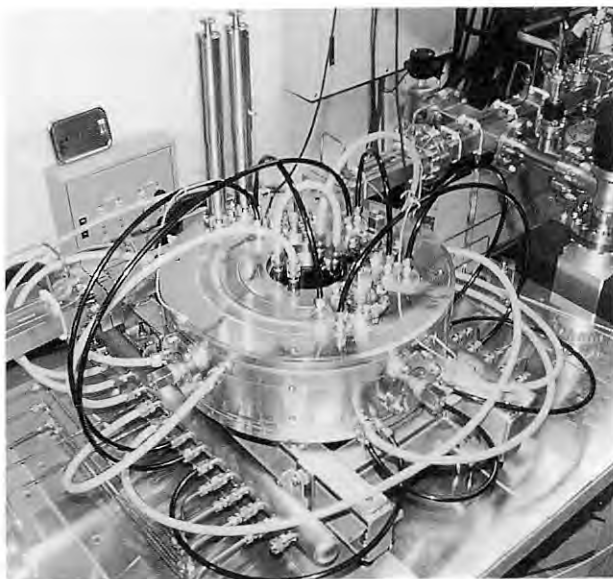


Fig. 26 High-power model of the traveling-wave resonator pulse compressor.

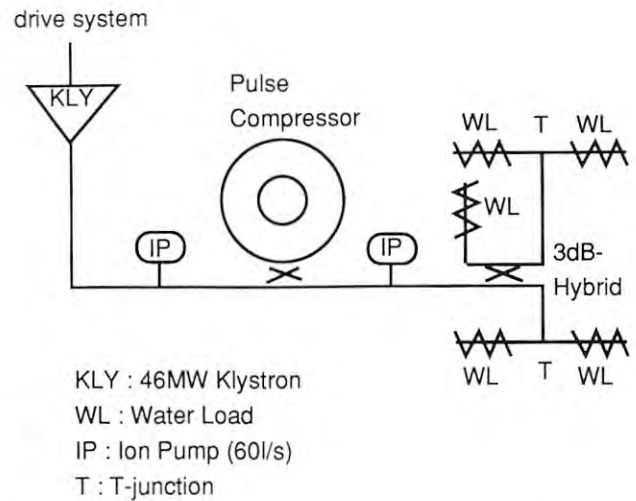


Fig. 27 Schematic drawing of the high-power test setup of the pulse compressor.

the new-type rf pulse compressor is shown in Fig. 28. At 45MW input power, a peak output power of 201MW and an average power gain of 3.07 were obtained. The flow rate of the cooling water ($30 \pm 0.1^\circ\text{C}$) for the cavity was 80 l/minute and the temperature rise of the cavity was 1.1°C at 45 MW input power. The dose-equivalent rate was $28 \mu\text{Sv/h}$ at a point 2 m away from the cavity. The maximum measured energy of the X-ray was 800 keV.

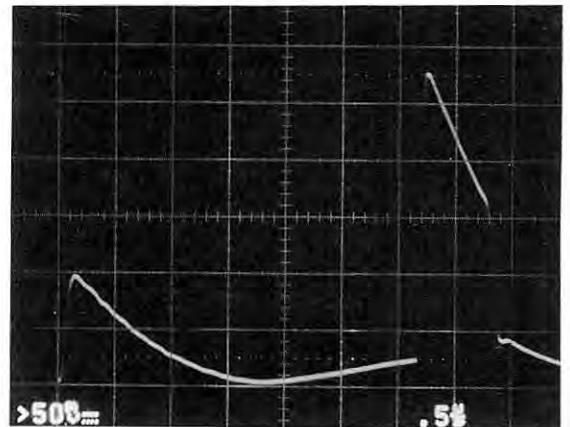


Fig. 28 Output wave form from the new-type rf pulse compressor. Pulse width and phase switching times are $3.8 \mu\text{s}$ and $3.2 \mu\text{s}$, respectively.

3. 50-MW KLYSTRON DEVELOPMENT

Concerning the newly designed 50-MW klystron, four prototype tubes were manufactured by two companies and tested; the tube names are the PV3050 (MELCO: Mitsubishi Electric Corp.) and the E3730 (Toshiba), respectively. Since both tubes were manufactured in accordance with KEK specifications, their interaction regions are the same and the overall size is also the same; the same focusing magnet, X-ray shield and socket must be mated with them. The rf window and the high-voltage ceramic-seal were designed by the manufacturers individually. The window of E3730 is of the long pill-box type. The shapes of the high-voltage ceramic are oval and conical in the PV3050 and E3730, respectively.

An output power of 50 MW and an efficiency of 45-46% were achieved in company and KEK tests. So far, the characteristics of the four tubes vary slightly; the required voltage for a 50-MW output power was slightly higher than that predicted (PV3050#1 and E3730#1), and the input power at the saturation point was also larger than that predicted (PV3050#1). Since some instability was observed in the E3730#1, this tube should be improved. The nominal micro perv is usually $2.10 \mu\text{A}/\text{V}^{3/2}$, while the PV3050#2 has been designed to have a higher micro perv ($2.18 \mu\text{A}/\text{V}^{3/2}$). The performance of this tube was better than that of other tubes: 50 MW output power at a 300 kV beam voltage and a high efficiency of about 47-49% were obtained.

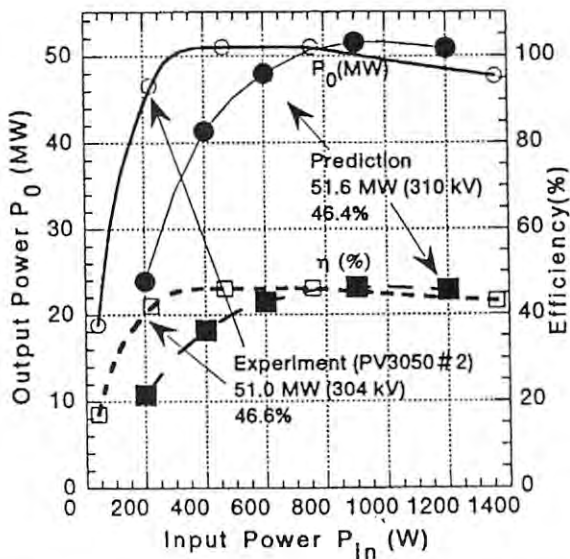


Fig. 29 Input-output power characteristics predicted by the FCI simulation code and experimental data.

These results agree with the design predictions.

Figure 29 shows one of the input-output characteristics with the FCI prediction, which is the particle-in-cell code developed by Dr. Shintake. The saturation point of the output power strongly depends on the magnetic-profile, especially the field near the input-cavity and the second cavity, which corresponds to the well-known gain section. Figure 30 shows the output-power characteristics as a function of the applied beam voltage. Figure 31 shows the waveforms of the beam-voltage pulse, the beam-current pulse and

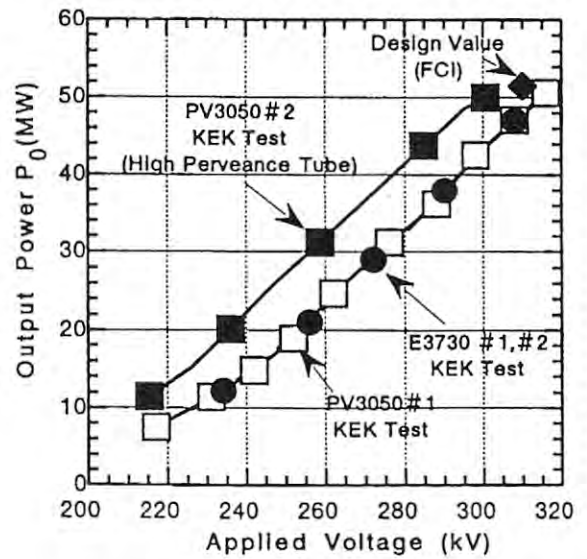


Fig. 30 Output power characteristics as a function of the applied beam voltage for prototype 50-MW klystrons.

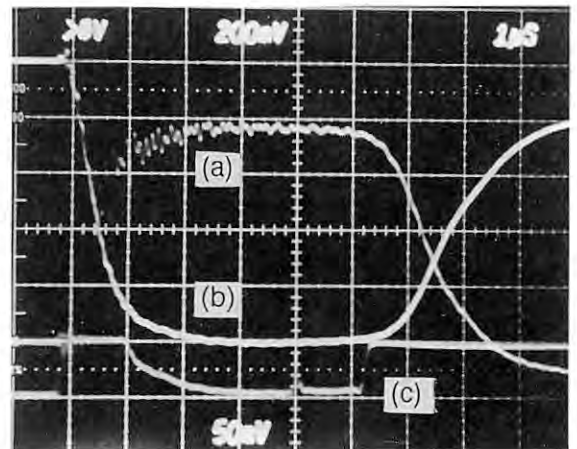


Fig. 31 Waveforms of the beam current pulse (a), the beam voltage pulse (b) and the rf pulse (c).

the rf pulse. The window property of the PV3050 tube was essentially the same as that of the PV3030A3: the short pill-box window and the highly pure alumina material. The Toshiba long pill-box window was tested up to the 200-MW level in the resonant ring at KEK; a glowing light was observed during the high-power test. It will be necessary to continue testing the window for an evaluation. A higher voltage application up to 350 kV was tested tentatively using the PV3050#2 and a 64-MW output power was observed with an efficiency of about 42%. The performance strongly depended on the magnetic-field distribution near the output-cavity region, as predicted by FCI.

4. RF DRIVE SYSTEM

The present rf drive system of the linac, which feeds rf signals to the high-power klystrons, comprises a main drive system and six sub-boosters. The main drive system generates 2856-MHz CW signals by multiplying a 119-MHz master oscillator signal, and transmits them by optical fibers. The sub-booster receives the optical signal, converts it into an electric signal and then amplifies it by two 10-kW klystrons.

In order to adopt an rf-pulse compressor, such as a SLED (SLAC Energy Doubler), we have been upgrading the drive system (Fig. 32) by:

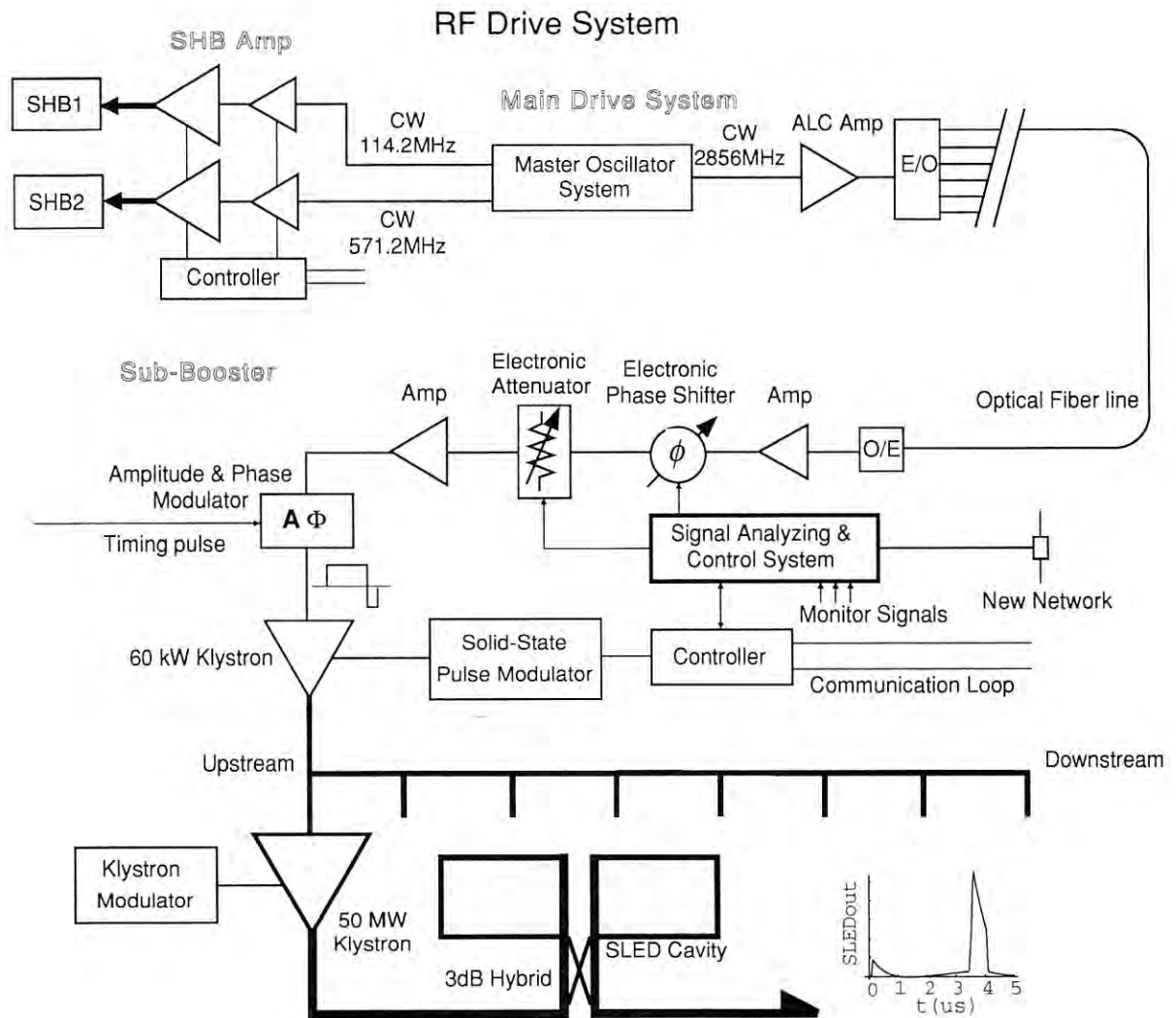


Fig. 32 Upgraded rf drive system for the KEKB injector linac.

- 1) Installing fast-phase and amplitude modulators in every sub-booster. The sub-booster can generate rectangular rf pulses with a 4- μ s width and can then reverse their phases of the last 0.5 μ s for SLED operation.
- 2) Moving the sub-booster station from the present position (center of a sector holding 8 high-power klystrons) to the head of the sector. Thus, the timing of the accelerating rf pulses to beam bunches can be optimized, and the beam energy can be subsequently maximized.
- 3) Installing a new 60-kW klystron which can drive eight 50-MW klystrons.
- 4) Replacing the switching tubes of the pulse power supplies with solid-state switches (36 kV, 16A) for higher reliability.
- 5) Replacing the present mechanical attenuators and phase shifters with electronic ones.

In addition to these upgrades, the sub-boosters will be increased from six to eight in order to drive the ten high-power klystrons which will be added to the present rf source.

Signal analyzing and control systems will be newly installed in order to precisely control the rf drive system and the high-power klystrons. For a clear understanding of the linac condition it is very important to be able to quickly detect any problem or symptom concerning some trouble in the rf system such as a defect in an rf waveform or variations in the vacuum of the waveguides. Therefore, this system will continuously relay various monitor signals to its computer. The computer will analyze the data and diagnose any problem of the rf source, and when and where it occurs.

Since the frequencies of subharmonic bunchers (SHBs) will be changed from 119 MHz and 476 MHz to 114.24 MHz and 571.20 MHz, respectively, new SHB amplifiers must be made. The final stages of the amplifiers will comprise solid-state devices, though the present ones are vacuum tube type.

In the spring of 1994, an rf power of 48 MW was fed into the first prototype SLED. The obtained energy gain per unit was 179 MeV (23.7 MeV/m), which is greater than the design value of 160 MeV, to achieve 8-GeV beam acceleration. The energy multiplication factor, which is defined as the ratio of the particle-energy gains with/without the SLED, was 1.89 on average.

5. HIGH-CURRENT SINGLE-BUNCH BEAM ACCELERATION

The PF 2.5-GeV linac is under reconstruction for the KEKB project, which requires S-band single-bunch beams of 8-GeV electrons ($> 8 \times 10^9 e^-$ /bunch) and 3.5 GeV positrons ($> 4 \times 10^9 e^+$ /bunch). In order to produce a sufficient number of positrons, it is necessary to accelerate high-current electron beams to high energy. In our design, an electron beam containing a 10 nC charge will be accelerated up to about 4 GeV before positrons are produced from the target.

We carried out some tests for producing high-current single-bunch beams and accelerating them to the end of the PF 2.5-GeV linac. Figure 33 shows the results. The 1-ns beams emitted from the electron gun (0-GUN) were compressed into single bunches in the region between 0-gun to 0-10, and accelerated to the end of the linac. The transmission rates were more than 80% before the center of the linac (3-42), which is consistent with the bunching-system design. The rates, however, gradually decreased in the second half of the linac to about 60% near the end of the linac. This is thought to have been mainly caused by wake fields due to misalignment and an insufficient adjustment of the beam transport. It is obvious from our experiments that operation becomes difficult and finer adjustments are required as the beam intensity increases. This means that adequate improvements such as fine alignment, precise position detection and quick beam control will be inevitable for the KEKB linac.

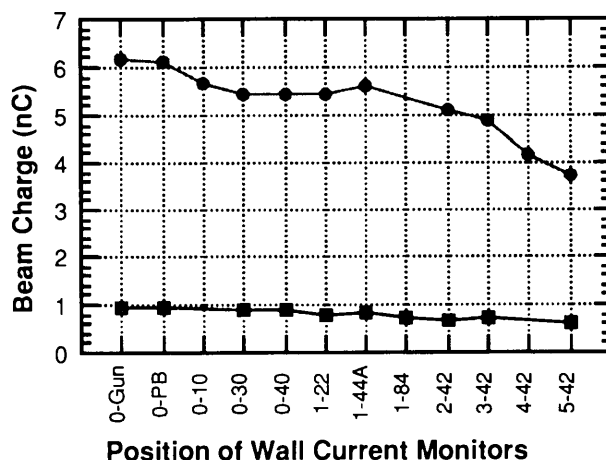


Fig. 33 Electron charge contained in single-bunch beams which were accelerated in the PF 2.5-GeV linac.

6. BEAM-POSITION MONITOR

A stripline-type beam position monitor (BPM) is under development at the PF 2.5-GeV linac for the KEKB. In order to suppress the transverse wake field due to the intense electron beam and to obtain a beam radius of less than 0.6 mm at the positron production target, the beam must be kept within 0.5 mm of the accelerator axis. The BPM equipment must provide information concerning the beam center of mass displacements with an accuracy of 100 μm .

The new-type BPM is shown in Fig. 34. It is a conventional stripline-type monitor made of stainless steel (SUS304) with $\pi/2$ rotational symmetry. The total length (195 mm) and the stripline length (132.5 mm) were chosen so that it can be installed into the upgraded beam line. A 10-mm bellow is attached to one side of the BPM. Two types of quadrupole, 44- and 23-mm bore diameters are used in the linac. The outer diameter of the beam pipe is fixed at 44mm, which can be inserted into all the quadrupole magnets except the 23mm type ones. The inner diameter (28mm) of the pick-up electrode (PUE) was decided so as to make a 50 Ω transmission line. The angular width of the electrode is set to 60 degrees. A 50 Ω SMA-vacuum-feedthrough is connected to the upstream side of each electrode, while the downstream ends are shortcircuited to the pipe. Quick-release flange couplings (manufacturer's standard KF flange) are used at one end of the BPM for easy installation into the beam line. The other end was attached to a small flange (44mm in diameter) for inserting BPMs inside the quadrupole magnets.

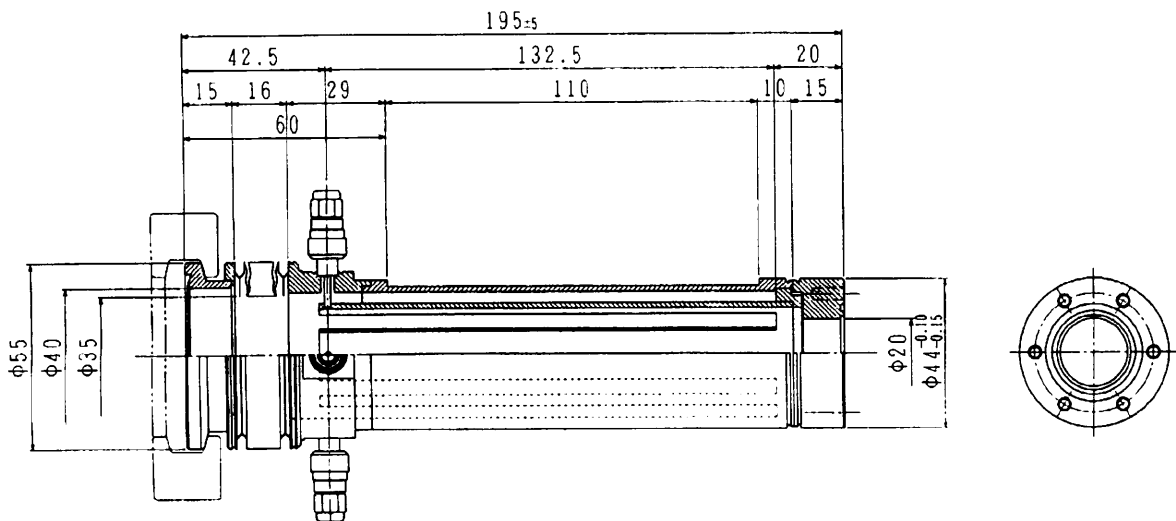


Fig. 34 Design of a stripline-type BPM for the KEKB.

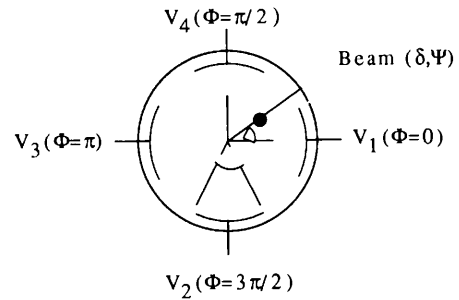


Fig. 35 BPM cross section.

The horizontal and vertical beam displacements (X, Y) can be approximated by the following fifth-order polynomials:

$$X = A_0 + A_1x + A_2y + A_3x^2 + A_4xy + A_5y^2 + A_6x^3 + A_7x^2y + A_8xy^2 + \dots + A_{20}y^5$$

and

$$Y = B_0 + B_1x + B_2y + B_3x^2 + B_4xy + B_5y^2 + B_6x^3 + B_7x^2y + B_8xy^2 + \dots + B_{20}y^5,$$

where x and y are given by $(V_1 - V_3)/(V_1 + V_3)$ and $(V_2 - V_4)/(V_2 + V_4)$, respectively. Here, V_1 to V_4 are the outputs from the electrodes (Fig. 35).

In the bench test, all of the coefficients from A_0 to B_{20} for each BPM with cables will be measured and stored in a workstation.

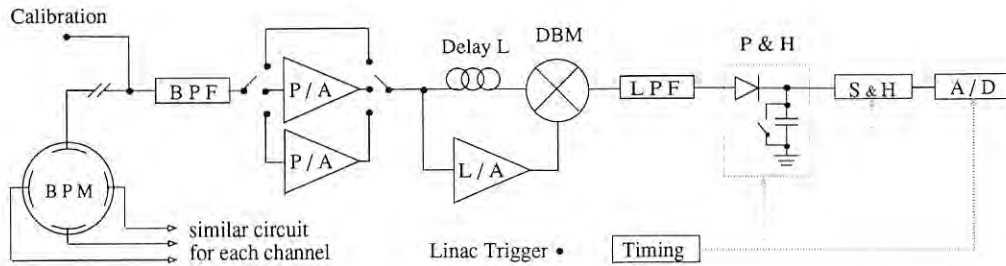


Fig. 36 Circuit block diagram.

Figure 36 shows the circuit configuration. The PUE signal is transmitted via a vacuum feedthrough to an SMA connector and further to a 30-m-long coaxial cable hooked to the front-end electronics. For easy maintenance and to avoid radiation damage, it will be installed in the klystron gallery.

The electronics consist of a band-pass filter (BPF) to provide bursting waves 200 ns wide, a set of rf amplifiers with different gains, hard limiting amplifiers to accomplish normalization, a double-balanced mixer (DBM) used as a downconverter, a low-pass filter to smooth the IF output, of which the amplitude is proportional to the beam-induced signal at the PUE, a peak-hold circuit (P&H) and a 12-bit A/D converter.

The PUE output is proportional to the beam intensity and varies with the beam position. The electronics system needs a 50 dB dynamic range to cover the intensity change from the positron beam (0.64 nC) to the primary electron beam for positron production (10 nC) and beam displacement. Further, an additional fifteen dB is to be added for commissioning the positron beam. Thus, the total dynamic range needs to be extended to 65 dB covered with three overlapping sections, each comprising 34 dB. The results of the bench test show a dynamic range of 34 dB with linearity better than 2% for low and medium ranges. The high range is under tuning. The linearity error is defined here as the difference in the circuit response (V_{out} vs. V_{in}) with respect to the ideal straight line. Further study is now underway.

D. SLOW-POSITRON SOURCE

1. SLOW-POSITRON BEAM INTENSITY

A high-power primary electron beam was used to produce slow positrons at the beginning of FY 1994. In a preliminary test with a 2.2 GeV electron beam (0.93 μ s pulse width, 12.5 pulses/s, 1.25 kW average power), a positron beam intensity of 3×10^6 e⁺/s was observed by detecting annihilation γ -rays at the end of the 30 m long beam-transport line. A part of the beam was lost in the beam-transport line. Further improvement of the beam intensity will be achieved by tuning the magnetic field distribution.

2. POSITRON MODERATOR

The pulsed electron beam is projected onto a dense high-Z target (tantalum in our case), creating bremsstrahlung. By pair production, fast positrons are produced in the target. The fast positrons are implanted into a moderator, where they reach thermal energies within nearly 10 ps. After diffusing in the moderator, a fraction reaches the surface; the rest are partially trapped by defects and annihilate with electrons.

This means that the existence of lattice defects reduces the conversion efficiency from fast positrons to slow positrons. This is the reason why we anneal the moderator: tungsten foils in our case under ultra-

high-vacuum conditions. Annealing of the moderator foil was carried out at 2270K for 10 min. The base pressure of the annealing chamber was 5×10^{-7} Pa, or below.

The positron production target, a tantalum brick, was also annealed at 670K for 1 week for degassing. A verification test of the thermal treatment of the moderator and the target will soon be performed by measuring the slow-positron flux.

3. POSITRON RE-EMISSION MICROSCOPE

A prototype of a positron re-emission microscope (PRM) was designed. Fig. 37 shows a schematic drawing of the electrostatic-lens configuration of the PRM. The incident slow-positron beam optics comprised a two-stage electrostatic lenses: a condenser lens and an objective lens. Each lens has two alignment electrodes. The objective lens has a stigmator and two deflection electrodes.

For the secondary beam (i.e. the re-emission positron beam), the optics were designed as follows: two electrostatic lens stages, a stigmator and two alignment electrodes. An image of the sample is projected onto a screen comprising a microchannel plate (MCP) and a phosphorescence screen. Under test operation of this PRM, positrons having an energy of 10 keV are injected onto a sample having a potential of +5 kV; the entrance surface of the MCP is at ground potential.

The magnification values are restricted by the lens aberration. The magnification of each lens is tens of magnitude. The non-magnetic field environment is essentially important in PRM experiments. This is why we selected the electrostatic-lens configuration.

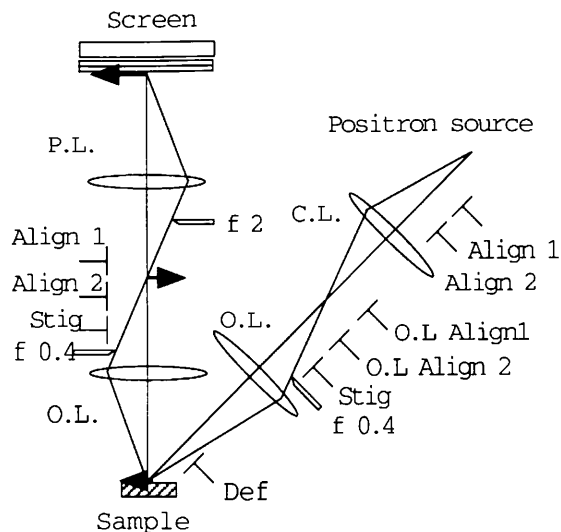


Fig. 37 Schematic of the electrostatic lens configuration of Positron Re-emission Microscope.

4. HIGH-VOLTAGE APPLYING TEST

A high-voltage applying test for a high-voltage section was performed during the summer shutdown. This section was constructed so as to make a DC positron beam (Fig. 38). During the test, we monitored the status of the high-voltage dome using a CCD camera and a current monitor of the ion pump. Up to 30 kV DC was applied to the positron production target chamber and the following 8-m straight section. About 1 hour after applying 30 kV DC, no breakdown was detected. This section contains a 150 l/s ion pump, five 60 l/s ion pumps, an electron multiplier for positron detection, etc. The base pressure of this section is 8×10^{-8} Pa. This high-voltage system enables us to perform experiments using variable-energy and DC slow-positron beams.

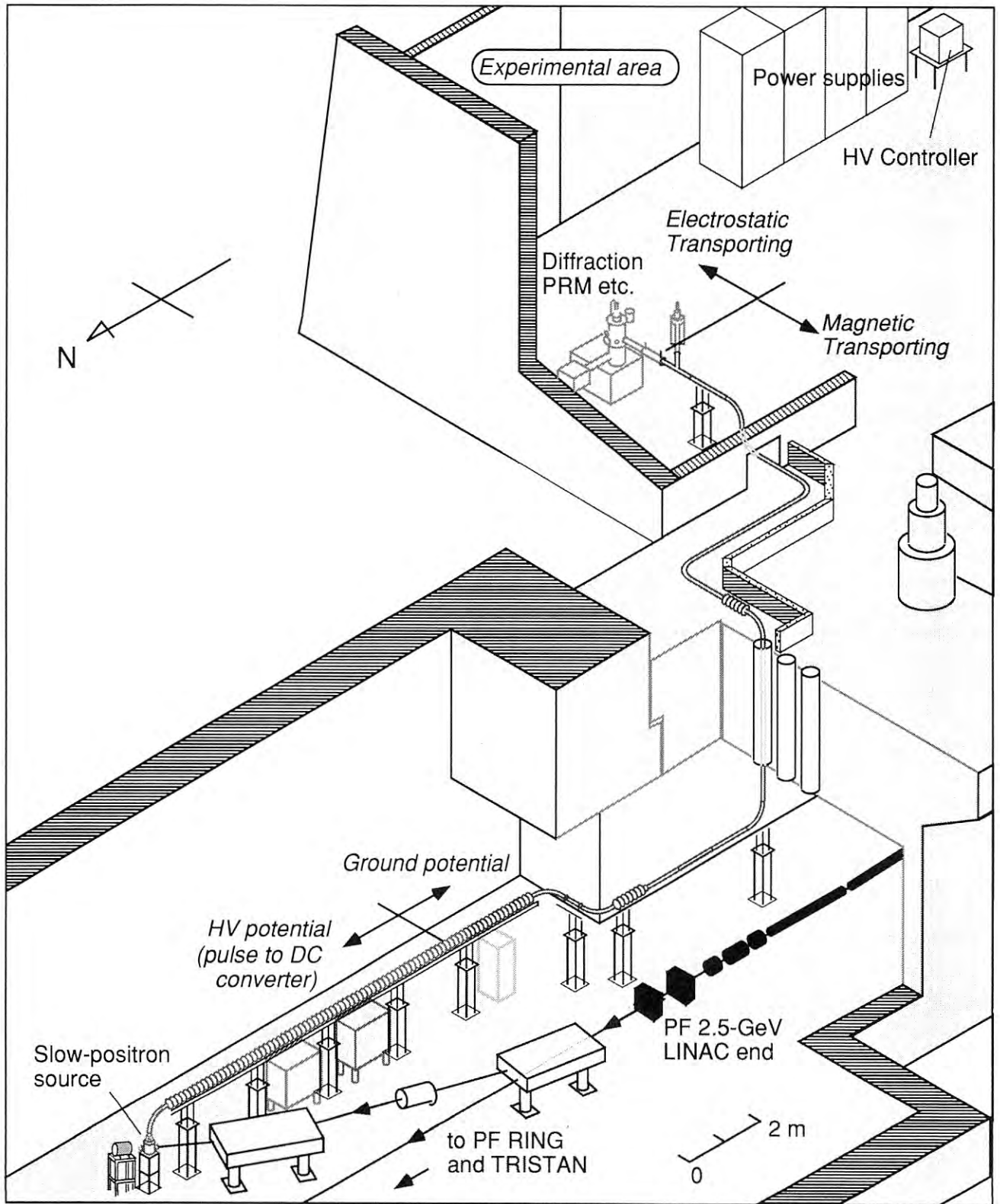
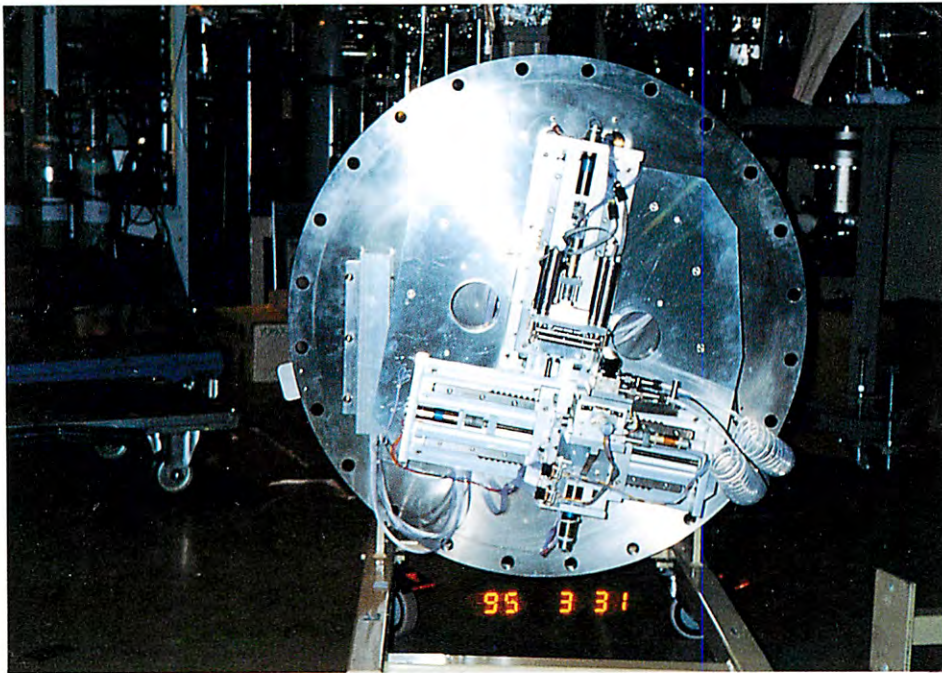


Fig. 38 Bird's-eye view of the slow-positron beam line at the PF Linac.

Collaborations



Phase II Monochromator in the Australian Beamline

You can jump to the article by clicking its title.

CONTENTS

	Page
A. INTRODUCTION	C - 1
B. RESEARCH CENTER FOR SPECTROCHEMISTRY, UNIV. OF TOKYO	C - 1
1. PRESENT STATUS OF BL7A AND 7B	C - 1
2. RESEARCH ACTIVITIES USING BL7A AND 7B IN 1993-1994	C - 1
2.1 Photo-decomposition of $(\text{CH}_3)_2\text{GeH}_2$ on Si(100) by synchrotron radiation	C - 1
2.2 Surface electronic states at step edges on Ni(7 9 11) surfaces	C - 2
2.3 Electronic and atomic structures of SO_2 on Ni(100)	C - 2
C. SYNCHROTRON RADIATION LABORATORY, INSTITUTE FOR SOLID STATE PHYSICS, UNIV. OF TOKYO	C - 3
1. BL18A	C - 4
2. BL19A AND 19B	C - 5
D. OTHER MINISTRIES	C - 6
E. INDUSTRY BEAMLINES	C - 9
F. THE AUSTRALIAN NATIONAL BEAMLINE FACILITY	C - 11
1. INTRODUCTION	C - 11
2. HARDWARE	C - 12
3. EXPERIMENTS AVAILABLE AT BL20B	C - 13
4. HIGH RESOLUTION POWDER DIFFRACTION	C - 13
5. X-RAY ABSORPTION SPECTROSCOPY (XAS)	C - 13
6. OTHER TECHNIQUES	C - 14
7. CONCLUSION	C - 14

A. INTRODUCTION

Collaborative research works between the Photon Factory and other institutions are also very important parts of our activities. We summarize here our such collaborations with universities, other ministries, industrial companies and also with foreign institutions.

B. RESEARCH CENTER FOR SPECTROCHEMISTRY, UNIV. OF TOKYO

1. PRESENT STATUS OF BL7A AND 7B

BL 7A and 7B are equipped with a plane grating monochromator and a 1 m Seya-Namioka monochromator, respectively. Both of them are intended to use for the studies of electronic and geometric surface structures and surface photochemical reactions. Thermal damage and thermal instability of the optical systems had been serious problems. In the case of BL 7A, a replica grating had deteriorated very rapidly and was replaced with an original grating made of SiC which has been used satisfactorily. Thermal deformation of the first bent-toroidal mirror made of fused quartz had been a main cause of beam fluctuation. In the last year, it was replaced with a toroidal mirror with an ultra smooth surface made of Glidcop (Cu dispersed by Alumina fine particles). This mirror was fabricated in the KEK workshop. A performance test will be carried out in the first period of the next fiscal year. For BL 7B, an Si single crystal mirror was newly developed and installed as the first mirror. Beam fluctuation has been greatly suppressed compared with the previous system using a mirror made of CFHC Cu.

2. RESEARCH ACTIVITIES USING BL7A AND 7B IN 1993-1994

2.1 Photo-decomposition of $(\text{CH}_3)_2\text{GeH}_2$ on Si(100) by synchrotron radiation

Photo-decomposition of metal-organic molecules on surfaces is one of the important processes of semiconductor device technology. Synchrotron radiation is a very promising light source for photo-chemical reactions because it might be possible to

control and select surface reactions by tuning the photon energy. We have studied the fundamental processes of photo-chemical reactions of simple molecules on surfaces at BL 7B. The following are the results of the photo-decomposition of dimethyl germane $(\text{CH}_3)_2\text{GeH}_2$ adsorbed on Si(100) surface^{1,2)}. Fig. 1 shows the change of UPS spectra by irradiation with SR photons below 60 eV. The Ge 3d peak at 30 eV keeps the same intensity, but the C 2s peak at 16 eV reduces with irradiation time. This clearly indicates that the Ge-CH₃ bond is broken and Ge atoms stay on the surface, but some of the CH₃ group are decomposed and desorbed by SR irradiation. A(2×1) LEED pattern can be observed even after long irradiation which means the Si dimer bond is maintained. A possible model of photo-decomposition is shown in Fig. 2. This photo-decomposition process is quite different from thermal decomposition process, in which both CH₃ species and Ge atoms are desorbed and the Si(100) surface loses its periodicity completely.

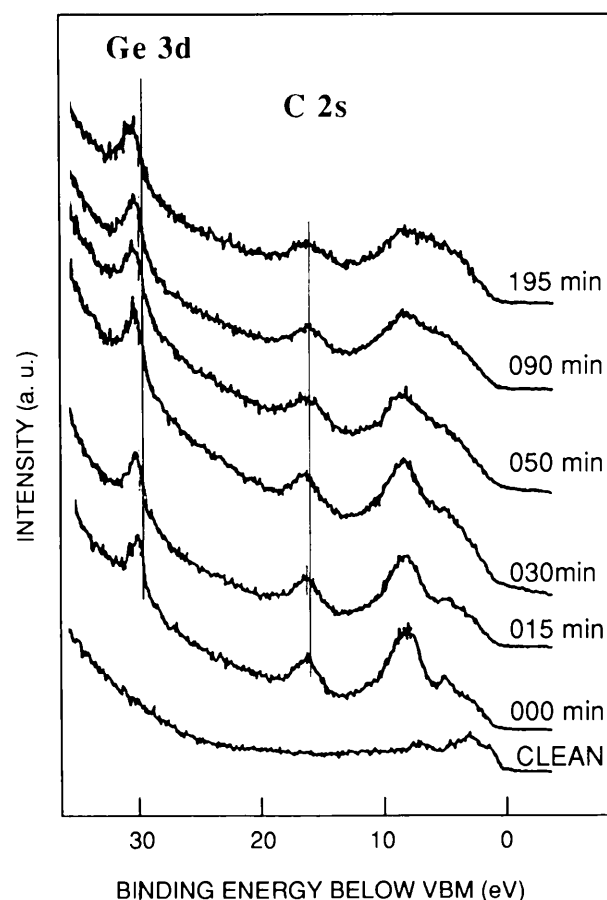


Fig. 1 UPS spectra of $(\text{CH}_3)_2\text{GeH}_2$ on Si(100) after irradiation with SR below 60 eV

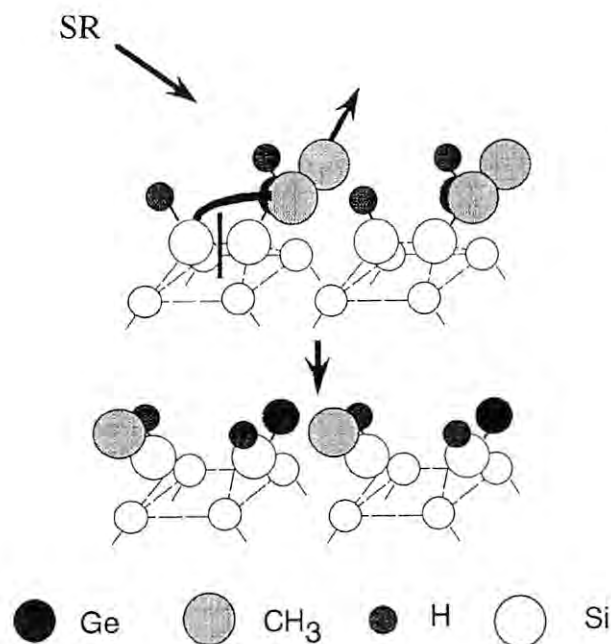


Fig. 2 Possible model of photo-decomposition of $(\text{CH}_3)_2\text{GeH}_2$ adsorbed on $\text{Si}(100)$

2.2 Surface electronic states at step edges on $\text{Ni}(7\ 9\ 11)$ surfaces

On a stepped metal crystal surface, there are one-dimensional arrays of steps and/or kinks separated by planar terraces. These steps have been regarded as a model of surface defects having high activity in surface chemical reactions. Properties of stepped metal surfaces have been studied by a number of surface-sensitive techniques, but no one has ever succeeded in directly observing the electronic state of these steps.

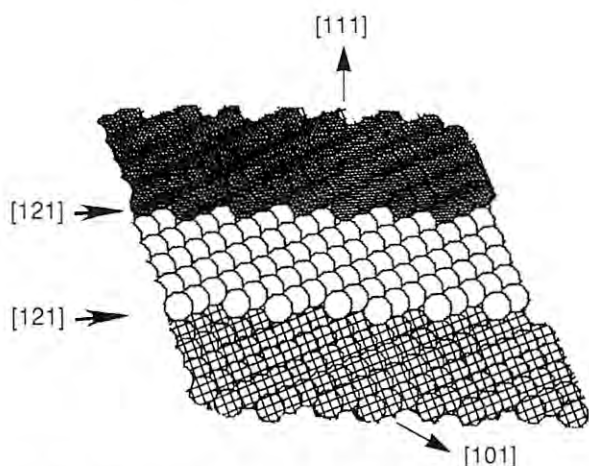


Fig. 3 Schematic view of $\text{Ni}(7\ 9\ 11)$ stepped surface

Recently, we found new electronic states localized at steps on a metal surface by using angle-resolved UPS with linearly polarized synchrotron radiation as the light source⁹. An experiment was performed at BL 7B on an $\text{Ni}(7\ 9\ 11)$ sample, whose surface structure is shown in Fig. 3. Fig. 4 shows the UPS spectra from clean and 0.38 ML Na-desorbed $\text{Ni}(7\ 9\ 11)$ measured at $h\nu = 10\text{ eV}$. The spectrum from clean Ni consists of three bands, S, T and B1. The T and B1 bands are also observed in $\text{Ni}(111)$, but the peak S appears only in $\text{Ni}(7\ 9\ 11)$, which can be assigned to a step-induced electronic state. Both peaks, T and S, are sensitive to adsorption of alkali metals. The difference spectrum in Figure 4 clearly indicates that S is more sensitive to alkali adsorption. Detailed analyses of Na coverage, excitation energy and polarization dependencies of ARUPS have elucidated the character and energy dispersion of the electronic state induced by the step site of $\text{Ni}(7\ 9\ 11)$.

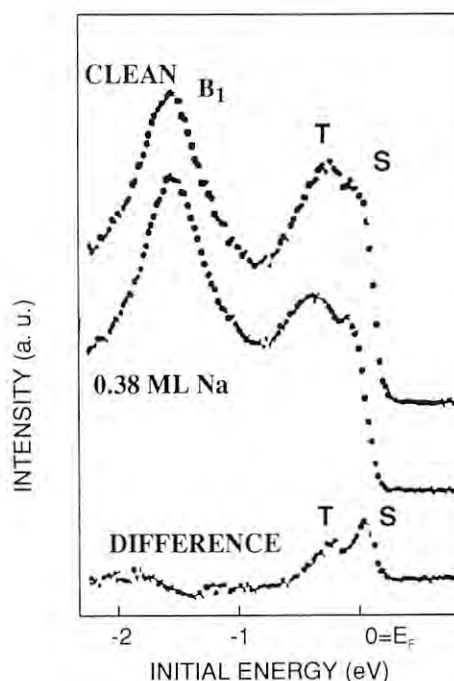


Fig. 4 UPS from Na-covered and clean $\text{Ni}(7\ 9\ 11)$. Photon energy is 10 eV. The difference spectrum is also shown.

2.3 Electronic and atomic structures of SO_2 on $\text{Ni}(100)$

SO_2 is known as a dangerous air pollutant and is also responsible for the corrosion of metals. Surface adsorbed structures of SO_2 on several metals such as

Ag, Cu, Pd and Ni have been studied by ARUPS, HREELS and NEXAFS. All the previous results indicate that SO_2 is adsorbed with the molecular plane perpendicular to the metal surfaces. Recently, we studied the adsorbed structures of SO_2 in Ni(100), (110) and (111) by S K-XAFS and found that SO_2 lies flat on the surface in the above three cases⁴⁾. In order to obtain both electronic and atomic structures of adsorbed SO_2 on Ni(100), we also performed UPS and O K-NEXAFS experiments at BL 7A.⁵⁾

Fig. 5 shows the polarization dependence of O K-edge NEXAFS spectra from submonolayer SO_2 on Ni(100). Two intense resonance peaks are ascribed to the transitions of O 1s to π^* and σ^* , and their polarization dependence clearly indicates that SO_2 lies on the surface. The NEXAFS spectrum from multilayer SO_2 is also shown in Fig. 5, where π^* and σ^* resonance peaks are more enhanced. Peak intensity is related to the occupancy of the corresponding vacant level. The π^* peak intensity from the submonolayer at the incident angle of 55 is suppressed by more than two times compared with that from the multilayer. This suggests partial occupancy of the π^* orbital due to the charge transfer from the Ni 3d band.

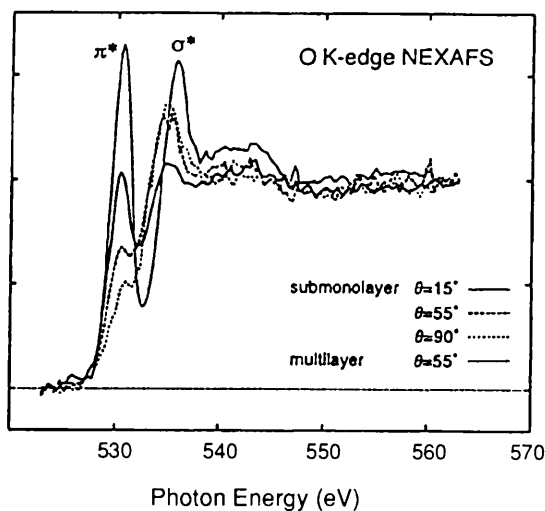


Fig. 5 O K-edge NEXAFS of multilayer and submonolayer $\text{SO}_2/\text{Ni}(100)$

This partial occupancy is confirmed by UPS measurement. Fig. 6 shows the difference spectrum between submonolayer $\text{SO}_2/\text{Ni}(100)$ and clean Ni(100). A shoulder labeled N at around 3 eV is assigned to the lowest unoccupied MO in a free molecule.

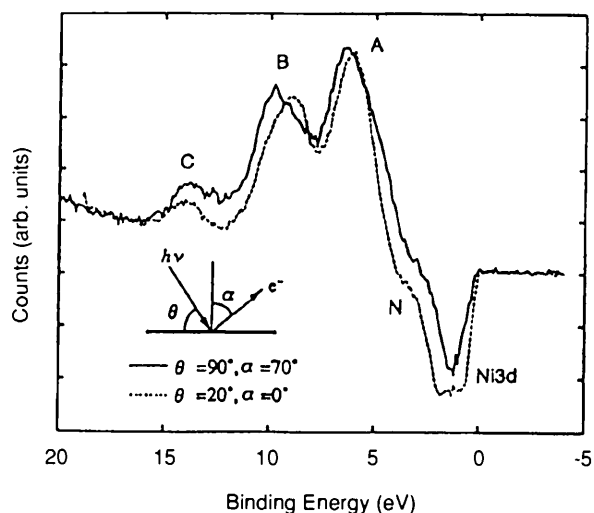


Fig. 6 The difference of UPS between submonolayer $\text{SO}_2/\text{Ni}(100)$ and clean Ni(100)

These experiments demonstrate that the combined use of NEXAFS and UPS is useful to elucidate both electronic and geometric properties of adsorbates.

T. Ohta, Univ. of Tokyo

References

- 1) H. Namba et al.; Surf. Sci. **283** (1993) 132.
- 2) H. Namba et al.; Appl. Surf. Sci. **79/80** (1994) 449.
- 3) H. Namba et al.; Phys. Rev. Lett. **71** (1993) 4027.
- 4) T. Yokoyama et al.; Surf. Sci. **324** (1995) 25.
- 5) T. Yokoyama et al.; Surf. Sci.

C. SYNCHROTRON RADIATION LABORATORY, INSTITUTE FOR SOLID STATE PHYSICS, UNIV. OF TOKYO

The Synchrotron Radiation Laboratory of the Institute for Solid State Physics, University of Tokyo, has constructed the Revolver undulator and three beamlines, BL18A, BL19A and BL19B, in the Photon Factory and opened them to general users in collaboration with the Photon Factory¹⁻³⁾. In the following we provide a brief introduction of these beamlines and report on a few recent scientific activities which were performed during fiscal 1993 and 1994.

1. BL18A

This beamline has been constructed to be dedicated to surface and interface photoemission experiments with high energy and angle resolutions. Since it was opened to users in 1991, many active users have investigated the electronic structures of various materials with this beamline. The beamline is equipped with a constant deviation angle grazing incidence monochromator and a commercial angle-resolved photoelectron spectrometer (VG ADES 500). The beamline accepts 2 mrad of horizontal divergence of the radiation and is laid out for photon energy from 15 to 150 eV. An energy resolution of 50 meV is achieved at the Fermi edge of Au at a photon energy of 15 eV at room temperature and the angle resolution is found to be 0.5° . With the sample holder, which could be cooled down to liq. N_2 temperature, an energy resolution of 65 meV is achieved at an excitation energy of around 120 eV, which corresponds to the $4d$ electron excitation energy of light rare earth elements.

Most of the recent work performed in this beamline could be divided into three groups: (1) angle-resolved photoemission experiments of metal and semiconductor surfaces; (2) angle-resolved photoemission experiments of metal over layers on Si surfaces, and (3) high-resolution photoemission experiments of rare earth compounds utilizing $4d$ - $4f$ resonant photoemission. High energy- and angle-resolution of this beamline enables us to investigate the precise difference of the electronic structures accompanying the structural change of the surface and other geometrical rearrangements of adsorbates.

An Si(111) surface is known to reveal various electronic structures depending on the adsorbates on it⁹. Figure 1 shows the angle-resolved photoemission spectra of Si(111)3×1-K along (a) [112] and (b) [101] directions, respectively⁴. Any spectrum in Fig. 7 (a) and (b) does not show an appreciable intensity at the Fermi level and no structure is observed at the binding energy of 0.2 eV, where the occupied surface state is observed on the Si(111)7×7 surface. From these results, the Si(111)3×1-K surface is found to be no longer metallic like the Si(111)7×7 surface, but is semiconducting. The Si(111)3×1-K surface geometrical structural model was found to be consistent to an STM image.

The Electronic structures of strongly correlated electron systems have also been extensively

investigated in this beamline^{7,9}. To manifest the $4f$ electronic structures of rare earth compounds, high resolution $4d$ - $4f$ resonant photoemission experiments have been achieved by utilizing higher order light of the monochromator. Fig. 8 shows the high-resolution $4d$ - $4f$ resonant photoemission spectrum of CeB_6 ⁹, which is known to be a typical dense Kondo material with $T_K = 4$ K. The spin-orbit splitting of the $4f$ level in the final state of photoexcitation can be clearly observed in the figure. The line shape analysis shows that the $4f$ occupancy of CeB_6 is very close to unity and the hybridization between $4f$ and other valence states is quite small.

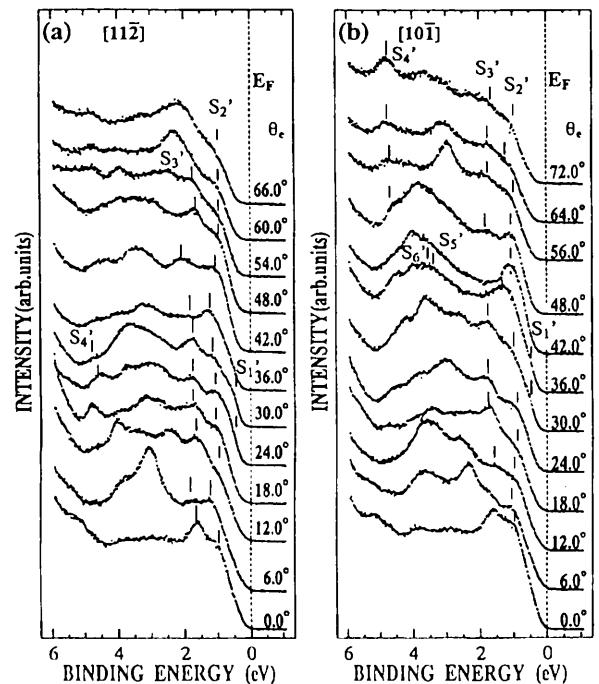


Fig. 7 Angle-resolved photoemission spectra of Si(111)3×1-K along (a) [112] and (b) [101] directions, respectively⁴.

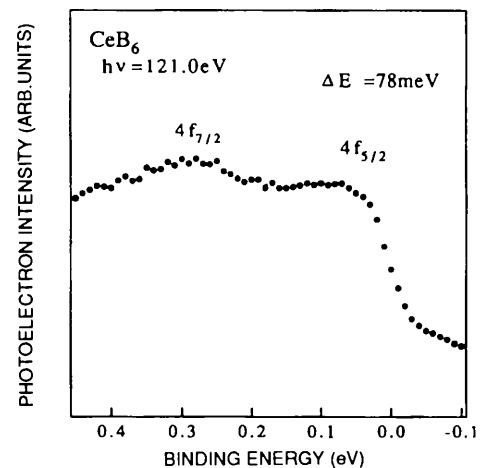


Fig. 8 $4d$ - $4f$ resonant photoemission spectrum of CeB_6 ⁹.

2. BL19A AND 19B

This beamline is specially designed to accept radiation from the Revolver undulator and to lead into two branch beamlines, BL19A and BL19B, by means of a reflecting mirror system¹⁻³⁾. They have been constructed to be dedicated to solid state spectroscopies which need high light intensity from the undulator. To hold out the high heat load of the undulator light, the substrate of the optical elements of this beamline is made of SiC. Among these two beamlines, BL19A was opened to users in 1992. BL19B will be opened to users in the second half of FY 1995.

BL19A is equipped with a constant deviation angle grazing incidence monochromator and covers the output photon energy from 20 to 250 eV. BL19A is dedicated to spin- and angle-resolved photoemission (SARPES) experiments. The photoemission spectrometer consists of a hemispherical electron energy analyzer, a 100 keV Mott detector for electron spin analysis, a sample chamber and other equipments for the characterization of sample surfaces. After some preliminary experiments to characterize the beamline¹⁰⁻¹²⁾, the SARPES of Ni(110) and other magnetic compounds were measured in 1993 and 1994^{13,14)}.

Fig. 9 shows SARPES of Ni(110) single crystals near X- and K-points in the Brillouin zone at various temperatures¹⁵⁾. The majority and minority spin state spectra apparently show a collapsing behavior as the temperature increases to T_c . Based on the assumption that each spectrum consists of two kinds of photoelectrons, those which follow the local exchange field and those which follow the magnetic field averaged over many local exchange fields, the observed temperature and wave vector dependence of the SARPES are consistently explained by the local band theory.

BL19B has a plane grating monochromator with varied-space plane gratings (VSPG). It covers photon energy range from 10 to 1000 eV. A precise characterization of the beamline was accomplished during 1993 and 1994 after replacing the VSPG with a new, originally ruled one. Fig. 10 shows an Ar ion yield spectra around a photon energy of Ar 2p threshold, which reveals that the energy resolution of this beamline exceeds 4000.

BL19B was originally considered to be dedicated to photoelectron spectroscopic studies of solids at various temperatures. It was equipped with a

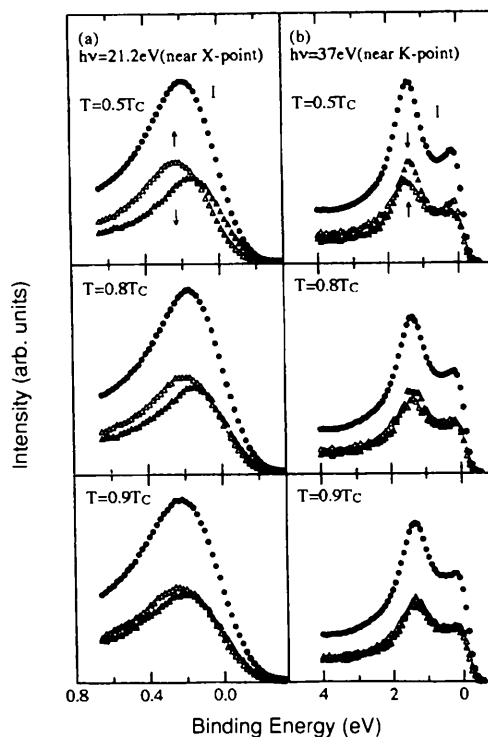


Fig. 9 Spin- and angle-resolved photoemission of Ni(110)

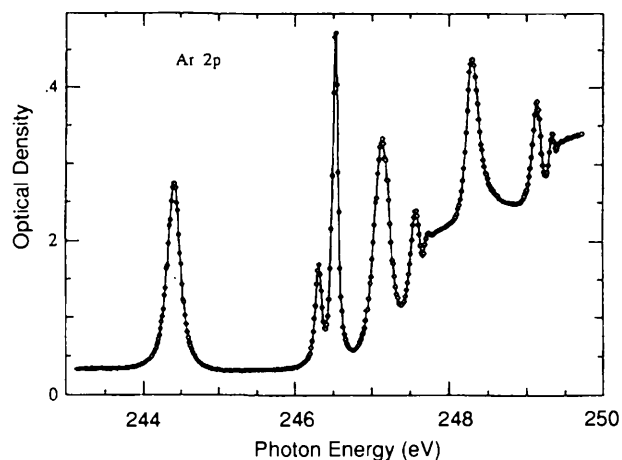


Fig. 10 Ar ion yield spectra around the photon energy of Ar 2p threshold

hemispherical electron energy analyzer with a spin-polarized low energy electron diffraction (SPLEED) detector for electron spin analysis, a sample preparation chamber with a sample manipulator which could be cooled down to 20 K and an electron counting system

The first SARPES experiments were performed in 1994 on 3p and 3s core levels of ferromagnetic Ni(110). Since the beamline covers a wide photon energy range up to 1000 eV with considerable light intensity, it is quite suitable to investigate the second order process of

photoexcitation. The experimental apparatuses for soft x-ray fluorescence measurements are also attached to this beamline, and extensive investigation was started very recently.

*A. Kakizaki, Institute for Solid State Physics,
Univ. of Tokyo*

References

- 1) G. Isoyama et al.: Rev. Sci. Instrum. **60** (1989) 1863 .
- 2) A. Kakizaki et al.: Rev. Sci. Instrum. **60** (1989) 1893 .
- 3) A.Kakizaki *et al.*: Nucl. Instrum. Methods **A311** (1992) 620.
- 4) K.Sakamoto *et al.*: Phys. Rev. **B50** (1994) 1725.
- 5) T.Okuda et al.: Surf. Sci. **321** (1994) 105 .
- 6) H.W.Yoem et al.: Surf. Sci. **321** (1994) L177.
- 7) T.Kashiwakura *et al.*: Phys. Rev. **B47** (1993) 6885.
- 8) A.Kakizaki *et al.*: J. Phys. Soc. Jpn. **62** (1993) 3327.
- 9) A.Kakizaki *et al.*: J. Phys. Soc. Jpn. **64** (1995) 302.
- 10) S.Shin *et al.*: Phys. Rev. **B46** (1992) 9224.
- 11) I.H.Inoue *et al.*: Phys. Rev. **B47** (1992) 12917.
- 12) A.Kakizaki *et al.*: Physica **B186-188** (1993) 80.
- 13) T.Kinoshita *et al.*: Phys. Rev. **B47** (1993) 6787.
- 14) A.Kakizaki *et al.*: Phys. Rev. Lett. **72** (1994) 2781.
- 15) J.Fujii *et al.*: Solid State Commun. **94** (1995) 391.

D. OTHER MINISTRIES

Research on the advanced material characterization was conducted as collaborative projects between three national institutes in Tsukuba and the Photon Factory at the multipole wiggler/undulator beamline BL13. The participating institutes were: *National Institute of Research for Inorganic Materials (NIRIM)*, Science and Technology Agency (STA), *National Institute of Materials and Chemical Research (NIMCR)*, Agency of Industrial Science and Technology (AIST)/Ministry of International Trade and Industry (MITI), *Electrotechnical Laboratory (ETL)*, AIST/MITI and *National Research Laboratory of Metrology (NRLM)*, AIST/MITI. The multipole wiggler beamline were

designed and built by the three national institutes (NIRIM, NIMCR, ETL, NRLM) and *The Institute of Physical and Chemical Research (RIKEN)* of STA.

Since the beamline became in operation, these institutes studied a variety of advanced materials using various techniques ranging from photoemission (soft X-ray) to X-ray scattering (hard X-ray). The 27-pole wiggler/undulator provides the intense X-rays covering the hard X-ray (4-29 keV) and the soft X-ray (200-2.000 eV) regions. The availability of multipole wiggler/undulator as a high brilliance light source has made possible structural and spectroscopic studies over a wide range in energy varying the deflection parameter. Recently, much attention has been paid to *in situ* structural studies. Two hard X-ray branches (BL13A, BL13B) and one soft X-ray branch (BL13C) were constructed. Fig. 11 shows the arrangements of optical components of BL13. About 2 mrad of the wiggler radiation is diffracted in a horizontal plane by an asymmetric (422) diffraction of silicon. Two asymmetric crystals are arranged in a double crystal parallel setting with fixed exit geometry.

X-rays with energy up to 60 keV is available. A monolithic monochromator with successive (331-331) diffraction provides X-ray with a wavelength of 57 pm. The short wavelength X-ray is conveniently used for Laue case diffraction where refraction effect is reduced and improved the accuracy in the Bragg angle measurement to an angular resolution of 0.07". At BL13A, studies on the precise measurement of lattice constant were conducted by NRLM.

At the central branch BL13B, the heat load on a monochromator crystal has been a serious problem, but the new design of directly water-cooled Si(111) monochromator can provide the intense beam with an energy resolution $\Delta E/E \sim 2 \times 10^{-4}$. The horizontal acceptance of the X-ray optics ~ 4 mrad is sagittally focused to a 4 mm \times 1 mm spot at a point ~ 36 m away from the source point. The capability of an insertion device for studies of dilute systems is demonstrated in structural studies of surface overlayers under ultra high vacuum (UHV) at station B1 or high temperature/pressure at station B2. At BL13B1, surface-sensitive X-ray absorption fine structure (XAFS) studies were used to study the strain-induced atomic arrangements on Si surfaces. In Fig. 12, the photograph shows the XAFS/X-ray diffraction apparatus for *in-situ* surface studies. Fig. 13 shows the bird's-eye view of asymmetric Ge dimer on Si(001).

BL-13

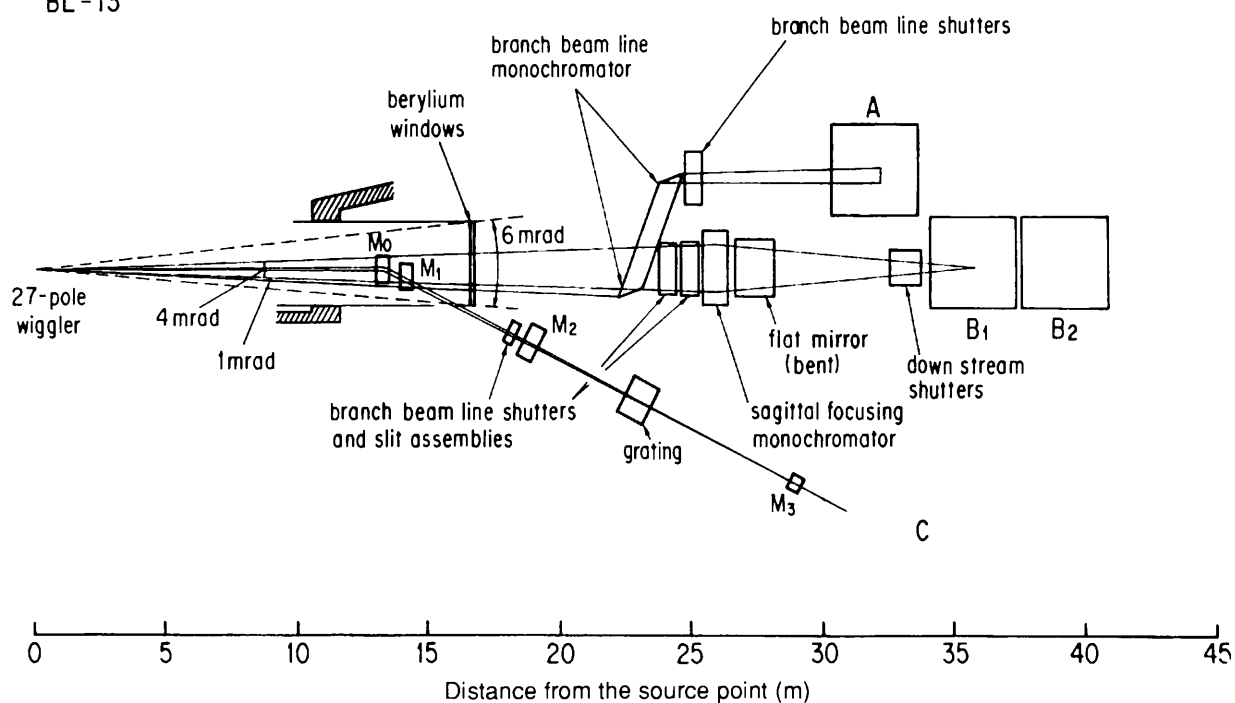


Fig. 11 Schematic arrangements of optical components at BL13 consisting of two hard X-ray branches (BL13A and BL13B) and a soft X-ray branch (BL13C). A 27-pole wiggler/undulator is in operation in a wiggler mode and an undulator mode for the former and latter branches, respectively. Two experimental stations (BL13B1 and BL13B2) share the central beam while BL13A accepts a small part of the beam horizontally.

Light blue balls represent Si atoms while orange balls indicate Ge adatoms. The results of LDA total energy calculation for 1 ML Ge dimers, having essentially the same local structure with that of clean Si(001) (2x1) such as an intra-dimer charge transfer evidenced by short dimer bond length. However, the elongated dimer structure has been confirmed by the surface-sensitive XAFS study using the facility shown in Fig. 12, ruling out the model structure based on the total energy calculation. Using the UHV-compatible 7-element Si(Li) detector for surface studies and the broad spectral distribution of multipole wiggler, BL13B allows one to study K- and L-absorption edges for atoms with $Z > 20$ and submonolayer sensitivity. A newly developed 19-element pure Ge detector provided the total count rate of 2.5×10^6 cps.

High temperature/pressure experiments were carried out at BL13B2 by researchers from NIRIM, using a cubic-anvil apparatus called MAX-90 and a diamond anvil cell. For example, the phase transition of BN were intensively studied by *in situ* X-ray diffraction as a function of high pressure (20 kbar, 2000°C). XAFS

experiments under high pressure are also possible at BL13B2. The structure of amorphous selenium at high pressure were studied. BL13C is a soft X-ray branch by NIMCR, which features the dragon type monochromator for undulator radiation. This branch provides an intense soft X-ray beam with $E/\Delta E \sim 5000$ (400 eV). A typical spot size on a specimen is $1 \text{ mm}^{(9)}$ x $200\text{-}300 \mu\text{m}^{(10)}$. The local structures of $(\text{BN})_x\text{C}_{1-x}$ families, which have attracted great interests because of their peculiar properties and isoelectric structures to graphite or diamond, were investigated by the measurements of B, C, and N K-edge X-ray absorption spectra. The beamline was also applied to the study of the unoccupied orbital of fullerenes, particularly carbon nanotubes which were highly purified by an original procedure developed by NIMCR. In Fig. 14, the C K-XANES spectra are shown for C60, C70 and carbon nanotube, which demonstrates the difference of π -bonding among these compounds. NIMCR is also collaborating with several petroleum refining companies in XAFS analysis of hydroprocessing catalyst.

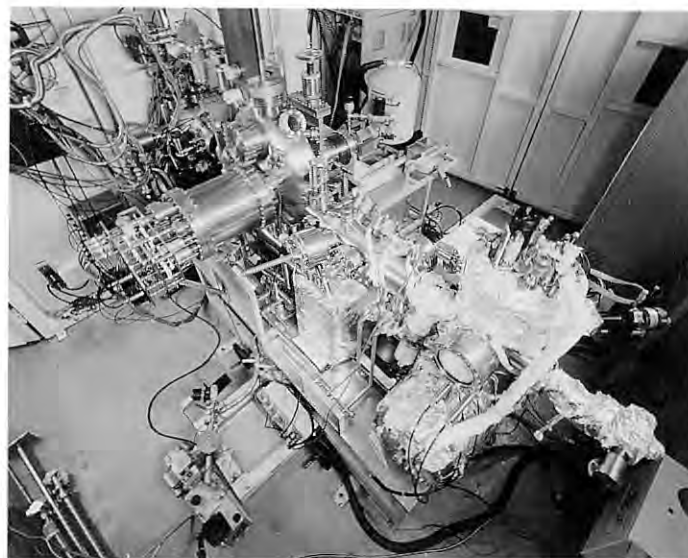


Fig. 12 Photograph shows the surface-sensitive XAFS/X-ray diffraction apparatus for *in-situ* studies. The use of multi-element Si(Li) detector and a grazing-incidence fluorescence excitation has established the surface-sensitive XAFS in the hard X-ray region (>4 keV) covering elements heavier than Ca ($z > 20$). The main analysis chamber is connected to the molecular beam epitaxy (MBE) chamber.



Fig. 13 Bird's-eye view of asymmetric Ge dimer on Si(001) based on the energy minimization. Light blue balls represent Si atoms while orange balls indicate Ge adatoms. The theoretically predicted bond length shortening is ruled out by the XAFS results which observed the dimer bond length elongation.

Japan Atomic Energy Research Institute (JAERI) of STA has actively conducted researches on radioactive materials and radiation biology at the bending magnet beamline BL27 which they built in collaboration with the Photon Factory, using X-ray photoelectron spectroscopy (XPS), X-ray diffraction, and absorption. Two branches are in operation: BL27A being a soft X-ray (1.8-6 keV) beamline and BL-27B an X-ray (4-20 keV) beamline. BL-27A has a focusing optical system consisting of a cylindrical mirror with a bender and an InSb(111) double-crystal

monochromator. For irradiation of biological samples, the beam size is about 2×20 mm² and the photon flux is 4×10^2 photons/sec/mm² at 2.1 keV, while for the XPS experiments the photons are focused to give 1.5×10 photons/sec/mm² with $\Delta E/E$ of 4×10^{-4} . BL-27B has a Si double-crystal monochromator with the second crystal sagittally focusing the beam to provide 2×10 photons/sec/mm² for the diffractometer with $\Delta E/E$ of 2×10^{-4} . In order to prevent the intrusion of radioactive materials into the beamline and the storage ring, various special precautions are taken.

The maximum amount of radioactive isotopes permitted per day is 1 mCi normalized to the fourth group in the radioactive regulation rules. Researchers from JAERI have mainly worked on the structural studies of radioactive compound such as uranium oxide UO_2 . Fig. 15 shows the U L_3 -edge absorption spectrum of UO_2 .

Collaborative researches between the Photon Factory and national institutes of other ministries continue to grow in number. The advantage of this research is that the specially designed beamline is devoted to a specific topic so that intensive studies can be made. Reflecting this, proposals for research using these special beamlines and equipment attract great attention of other researchers.

H. Oyanagi, Electro-Technical Laboratory

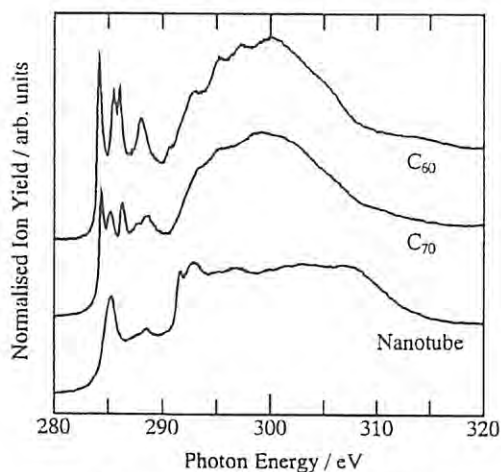


Fig. 14 C K-XANES spectra for C60 (top), C70 (middle) and carbonnanotube (bottom). The features at 285 eV indicates the strong dependence of π -bond on local structure.

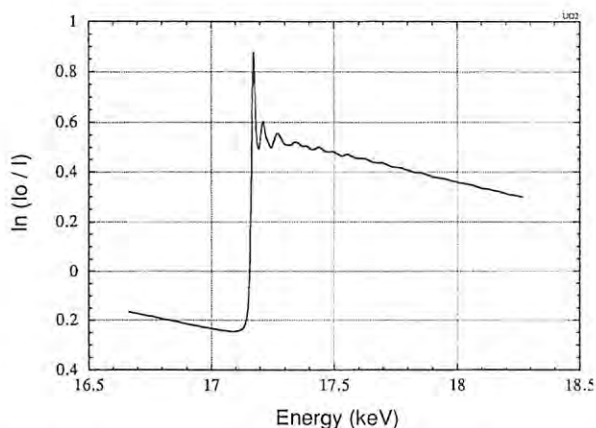


Fig. 15 U L_3 -edge absorption spectrum for UO_2 measured in a transmission mode.

E. INDUSTRY BEAMLINES

At BL-1, which is an NTT (Nippon Telegraph & Telephone Co.) beamline, a big change occurred at the end of fiscal 1993. After the start of the beamline construction of BL-1 in 1983, NTT was engaged in a solid surface analysis at BL-1A, X-ray lithography at BL-1B, and photochemical reaction at BL-1C. However, in order to develop more application-oriented SR technologies at the NTT compact storage ring located at the NTT Atsugi R&D Center, NTT shifted the lithography and photochemical reaction research activities from BL-1B and C to Atsugi at the end of fiscal 1993. At present, only BL-1A is the NTT beamline, where NTT is engaged in surface and interface analysis. BL-1B and 1C were returned to the PF, as the public beamlines.

At BL-1A, surface and interface studies were performed using soft X-rays (X-ray standing waves: XSW and EXAFS) and VUV (photoelectron spectroscopy) mainly on GaAs-related materials for nanoelectronic device applications. Here at BL-1A two analysis chambers, namely a combined XSW and EXAFS apparatus and a photoelectron spectroscopy apparatus, are installed in a tandem style. One of the main topics in 1993-94 was the surface structure analysis of sulfur-passivated GaAs (111) and (100) surfaces by means of XSW and EXAFS. A three-dimensional structure of upper-most sulfur atoms was determined by using symmetrical and asymmetrical reflection XSW methods. By combining these results with the EXAFS result, it was concluded that the surface relaxation due to sulfur passivation is much smaller than expected. Furthermore, a unique structure analysis technique called "Chemical state-resolved X-ray standing waves" was developed by using X-ray absorption near edge under standing wave conditions, as shown in Fig. 16. Two chemical states, namely Ga-S bonds and SO_x bonds were clearly resolved, and it was concluded that while the Ga-S bond components are well-ordered on the GaAs (111) surface, SO_x components are completely disordered. This result was published in Phys. Rev. Lett. **71** (1993) 2611. In addition to the sulfur passivation technique, the selenium passivation technique for GaAs surfaces was investigated using *in situ* MBE growth and photoelectron spectroscopy in order to check the feasibility of growing InAs nanocrystals for quantum dot laser applications. So far, InAs and InSb

nanocrystals of less than 50 nm size were successfully grown on Se/GaAs(100). (published in Nanostructure and Quantum Effects, Springer-Verlag, 1994, p. 242, Appl. Surf. Sci. **82/83** (1994)136.) For much higher energy resolution of photoelectron spectroscopy, a new electron analyzer, SES200 was installed into the *in situ* photoelectron spectroscopy system. Two different chemical states of In4d in InAs nanocrystals were clearly resolved at a photon energy of 100 eV.

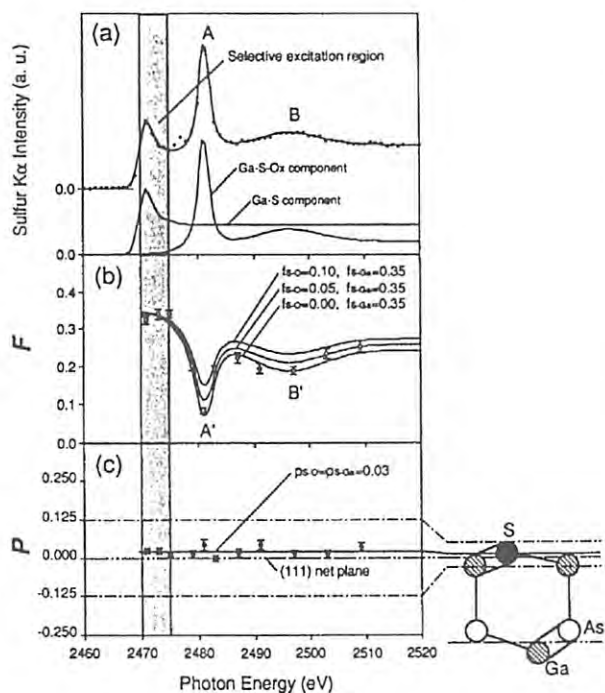


Fig. 16 (a) Sulfur K-edge XANES spectra of oxidized S/GaAs(111)B, (b) photon energy dependence's of coherent fraction F , and (c) coherent position P determined by XSW experiments.

At BL-8, which is a Hitachi beamline, several activities were performed. (Nuc. Instrum. & Meth. **A327** (1993) 256.) At BL-8A, micro-XPS using a Wolter-type mirror to form a micro beam at a photon energy of 150eV was achieved. The intensity of photoelectrons from 0.5 μm line-and-space stripes scanned by a 1.8 μm beam indicated a lateral resolution to be 0.3 μm . (published in Jpn. J. Appl. Phys. **33** (1994) L550.)

At BL-8B, a new tandem-type monochromator was installed for XAFS analysis. It covers from 1.68 to 21.8 keV range with InSb(111) and Si(311) crystals.

At BL-8C1, projection imaging experiments were performed using a 20:1 Schwarzschild optics at a photon energy of 95 eV with multilayer reflection masks. A 0.07- μm line-and-space pattern was clearly printed on resist films. Furthermore at BL-8C2, two kinds of experiments were carried out. One was the X-ray CT experiment for elucidating the degradation mechanism of an SiC fiber reinforced aluminum composite (SiC/A2024) with 10- μm resolution, which was done in collaboration with National Research Institute for Metals. Fig. 17 shows a 3-D CT image of an SiC/A2024 composite, where arrows b and c indicate voids caused by a pull-out of the fiber. Furthermore, a new phase-contrast X-ray CT technique was developed, which is sensitive to light elements compared to the conventional X-ray CT. (Nucl. Instrum. & Meth. A in press.) Fig. 18 shows an image of a cancerous rabbit liver obtained using 13-keV X-rays. The other experiment is the fluorescent X-ray interference patterning from monolayer of a Zn-labeled protein (bovine serum albumin: BSA) bound on a gold substrate. (Science **263** (1994) 62.) From the interference pattern, the distance of Zn atoms from the substrate was determined. In addition to these activities, polarization analysis of soft X-rays and applications of scanning hard X-ray microscopy are now in progress.

BL-9, which is an NEC beamline, consists of three branch beamlines, BL-9A, 9B and 9C. At BL-9A, basic experiments on X-ray lithography have been conducted since 1986. Various experiments have been

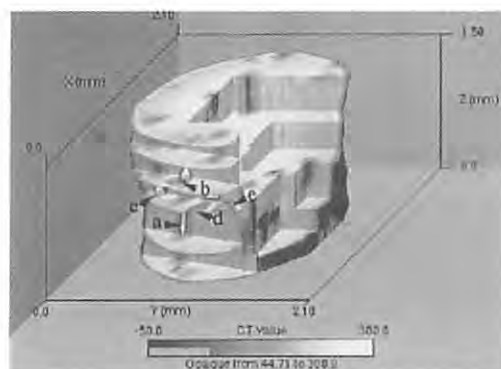


Fig. 17 3-D CT image of the SiC/A2024 composite.



Fig. 19 Phase-contrast image of the cancerous rabbit liver.

conducted such as optical/X-ray hybrid lithography for sub-half micrometer devices, resist-hardening by X-ray irradiation, and study for the mechanisms of high aspect ratio resist pattern collapse. In order to proceed to the next development stage, NEC decided to shift its major activity to SORTEC or Sumitomo Heavy Industries Ltd.

At BL-9B, photon energy dependence of SR irradiation effect on Al-thermal-CVD was examined. Clear difference was observed between valence and core electron excitations. The core electron excitation was found to be effective to suppress the CVD reaction, while the valence electron was effective in initiating the reaction. The mechanism of this drastic energy dependence was cleared by the AES chemical shift analysis of surface layer which was formed by SR photochemical reaction.

At BL-9C, which is an X-ray diffraction- and XAFS-beamline, several kinds of experiments were carried out as follows. Si surface imperfection was investigated using extremely asymmetric (311) reflection, in which the glancing angle of the incident X-rays was near the critical angle of total reflection. (published in *Jpn. J. Appl. Phys.* **32** (1993) L1581.) Also, the density of various thickness SiO₂ films, which is one of the key materials for ULSI devices, was determined by a similar technique, and found that a transition layer exists in the films in terms of the density. Thin films of Ta₂O₅, which is one of the promising high- ϵ materials for device applications, were studied by XAFS measurements to clarify the relation between electronic properties and structure. It

was found that the electronic properties were strongly dependent on oxygen deficiency, but not on crystal structure (long range order) which was believed to be important. These results will appear in the proceedings of MRS fall meeting in 1994, and *Appl. Phys. Lett.* in 1995. Also DAFS measurements were carried out on Rare-Earth-Iron Garnet in order to elucidate the near-edge feature around the tetra-site and octa-site iron in the crystal separately. As a result, a well-known pre-edge peak was found to originate from the tetra-site. Another experiment of an energy-dispersive grazing incidence in-plane diffraction with white X-rays was carried out to study a 0.5 μ m thick Ta-silicide layer and very thin poly-Si films.

At BL-17, which is a Fujitsu beamline, a new X-ray diffractometer using grazing incidence condition was constructed and installed at BL-17C. This diffractometer is mainly composed of two goniometers; (1) a goniometer for grazing incidence angle control and (2) a goniometer for a sample and detector rotation as θ -2 θ scan. The axes of two goniometers are orthogonal to each other. In addition, the refinement goniometer is set on the θ -2 θ one for setting a specimen parallel to X-rays. Furthermore, a detector moves parallel and vertical to the sample surface. Therefore, it is possible to easily measure X-ray diffraction for vertical or inclined to the surface under freely desirable incidence condition. This will be published in *Rev. Sci. Instrum.* **66**(2) Feb. 1995.

*M. Oshima (NTT), Y. Hirai (Hitachi),
J. Mizuki (NEC) and S. Komiya (Fujitsu)*

F. THE AUSTRALIAN NATIONAL BEAMLINE FACILITY

1. INTRODUCTION

In 1994, the Australian Beamline project entered the final year of its three-year construction and commissioning phase. With the goal of opening the beamline to the general user community by 1995, work continued in the areas of beamline component installation and testing, experimental instrumentation commissioning and the development of software for data collection, reduction and analysis. The details of this progress are described below.

2. HARDWARE

The main hardware developments in 1994 concerned the beamline monochromators. The Si(111) channel-cut crystal in the Phase I monochromator (See 1993 Activity Report) was replaced with another Si(111) channel-cut of a more advanced design which allows de-tuning of the second face of the crystal relative to the first in order to remove higher-order harmonic radiation from the monochromatic beam. This crystal, designed and manufactured by Professor Michael Hart, combines harmonic rejection with the intrinsic stability and ease of operation of a channel-cut design monochromator. This improvement has allowed high-quality XAFS data to be collected at BL-20B and has improved the quality of diffraction data by removing features due to diffraction of the higher-order radiation.

The last major beamline component, the Phase II monochromator, was completed and tested at the beamline in 1994. This monochromator, which is interchangeable with the Phase I version, incorporates the features of sagittal focusing and fixed beam-exit height. The monochromator is of a design adapted from that of Matsushita et al.¹³ and consists of two Si(111) crystals which move independently. By positioning the second (downstream) crystal on the monochromator axis of rotation, and allowing the first (upstream) crystal to move along two axes normal to each other, a fixed exit-beam height has been achieved over the full useful energy range of BL-20B. The sagittal focusing is accomplished by bending a ribbed

Si(111) wafer into a cylindrical shape using a "four-point" bending mechanism. Such a mechanism gives superior control over such crystal distortions as twist and spiral. Fig. 19 is a photograph of the mechanism of the Phase II monochromator. Two commissioning runs were carried out on the Phase II monochromator with promising results. To date, a 20-fold increase in X-ray flux at the sample position has been recorded using a 0.1×0.1 mm aperture at a wavelength of 1.0 Å. Further testing and experimental application of the Phase II monochromator is planned for 1995. In terms of experimental instrumentation, work continued throughout 1994 on the main beamline instrument, the multi-configuration diffractometer. A number of modes of the diffractometer were tested and commissioned as described below. It is hoped that in the foreseeable future, further expansion of the capabilities of the Australian diffractometer be obtained by the addition of high and low temperature sample environment stages. The development of a small-angle X-ray scattering (SAXS) camera mode of operation is also being considered.

The XAFS station at BL-20B also continues to advance. During 1994, funding was approved for a further major addition to XAFS instrumentation in the form of a multi-element solid-state detector system for the recording of fluorescence XAFS of very dilute samples. The installation of this detector in 1995 will allow previously impossible measurements on dilute solutions, surfaces and single crystals to be carried out at BL-20B.

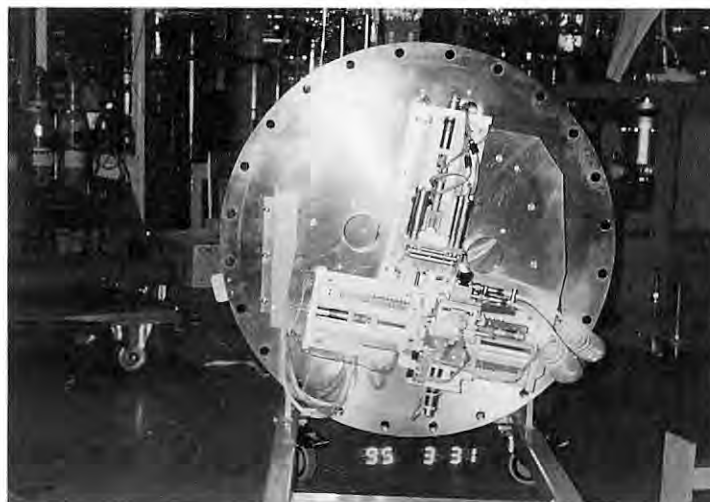


Fig. 19 Photograph showing the mechanism of the Phase II monochromator in use at the Australian Beamline

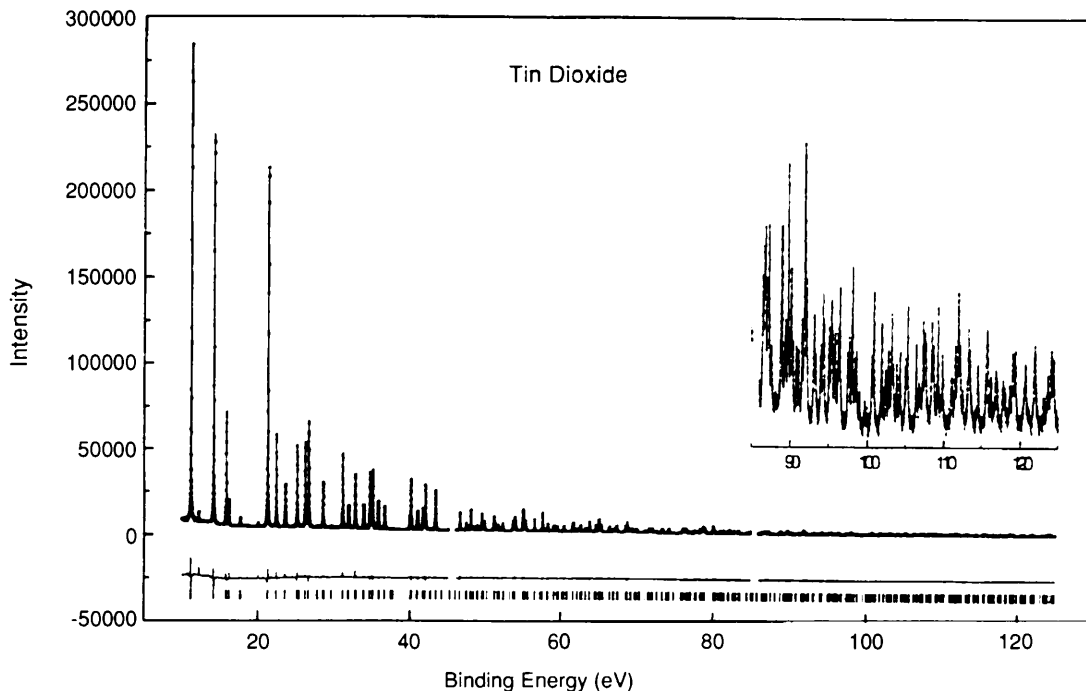


Fig. 20 Example of powder diffraction data extracted from IPs and refined using Rietveld analysis

3. EXPERIMENTS AVAILABLE AT BL20B

The multi-purpose nature of the Australian Beamline and the instrumentation installed there has resulted in many different experimental configurations being commissioned, tested and successfully employed during 1994. The status and application of some of these techniques is described below.

4. HIGH RESOLUTION POWDER DIFFRACTION

The major design goal for the Australian Beamline diffractometer was that it be able to be used for high-resolution powder diffraction using both imaging plates (IPs) in Debye-Scherrer camera mode and conventional detectors and analysers in scanning mode. To this end, a great deal of effort has gone into developing this capability and testing its performance on standard and unknown samples. In particular, the use of IPs to collect powder diffraction data proved to be very successful and the results of testing carried out in 1994 were published.²⁹ Because the use of IPs to collect full pattern powder diffraction data is novel, software to extract the data and output it in a useable form was required and developed by Australian Beamline staff.

Fig. 20 shows an example of a powder diffraction pattern collected at BL-20B and the fitting that was achieved using a Rietveld refinement technique. The quality of the refined data compared to that obtained for the same sample using neutron diffraction is shown in Table 1.

It is apparent that, the X-ray IP data is in good agreement and has allowed the successful determination of such characteristics as atomic positional parameters and isotropic thermal parameters for the unknown sample in question.

It is anticipated that the powder diffraction capability of the Australian Beamline will be open to the general user community of the Photon Factory in mid-1995.

5. X-RAY ABSORPTION SPECTROSCOPY (XAS)

The addition of the harmonic rejection capability to the Phase I monochromator has made it possible to collect high-quality X-ray absorption spectroscopic data at BL-20B. At present, it is possible to collect both transmission and fluorescence XAS data using two or three ion chamber detectors in the former case and a Lytle detector for fluorescence experiments.

Table 1 Summary of Parameters refined from IP Powder Data of SnO₂ collected at $\lambda = 0.65 \text{ \AA}$ compared to Neutron Diffraction Data

	IP data angle range			neutron	
	5-45	45-85	85-125	5-125	data
a	4.7367(2)	4.7341(2)	4.7361(6)	4.7350(1)	4.7374(1)
c	3.1860(1)	3.1843(1)	3.1856(5)	3.1848(1)	3.1864(1)
x	0.305(1)	0.3070(4)	0.3050(4)	0.3053(4)	0.3056(1)
B(Sn)	0.18(2)	0.24(1)	0.29(1)	0.22(1)	0.27(1)
B(O)	0.43(14)	0.43(2)	0.37(2)	0.38(3)	0.34(1)
R _p	7.66	2.79	2.14	4.87	5.07
R _{Bragg}	1.23	1.56	1.63	*	1.33
Peaks	43	160	237	440	74

Both XAFS and XANES techniques were successfully employed and demand for this experimental capability continues to increase. During 1994, the following XAS studies were successfully carried out at the Australian Beamline.

- Transmission XAFS studies of carbon monoxide-bound iron and halide-bound manganese porphyrins
- Transmission XANES study of SYNROC model compounds and precursors
- Fluorescence XAFS study of zeolite-supported organo-metallic catalysts
- Fluorescence XAFS study of germanium defect sites in optical fibres

6. OTHER TECHNIQUES

A number of other experimental configurations using the diffractometer at BL-20B were commissioned during 1994. The unique ability to operate in a vacuum has resulted in very impressive results being recorded when the instrument was used as a triple-axis diffractometer⁹ and for measuring off-specular reflectivity of surfaces⁹. The use of IPs to record diffraction data from multilayer materials has also produced exciting results and further application of the diffractometer to this field of study is expected. Finally, the intensity gain achieved with the Phase II monochromator allowed preliminary testing of the diffractometer in protein camera mode. Further development of this mode is planned for 1995.

7. CONCLUSION

The progress made at the Australian Beamline during 1994 reflects not only the efforts of the beamline staff and the researchers who have assisted in the many commissioning experiments, but is also greatly due to the advice, assistance and cooperation of the Photon Factory staff. The ANBF wishes to thank the academic, technical and administrative staff of the PF and KEK for support and we look forward to a continuation of what is already a successful and fruitful collaboration.

G. J. Foran

References

- 1) Matsushita, T.; Ishikawa, T.; Oyanagi, H. *Nucl. Instrum. and Methods* **A246** (1986) 377.
- 2) Sabine, T. M.; Kennedy, B. J.; Garrett, R. F.; Foran, G. J.; Cookson, D. J. *J. App. Cryst.* in press.
- 3) Garrett, R. F.; Cookson, D. J.; Foran, G. J.; Sabine, T. M.; Kennedy, B. J.; Wilkins, S. W. *Rev. Sci. Instrum.* **66**(2) (1995) 1351.
- 4) Nikulin, A. Yu.; Stevenson, A. W.; Hashizume, H.; Wilkins, S. W.; Cookson, D. J.; Foran, G. J.; Garrett, R. F. *J. Appl. Cryst.* **28** (1995) 57.
- 5) Yamaguchi, Y.; Sakata, O.; Hashizume, H.; Foran, G. J.; Cookson, D. J. *Photon Factory Act. Rep.* 1994.

***PHOTON FACTORY
ACTIVITY REPORT***

1994

PHOTON FACTORY ACTIVITY REPORT 1994

#12

#12